ADVANCED COMBUSTION TECHNOLOGIES FOR LOW CARBON EMISSIONS

EDITED BY: Jun Li, Noroyuki Kobayashi and Zhihua Wang
PUBLISHED IN: Frontiers in Energy Research

frontiers Research Topics

ISSN 1664-8714
ISBN 978-2-8325-0345-4
DOI 10.3389/978-2-8325-0345-4

About Frontiers

Frontiers is more than just an open-access publisher of scholarly articles: it is a pioneering approach to the world of academia, radically improving the way scholarly research is managed. The grand vision of Frontiers is a world where all people have an equal opportunity to seek, share and generate knowledge. Frontiers provides immediate and permanent online open access to all its publications, but this alone is not enough to realize our grand goals.

Frontiers Journal Series

The Frontiers Journal Series is a multi-tier and interdisciplinary set of open-access, online journals, promising a paradigm shift from the current review, selection and dissemination processes in academic publishing. All Frontiers journals are driven by researchers for researchers; therefore, they constitute a service to the scholarly community. At the same time, the Frontiers Journal Series operates on a revolutionary invention, the tiered publishing system, initially addressing specific communities of scholars, and gradually climbing up to broader public understanding, thus serving the interests of the lay society, too.

Dedication to Quality

Each Frontiers article is a landmark of the highest quality, thanks to genuinely collaborative interactions between authors and review editors, who include some of the world's best academicians. Research must be certified by peers before entering a stream of knowledge that may eventually reach the public - and shape society; therefore, Frontiers only applies the most rigorous and unbiased reviews.
Frontiers revolutionizes research publishing by freely delivering the most outstanding research, evaluated with no bias from both the academic and social point of view. By applying the most advanced information technologies, Frontiers is catapulting scholarly publishing into a new generation.

What are Frontiers Research Topics?

Frontiers Research Topics are very popular trademarks of the Frontiers Journals Series: they are collections of at least ten articles, all centered on a particular subject. With their unique mix of varied contributions from Original Research to Review Articles, Frontiers Research Topics unify the most influential researchers, the latest key findings and historical advances in a hot research area! Find out more on how to host your own Frontiers Research Topic or contribute to one as an author by contacting the Frontiers Editorial Office: frontiersin.org/about/contact

ADVANCED COMBUSTION TECHNOLOGIES FOR LOW CARBON EMISSIONS

Topic Editors:
Jun Li, Guangzhou Institute of Energy Conversion, Chinese Academy of Sciences (CAS), China
Noroyuki Kobayashi, Nagoya University, Japan
Zhihua Wang, Zhejiang University, China

Citation: Li, J., Kobayashi, N., Wang, Z., eds. (2023). Advanced Combustion Technologies for Low Carbon Emissions. Lausanne: Frontiers Media SA.
doi: 10.3389/978-2-8325-0345-4

Table of Contents

frontiers | Frontiers in Energy Research

TYPE Editorial
PUBLISHED 13 September 2022
DOI 10.3389/fenrg.2022.956479

OPEN ACCESS

EDITED AND REVIEWED BY
Chungen Yin,
Aalborg University, Denmark

*CORRESPONDENCE
Jun Li,
lijun@ms.giec.ac.cn

SPECIALTY SECTION
This article was submitted to Advanced Clean Fuel Technologies, a section of the journal Frontiers in Energy Research

RECEIVED 30 May 2022
ACCEPTED 25 July 2022
PUBLISHED 13 September 2022

CITATION
Li J, Kobayashi N and Wang Z (2022), Editorial: Advanced combustion technologies for low carbon emissions. *Front. Energy Res.* 10:956479. doi: 10.3389/fenrg.2022.956479

Editorial: Advanced combustion technologies for low carbon emissions

Jun Li[1]*, Noriyuki Kobayashi[2] and Zhihua Wang[3]

[1]Guangzhou Institute of Energy Conversion, Chinese Academy of Sciences, Guangzhou, China, [2]Department of Chemical Systems Engineering, Nagoya University, Nagoya, Japan, [3]State Key Laboratory of Clean Energy Utilization, Zhejiang University, Hangzhou, China

KEYWORDS

low carbon emission, ammonia, combustion characteristics, pollutant emissions, carbon-free fuel

Editorial on the Research Topic
Advanced combustion technologies for low carbon emissions

CO_2 emissions from typical fossil fuel combustion process, such as heat supply, power generation, engine-driven vehicles, aircraft and rockets et al., lead to the global warming. Advanced combustion technologies for fossil fuels and carbon free fuels can reduce CO_2 emission during the practical applications. Hence, the combustion behaviors and the reactivity, flame instability, amount of pollutant emissions from fossil fuels, carbon-free or carbon-neutral fuels such as H_2, NH_3, methanol, and biofuels, are drawing increasing attention in the current world. Many challenges should be solved with advanced combustion technologies. This subject set advanced combustion technologies including pyrolysis, mild combustion, catalytic combustion and carbon free fuels combustion, diagnostic technologies including flow velocity, species and temperature etc., which will helping to obtain fundamental understanding of the advanced combustion technologies.

Co-combustion characteristics of typical biomass and coal blends by thermogravimetric analysis was reported by Yuan et al. The reaction stages, ignition and burnout temperature, maximum weight loss rate, and different combustion indices of the coal and biomass blends were experimentally determined. The results shown that the value of activation energy and the pre-exponential factor increased with the decreasing biomass percentage in the blends, which can provide data on blending fuels in their combustion applicability. Li et al. reported a comprehensive review on combustion characteristics of ammonia as a carbon-free fuel. The experimental and numerical studies of the application of NH_3 as a fuel during combustion process, including the combustion properties of laminar burning velocity, flame structures, pollutant emissions for the application of NH_3 as a carbon free fuel are summarized, which aims to review and describe the suitability of NH_3 as a fuel. Effects of temperature and additives on NO_x emission from combustion of fast-growing grass has been experimentally investigated by Liu et al. A highest denitration rate of 63.28% has been gotten at SiO_2 addition of 5% and

combustion temperature of 600°C. The optimal conditions to limit NO_x emissions at various temperature have been obtained to control the NO_x emissions. Yan et al. and Zhang et al. numerically investigated the injection timing effects on a gasoline direct injection engine performance of in-cylinder combustion process and in-cylinder emission formation and oxidation process, respectively. They concluded that droplet-wall impingement and available duration for mixing were dominant trade-off factors for mixture formation and following combustion process during the whole process from injection to combustion. Furthermore, the fuel–gas mixture was more uniformly distributed and combusted more completely. CO, uHC, soot, and NO_x emission has decreased more than 80% with the injection timing advancing. Zhang et al. proposed a modified conjugate heat transfer model of the combustion chamber and the cooling medium to analyze the temperature distribution of the cylinder heat with the motive of modifying and calibrating the Woschni formula at different altitudes. They pointed out that the modified in-cylinder conjugate heat transfer model can be used to predict the thermal load of diesel engine combustion chamber components under different altitude operating conditions. NH_3 and NO_x interaction chemistry with CH_4 and C_2H_4 at moderate temperature and various pressures was explored by Deng et al. The results showed that the adding of CH_4/C_2H_4, NO/NO_2 ratio and pressure are the main factors to affect NO concentrations. The rate production and sensitivity analyses was performed with a detailed kinetic model. The additional chain-branching pathways regarding NO/NO_2 interconversion were activated with the addition of hydrocarbons because the active radical pool was enriched, the reaction $C_2H_3 + O_2 = CH_2CHO + O$ was crucial reaction to drive the reactivity of $CH_4/C_2H_4/NH_3/NO/NO_2$ mixture. Li et al. studied the effect of wall thickness on the combustion characteristics of non-premixed hydrogen micro-jet flame. They found that the temperature distribution, flame shape, and heat recirculation are changed with the fuel flow velocity were affected by wall thickness. Zhang et al. the combustion characteristics of a laminar non-premixed methane jet flame in oxygen/carbon dioxide co-flow. The simulation results of OH distributions showed good consistency with the results obtained from the experiments. The third-body effect and transport properties of CO_2 didn't exert remarkable effects on the laminar non-premixed flame, while the chemical effect of CO_2 on the laminar non-premixed jet flame was significant.

This Research Topic had a cumulative view of 16,386 at the time of writing this Editorial preface, with 1,862 downloads of the various articles from the researchers all over the world, which show the great interest in the low carbon emissions combustion technologies.

Author contributions

All authors listed have made a substantial, direct, and intellectual contribution to the work and approved it for publication.

Conflict of interest

The authors declare that the research was conducted in the absence of any commercial or financial relationships that could be construed as a potential conflict of interest.

Publisher's note

frontiers in Energy Research

REVIEW
published: 06 October 2021
doi: 10.3389/fenrg.2021.760356

A Review on Combustion Characteristics of Ammonia as a Carbon-Free Fuel

Jun Li[1,2,3,4], *Shini Lai*[1,4], *Danan Chen*[1,4], *Rongjun Wu*[5], *Noriyuki Kobayashi*[5], *Lisheng Deng*[1,2,3] *and Hongyu Huang*[1,2,3,4]*

[1]Guangzhou Institute of Energy Conversion, Chinese Academy of Sciences, Guangzhou, China, [2]Guangdong Key Laboratory of New and Renewable Energy Research and Development, Guangzhou, China, [3]Southern Marine Science and Engineering Guangdong Laboratory (Guangzhou), Guangzhou, China, [4]School of Energy Science and Engineering, University of Science and Technology of China, Guangzhou, China, [5]Department of Chemical Systems Engineering, Nagoya University, Nagoya, Japan

A comprehensive review of combustion characteristics of ammonia (NH_3) as a carbon free fuel is presented. NH_3 is an attractive alternative fuel candidate to reduce the consumption of fossil fuel and the emission of CO_2, soot, and hydrocarbon pollutants, due to its comparable combustion properties, productivities from renewable sources, and storage and transportation by current commercial infrastructure. However, the combustion properties of NH_3 are quite different from conventional hydrocarbon fuels, which highlight the specific difficulties during the application of NH_3. Therefore, this paper presents comparative experimental and numerical studies of the application of NH_3 as a fuel during combustion process, including the combustion properties of laminar burning velocity, flame structures, pollutant emissions for the application of NH_3 as a carbon free fuel. This paper presents the burning velocity and pollutant emissions of NH_3 alone and mixtures with other fuels to improve the combustion properties. The aim of this paper is to review and describe the suitability of NH_3 as a fuel, including the combustion and emission characteristics of NH_3 during its combustion process.

Keywords: ammonia, combustion characteristics, laminar burning velocity, pollutant emissions, carbon-free fuel

OPEN ACCESS

Edited by:
Xuezhong He,
Guangdong Technion-Israel Institute of Technology (GTIIT), China

Reviewed by:
Zhongde Dai,
Sichuan University, China
Guo-xiu Li,
Beijing Jiaotong University, China

***Correspondence:**
Hongyu Huang
huaghy@ms.giec.ac.cn

Specialty section:
This article was submitted to Advanced Clean Fuel Technologies, a section of the journal Frontiers in Energy Research

Received: *18 August 2021*
Accepted: *20 September 2021*
Published: *06 October 2021*

Citation:
Li J, Lai S, Chen D, Wu R, Kobayashi N, Deng L and Huang H (2021) A Review on Combustion Characteristics of Ammonia as a Carbon-Free Fuel. Front. Energy Res. 9:760356. doi: 10.3389/fenrg.2021.760356

INTRODUCTION

With the rapid economic development and population explosion of recent decades, the global primary energy consumption has increased dramatically. Coal, petroleum, and natural gas remain the major sources of energy across the world. Pollutants such as CO_2, CO, SO_2, NO_x, volatile organic compounds, particulate matter et al., are released by the combustion of petroleum, coal, and natural gas fuels (IEA, 2021). CO_2 is the major contributor to global warming. In the recent years, the development of new technologies aiming to reduce problems related to energy consumption, for application in both developed and developing countries, has become urgent, because of the increasing strictness of governmental regulation of energy and CO_2 emissions. Such developments lead to the search for carbon-free fuels, and the increasing importance of renewable energy sources (Astbury, 2008).

Combustion process during various industry processes contributed huge amount of CO_2 emissions. In order to obtain the target of zero-carbon emissions, it is necessary to reduce CO_2 emissions with the application of carbon-free fuel in combustion system. NH_3 is an attractive hydrogen carrier with a high hydrogen density of 17.8% per unit weight, which can be considered as a

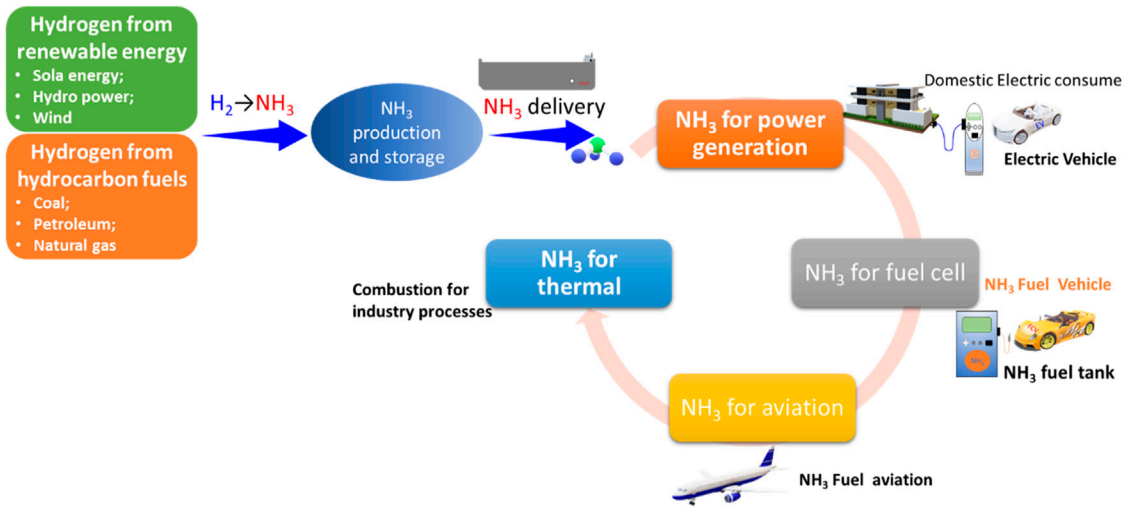

FIGURE 1 | Application of NH_3 as a near zero emission fuel system.

carbon-free fuel with the advantage of 1) CO_2, SO_x, and soot emission free; 2) production from various sources, such as fossil fuels, renewable sources, and biomass; 3) transport and storage with existing facility, such as fuel tanks, ships, trucks, and pipelines, which makes NH_3 as a favorable alternative fuel candidate (Wang et al., 2007; Zamfirescu and Dincer, 2008; Zamfirescu and Dincer, 2009; Andersson and Lundgren, 2014; Habgood et al., 2015; Afif et al., 2016; Chai et al., 2021). As shown in **Figure 1**, NH_3 is synthesized from energy sources such as wind power, nuclear energy, and fossil fuels with CO_2 capture and storage (CCS), etc., which means that NH_3 is fully CO_2 free recyclable as a promising carbon-free fuel.

The potential of NH_3 as a carbon-free fuel owing to its suitable storage and transportation properties has been demonstrated, and applications for its combustion in vehicular engines and turbines are apparent. However, major challenges for NH_3 combustion are to provide its alternative fuels capabilities with outstanding performance, durability and reliability, optimize combustion properties, and lower pollutant emissions, which needs a strict determination of combustion properties during the application of NH_3 as a fuel. The lack of understanding of the NH_3 combustion characteristics, methods of combustion enhancement, and optimization of NO_x formation in combustion have placed limits on the utilization of NH_3 as a fuel. It is necessary to have a comprehensive understanding of the combustion and emission characteristics of pure NH_3 and mixture with other fuels, which are expected to supply power for transport vehicles, electricity for power generation, and heating for industry with suitable combustion properties in future energy system.

PROPERTIES OF NH_3

As a carbon-free chemical compound, NH_3 is a colorless gas with a characteristic pungent smell. The chemical and physical properties of NH_3 are listed in **Table 1**. In 1909, German chemists Fritz Haber and Carl Bosch developed the NH_3 production process, now known as the Haber-Bosch process, which catalytically converts N_2 (from air) and H_2 (from industrial processes) to NH_3 using a metal catalyst under high-pressure (150–250 atm) and high-temperature (400–600°C) conditions. The production of NH_3 has dramatically increased in recent years. In 2020, the global NH_3 production was around 144 million metric ton (shown in **Figure 2**). The highest individual producers are China is (48.0 million ton: 33.3%), India (12.0 million ton: 8.3%), Russia (10.3 million ton: 7.2%), and the United States (9.2 million ton: 6.4%) (USGS, 2021). The majority of NH_3 is used in industrial and agricultural applications such as fertilizer, plastics, nitric acid, and explosives production, and refrigeration. NH_3 is a poisonous gas, and its safety hazard is a significant obstacle in its use. According to the US Department of Health and Human Services, the permissible exposure limit (PEL) for NH_3 is 35 ppm (27 mg m^{-3}) as a short-term (15 min) exposure limit (CDC, 1994).

TABLE 1 | Chemical and physical properties of gaseous NH_3 (NCBI, 2021).

Items	Symbols	Value	Unit
Molecular weight	M	17.031	g mol^{-1}
Critical temperature	T_{cr}	405.15	K
Critical pressure	P_{cr}	111.5	Atm
Density (STP)	P	0.769	kg m^{-3}
Viscosity (1 atm, 273 K)	M	9.8E-5	Poise
Heat capacity at constant P	C_p	0.037	kJ mol^{-1} K^{-1}
Heat capacity at constant V	C_v	0.028	kJ mol^{-1} K^{-1}
Thermal conductivity	Λ	0.002219	W m^{-1} K^{-1}
		18.65	MJ kg^{-1}
Lower heating value	LHV	3,080	MJ L^{-1}
		317.56	kJ mol
Autoignition temperature	T_{ig}	903	K
Lower flammability limit	LFL	15%	—
Upper flammability limit	UFL	27%	—

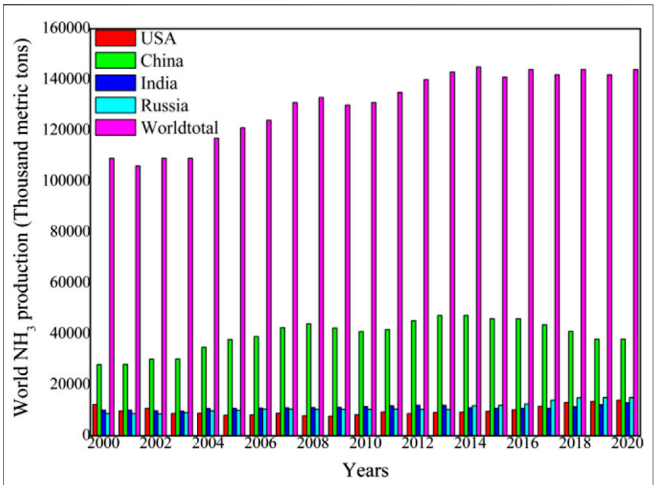

FIGURE 2 | World NH_3 production (Data from USGS, 2021).

Some characteristics of ammonia are compared with conventional liquefied fuels such as diesel, gasoline, and natural gas, which are listed in **Table 2** (Dimitriou and Javaid, 2020). The liquefied ammonia can be easily stored at 298 K and 10.2 atm. But the stored pressure of compressed liquid natural gas is 245.0 atm at 298 K, which is much higher than that of ammonia. Although the fuel density and energy density of ammonia are lower than those of gasoline and diesel, the fuel density of ammonia is three times as many as that of natural gas and the energy density is also much higher than that of natural gas. The octane rating of ammonia is 110 RON, which is higher than those of natural gas and gasoline. It indicates that the engine fueled by ammonia can be operated at higher pressure. What's more, ammonia exhibits much higher absolute minimum ignition energy than gasoline, which can be improved through some methods like co-firing with hydrogen. Ammonia has potential to be used as a fuel and the performance can be comparable to that of conventional fuel. For example, when directly using ammonia in an internal combustion engine, the driving range can reach 592 km, which is comparable to that of LPG and slightly lower than that of gasoline (Zamfirescu and Dincer, 2008).

NH_3 has been widely used in the industry. It has been used in the manufacture of fertilizers, in organic and inorganic synthesis of chemical compounds as HNO, urea, plastics fibers and so on, in mining and metallurgy, in petroleum refining as neutralizing agent, and also NH_3 can be used as commercial refrigerant in food processing, as a substitute for calcium in bisulfite pulping of wood, and to purify municipal and industrial water supplies. Effective methods such as process enclosure, local exhaust ventilation, general dilution ventilation, and personal protective equipment, should be followed in controlling worker exposures or lead of this substance when used it as a fuel.

The use of NH_3 as a fuel by adding it to methane (Williams et al., 1991; Bell et al., 2002; Sullivan et al., 2002; Henshaw et al., 2005; Barbas et al., 2015), diesel (Reiter and Kong, 2011; Gill et al., 2012), DME (Gross and Kong, 2013), and H_2 (Skreiberg et al., 2004; Mendiara and Glarborg, 2009; Mørch et al., 2011; Joo and Kwon, 2012; Um et al., 2013; Choi et al., 2015) has been investigated. NH_3 has often been used as an agent for decreasing NO_x emissions in industrial treatment processes through selective catalytic reactions (Xu et al., 2002; Grossale et al., 2009; Yun and Kim, 2013). For CH_4 combustion, both the CO and NO emissions decreased with increasing excess oxygen coefficient. A higher CO emission and lower NO emission would result from a decreased oxygen concentration in the oxidizer under the O_2/CO_2 combustion atmosphere. Conversely, a higher NO_x emission and a significantly lower CO emission are formed in oxy-fuel firing compared with those formed with air firing. CO and NO_x formation and decomposition would be completely different when NH_3 is added to carbon-based fuels. In the absence of NH_3 seeding combustion, the most important NO formation process for CH_4 combustion is prompt-NO formation, followed by the NNH, thermal-NO, and N_2O formation processes. When the combustion mixture is seeded with NH_3 at concentrations of several to several thousand ppm, fuel-NO formation becomes the dominant process; with higher NH_3 concentrations, a greater portion is converted to N_2 rather than to NO (Williams et al., 1991; Barbas et al., 2015). In the ignition engine, the addition of NH_3 leads to a longer ignition delay and limits the engine load because of the high autoignition temperature and low combustion rate (or low burning velocity). The combustion pressure and temperature would also be reduced with the addition of NH_3, leading to higher CO and HC emissions. NO_x formation would be enhanced because of NO_x formation from fuel-nitrogen when NH_3 is added. However, soot formation would be extremely low (Gross and Kong, 2013). Furthermore, the substitution of NH_3 could be favored, not only because of the replacement of the carbon-based fuel, but also because it is an efficient method for reducing overall CO_2 emissions (Gill et al., 2012; Gross and Kong, 2013).

TABLE 2 | Some characteristics of NH_3 versus natural gas, gasoline, and diesel (Dimitriou and Javaid, 2020).

Properties	Ammonia	Natural gas	Gasoline	Diesel	Units
Storage method	Compressed Liquid	Compressed Liquid	Liquid	Liquid	—
Storage temperature	298	298	298	298	K
Storage pressure	10.2	245.0	1.0	1.0	atm
Absolute minimum ignition energy	8	—	0.14	—	mJ
Fuel density	602.8	187.2	698.3	838.8	kg/m^3
Energy density	11,333	7,132	31,074	36,403	MJ/m^3
Octane rating	110	107	90–98	—	RON

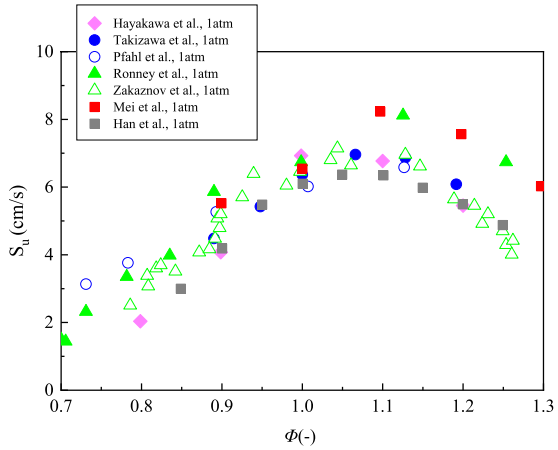

FIGURE 3 | Laminar burning velocity of NH_3 flame with a function of equivalence ratio at 298 K and 1 atm, replotted from (Han et al., 2019; Kobayashi et al., 2019; Mei et al., 2019).

LAMINAR BURNING VELOCITY OF NH_3

Laminar burning velocity is a significant important parameter during fuel combustion. The laminar burning velocity is the speed at which unburned gases move through the combustion wave in the direction normal to the wave surface, which can be calculated by the Metghalchi and Kech power-law relation as follows (Metghalchi and Keck, 1982):

$$S_u = S_{u0}\left(\frac{T_u}{T_0}\right)^{\alpha}\left(\frac{p}{p_0}\right)^{\beta} \quad (1)$$

where S_u is the laminar burning velocity (m/s), T_u is the unburned temperature (K), T_0 = 298 K, p is pressure (atm), p_0 = 1 atm, S_{u0}, α, and β are constants.

Many researches about laminar burning velocity of ammonia/air flames have been reported, most of which were studied under ambient condition (Zakaznov et al., 1978; Ronney, 1988; Pfahl et al., 2000; Takizawa et al., 2008; Hayakawa et al., 2015a; Han et al., 2019, Mei et al., 2019). Zakaznov et al. measured the burning velocity by cylindrical-tube method at room temperature and atmospheric pressure (Zakaznov et al., 1978). Ronney et al. measured the flame speed by a constant-volume cylindrical combustion vessel at microgravity condition (Ronney, 1988). Pfahl et al. measured the behavior of ammonia/air flames by using the schlieren system in a constant volume combustion vessel (Pfahl et al., 2000). In order to minimize the uncertainty caused by the buoyancy effect, they also measured the horizontal component of the flame motion. Takizawa et al. measured the laminar burning velocity using the spherical-vessel method in a constant volume combustion vessel (Takizawa et al., 2008). Hayakawa et al. measured the flame speed using high speed schlieren photography in a constant volume combustion chamber (Hayakawa et al., 2015a). Recently, Han et al. measured the flame propagation of ammonia/air by using heat flux method (Han et al., 2019). And the laminar burning velocities of ammonia/air mixtures was also investigated using a high-pressure constant-volume cylindrical combustion vessel by Mei et al. (2019). **Figure 3** shows the relationship between laminar burning velocities of NH_3/air flames and equivalence ratio at 298 K and 1 atm. The range of the flame velocity is roughly from 1.4 to 8.23 cm/s at φ = 0.7–1.3. It can be observed that the results measured by different groups reach their peaks around φ = 1.1, while the maximum values vary from 6.3 to 8.2 cm/s. The relative differences are little at lean conditions, however, a discrepancy more than 2 cm/s appears under fuel-rich condition between the experimental results. The burning velocity of NH_3/air flame is relatively low when compared with that of CH_4/air flame whose maximum value is about 35 cm/s (Law, 2006).

Ronney et al. measured the flame speed at p = 0.066, 0.132, 0.329, 1, and 1.974 atm. They found that the change of pressure had a modest influence on the flame velocity (Ronney, 1988). Duynslaegher et al. investigated the ammonia/air flame speed by using Konnov mechanism at T = 300K, P = 1–40 atm and φ = 1.0 (Duynslaegher et al., 2010). Results show an increase of pressure had a negative effect on the flame propagation, especially at the low pressure. With the pressure increased from 1 to 10 atm, the flame speed rapidly decreased from 12.67 cm/s to 8.15 cm/s. But with the pressure increased from 30 to 40 atm, the burning velocity decreased smoothly from 6.13 to 5.65 cm/s. Hayakawa et al. studied the laminar burning velocity of ammonia/air flames at elevated pressures by five detailed mechanism, which was validated by the measured experimental results (shown in **Figure 4**, Hayakawa et al., 2015a). **Figure 4** shows the laminar burning velocities under different initial pressure P_i and equivalence ratio φ, plotted along with simulation results by using Tian, Miller, Konnov, GRI 3.0, and Lindsted mechanism (Lindstedt et al., 1994; Miller et al., 1983; Frenklach et al., 2000; Konnov, 2009; Tian et al., 2009). The flame velocity decreases with the increase of initial pressure under the equivalence ratios of 0.9, 1.0, and 1.2. The tendency of the experimental and simulation results is the same as those of hydrocarbon. But it is different from the results of Ronney et al., which are indicated that pressure had a little influence on the flame speed (Ronney, 1988). The initial pressure has a larger effect on flame propagation speed at φ = 1. For example, as pressure increased from 1 to 5 atm, the laminar burning velocity of measured stoichiometric NH_3/air flame deceased from 6.9 to 4 cm/s (shown in **Figure 4B**), while the differences is about 1 cm/s at φ = 0.9 and 1.2 (shown in **Figures 4A,C**). As shown in **Figure 4**, most mechanism significantly over-predict the measured burning velocity. It is notable that the simulation results by Konnov mechanism is about two times larger than the measured values while the prediction results by GRI 3.0 mechanism closely agree with the experimental data. However, GRI 3.0 mechanism lacks some ammonia oxidation reactions which are very important for the numerical simulation of NO concentration in ammonia/air flame. Therefore, further improvements of those mechanisms are very necessary. Liu et al. experimentally and numerically studied the variations of laminar burning velocity with initial pressure for ammonia/air flame (Liu et al., 2019a). The flame speed has been measured at

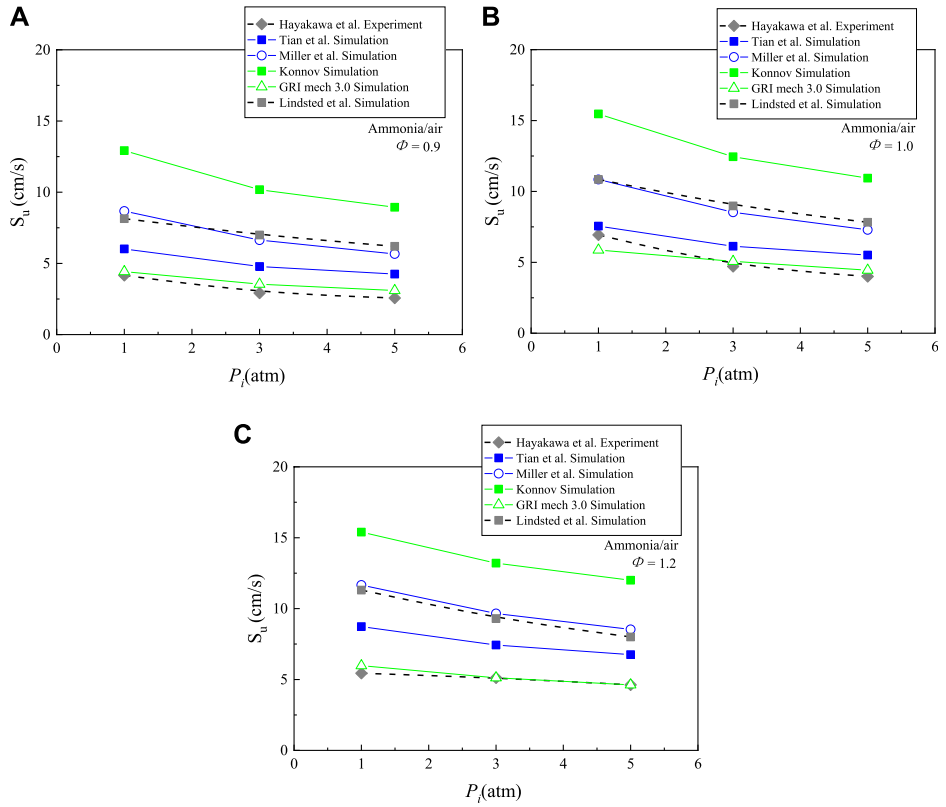

FIGURE 4 | Laminar burning velocity of NH_3 flame with a function of initial mixture pressure at φ = 0.9, 1 and 1.2, replotted from (Hayakawa et al., 2015a).

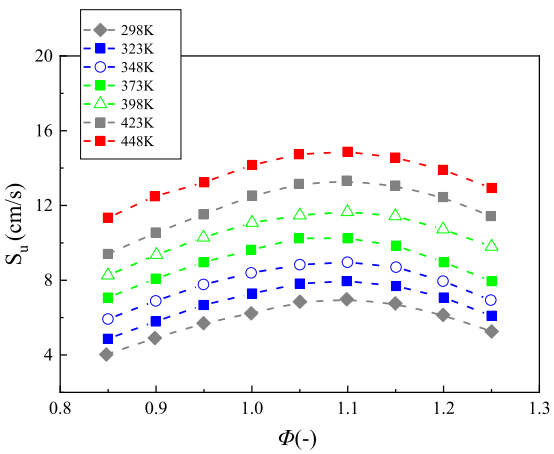

FIGURE 5 | Laminar burning velocity of NH_3 flame with a function of equivalence ratio at various temperature, replotted from (Han et al., 2020).

initial pressure from 0.3 to 1.6 atm, covering equivalence ratios from 0.5 to 1.3 and at 298 K. The measured laminar burning velocities of NH_3 flame firstly increased slightly and then decreased with the increasing pressure. The burning velocity of stoichiometric flame reaches the peak value at 0.5 atm. The maximum values exist at 0.7 atm when the equivalence ratio is 0.5 or 1.3. Generally, the laminar burning velocity decreases with an increase in pressure, which is agreeable with the observation obtained by Hayakawa et al. (2015a). The numerical simulation was calculated by using the GRI 3.0 mechanism under initial pressure ranged from 0.3 to 1.6 atm, and equivalence ratio of 1.0 and temperature of 298 K. The difference between the measurements and the calculations is around 12 cm/s.

The influence of temperature is rarely investigated. Cohen measured the laminar burning velocity of ammonia/air flame at temperature ranged from 323 to 423 K by using a flat flame burner (Cohen, 1955). Recently, Lhuillier et al. measured the flame speed at 1 atm and temperature from 298 to 473 K by the spherical flame method (Lhuillier et al., 2020a). Han et al. measured the laminar burning velocity of NH_3 flame using the heat flux method at temperature from 298 to 448 K and 1 atm (shown in **Figure 5**, Han et al., 2020). Li et al. numerically investigated the effect of preheating temperature on the combustion and NO emission characteristics of ammonia flame (Li et al., 2016a; Li et al., 2016b). In all temperature ranges, the laminar burning velocities increase firstly before the equivalence ratio reaches 1.1, and then decrease when the equivalence ratio is large than 1.1. The maximum value of flame speed at different temperatures ranges from 6.98 to 14.87 cm/s. With the temperature increasing, the flame speed exponentially increases. The results measured by Han et al. at 423 K were compared with those from Cohen and Lhuillier (Cohen, 1955;

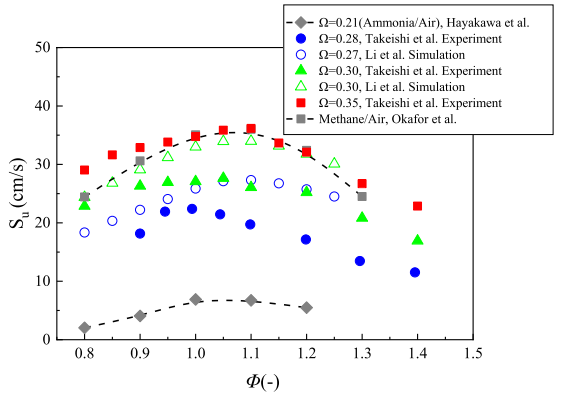

FIGURE 6 | Laminar burning velocity of NH_3 flame with a function of equivalence ratio at various oxygen enrichment level, replotted from (Hayakawa et al., 2015a, Takeishi et al., 2015; Li et al., 2015; Okafor et al., 2018; Kobayashi et al., 2019).

Han et al., 2020; Lhuillier et al., 2020b). It was found that the experimental values obtained by Han et al. are lower than those from Cohen and Lhuillier. The difference between the measurements is around 2 cm/s, which is larger at fuel-lean conditions. The simulation results by using five mechanisms were also performed. Comparison of numerical and experimental data showed that the simulations results by using Okafor mechanism (Okafor et al., 2018) and Otomo mechanism (Otomo et al., 2018) performed best.

Oxygen enriched combustion can be considered as a promising approach to increase burning velocity. The experimental results measured by Takeishi are shown in **Figure 6** (Takeishi et al., 2015). It can be observed that the velocities can be close to those of CH_4/air flames when the O_2 concentration up to 0.35 and the maximum velocity improves to 36.1 cm/s, which is around 5 times the value measured under the air condition. Li et al. (2015) numerically investigated the effect of the oxygen content towards the burning velocity of NH_3/air flame by using the Millar mechanism (Millar and Bowman, 1989) and the Reductive Konnov mechanisms (Duynslaegher et al., 2009; Duynslaegher et al., 2012). The maximum laminar burning velocity increases from 27.5 to 33.9 cm/s when the O_2 content increases from 0.27 to 0.30, and the values of laminar burning velocity at the O_2 content of 0.30 are always 6–7 cm/s higher than those at the O_2 content of 0.27. It is mainly due to an increase of the reaction rates of OH, H, O, and NH_2 radicals under a higher O_2 concentration. It is found that the laminar burning velocities calculated by Li et al. are over-predicted when compared with the results of Takeishi's experiment at the O_2 content of 0.30, especially at fuel rich conditions. For example, the difference between experimental and numerical results reaches 7.9 cm/s at the equivalence ratio of 1.1, while the discrepancy is around 1.5 cm/s at the equivalence ratio of 0.8. Recently, it was found that the burning velocities of ammonia are proper for the practical applications when the range of O_2 volume concentration in O_2/N_2 mixture is roughly from 0.35 to 0.40 (Kim et al., 2021). Mei et al. measured the ammonia/air flame speed under the O_2 content ranged from 0.21 to 0.45 at 298 K, the pressure ranged from 1 to 5 atm and the equivalence ratios from 0.7 to 1.5 by using more complicated constant pressure spherical flame method (Mei et al., 2019). The flame speed increases with an increase of the O_2 concentration, but decrease with an increase of initial pressure. The experimental results showed that the flame propagation speeds are lower than those of CH_4/air flames at the O_2 concentration of 0.35. It is different from the results of Takeishi et al., which indicated that the laminar burning velocities at the O_2 concentration of 0.35 are almost the same as those of CH_4/air flames (Takeishi et al., 2015). In addition, they constructed a model of ammonia combustion with 38 species and 265 reactions, which can predict the results with a favorable satisfaction. Wang et al. measured the oxy-ammonia flame speed in a constant volume vessel at the temperatures ranged from 303 to 393 K, the O_2 content ranged from 0.6 to 1.0 and the equivalence ratios ranged from 0.6 to 1.4 (Wang et al., 2020). Results show that the peak value of laminar burning velocity can reach 125.1 cm/s at the O_2 content of 1.0. The equivalence ratio corresponding maximum value is around 0.9. Besides, the flame velocity increases with the increasing temperature, which is more sensitive to the change of temperature under lower O_2 content.

Due to low burning velocity, ammonia usually is burned with the addition possessing higher reactivity such as hydrogen. Ichikawa et al. measured the ammonia/hydrogen/air flame speed at pressure of 1, 3, and 5 atm by using a high-pressure constant volume chamber (shown in **Figure 7**, Ichikawa et al., 2015). The experimental results show an exponential variation of laminar burning velocity under different volumetric hydrogen fraction and the ammonia/hydrogen/air flame speed decreased with an increase in pressure under the same hydrogen concentration. It is obvious that the laminar burning velocity largely decreased when the pressure increased from 1 to 3 atm, while the values of burning velocities at 3 atm were almost the same as those of flame speeds at 5 atm. This means that the influence of initial pressure conspicuously appeared under low pressure, but that effects barely occurred under high pressure. Lee

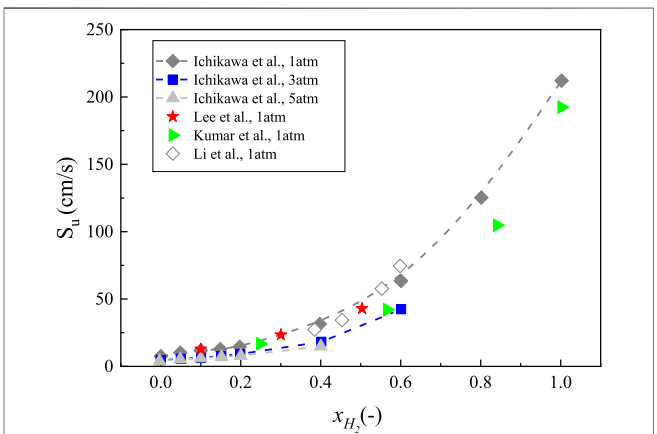

FIGURE 7 | Laminar burning velocity of NH_3 flame with a function of volumetric hydrogen fraction at 298 K, replotted from (Lee et al., 2010; Kumar and Meyer, 2013; Li et al., 2014; Ichikawa et al., 2015).

et al., Kumar et al., and Li et al. also investigated the flame propagation speed of ammonia/hydrogen/air mixture at 1 atm (Lee et al., 2010; Kumar and Meyer, 2013; Li et al., 2014; Li et al., 2017; Li et al., 2019a). The differences among experimental results were small and the tendencies were consistent with that measured by Ichikawa et al. (2015). It also can be observed that the value of flame speed was around 35.1 cm/s at the hydrogen concentration of 0.45 which was close to that of CH_4/air mixture, indicating that the addition of hydrogen can effectively improve ammonia combustion. Han et al. measured the laminar burning velocities of NH_3/H_2/air by using the heat flux method (covering φ = 0.7–1.6, χ_{H_2} = 0.15–0.4, P = 1atm, K = 298 K) (Han et al., 2019). Results show that the values of measurements reached their peaks at φ = 1.05 when the hydrogen ratio ranged from 0 to 0.35. However, the peak velocity occurred at the equivalence ratio of 1.1 when the hydrogen ratio increased up to 0.4. This tendency has good agreement with the finding that the peak value of the hydrogen/air flame speed occurs at the equivalence ratio of 1.8 (Kwon and Faeth, 2001). They also found that mixing ammonia with the addition of H_2 is the most effective way to improve the flame propagation by comparing with the burning velocity of NH_3/CH_4 mixture, NH_3/H_2 mixture, and NH_3/CO mixture. The flame speeds of NH_3/H_2 flames (the hydrogen concentration ranged from 0.0 to 0.3) and pure ammonia at oxygen rich conditions (the oxygen concentration ranged from 0.21 to 0.30) were measured by Shrestha et al. at P = 1–10 atm and T = 298–473 K (Shrestha et al., 2021). They also developed a mechanism for the oxidation of ammonia/hydrogen mixtures and ammonia. Based on this model, they found that the N_2H_2 formation path was favored in fuel rich condition, which is very important for numerical simulation.

Different from adding hydrogen, hydrogen production can also be from ammonia decomposition, since ammonia has high hydrogen density (Valera-Medina et al., 2018; Kobayashi et al., 2019). It was found that ammonia started to crack when the temperature reached 473.15 K and the conversion efficiency can reach 98–99% when the temperature up to 698.15 K (Klerke et al., 2008; Lan et al., 2012). What's more, in contrast to co-firing hydrogen, using partially cracked ammonia is more economical and easier to implement (Yang et al., 2019). However, the deep insight into the combustion characteristics of $NH_3/H_2/N_2$ mixtures are limited (Mei et al., 2021; Wiseman et al., 2021). Very recently, Mei et al. experimentally investigated the laminar burning velocities of partially cracked NH_3/air mixtures in a high-pressure constant volume cylindrical combustion vessel at the initial pressure of 1–10 atm, the equivalence ratios from 0.7 to 1.4 and the initial temperature of 298 K (Mei et al., 2021). Results showed that the laminar flame speed of $NH_3/H_2/N_2$/air mixtures increased with an increase of the cracking ratio due to the increase of H_2 concentration. It was found that the flame speed could reach 38.1 cm/s at 1 atm and the cracking ratio of 40%, which is close to that of methane/air mixtures. They also found that the increase of N_2 concentration and the initial pressure had a negative effect on the flame speed. Then though the numerical simulation, they recognized that $H + O_2 (+M) = HO_2 (+M)$ plays an important in flame propagation.

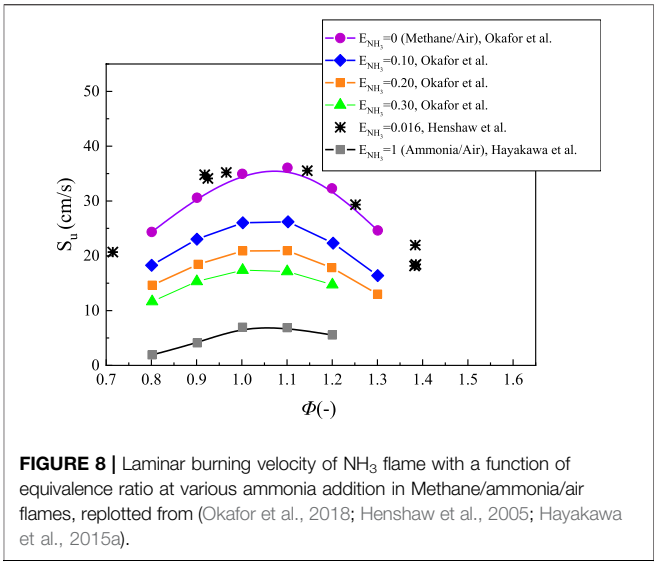

FIGURE 8 | Laminar burning velocity of NH_3 flame with a function of equivalence ratio at various ammonia addition in Methane/ammonia/air flames, replotted from (Okafor et al., 2018; Henshaw et al., 2005; Hayakawa et al., 2015a).

Blending ammonia with methane is also an effective method to improve the combustion characteristics of NH_3/air flames propagation. Konnov et al. experimentally investigated the laminar burning velocity of $CH_4/O_2/N_2$ flames doped with 0.5% NH_3 by using a heat flux method. Results show that ammonia had no significant influence on the flame speed (Konnov et al., 2006). Okafor et al. and Henshaw et al. measured the flame speeds of NH_3/CH_4/air flames as a function of the equivalence ratio at 298 K and 1 atm (Henshaw et al., 2005; Okafor et al., 2018). Zhou et al. experimentally and numerically investigated the laminar flames of NH_3/syngas/air and NH_3/bio-syngas/air at elevated temperature (Zhou et al., 2021). Wang et al. experimentally and numerically investigated the laminar burning velocities of NH_3 mixing with CH_3OH and C_2H_5OH in premixed flames (Wang et al., 2021a). **Figure 8** shows that the flame speeds decreased with the heat fraction of ammonia E_{NH3} increased and the flame speed were close to those of methane/air mixture when E_{NH3} reached 0.016. Obviously, the burning velocity decreased more sharply when E_{NH3} ranged from 0 to 0.1. The difference between the flame speed at E_{NH3} = 0.1 and E_{NH3} = 0.3 is about 8.8 cm/s, while the discrepancy is around 9.8 cm/s when the E_{NH3} increases from 0 to 0.1. Xiao et al. investigated the laminar burning velocity of NH_3/CH_4 mixtures with the ammonia fraction ranged from 0 to 100% (Xiao et al., 2017b). They also found that ammonia had a negative impact on flame propagation. Shu et al. studied the fundamental combustion characteristics of NH_3/CH_4/air mixtures by using expending spherical flames (Shu et al., 2021). They found that the laminar burning velocity varied almost linearly with the methane volume fraction and the H/OH radicals were very important for the propagation of flames under fuel lean conditions. Furthermore, the laminar burning velocity had a strong linear relationship with the maximum mole fraction of (H + OH) radicals under lean conditions when the pressure ranged from 1 to 15 atm and the methane volume fraction ranged from 0.30 to 0.70. The laminar burning velocity of ammonia/methane mixture under variable O_2 and CO_2 mole fractions of

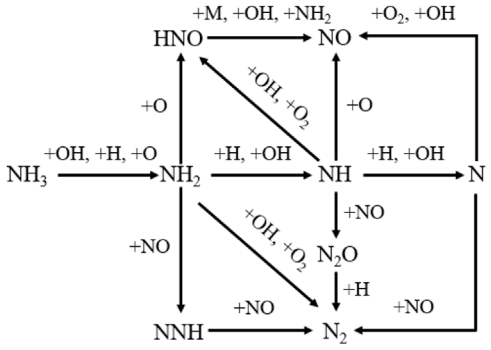

FIGURE 9 | Diagram of ammonia oxidation pathway, replotted from (Millar and Bowman, 1989).

0.35–0.40 and 0.45 to 0.65, respectively, was experimentally investigated by Liu et al. (2019b). They found that the maximum flame speed decreased from 35.6 to 25.6 cm/s when the CO_2 mole fraction increased from 0.45 to 0.65, while the peak speed increased from 25.6 to 36.6 cm/s when the O_2 concentration increased from 0.35 to 0.40. Through the simulation results by using HUST Mechanism, it can be observed that the burning velocity has linear correlations between CO_2 and O_2 concentration.

NO_X EMISSIONS

When ammonia is completely combusted, it only produces nitrogen and water without involving the production of NO_x. However, NO_x emission is relatively high in practical combustion, which is a main challenge of ammonia combustion. In order to reduce the production of NO_x, some detailed mechanism of ammonia combustion is necessary. NO_x is mainly composed of thermal NO_x and fuel NO_x. Thermal NO is usually produced by the oxidation of N_2 at temperature up to 1800 K. The extended Zeldovich mechanism is widely used to describe the formation of thermal NO. The reactions of thermal NO have three important pathways: $N_2 + O=NO + N$, $N + O_2 = NO + O$, and $N + OH = NO + H$. The first reaction limits the reaction rate and usually take place when the temperature above 1,800 K. Therefore, controlling temperature is an effective way to reduce thermal NO production.

Fuel NO_x emission is widely studied by many researchers. Miller et al. studied the reaction path of NH_3 oxidation and proposed a kinetics including 22 species and 98 elementary reactions (shown as **Figure 9**, Millar and Bowman, 1989). Firstly, ammonia is converted to NH_2 by the reaction with OH, which is the primary path under both fuel rich and lean conditions. It is also consumed by O to produce NH_2 under fuel lean condition and is consumed by H under rich condition. The reason of this phenomenon is that rich burning flame needs more oxygen or oxygen atoms, which results in the proportion of H in O/H radicals is high when compared to fuel lean conditions (Chai et al., 2021). It is obvious that the reactions involving NH_i (i = 0, 1, 2) have very significant impact on the formation and reduction of NO. And HNO intermediate make great contribution to NO formation via reacting with OH, NH_2, and M. Lindstedt et al. also found that fuel NO is mainly produced by the reactions involving HNO (Lindstedt et al., 1994). For ammonia flames, HNO + M = NO + H + M reaction plays a key role and HNO + OH = NO + H_2O reaction becomes important when the equivalence ratio less than 1. What's more, for the conversion of NO, the reaction between NO and NH_2 is the major path.

Dean et al. found that NNH dissociation plays an important role in the formation of N_2 under fuel rich conditions, which mainly produced by N_2H_2 (Dean et al., 1984). The NH_i radicals can be converted to N_2 without including NO, which has a potential to reduce the formation of NO. They developed the NNH mechanism (Dean and Bozzelli, 2000). The reaction between NNH intermediate and O atom is the main path to generate NO, and the related reaction are shown as follow: NNH + O=NH + NO, NNH + O=N_2O + H, and NNH + O=N_2 + OH. Klippenstein et al. calculated the reaction rate constant of NNH by using an improved model based on the Miller mechanism (Miller and Glarborg, 1999; Klippenstein et al., 2011). They found that the rate constant of NNH + O=N_2 + OH is over-predicted by Dean et al. and the NNH + O reaction is very fast.

Some factors like equivalence ratio and pressure are also very important for NO_x emissions. The main component of NO_x is NO. It was found that with an increase of the equivalence ratio, the mole fraction of NO in NH_3/air flame firstly increased before the equivalence ratio reaches 0.9 and then rapidly decreased when the equivalence ratio is large than 0.9 (Kobayashi et al., 2019). The production of NO is extremely low after the equivalence ratio up to 1.3. Therefore, it seems that burning under fuel rich condition is an effective way to reduce NO_x emission. Hayakawa et al. experimentally and numerically studied the characteristics of

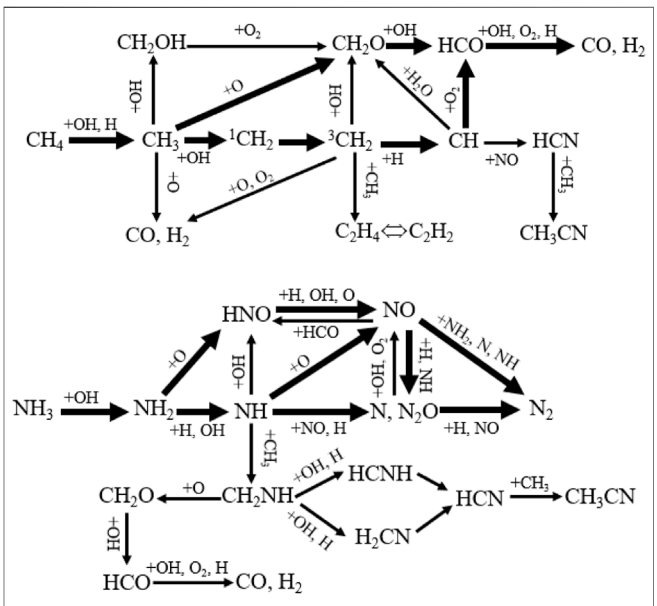

FIGURE 10 | Diagram of ammonia/methane mixture oxidation pathway, replotted from (Tian et al., 2009).

NO_x formation in ammonia/air flames at different pressures and equivalence ratios (covering p = 1.0–3.0 atm and φ = 0.7–1.1) (Hayakawa et al., 2015b). The experiments were performed in a nozzle-type burner and the numerical simulation used the Tian mechanism (Tian et al., 2009). Results show that the NO concentration decreased with an increasing equivalence ratio at pressure of 1 atm, which is mainly due to surplus production of NH_i (i = 0, 1, 2) under fuel rich conditions. Besides, with the increasing pressure, the concentration of NO decreased while the reaction rate of OH + H + M = H_2O + M increased. Therefore, they proposed that H and OH radicals mentioned above limited the formation of NO.

In order to use pure ammonia in practical applicants, some researches were performed to provide a deep insight into the characteristic of NO_x emission. Lee et al. proposed a combustion strategy in order to use pure ammonia in the internal combustion engine (Lee and Song, 2018). In this strategy, they injected the lean ammonia/air mixture during the intake process which was auto-ignited in the next step. This method can raise the temperature and pressure of the cylinder and it has a positive effect on ammonia spray combustion. Then they studied the mechanism of NO formation and found that NO emission in this engine largely depend on the main SOI variation. For instance, the maximum value of NO formation up to 8,500 ppm, while the reduction of NO emission can reach 5,460 ppm by changing the SOI timing. Kurata studied the emission characteristics of non-premixed NH_3/air in gas turbine power generations (Kurata et al., 2017). It was found that the production of NO_x and slip NH_3 were strongly influenced by the combustor inlet temperature. The existence of NO_x and slip NH_3 at the mid-range of combustor inlet temperature implied that there is a possibility of NO reduction through selective non-catalytic reduction. They also developed a low-NO_x NH_3-air non-premixed combustor for actual gas-turbine operations and found that the NO production of this gas turbine power generation could be lowered to 337 ppm when O_2 content reached 16% (Kurata et al., 2019). Okafor et al. designed a two-stage combustor for a micro gas turbine and found that NO_x emission was around 42 ppm at initial pressure of 3 atm and initial temperature of 298K when the equivalence ratio of the primary stage reached 1.1 and the equivalence ratio of the secondary stage was 0.4 (Okafor et al., 2019). Somarathne et al. numerically investigated the NO_x and NH_3 emission of turbulent premixed ammonia/air flames in a gas turbine like combustor by using the large eddy simulation at elevated pressure up to 5 atm and various equivalence ratios (Somarathne et al., 2017). They found that NO production decreased when the initial pressure increased and the minimum value of NO and unburnt NH_3 emission could reach 200 ppm at initial pressure of 5 atm and the equivalence ratio of 1.2. What's more, the NO emission of ammonia/air flames with the secondary air injection could be lowered to 100 ppm at O_2 content of 16%. Rocha et al. numerically studied the NO_x emission characteristics of ammonia/air mixtures under the typical conditions of commercial gas turbines by using three modern stationary gas turbine concepts (Rocha et al., 2020). They found that rich-burn, quick-quench and lean-burn (RQL) concept and moderate or intense low oxygen dilution (MILD) concept are able to reach low NO_x emission while the NO_x emission by using lean-burn dry-low emissions (DLE) concept is high.

There are also some researches about the NO_x emission of NH_3/H_2/air flames. Li et al. experimentally measured the NO_x concentration of NH_3/H_2/air flames covering the NH_3 concentration from 0.440 to 0.544 at the equivalence ratios from 1.00 to 1.25 (Li et al., 2014). They found that NO_x emission decreased when the equivalence ratio increased from 1.00 to 1.25 under different NH_3 contents. It can be observed that a more significant change occurs when the equivalence ratio increased from 1.00 to 1.10, while the change is small when the equivalence ratio increased from 1.10 to 1.25. As the NH_3 concentration increase the production of NO_x decrease, which due to the low flame temperature. The peak value of NO_x content is 1,450 ppm at NH_3 content of 0.500 and stoichiometric condition, while the maximum content is around 1,660 ppm when NH_3 content of NH_3/H_2 mixture reaches 0.416 under stoichiometric condition. They also concluded that fuel NO_x plays a significant role in NO_x emission, whereas thermal NO_x is negligible. Nozari et al. also studied the variation of the NO_x emission with the equivalence ratio at elevated pressure of 17 atm and temperature of 673 K (Nozari, 2015). They found that the NO_x concentration increased first and then decreased when the equivalence ratio ranged from 0.5 to 1.2 in all hydrogen content ranges. The maximum mole fraction of NO_x occurred under fuel lean conditions, which is similar to that of ammonia/air flames. Wang et al. also found that the NO concentration in exhaust gas was non-monotonically changed with equivalence ratios and hydrogen mole ratio, because the competition between the effects by the reduction of N-atom and the enrichment of H/O radicals when hydrogen is added to ammonia flame (Wang et al., 2021b). Lee et al. also found that both NO_x and N_2O emissions are low in fuel rich condition when compared to those under lean conditions (Lee et al., 2010).

The influences of pressure and hydrogen content on NO_x emissions are also significant. Xiao et al. numerically investigated the influence of pressure in NH_3/H_2 flames by using an improved mechanism based on the work performed by Mathieu et al. (Mathieu and Petersen, 2015; Xiao et al., 2017a). Results show that the concentration of NO_x significantly decreased with an increasing pressure. NO_x emission can be less than 5 ppm when the pressure reaches 10 atm and less than 1 ppm when the pressure up to 20 atm. Rocha et al. numerically investigated the variation of NO_x emission with hydrogen addition ratio ranged from 0 to 1 by ten mechanisms for ammonia/hydrogen/air flames at 1 atm and 298 K (Rocha et al., 2019). Results show that with an increase of the H_2 content, the NO_x emission increased before the mole fraction of H_2 reached 0.80 and then rapidly decreased when the mole fraction of H_2 large than 0.80. They presumed that the presence of OH/O radicals at high temperature resulted in the increasing content of NO_x before the H_2 concentration reached 0.80, while the decreasing concentration of ammonia leads to the decrease of NO_x when the mole fraction of H_2 large than 0.80.

Lhuillier et al. experimentally investigated the NO_x emission of NH_3/H_2/air mixtures in spark ignition engine at the intake

temperature of 323 K and pressure of 1.2 atm (Lhuillier et al., 2020a). It was found that NO_x production firstly increased and then decreased with an increased of the equivalence ratio. The peak values of NO_x formation occurred at the equivalence ratio of 0.8–0.9 and the minimal NO_x emission was found under rich conditions. What's more, as the H_2 concentration of NH_3/H_2/air mixtures increased, the emission increased. Very recently, Franco et al. also designed a laboratory combustor which had good performance in NO_x emission (Franco et al., 2021). Valera-Medina et al. numerically and experimentally investigated the NO_x emission of premixed 50%NH_3/50%H_2 mixtures under fuel lean condition in a swirl combustor and found that the pollution emission was high when compared with that under fuel rich condition (Valera-Medina et al., 2017). Then they studied characteristics of 70%NH_3/30%H_2 mixtures under gas turbine conditions through a numerical GT cycle model and found that NO_x emission could as low as 50 ppm because the hot unburned ammonia was able to react with NO_x (Valera-Medina et al., 2019). Hussein et al. found that injecting some NH_3/H_2 blend downstream the primary zone could significantly reduce the NO_x emission which was a promising method to minimize the pollution emission (Hussein et al., 2019).

Recently, many researches have studied the NO_x emission of CH_4/NH_3 flames. Among them, Tian mechanism is widely used to predict the NO_x emission of CH_4/NH_3 mixtures, which has a satisfactory prediction of the experimental results (Tian et al., 2009). Tian et al. investigated the intermediates and products for ammonia/methane/air/Ar flames at 0.04 atm and $\varphi = 1$ by using tunable synchrotron vacuum ultraviolet photoionization and molecular-beam mass spectrometry (Tian et al., 2009). Results show that the formation of NO_2 decreased while those of NO and N_2 increased with the mole ratios of NH_3/CH_4 increasing from 0 to 1. They also developed a detailed mechanism including 84 species and 703 elementary reactions, which can predict the major combustion species and intermediates well (shown as **Figure 10**). The process of CO formation is described below. Firstly, methane is converted to CH_3 by the reaction with OH and H. Then CH_3 mainly reacts with O addition to generate CH_2O and reacts with OH to form singlet CH_2 which can transform to triplet CH_2. CH_2 is converted to CH by reacting with H and then CH transforms to HCO by reacting with O_2. Besides, HCO also can be produced by the reaction of CH_2O with OH. Finally, HCO is converted to CO and H_2 by reacting with OH, O_2, and H. However, NO is produced by the reaction of NH with O and the reaction of HNO with H, OH, and O. It seems that the addition of CH_4 has no significant influence on the major formation and reduction of NO. Though the numerical simulation, it also can be found that four reactions including $H + O_2 = O + OH$, $NH_2 + O = HNO + H$, $NH_2 + NO = N_2 + H_2O$, and $NH + NO = N_2O + H$ are important for the conversion of NO and N_2.

Ramos et al. measured the NO_x emissions from CH_4/NH_3 flames at NH_3 content ranged from 0 to 0.7 and the equivalence ratio of 0.8, 0.9, and 1 by using a laboratory scale laminar flame burner (Filipe Ramos et al., 2019). They found that the production of NO_x firstly increased and then slightly decreased with an increasing NH_3 content and the maximum NO_x emission occurred when the concentration of NH_3 reached 0.50. Xiao et al. numerically studied the emission characteristics of CH_4/NH_3 mixtures at the ammonia ratio from 0 to 1 by using an improved model based on the Konnov mechanism and found the same tendency (Konnov, 2009; Xiao et al., 2017b). It was found that the addition of ammonia had a significant positive effect on NO_x emission under high methane proportion mixtures while it had a negative effect under high ammonia concentration. The probable reason of this phenomenon is that $H + NO = HNO$ inhibits the formation of NO at high ammonia concentration (Rocha et al., 2021). The equivalence ratio and initial pressure also has a strong impact on NO_x emission. Ramos et al. found that the peak values of the NO_x concentration are around 4,300, 3,600, and 2,800 ppm at the equivalence ratio of 1, 0.9, and 0.8, respectively, (Filipe Ramos et al., 2019). It is obvious that NO_x emissions decrease with a decrease of the equivalence ratio. Xiao et al. also studied the influence of the equivalence ratio and found that the maximum NO_x emission is presented at the equivalence ratio of 0.9 when the ammonia mole fraction ranged from 0.20 to 0.80 (Xiao et al., 2017b). Then they numerically studied the reaction involving NO by using Tian mechanism (Xiao et al., 2020). It was found that NH_2+O=HNO + H reaction is the most promoting reaction at $\varphi = 0.8$, while $H + O_2 = O + OH$ is the most promoting reaction at $\varphi = 1, 1.2$. The most inhibiting reaction is $NH_2+NO = N_2+H_2O$, $NH + NO = N_2O + H$, $NH_2+NO = NNH + OH$ at $\varphi = 0.8$, 1 and 1.2, respectively. For NO_x emission, the initial pressure plays an important role. The NO mole fraction decreased with the increasing pressure and the NO production was more sensitive to the change of the pressure than CO (Xiao et al., 2017b). What's more, it was found that the formation of NO is mainly through the $NH + OH = HNO + H$ reaction at high pressure (Valera-Medina et al., 2017). Zhang et al. investigated the emission characteristics of ammonia/air combustion in a model combustor with the addition of methane and hydrogen. They found NO and OH radicals showed a positive correlation, and the temperature had a secondary role on promoting NO_x formation comparing with CH_4/air flame (Zhang et al., 2021a). The thermal performance and NO_x emission on a premixed methane/ammonia/flame at a micro-planar combustor were also investigated. Results showed that ammonia addition reduced CO_2 emission, but increased NO emission increased. While N_2O emission increased first and then decreased with increasing ammonia ratio. (Cai et al., 2020; Cai et al., 2021; Han et al., 2021; Sun et al., 2021). An et al. found that the OH and NO were closely correlated in premixed CH_4/NH_3/air flames as they were both strongly related to flame temperature. While N_2O had a correlation with NH and HNO components (An et al., 2021), which is similar with the results by the same combustion group. (Zhang et al., 2020; Zhang et al., 2021b; Wei et al., 2021).

Recently, CH_4/NH_3 blends are also considered as a substitute fuel in practical applications. Liquefied natural gas is an alternative fuel and has been widely used in marine engines (Schinas and Butler, 2016). What's more, it also can improve the poor combustion characteristics of pure ammonia. Therefore, Oh et al. investigated the pollution emission of ammonia mixed with methane and found that NO_x emissions of CH_4/NH_3 blends in spark ignited engine rapidly increased before the split ratio of NH_3 reached 40% and then slightly decreased when the split ratio

large than 40% (Oh et al., 2021). Besides, the maximum NO_x emission of this study was lower than 40 g/kWh. Xiao et al. compared the simulation results under gas turbine conditions by using Tian, Konnov, Mendiara, GRI 3.0 and ÅA mechanism and found that Tian mechanism performed best in NO_x prediction (Xiao et al., 2017c, Tian et al., 2009, Mendiara and Glarborg, 2009, GRI, 2000, Åbo Akademi University, 2005). What's more, they found that the oxidation of N and HNO played the most important role in the production of NO under gas turbine conditions. Li et al. also studied the NO_x emission of CH_4/NH_3 mixtures under gas turbine conditions and recognized that NO_x formation increased when the NH_3 concentration increased, which is mainly due to the enhanced HNO pathway (Li et al., 2019b). Furthermore, they found that the availability of oxygen has significant influence on the production of NO_x through HNO pathway and proposed a combustion system in which NO_x production can as low as 30 ppm even when the NH_3 concentration up to 40%. Okafor et al. used rich-lean combustion to control NO_x emission and proposed the optimum equivalence ratio of the primary zone ranged from 1.30 to 1.35 (Okafor et al., 2020). This method can significantly reduce the formation of NO_x, for instance, NO_x emission can be lowered to 49ppm. Okafor et al. investigated the characteristics of liquid NH_3 spray co-fired with CH_4 and found that the minimum NO_x emission occurred when the equivalence ratio reached 1.06 (Okafor et al., 2021a). They also studied the NO_x emission characteristics of this kind of fuel in two-stage micro gas turbine combustors and recognized that the increased inlet temperature and decreased wall heat loss led to the reduction of NO and N_2O (Okafor et al., 2021b).

CONCLUSIONS AND PERSPECTIVES

This paper presents the burning velocity and pollutant emissions of NH_3 flames, NH_3/H_2 flames and CH_4/NH_3 flames. At 1 atm and 298 K, the laminar burning velocities increase before the equivalence ratio reaches 1.1, and then decrease when the equivalence ratio is large than 1.1. The maximum value of laminar burning velocity is less than 10 cm/s, which is relatively low when compared with that of CH_4/air flame. Under different pressure conditions, it can be found that the flame velocity decreases with an increase of the initial pressure. The influence of temperature is also studied. With the initial temperature increasing, the flame speed exponentially increases. In order to increase the laminar burning velocity of NH_3/air flames, oxygen enriched combustion is proposed as a promising approach. The flame speed of NH_3/air flames under oxygen enrichment conditions increases with an increase of the O_2 concentration, but decrease with an increase of initial pressure under oxygen enrichment conditions. And the flame velocity increases with the increasing temperature, which is more sensitive to the change of temperature under lower O_2 content. Besides, ammonia is usually burned with the additions of hydrogen and methane to improve the combustion characteristics. The addition of H_2 or CH_4 can significantly increase the flame speed.

NO_x is composed of the thermal NO_x and the fuel NO_x, which is the major pollution of ammonia combustion. Thermal NO_x is usually produced by the oxidation of N_2 when the temperature reaches 1,800 K. The generation of the thermal NO is satisfactorily described by the extended Zeldovich mechanism. It can be reduced by controlling temperature. Fuel NO_x is mainly generated by the oxidation of NH_3. HNO intermediate plays an important role in NO formation by reacting with OH and NH_2. It was found that burning under rich condition and high pressure can effectively reduce NO_x emission. The effects of equivalence ratio and pressure in NH_3/H_2 flames are similar to those of NH_3/air flames. The NO_x production firstly increased with an increase of the H_2 content before the H_2 concentration reached 0.8, and then rapidly decreased after the mole fraction of H_2 large than 0.8. The reaction pathways in the combustion of NH_3/CH_4 fuels are described by using Tian mechanism. It seems that the addition of CH_4 has no significant influence on the major formation and reduction of NO. The NO_x production is high under high ammonia content, high temperature and stoichiometric condition. What's more, the concentration of CO_2 also influences the formation of NO_x. The high CO_2 content has a positive impact on NO_x production under fuel rich condition, while has a negative effect under stoichiometric and lean conditions.

Although the fundamental characteristics of ammonia-based flames has been widely studied, the practical application of this kind of fuel is still unsatisfying. Therefore, further studies are needed to overcome the problems, including low burning velocities and high NO_x emission. For example, one of the main challenges in the investigation of ammonia-based fuel is that the numerical simulations by using mechanisms usually overpredict or underpredict when compared with those are obtained during the actual combustion processing. In order to fully understand the combustion characteristics of ammonia-based flames, developing an accurate mechanism is necessary. What's more, for emission characteristics of CH_4/NH_3 mixtures, many researches focused on reducing NO_x emission, and few studies on the carbon capture can be found. Therefore, it still need further studied.

AUTHOR CONTRIBUTIONS

Conceptualization, JL, HH, and NK; literature review and resources, JL, SL, DC, RW, and LD; writing, JL and SL; review and editing, HH and NK; funding acquisition, JL and HH. All authors have read and agree to the published version of the article.

FUNDING

This work was supported by Leading Key Projects of Chinese Academy of Sciences (No.QYZDY-SSW-JSC038), Key Special Project for Introduced Talents Team of Southern Marine Science and Engineering Guangdong Laboratory (Guangzhou) (GML2019ZD0108), and Science and Technology Planning Project of Guangdong Province, China (No. 2017A050501046).

REFERENCE

Åbo Akademi University (2005). Åbo Akademi (ÅA) Scheme. Available at: http://www.abo.fi/fakultet/ookforskkinetschem (Accessed Oct 5, 2020).

Afif, A., Radenahmad, N., Cheok, Q., Shams, S., Kim, J. H., and Azad, A. K. (2016). Ammonia-fed Fuel Cells: a Comprehensive Review. *Renew. Sustain. Energ. Rev.* 60, 822–835. doi:10.1016/j.rser.2016.01.120

An, Z., Zhang, M., Zhang, W., Mao, R., Wei, X., Wang, J., et al. (2021). Emission Prediction and Analysis on CH_4/NH_3/air Swirl Flames with LES-FGM Method. *Fuel* 304, 121370. doi:10.1016/j.fuel.2021.121370

Andersson, J., and Lundgren, J. (2014). Techno-economic Analysis of Ammonia Production via Integrated Biomass Gasification. *Appl. Energ.* 130, 484–490. doi:10.1016/j.apenergy.2014.02.029

Astbury, G. R. (2008). A Review of the Properties and Hazards of Some Alternative Fuels. *Process Saf. Environ. Prot.* 86, 397–414. doi:10.1016/j.psep.2008.05.001

Barbas, M., Costa, M., Vranckx, S., and Fernandes, R. X. (2015). Experimental and Chemical Kinetic Study of CO and NO Formation in Oxy-Methane Premixed Laminar Flames Doped with NH_3. *Combust. Flame* 162, 1294–1303. doi:10.1016/j.combustflame.2014.10.020

Bell, J. B., Day, M. S., Grcar, J. F., Bessler, W. G., Schulz, C., Glarborg, P., et al. (2002). Detailed Modeling and Laser-Induced Fluorescence Imaging of Nitric Oxide in a NH_3-seeded Non-premixed Methane/air Flame. *Proc. Combust. Inst.* 29, 2195–2202. doi:10.1016/s1540-7489(02)80267-x

Cai, T., Zhao, D., Wang, B., Li, J., and Guan, Y. (2020). NO Emission and thermal Performances Studies on Premixed Ammonia-Oxygen Combustion in a CO_2-free Micro-planar Combustor. *Fuel* 280, 118554. doi:10.1016/j.fuel.2020.118554

Cai, T., Zhao, D., Li, X., Shi, B., and Li, J. (2021). Mitigating NO Emissions from an Ammonia-Fueled Micro-power System with a Perforated Plate Implemented. *J. Hazard. Mater.* 401, 123848. doi:10.1016/j.jhazmat.2020.123848

CDC (1994). Immediately Dangerous to Life or Health Concentrations. Centers for Disease Control and Prevention. Available at: https://www.cdc.gov/niosh/idlh/7664417.html (Accessed Dec 24, 2020).

Chai, W. S., Bao, Y., Jin, P., Tang, G., and Zhou, L. (2021). A Review on Ammonia, Ammonia-Hydrogen and Ammonia-Methane Fuels. *Renew. Sustain. Energ. Rev.* 147, 111254. doi:10.1016/j.rser.2021.111254

Choi, S., Lee, S., and Kwon, O. C. (2015). Extinction Limits and Structure of Counterflow Nonpremixed Hydrogen-Doped Ammonia/air Flames at Elevated Temperatures. *Energy* 85, 503–510. doi:10.1016/j.energy.2015.03.061

Cohen, L. (1955). Burning Velocities of Ammonia in Air and in Oxygen. *Fuel* 34, S123–S127. doi:10.1002/j.2164-4918.1955.tb01284.x

da Rocha, R. C., Costa, M., and Bai, X.-S. (2019). Chemical Kinetic Modelling of Ammonia/hydrogen/air Ignition, Premixed Flame Propagation and NO Emission. *Fuel* 246, 24–33. doi:10.1016/j.fuel.2019.02.102

Dean, A. M., and Bozzelli, J. W. (2000). "Combustion Chemistry of Nitrogen," in *Gas-Phase Combustion Chemistry* (New York: Springer), 125–341. doi:10.1007/978-1-4612-1310-9_2

Dean, A. M., Chou, M.-S., and Stern, D. (1984). Kinetics of Rich Ammonia Flames. *Int. J. Chem. Kinet.* 16, 633–653. doi:10.1002/kin.550160603

Dimitriou, P., and Javaid, R. (2020). A Review of Ammonia as a Compression Ignition Engine Fuel. *Int. J. Hydrogen Energ.* 45, 7098–7118. doi:10.1016/j.ijhydene.2019.12.209

Duynslaegher, C., Jeanmart, H., and Vandooren, J. (2009). Flame Structure Studies of Premixed Ammonia/hydrogen/oxygen/argon Flames: Experimental and Numerical Investigation. *Proc. Combust. Inst.* 32, 1277–1284. doi:10.1016/j.proci.2008.06.036

Duynslaegher, C., Jeanmart, H., and Vandooren, J. (2010). Ammonia Combustion at Elevated Pressure and Temperature Conditions. *Fuel* 89, 3540–3545. doi:10.1016/j.fuel.2010.06.008

Duynslaegher, C., Contino, F., Vandooren, J., and Jeanmart, H. (2012). Modeling of Ammonia Combustion at Low Pressure. *Combust. Flame* 159, 2799–2805. doi:10.1016/j.combustflame.2012.06.003

Filipe Ramos, C., Rocha, R. C., Oliveira, P. M. R., Costa, M., and Bai, X.-S. (2019). Experimental and Kinetic Modelling Investigation on NO, CO and NH_3 Emissions from NH_3/CH_4/air Premixed Flames. *Fuel* 254, 115693. doi:10.1016/j.fuel.2019.115693

Franco, M. C., Rocha, R. C., Costa, M., and Yehia, M. (2021). Characteristics of NH_3/H_2/air Flames in a Combustor Fired by a Swirl and bluff-body Stabilized Burner. *Proc. Combust. Inst.* 38, 5129–5138. doi:10.1016/j.proci.2020.06.141

Frenklach, M., Bowman, T., and Smith, G. (2000). GRI-Mech 3.0. Available at: http://www.me.berkeley.edu/gri-mech/index.html (Accessed Jan 7, 2021).

Gill, S. S., Chatha, G. S., Tsolakis, A., Golunski, S. E., and York, A. P. E. (2012). Assessing the Effects of Partially Decarbonising a Diesel Engine by Co-fuelling with Dissociated Ammonia. *Int. J. Hydrogen Energ.* 37, 6074–6083. doi:10.1016/j.ijhydene.2011.12.137

Gross, C. W., and Kong, S.-C. (2013). Performance Characteristics of a Compression-Ignition Engine Using Direct-Injection Ammonia-DME Mixtures. *Fuel* 103, 1069–1079. doi:10.1016/j.fuel.2012.08.026

Grossale, A., Nova, I., and Tronconi, E. (2009). Ammonia Blocking of the "Fast SCR" Reactivity over a Commercial Fe-Zeolite Catalyst for Diesel Exhaust Aftertreatment. *J. Catal.* 265, 141–147. doi:10.1016/j.jcat.2009.04.014

Habgood, D. C. C., Hoadley, A. F. A., and Zhang, L. (2015). Techno-economic Analysis of Gasification Routes for Ammonia Production from Victorian Brown Coal. *Chem. Eng. Res. Des.* 102, 57–68. doi:10.1016/j.cherd.2015.06.008

Han, X., Wang, Z., Costa, M., Sun, Z., He, Y., and Cen, K. (2019). Experimental and Kinetic Modeling Study of Laminar Burning Velocities of NH_3/air, NH_3/H_2/air, NH_3/CO/air and NH_3/CH_4/air Premixed Flames. *Combust. Flame* 206, 214–226. doi:10.1016/j.combustflame.2019.05.003

Han, X., Wang, Z., He, Y., Liu, Y., Zhu, Y., and Konnov, A. A. (2020). The Temperature Dependence of the Laminar Burning Velocity and Superadiabatic Flame Temperature Phenomenon for NH_3/air Flames. *Combust. Flame* 217, 314–320. doi:10.1016/j.combustflame.2020.04.013

Han, L., Li, J., Zhao, D., Xi, Y., Gu, X., and Wang, N. (2021). Effect Analysis on Energy Conversion Enhancement and NO_x Emission Reduction of Ammonia/hydrogen Fuelled Wavy Micro-combustor for Micro-thermophotovoltaic Application. *Fuel* 289, 119755. doi:10.1016/j.fuel.2020.119755

Hayakawa, A., Goto, T., Mimoto, R., Arakawa, Y., Kudo, T., and Kobayashi, H. (2015a). Laminar Burning Velocity and Markstein Length of Ammonia/air Premixed Flames at Various Pressures. *Fuel* 159, 98–106. doi:10.1016/j.fuel.2015.06.070

Hayakawa, A., Goto, T., Mimoto, R., Kudo, T., and Kobayashi, H. (2015b). NO Formation/reduction Mechanisms of Ammonia/air Premixed Flames at Various Equivalence Ratios and Pressures. *Mech. Eng. J.* 2, 14–00402. doi:10.1299/mej.14-00402

Henshaw, P. F., D'Andrea, T., Mann, K. R. C., and Ting, D. S.-K. (2005). Premixed Ammonia-Methane-Air Combustion. *Combust. Sci. Techn.* 177, 2151–2170. doi:10.1080/00102200500240695

Hussein, N. A., Valera-Medina, A., and Alsaegh, A. S. (2019). Ammonia-Hydrogen Combustion in a Swirl Burner with Reduction of NO_x Emissions. *Energ. Proced.* 158, 2305–2310. doi:10.1016/j.egypro.2019.01.265

Ichikawa, A., Hayakawa, A., Kitagawa, Y., Kunkuma Amila Somarathne, K. D., Kudo, T., and Kobayashi, H. (2015). Laminar Burning Velocity and Markstein Length of Ammonia/hydrogen/air Premixed Flames at Elevated Pressures. *Int. J. Hydrogen Energ.* 40, 9570–9578. doi:10.1016/j.ijhydene.2015.04.024

IEA (2021). *Global Energy Review 2021*. Paris: International Energy Agency. Available at: https://www.iea.org/reports/global-energy-review-2021.

Joo, J. M., Lee, S., and Kwon, O. C. (2012). Effects of Ammonia Substitution on Combustion Stability Limits and NO_x Emissions of Premixed Hydrogen-Air Flames. *Int. J. Hydrogen Energ.* 37, 6933–6941. doi:10.1016/j.ijhydene.2012.01.059

Kim, H. K., Ku, J. W., Ahn, Y. J., Kim, Y. H., and Kwon, O. C. (2021). Effects of O_2 Enrichment on NH_3/air Flame Propagation and Emissions. *Int. J. Hydrogen Energ.* 46 (46), 23916–23926. doi:10.1016/j.ijhydene.2021.04.154

Klerke, A., Christensen, C. H., Nørskov, J. K., and Vegge, T. (2008). Ammonia for Hydrogen Storage: Challenges and Opportunities. *J. Mater. Chem.* 18, 2304–2310. doi:10.1039/b720020j

Klippenstein, S. J., Harding, L. B., Glarborg, P., and Miller, J. A. (2011). The Role of NNH in NO Formation and Control. *Combust. Flame* 158, 774–789. doi:10.1016/j.combustflame.2010.12.013

Kobayashi, H., Hayakawa, A., Somarathne, K. D. K. A., and Okafor, E. C. (2019). Science and Technology of Ammonia Combustion. *Proc. Combust. Inst.* 37, 109–133. doi:10.1016/j.proci.2018.09.029

Konnov, A. A., Dyakov, I. V., and De Ruyck, J. (2006). Probe Sampling Measurements of No in $Ch_4+O_2+N_2$ Flames Doped with NH_3. *Combust. Sci. Techn.* 178 (6), 1143–1164. doi:10.1080/00102200500296788

Konnov, A. A. (2009). Implementation of the NCN Pathway of Prompt-NO Formation in the Detailed Reaction Mechanism. *Combust. Flame* 156, 2093–2105. doi:10.1016/j.combustflame.2009.03.016

Kumar, P., and Meyer, T. R. (2013). Experimental and Modeling Study of Chemical-Kinetics Mechanisms for H_2-NH_3-air Mixtures in Laminar Premixed Jet Flames. *Fuel* 108, 166–176. doi:10.1016/j.fuel.2012.06.103

Kurata, O., Iki, N., Matsunuma, T., Inoue, T., Tsujimura, T., Furutani, H., et al. (2017). Performances and Emission Characteristics of NH_3-air and NH_3CH_4-air Combustion Gas-Turbine Power Generations. *Proc. Combust. Inst.* 36, 3351–3359. doi:10.1016/j.proci.2016.07.088

Kurata, O., Iki, N., Inoue, T., Matsunuma, T., Tsujimura, T., Furutani, H., et al. (2019). Development of a Wide Range-Operable, Rich-Lean Low-NO_x Combustor for NH_3 Fuel Gas-Turbine Power Generation. *Proc. Combust. Inst.* 37, 4587–4595. doi:10.1016/j.proci.2018.09.012

Kwon, O. C., and Faeth, G. M. (2001). Flame/stretch Interactions of Premixed Hydrogen-Fueled Flames: Measurements and Predictions. *Combust. Flame* 124, 590–610. doi:10.1016/s0010-2180(00)00229-7

Lan, R., Irvine, J. T. S., and Tao, S. (2012). Ammonia and Related Chemicals as Potential Indirect Hydrogen Storage Materials. *Int. J. Hydrogen Energ.* 37, 1482–1494. doi:10.1016/j.ijhydene.2011.10.004

Law, C. K. (2006). *Combustion Physics*. Cambridge: Cambridge University Press, 347.

Lee, D., and Song, H. H. (2018). Development of Combustion Strategy for the Internal Combustion Engine Fueled by Ammonia and its Operating Characteristics. *J. Mech. Sci. Technol.* 32 (4), 1905–1925. doi:10.1007/s12206-018-0347-x

Lee, J. H., Kim, J. H., Park, J. H., and Kwon, O. C. (2010). Studies on Properties of Laminar Premixed Hydrogen-Added Ammonia/air Flames for Hydrogen Production. *Int. J. Hydrogen Energ.* 35 (3), 1054–1064. doi:10.1016/j.ijhydene.2009.11.071

Lhuillier, C., Brequigny, P., Contino, F., and Mounaïm-Rousselle, C. (2020a). Experimental Study on Ammonia/hydrogen/air Combustion in Spark Ignition Engine Conditions. *Fuel* 269, 117448. doi:10.1016/j.fuel.2020.117448

Lhuillier, C., Brequigny, P., Lamoureux, N., Contino, F., and Mounaïm-Rousselle, C. (2020b). Experimental Investigation on Laminar Burning Velocities of Ammonia/hydrogen/air Mixtures at Elevated Temperatures. *Fuel* 263, 116653. doi:10.1016/j.fuel.2019.116653

Li, J., Huang, H., Kobayashi, N., He, Z., and Nagai, Y. (2014). Study on Using Hydrogen and Ammonia as Fuels: Combustion Characteristics and NO_x formation. *Int. J. Energ. Res.* 38, 1214–1223. doi:10.1002/er.3141

Li, J., Huang, H., Kobayashi, N., He, Z., Osaka, Y., and Zeng, T. (2015). Numerical Study on Effect of Oxygen Content in Combustion Air on Ammonia Combustion. *Energy* 93, 2053–2068. doi:10.1016/j.energy.2015.10.060

Li, J., Huang, H., Yuan, H., Zeng, T., Yagami, M., and Kobayashi, N. (2016a). Modelling of Ammonia Combustion Characteristics at Preheating Combustion: NO Formation Analysis. *IJGW* 10, 230–241. doi:10.1504/ijgw.2016.077915

Li, J., Huang, H., Kobayashi, N., He, Z., Osaka, Y., and Zeng, T. (2016b). Research on Combustion and Emission Characteristics of Ammonia under Preheating Conditions. *J. Chem. Eng. Jpn.* 49, 641–648. doi:10.1252/jcej.15we075

Li, J., Huang, H., Kobayashi, N., Wang, C., and Yuan, H. (2017). Numerical Study on Laminar Burning Velocity and Ignition Delay Time of Ammonia Flame with Hydrogen Addition. *Energy* 126, 796–809. doi:10.1016/j.energy.2017.03.085

Li, J., Huang, H., Deng, L., He, Z., Osaka, Y., and Kobayashi, N. (2019a). Effect of Hydrogen Addition on Combustion and Heat Release Characteristics of Ammonia Flame. *Energy* 175, 604–617. doi:10.1016/j.energy.2019.03.075

Li, S., Zhang, S., Zhou, H., and Ren, Z. (2019b). Analysis of Air-Staged Combustion of NH_3/CH_4 Mixture with Low NO_x Emission at Gas Turbine Conditions in Model Combustors. *Fuel* 237, 50–59. doi:10.1016/j.fuel.2018.09.131

Lindstedt, R. P., Lockwood, F. C., and Selim, M. A. (1994). Detailed Kinetic Modelling of Chemistry and Temperature Effects on Ammonia Oxidation. *Combust. Sci. Techn.* 99, 253–276. doi:10.1080/00102209408935436

Liu, Q., Chen, X., Huang, J., Shen, Y., Zhang, Y., and Liu, Z. (2019a). The Characteristics of Flame Propagation in Ammonia/oxygen Mixtures. *J. Hazard. Mater.* 363, 187–196. doi:10.1016/j.jhazmat.2018.09.073

Liu, S., Zou, C., Song, Y., Cheng, S., and Lin, Q. (2019b). Experimental and Numerical Study of Laminar Flame Speeds of CH_4/NH_3 Mixtures under Oxy-Fuel Combustion. *Energy* 175, 250–258. doi:10.1016/j.energy.2019.03.040

Mathieu, O., and Petersen, E. L. (2015). Experimental and Modeling Study on the High-Temperature Oxidation of Ammonia and Related NO_x Chemistry. *Combust. Flame* 162 (3), 554–570. doi:10.1016/j.combustflame.2014.08.022

Mei, B., Zhang, X., Ma, S., Cui, M., Guo, H., Cao, Z., et al. (2019). Experimental and Kinetic Modeling Investigation on the Laminar Flame Propagation of Ammonia under Oxygen Enrichment and Elevated Pressure Conditions. *Combust. Flame* 210, 236–246. doi:10.1016/j.combustflame.2019.08.033

Mei, B., Zhang, J., Shi, X., Xi, Z., and Li, Y. (2021). Enhancement of Ammonia Combustion with Partial Fuel Cracking Strategy: Laminar Flame Propagation and Kinetic Modeling Investigation of $NH_3/H_2/N_2$/air Mixtures up to 10 Atm. *Combust. Flame* 231, 111472. doi:10.1016/j.combustflame.2021.111472

Mendiara, T., and Glarborg, P. (2009). Ammonia Chemistry in Oxy-Fuel Combustion of Methane. *Combust. Flame* 156, 1937–1949. doi:10.1016/j.combustflame.2009.07.006

Metghalchi, M., and Keck, J. C. (1982). Burning Velocities of Mixtures of Air with Methanol, Isooctane, and Indolene at High Pressure and Temperature. *Combust. Flame* 48, 191–210. doi:10.1016/0010-2180(82)90127-4

Miller, J. A., and Bowman, C. T. (1989). Mechanism and Modeling of Nitrogen Chemistry in Combustion. *Prog. Energ. Combust. Sci.* 15, 287–338. doi:10.1016/0360-1285(89)90017-8

Miller, J. A., and Glarborg, P. (1999). Modeling the thermal De-NO_x Process: Closing in on a Final Solution. *Int. J. Chem. Kinet.* 31, 757–765. doi:10.1002/(sici)1097-4601(1999)31:11<757:aid-jck1>3.0.co;2-v

Miller, J. A., Smooke, M. D., Green, R. M., and Kee, R. J. (1983). Kinetic Modeling of the Oxidation of Ammonia in Flames. *Combust. Sci. Techn.* 34, 149–176. doi:10.1080/00102208308923691

Mørch, C. S., Bjerre, A., Gøttrup, M. P., Sorenson, S. C., and Schramm, J. (2011). Ammonia/hydrogen Mixtures in an SI-Engine: Engine Performance and Analysis of a Proposed Fuel System. *Fuel* 90, 854–864.

NCBI (2021). PubChem-Ammonia. National Center for Biotechnology Information. Available at: https://pubchem.ncbi.nlm.nih.gov/compound/222 (Accessed May 15, 2021).

Nozari, H., and Karabeyoğlu, A. (2015). Numerical Study of Combustion Characteristics of Ammonia as a Renewable Fuel and Establishment of Reduced Reaction Mechanisms. *Fuel* 159, 223–233. doi:10.1016/j.fuel.2015.06.075

Oh, S., Park, C., KimKim, S. Y., Kim, Y., Choi, Y., and Kim, C. (2021). Natural Gas-Ammonia Dual-Fuel Combustion in Spark-Ignited Engine with Various Air-Fuel Ratios and Split Ratios of Ammonia under Part Load Condition. *Fuel* 290, 120095. doi:10.1016/j.fuel.2020.120095

Okafor, E. C., Naito, Y., Colson, S., Ichikawa, A., Kudo, T., Hayakawa, A., et al. (2018). Experimental and Numerical Study of the Laminar Burning Velocity of CH_4-NH_3-air Premixed Flames. *Combust. Flame* 187, 185–198. doi:10.1016/j.combustflame.2017.09.002

Okafor, E. C., Somarathne, K. D. K. A., Hayakawa, A., Kudo, T., Kurata, O., Iki, N., et al. (2019). Towards the Development of an Efficient Low-NO_x Ammonia Combustor for a Micro Gas Turbine. *Proc. Combust. Inst.* 37, 4597–4606. doi:10.1016/j.proci.2018.07.083

Okafor, E. C., Somarathne, K. D. K. A., Ratthanan, R., Hayakawa, A., Kudo, T., Kurata, O., et al. (2020). Control of NO_x and Other Emissions in Micro Gas Turbine Combustors Fuelled with Mixtures of Methane and Ammonia. *Combust. Flame* 211, 406–416. doi:10.1016/j.combustflame.2019.10.012

Okafor, E. C., Kurata, O., Yamashita, H., Inoue, T., Tsujimura, T., Iki, N., et al. (2021a). Liquid Ammonia spray Combustion in Two-Stage Micro Gas Turbine Combustors at 0.25 MPa; Relevance of Combustion Enhancement to Flame Stability and NO_x Control. *Appl. Energ. Combust. Sci.* 7, 100038. doi:10.1016/j.jaecs.2021.100038

Okafor, E. C., Yamashita, H., Hayakawa, A., Somarathne, K. D. K. A., Kudo, T., Tsujimura, T., et al. (2021b). Flame Stability and Emissions Characteristics of Liquid Ammonia spray Co-fired with Methane in a Single Stage Swirl Combustor. *Fuel* 287, 119433. doi:10.1016/j.fuel.2020.119433

Otomo, J., Koshi, M., Mitsumori, T., Iwasaki, H., and Yamada, K. (2018). Chemical Kinetic Modeling of Ammonia Oxidation with Improved Reaction Mechanism for Ammonia/air and Ammonia/hydrogen/air Combustion. *Int. J. Hydrogen Energ.* 43, 3004–3014. doi:10.1016/j.ijhydene.2017.12.066

Pfahl, U. J., Ross, M. C., Shepherd, J. E., Pasamehmetoglu, K. O., and Unal, C. (2000). Flammability Limits, Ignition Energy, and Flame Speeds in H_2-CH_4-NH_3-N_2O-O_2-N_2 mixtures. *Combust. Flame* 123, 140–158.

Reiter, A. J., and Kong, S.-C. (2011). Combustion and Emissions Characteristics of Compression-Ignition Engine Using Dual Ammonia-Diesel Fuel. *Fuel* 90, 87–97. doi:10.1016/j.fuel.2010.07.055

Rocha, R. C., Costa, M., and Bai, X. S. (2020). Combustion and Emission Characteristics of Ammonia under Conditions Relevant to Modern Gas Turbines. *Combust. Sci. Technol.*, 1–20. doi:10.1080/00102202.2020.1748018

Rocha, R. C., Zhong, S., Xu, L., Bai, X.-S., Costa, M., Cai, X., et al. (2021). Structure and Laminar Flame Speed of an Ammonia/methane/air Premixed Flame under Varying Pressure and Equivalence Ratio. *Energy Fuels* 35 (9), 7179–7192. doi:10.1021/acs.energyfuels.0c03520

Ronney, P. D. (1988). Effect of Chemistry and Transport Properties on Near-Limit Flames at Microgravity. *Combust. Sci. Techn.* 59, 123–141. doi:10.1080/00102208808947092

Schinas, O., and Butler, M. (2016). Feasibility and Commercial Considerations of LNG-Fueled Ships. *Ocean Eng.* 122, 84–96. doi:10.1016/j.oceaneng.2016.04.031

Shrestha, K. P., Lhuillier, C., Barbosa, A. A., Brequigny, P., Contino, F., Mounaïm-Rousselle, C., et al. (2021). An Experimental and Modeling Study of Ammonia with Enriched Oxygen Content and Ammonia/hydrogen Laminar Flame Speed at Elevated Pressure and Temperature. *Proc. Combust. Inst.* 38, 2163–2174. doi:10.1016/j.proci.2020.06.197

Shu, T., Xue, Y., Zhou, Z., and Ren, Z. (2021). An Experimental Study of Laminar Ammonia/methane/air Premixed Flames Using Expanding Spherical Flames. *Fuel* 290, 120003. doi:10.1016/j.fuel.2020.120003

Skreiberg, Ø., Kilpinen, P., and Glarborg, P. (2004). Ammonia Chemistry below 1400 K under Fuel-Rich Conditions in a Flow Reactor. *Combust. Flame* 136, 501–518. doi:10.1016/j.combustflame.2003.12.008

Somarathne, K. D. K. A., Hatakeyama, S., Hayakawa, A., and Kobayashi, H. (2017). Numerical Study of a Low Emission Gas Turbine like Combustor for Turbulent Ammonia/air Premixed Swirl Flames with a Secondary Air Injection at High Pressure. *Int. J. Hydrogen Energ.* 42, 27388–27399. doi:10.1016/j.ijhydene.2017.09.089

Sullivan, N., Jensen, A., Glarborg, P., Day, M. S., Grcar, J. F., Bell, J. B., et al. (2002). Ammonia Conversion and NO_x Formation in Laminar Coflowing Nonpremixed Methane-Air Flames. *Combust. Flame* 131, 285–298. doi:10.1016/s0010-2180(02)00413-3

Sun, Y., Cai, T., and Zhao, D. (2021). Thermal Performance and NO_x Emission Characteristics Studies on a Premixed Methane-Ammonia-Fueled Micro-planar Combustor. *Fuel* 291, 120190. doi:10.1016/j.fuel.2021.120190

Takeishi, H., Hayashi, J., Kono, S., Arita, W., Iino, K., and Akamatsu, F. (2015). Characteristics of ammonia/N_2/O_2 Laminar Flame in Oxygen-Enriched Air Condition. *Trans. JSME* 81, 14–00423. doi:10.1299/transjsme.14-00423

Takizawa, K., Takahashi, A., Tokuhashi, K., Kondo, S., and Sekiya, A. (2008). Burning Velocity Measurements of Nitrogen-Containing Compounds. *J. Hazard. Mater.* 155, 144–152. doi:10.1016/j.jhazmat.2007.11.089

Tian, Z., Li, Y., Zhang, L., Glarborg, P., and Qi, F. (2009). An Experimental and Kinetic Modeling Study of Premixed NH_3/CH_4/O_2/Ar Flames at Low Pressure. *Combust. Flame* 156, 1413–1426. doi:10.1016/j.combustflame.2009.03.005

Um, D. H., Joo, J. M., Lee, S., and Kwon, O. C. (2013). Combustion Stability Limits and NO_x Emissions of Nonpremixed Ammonia-Substituted Hydrogen-Air Flames. *Int. J. Hydrogen Energ.* 38, 14854–14865. doi:10.1016/j.ijhydene.2013.08.140

USGS (2021). Nitrogen Statistics and Information. U. S. Geological Survey. Available at: https://www.usgs.gov/centers/nmic/nitrogen-statistics-and-information (Accessed May 20, 2021).

Valera-Medina, A., Pugh, D. G., Marsh, P., Bulat, G., and Bowen, P. (2017). Preliminary Study on Lean Premixed Combustion of Ammonia-Hydrogen for Swirling Gas Turbine Combustors. *Int. J. Hydrogen Energ.* 42, 24495–24503. doi:10.1016/j.ijhydene.2017.08.028

Valera-Medina, A., Xiao, H., Owen-Jones, M., David, W. I. F., and Bowen, P. J. (2018). Ammonia for Power. *Prog. Energ. Combust. Sci.* 69, 63–102. doi:10.1016/j.pecs.2018.07.001

Valera-Medina, A., Gutesa, M., Xiao, H., Pugh, D., Giles, A., Goktepe, B., et al. (2019). Premixed Ammonia/hydrogen Swirl Combustion under Rich Fuel Conditions for Gas Turbines Operation. *Int. J. Hydrogen Energ.* 44, 8615–8626. doi:10.1016/j.ijhydene.2019.02.041

Wang, F., Zhou, Z., Dai, Z., Gong, X., Yu, G., Liu, H., et al. (2007). Development and Demonstration Plant Operation of an Opposed Multi-Burner Coal-Water Slurry Gasification Technology. *Front. Energ. Power Eng. China* 1, 251–258. doi:10.1007/s11708-007-0035-5

Wang, D., Ji, C., Wang, Z., Wang, S., Zhang, T., and Yang, J. (2020). Measurement of Oxy-Ammonia Laminar Burning Velocity at normal and Elevated Temperatures. *Fuel* 279, 118425. doi:10.1016/j.fuel.2020.118425

Wang, D., Ji, C., Wang, S., Yang, J., and Wang, Z. (2021a). Numerical Study of the Premixed Ammonia-Hydrogen Combustion under Engine-Relevant Conditions. *Int. J. Hydrogen Energ.* 46, 2667–2683. doi:10.1016/j.ijhydene.2020.10.045

Wang, Z., Han, X., He, Y., Zhu, R., Zhu, Y., Zhou, Z., et al. (2021b). Experimental and Kinetic Study on the Laminar Burning Velocities of NH_3 Mixing with CH_3OH and C_2H_5OH in Premixed Flames. *Combust. Flame* 229, 111392. doi:10.1016/j.combustflame.2021.02.038

Wei, X., Zhang, M., An, Z., Wang, J., Huang, Z., and Tan, H. (2021). Large Eddy Simulation on Flame Topologies and the Blow-Off Characteristics of Ammonia/air Flame in a Model Gas Turbine Combustor. *Fuel* 298, 120846. doi:10.1016/j.fuel.2021.120846

Williams, W. R., Zhao, J., and Schmidt, L. D. (1991). Ignition and Extinction of Surface and Homogeneous Oxidation of NH_3 and CH_4. *AIChE J.* 37, 641–649. doi:10.1002/aic.690370502

Wiseman, S., Rieth, M., Gruber, A., Dawson, J. R., and Chen, J. H. (2021). A Comparison of the Blow-Out Behavior of Turbulent Premixed Ammonia/hydrogen/nitrogen-Air and Methane-Air Flames. *Proc. Combust. Inst.* 38, 2869–2876. doi:10.1016/j.proci.2020.07.011

Xiao, H., Valera-Medina, A., and Bowen, P. J. (2017a). Modeling Combustion of Ammonia/Hydrogen Fuel Blends under Gas Turbine Conditions. *Energy Fuels* 31 (8), 8631–8642. doi:10.1021/acs.energyfuels.7b00709

Xiao, H., Valera-Medina, A., and Bowen, P. J. (2017b). Study on Premixed Combustion Characteristics of Co-firing Ammonia/methane Fuels. *Energy* 140, 125–135. doi:10.1016/j.energy.2017.08.077

Xiao, H., Valera-Medina, A., Marsh, R., and Bowen, P. J. (2017c). Numerical Study Assessing Various Ammonia/methane Reaction Models for Use under Gas Turbine Conditions. *Fuel* 196, 344–351. doi:10.1016/j.fuel.2017.01.095

Xiao, H., Lai, S., Valera-Medina, A., Li, J., Liu, J., and Fu, H. (2020). Study on Counterflow Premixed Flames Using High Concentration Ammonia Mixed with Methane. *Fuel* 275, 117902. doi:10.1016/j.fuel.2020.117902

Xu, L., McCabe, R. W., and Hammerle, R. H. (2002). NO_x Self-Inhibition in Selective Catalytic Reduction with Urea (Ammonia) over a Cu-Zeolite Catalyst in Diesel Exhaust. *Appl. Catal. B: Environ.* 39, 51–63. doi:10.1016/s0926-3373(02)00074-7

Yang, G., Guo, H., Kang, Z., Zhao, L., Feng, S., Jiao, F., et al. (2019). Green Hydrogen Separation from Nitrogen by Mixed-Matrix Membranes Consisting of Nanosized Sodalite Crystals. *ChemSusChem* 12, 4529–4537. doi:10.1002/cssc.201802577

Yun, B. K., and Kim, M. Y. (2013). Modeling the Selective Catalytic Reduction of NO_x by Ammonia over a Vanadia-Based Catalyst from Heavy Duty Diesel Exhaust Gases. *Appl. Therm. Eng.* 50, 152–158. doi:10.1016/j.applthermaleng.2012.05.039

Zakaznov, V. F., Kursheva, L. A., and Fedina, Z. I. (1978). Determination of Normal Flame Velocity and Critical Diameter of Flame Extinction in Ammonia-Air Mixture. *Combust. Explos.* 14, 710–713.

Zamfirescu, C., and Dincer, I. (2008). Using Ammonia as a Sustainable Fuel. *J. Power Sourc.* 185, 459–465. doi:10.1016/j.jpowsour.2008.02.097

Zamfirescu, C., and Dincer, I. (2009). Ammonia as a green Fuel and Hydrogen Source for Vehicular Applications. *Fuel Process. Techn.* 90, 729–737. doi:10.1016/j.fuproc.2009.02.004

Zhang, M., Wei, X., Wang, J., Huang, Z., and Tan, H. (2020). The Blow-Off and Transient Characteristics of Co-firing Ammonia/methane Fuels in a Swirl Combustor. *Proc. Combust. Inst.* 38, 5181–5190. doi:10.1016/j.proci.2020.08.056

Zhang, M., An, Z., Wang, L., Wei, X., Jianayihan, B., Wang, J., et al. (2021a). The Regulation Effect of Methane and Hydrogen on the Emission Characteristics of Ammonia/air Combustion in a Model Combustor. *Int. J. Hydrogen Energ.* 46, 21013–21025. doi:10.1016/j.ijhydene.2021.03.210

Zhang, M., An, Z., Wei, X., Wang, J., Huang, Z., and Tan, H. (2021b). Emission Analysis of the CH_4/NH_3/air Co-firing Fuels in a Model Combustor. *Fuel* 291, 120135. doi:10.1016/j.fuel.2021.120135

Zhou, S., Yang, W., Tan, H., An, Q., Wang, J., Dai, H., et al. (2021). Experimental and Kinetic Modeling Study on NH_3/syngas/air and NH_3/bio-syngas/air

Premixed Laminar Flames at Elevated Temperature. *Combust. Flame* 233, 111594. doi:10.1016/j.combustflame.2021.111594

Conflict of Interest: The authors declare that the research was conducted in the absence of any commercial or financial relationships that could be construed as a potential conflict of interest.

Publisher's Note: All claims expressed in this article are solely those of the authors and do not necessarily represent those of their affiliated organizations, or those of the publisher, the editors and the reviewers. Any product that may be evaluated in this article, or claim that may be made by its manufacturer, is not guaranteed or endorsed by the publisher.

frontiers in Energy Research

ORIGINAL RESEARCH
published: 13 October 2021
doi: 10.3389/fenrg.2021.753622

Co-Combustion Characteristics of Typical Biomass and Coal Blends by Thermogravimetric Analysis

Ye Yuan, Yong He, Jiaxin Tan, Yongmeng Wang, Sunel Kumar and Zhihua Wang*

State Key Laboratory of Clean Energy Utilization, Zhejiang University, Hangzhou, China

In this study, the co-combustion characteristics of coal and biomass blends (20, 40, 60, 80, and 100 wt%) were investigated by thermogravimetric analysis. All the samples were operated under an oxidative atmosphere, with a heating rate of 20 C/min. The reaction stages, ignition and burnout temperature, maximum weight loss rate, and different combustion indices were determined. When the percentage of biomass in the blends was increased, the maximum mass loss rate was enhanced in the second region, and the ignition and burnout temperature was lowered, indicating the higher reactivity and better combustion performance of the samples. The comprehensive performance index presented an N shape with the increasing biomass blending ratio. Based on various combustion indices, 20% was an optimum percentage for the co-utilization of coal-biomass blends. A significant promoting interaction was observed between corn straw and rice straw blends, while inhibiting effects occurred between rice husk and coal. The kinetic parameters of the blends were evaluated by the Coats and Redfern method using the *n*th-order reaction model. The value of activation energy and the pre-exponential factor increased with the decreasing biomass percentage in the blends.

Keywords: co-combustion, characteristics, kinetics, coal, biomass

OPEN ACCESS

Edited by:
Xuezhong He,
Guangdong Technion-Israel Institute of Technology, China

Reviewed by:
Linfeng Lei,
East China University of Science and Technology, China
Yang Xiao,
Xi'an University of Science and Technology, China

****Correspondence:***
Yong He
heyong@zju.edu.cn

Specialty section:
This article was submitted to Advanced Clean Fuel Technologies, a section of the journal Frontiers in Energy Research

Received: *05 August 2021*
Accepted: *03 September 2021*
Published: *13 October 2021*

Citation:
Yuan Y, He Y, Tan J, Wang Y, Kumar S and Wang Z (2021) Co-Combustion Characteristics of Typical Biomass and Coal Blends by Thermogravimetric Analysis. Front. Energy Res. 9:753622. doi: 10.3389/fenrg.2021.753622

INTRODUCTION

In recent years, the rapid economic development has caused increasing energy consumption, but the limited amount of nonrenewable energy resources and the depletion in the future pose a profound challenge to energy demand. In addition, the combustion of fossil fuels aggravates environmental pollution because of the emissions of nitrogen and sulfur pollutants as well as CO_2. Thus, the utilization of renewable energy has attracted considerable critical attention. Among these renewable energies, biomass may play an essential role due to its advantages of fuel flexibility, high combustion efficiency, low pollutant emission, and carbon neutrality (Jayaraman et al., 2017).

Numerous technologies have been extensively investigated for potential utilization of biomass, including combustion, pyrolysis, gasification, and liquefaction (Gil et al., 2010). Co-combustion is considered the state-of-the-art technology to utilize biomass for replacing fossil fuels, such as coal, to meet the stationary energy demand. Several reasons account for mixing biomass with coal before burning. The co-combustion of coal and biomass blends would directly help to cut down the consumption of fossil fuels. At the same time, a biofuel product is added to coal to obtain better burning performance during the combustion reaction (Wang et al., 2009). During the co-combustion process, a higher volatile matter content (normally more than 35%) is considered to provide a stable flame (Sahu et al., 2014), attained by the addition of biomass. The slagging and fouling problems of heating surfaces commonly faced in biomass combustion could be mitigated or eliminated through

co-combusting of coal and biomass (Haykiri-Acma and Yaman, 2008). Additionally, there is no need for existing power plants to undergo many modifications for continuous use. In conclusion, the co-utilization of biomass and coal blends in present coal-fired power plants possibly leads to a mass of benefits in the environment, technology, and economy (Kastanaki and Vamvuka, 2006).

Knowledge of combustion characteristics and kinetic mechanisms is crucial for comprehension and modeling in industrial-scale furnaces, co-firing of biomass and coal, and burning of coal alone (Hu et al., 2019). Thermogravimetric (TG) analysis is commonly used to obtain a rapid investigation and comparison in thermal characteristics and kinetic parameters during the combustion of various fuels, including coal and biomass. Many researchers (Gil et al., 2010; Yanfen and Xiaoqian, 2010; Su et al., 2013; Lin et al., 2015; Lu and Chen, 2015; Jayaraman et al., 2017; Chen et al., 2018; Hu et al., 2019; Wang et al., 2019; Wang et al., 2020) have studied the co-combustion behaviors of different biomass and coal/biomass blends. A significant decrease in ignition and burnout temperature was observed by Wang et al. (2019) and Konwar et al. (2019). According to Chen et al. (2018) and Liu et al. (2015), the combustion indices, such as maximum mass loss, ignition performance, and the comprehensive combustion index, were evaluated. Guo et al. (2020) and Shi et al. (2019) found the interaction between coal and biomass, including promoting synergy and inhibiting effects. The combustion kinetic parameters, including activation energy and the pre-exponential factor, using the Coats and Redfern method (Gil et al., 2010; Wang et al., 2012; Lin et al., 2015; Jayaraman et al., 2017; Chen et al., 2018) and the Flynn–Wall–Ozawa method (Xie and Ma, 2013; Liu et al., 2015; Konwar et al., 2019; Wang et al., 2019; Guo et al., 2020) were determined.

Crop straws and rice husk are the most fundamental agricultural residues in quantitative terms (Sathitruangsak and Madhiyanon, 2017). As the world's largest grain manufacturer, China owns plentiful biomass resources, and the amount of collectable straw was approximately 674 million tons in 2017 (Huo et al., 2020). Also, China is the leading country to cultivate rice, producing the most rice paddy (Hossain et al., 2018). Compared with other biomass, straw and rice husk char contain more high alkali and alkaline earth metals, which could catalyze the co-combustion process with coal and enhance combustion performance. Therefore, it was necessary to study the combustion and co-combustion characteristics and kinetic mechanisms to provide a theoretical basis and an optimal blending ratio of coal and biomass fuel.

In this research, co-combustion characteristics and kinetic parameters of mixed coal and three biomass samples (corn straw, rice straw, and rice husk) and their blends are examined under an oxidative atmosphere with TG equipment. The main objective of this study is to analyze the thermal behaviors and kinetic mechanisms of coal and biomass blends. This study also provides data on blending fuels in their combustion applicability. Finally, these results can thoroughly control the coal/biomass characteristics according to the demand.

MATERIALS AND METHODS

Materials

The corn straw (CS), rice straw (RS), and rice husk (RH) used in this study were collected from Jilin Province, China. Coal was obtained from Inner Mongolia, which is a mixture of brown and bituminous coal. The samples were milled into powder with a particle size of 75–150 μm. Then, different blend ratios were prepared with biomass of 20, 40, 60, and 80 wt% and named, for example, 20% CS, 40% RS, and 60% RH, depending on the proportion of the biomass in the blends. The prepared mixtures of coal and biomass were mixed manually into a homogeneous distribution. The photographs of raw, ground, and mixed samples are shown in **Figure 1**, and the ultimate and proximate analyses of biomass and coal samples are presented in **Table 1**.

Experimental Setup and Methods

Non-isothermal experiments were carried out employing a NETZSCH analyzer (model STA 449 F3) to investigate co-combustion behaviors and kinetic parameters of the samples. The sample mass for each test was approximately 5 mg. The experiment temperature was set from ambient temperature (20 C) to 1,000 C with a 20 C/min heating rate and a flow rate of 60 ml/min under air conditions. All experiments were reduplicated to ensure the reproducibility and consistency of the results. The weight loss and derivative thermogravimetry (DTG) of the samples were analyzed as a function of the temperature.

Combustion Parameters

The characteristic parameters of the combustion process were obtained from TG and DTG profiles. The ignition temperature (T_i) was determined using the intersection method (IM) (Lu and Chen, 2015), and the burnout temperature (T_b) was defined when the conversion reached 98% (Wang et al., 2019). In order to have a comprehensive analysis of the combustion characteristics of the samples, the flammability index, C, and the comprehensive combustion index, S, were introduced to compare the co-combustion performance and are shown as follows (Hu et al., 2019):

$$C = \frac{DTG_{max}}{T_i^2}, \tag{1}$$

$$S = \frac{DTG_{max} DTG_{mean}}{T_i^2 T_b}, \tag{2}$$

where DTG_{max} and DTG_{mean} are the maximum and average mass loss rates, respectively. The higher index S represents the more vigorous burning of the samples and the faster burnout of char.

Kinetic Analysis

The reaction of coal, biomass, and their blends is generally considered as a heterogeneous solid-phase reaction (Gil et al., 2010; Sahu et al., 2014), which follows the Arrhenius law, and can be described as

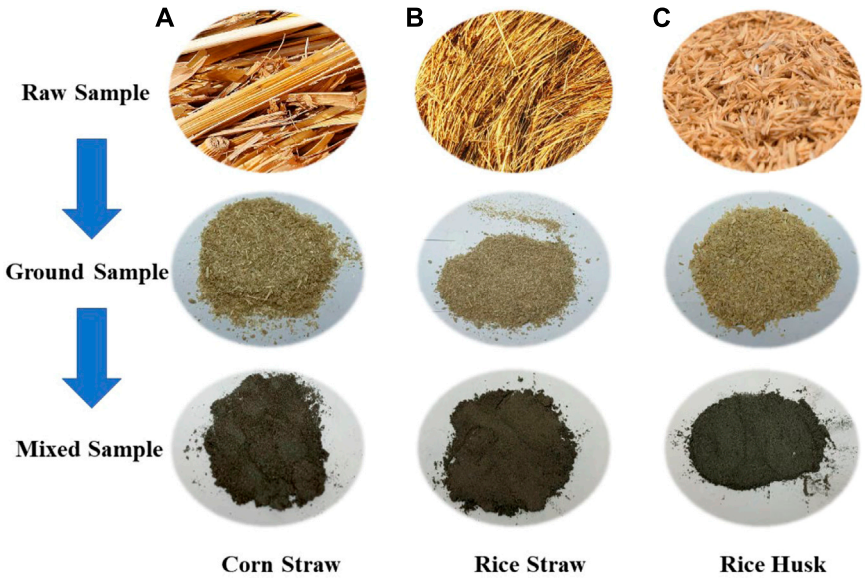

FIGURE 1 | Pictures of raw, ground, and mixed samples.

TABLE 1 | Proximate and ultimate analyses of samples on an air-dry basis.

Samples	Ultimate analysis (wt%)					Proximate analysis (wt%)				$Q_{net,ad}$ (MJ/kg)
	C	H	O[a]	N	S	V	FC	A	M	
Coal	58.27	3.01	18.38	0.7	0.32	29.4	51.28	8.96	10.36	25.59
CS	42.04	4.36	39.58	0.19	0.39	69.01	17.55	3.28	10.16	16.24
RS	37.35	3.81	34.76	0.73	0.19	62.01	14.83	12.02	11.14	14.61
RH	35,22	3.44	28.94	0.42	0.11	54.12	14.01	20.72	11.15	13.82

[a]*Calculated by difference.*

$$\frac{d\alpha}{dt} = k(T)f(\alpha), \tag{3}$$

where $\alpha = (m_0 - m_t)/(m_0 - m_\infty)$ is the conversion degree or mass conversion ratio obtained from TG curves, of which m_0 and m_∞ are the initial mass and final masses of the samples, respectively, and m_t represents the sample mass at time t.

From the Arrhenius equation, the reaction rate constant can be expressed as

$$k(T) = A\,exp\left(\frac{-E}{RT}\right), \tag{4}$$

where A, R, and E are the pre-exponential factor, universal gas constant, and activation energy, respectively.

For nonisothermal reactions, the heating rate remains constant ($\beta = dT/dt$). Therefore, the following could be inferred combining the equation:

$$\frac{d\alpha}{dT} = \frac{A}{\beta}exp\left(-\frac{E}{RT}\right)f(\alpha). \tag{5}$$

In this study, the Coats and Redfern (CR) method (Coats and Redfern, 1964) is used to determine the activation energy and reaction mechanism, which is widely used to estimate kinetic parameters for biomass combustion. The hypothetical model of the reaction is based on the nth reaction model (Wang et al., 2016; Chen et al., 2018); therefore, $f(\alpha) = (1-\alpha)^n$. The detailed form is shown as

$$In\left[-\frac{ln(1-\alpha)}{T^2}\right] = In\left[\frac{AR}{\beta E}\left(1-\frac{2RT}{E}\right)\right] - \frac{E}{RT};\ n = 1, \tag{6}$$

$$In\left[\frac{1-(1-\alpha)^{1-n}}{T^2(1-n)}\right] = In\left[\frac{AR}{\beta E}\left(1-\frac{2RT}{E}\right)\right] - \frac{E}{RT};\ n \neq 1. \tag{7}$$

For the basis of $\frac{E}{RT} \gg 1$, $1 - \frac{2RT}{E} \approx 1$, and the final form takes the following equation:

$$In\left[-\frac{ln(1-\alpha)}{T^2}\right] = In\left(\frac{AR}{\beta E}\right) - \frac{E}{RT};\ n = 1, \tag{8}$$

$$In\left[\frac{1-(1-\alpha)^{1-n}}{T^2(1-n)}\right] = In\left(\frac{AR}{\beta E}\right) - \frac{E}{RT};\ n \neq 1. \tag{9}$$

By plotting $In\left[-\frac{ln(1-\alpha)}{T^2}\right]$ and $In\left[\frac{1-(1-\alpha)^{1-n}}{T^2(1-n)}\right]$ vs. $1/T$, E could be obtained from the slope of a straight line. Different reaction order values were chosen to determine the best fitting ones.

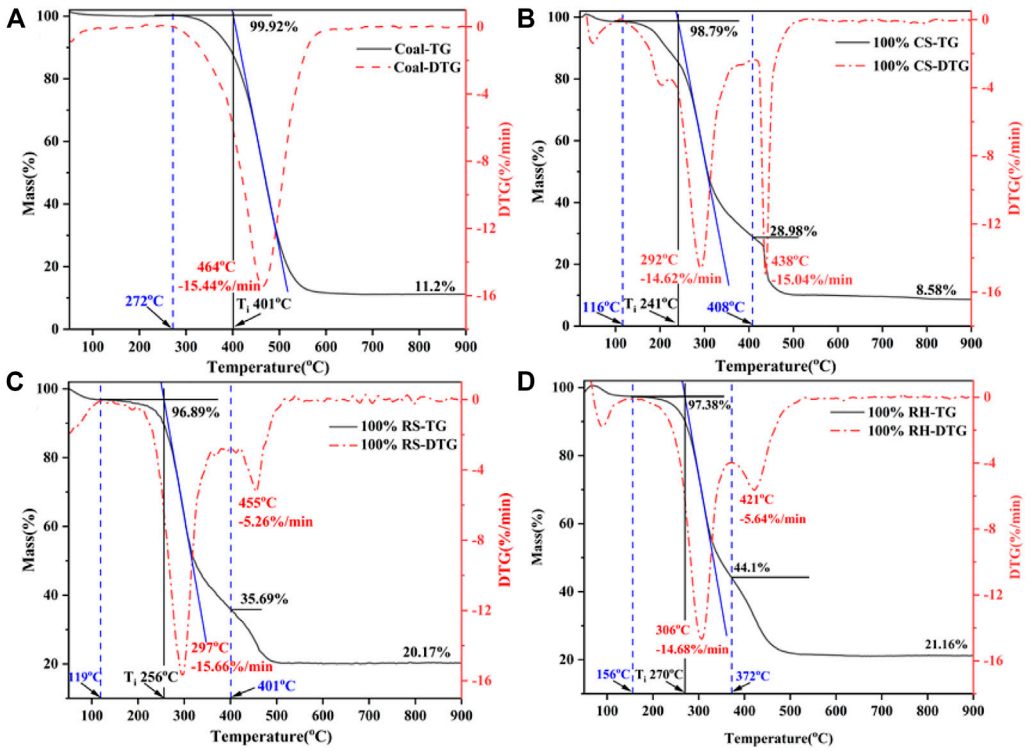

FIGURE 2 | Schematic diagrams of mass loss, stage division, and ignition temperature determination.

TABLE 2 | Temperature interval and weight loss of coal and biomass fuels.

Sample	Temperature interval (°C)		Weight loss (%)		Total loss (%)
	Stage B	Stage C	Stage B	Stage C	
Coal	-	272–684	-	88.98	88.98
CS	116–408	408–523	69.6	20.38	89.98
RS	119–401	401–516	61.35	15.46	76.81
RH	156–372	372–662	53.28	23.02	76.3

RESULTS AND DISCUSSION

Fuel Properties of a Single Sample

The thermochemical behaviors demonstrated by TG analysis could offer vital insights into the combustibility and transforming patterns of fuels (Luo et al., 2014). As shown in **Figure 2**, the ignition temperature for coal, CS, RS, and RH was 401°C, 241°C, 256°C, and 270°C, respectively, and the burnout temperature for the four samples was 557°C, 486°C, 481°C, and 479°C, respectively. These results indicated that the biomass fuels had a much lower ignition temperature and were easier to achieve burnout due to the higher volatile content in biomass, resulting in better thermal reactivity. Besides, the higher carbon content and the lower oxygen content in coal also contributed to the higher decomposition temperature as the chemical bond energy for breaking the C–C bond was higher than that for the C–O and C–H bonds (Konwar et al., 2019). Therefore, the destruction of the macromolecular structure and chemical bonds delayed the burnout of coal, and the reaction occurred at a higher temperature. The proximate analysis of coal and biomass in **Table 1** also confirmed all these results shown above.

The temperature ranges of the main stages, together with the weight loss, are shown in **Table 2**. It could be inferred that the combustion process of three biomass samples was partitioned into three stages (Jayaraman et al., 2017; Wang et al., 2019): the dehydration process (stage A), the release and combustion of the volatiles (stage B), and the burning and burnout of residues and fixed carbon (stage C). The demarcation of each stage was clarified by the inflection point in the DTG curves (Lin et al., 2015). In the case of the coal sample, there was only one stage during its combustion process after the moisture evaporation, which was the primary carbonizing stage accompanying the released carbon dioxide and hydrogen (Jayaraman et al., 2017). A single weight-loss peak with a wider temperature range was observed, corresponding to a longer overlapping reaction process with the combustion of the volatiles and char oxidation (Vamvuka and Sfakiotakis, 2011).

In all samples, the initial stage was observed from indoor temperature to 120°C. In this stage, the mass loss depended on the moisture content of the fuel properties, and a small DTG peak occurred in the DTG curve. The second stage for CS, RS, and RH was extended from 116 to 408°C, from 119 to 401°C, and from 156 to 372°C, and the mass loss was 69.6, 61.35, and 53.28%, respectively. It was seen that the weight loss during this stage was almost close to the volatile content in **Table 1**, accounting for

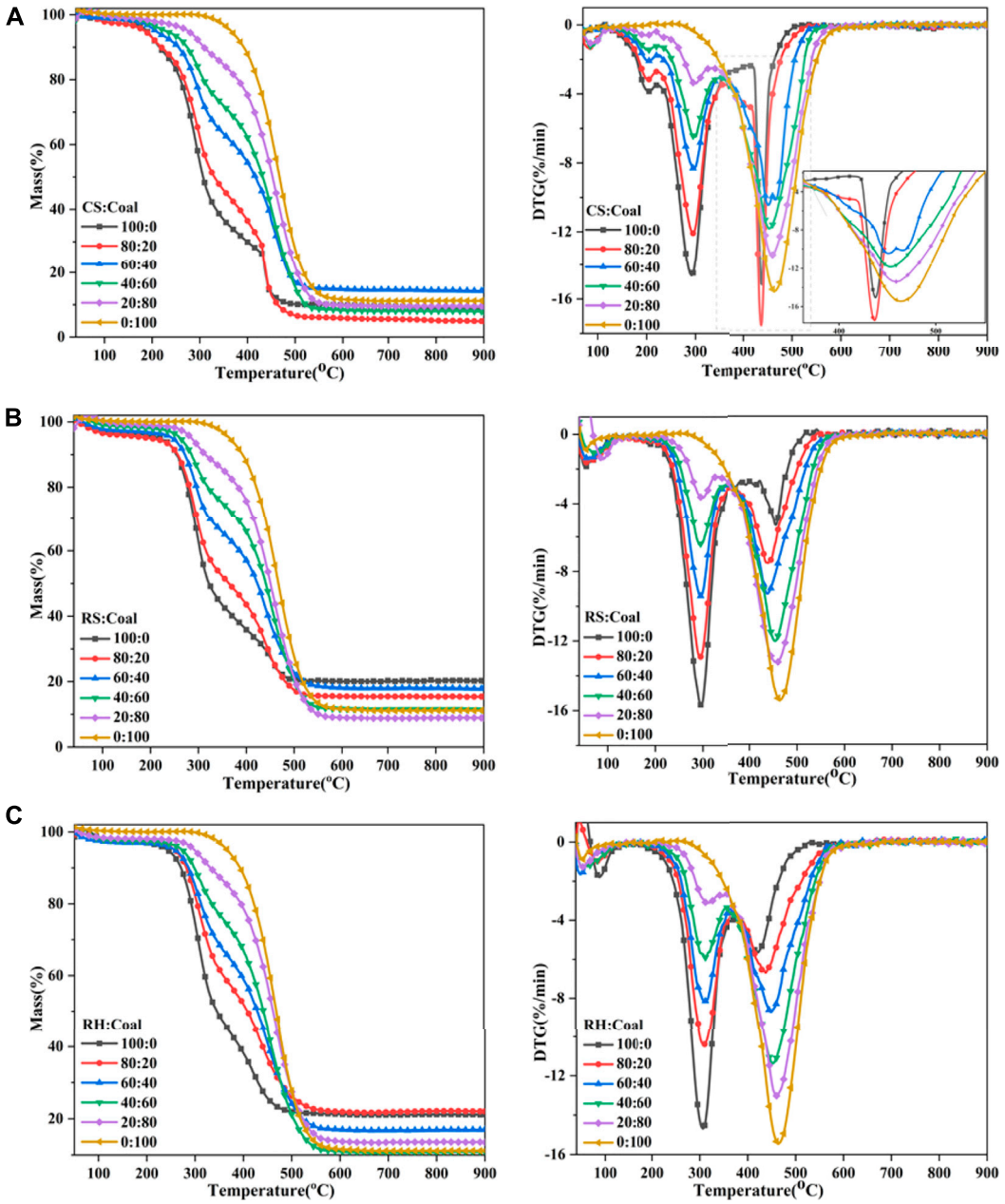

FIGURE 3 | TG and DTG curves of the blends: **(A)** CS, **(B)** RS, and **(C)** RH.

the majority of the total weight mass loss. This result confirmed that the predominant form of combustion in the second stage is *via* volatile releasing and burning, and a higher DTG peak was observed at around 300 C for three samples. It was attributed to the decomposition and combustion of celluloses (hemicellulose and cellulose), and a small account of lignin also combusted in this stage. The hemicellulose consists of a low degree of the amorphous structure, resulting in bad thermal stability, and the decomposition temperature extended from 220 to 315°C. However, the macromolecular structure of the cellulose is composed of glucose without branching, leading to a higher decomposition temperature (315–390 C). However, the thermal behavior of lignin occupied the whole decomposition process with a wider temperature range. This highly cross-linked polymer contained various chemical bonds, such as C–C bonds and ether bonds, causing a wide decomposition temperature (160–627 C). The third stage occupied the remaining small part of the total loss with a higher temperature range, as shown in **Table 2**. During this stage, the DTG peak for three biomass samples appeared at around 420 °C, and CS showed a sharp and narrow peak, while RH and RS presented a smaller and smoother peak. A deduction was that the decomposition process

TABLE 3 | Combustion characteristic parameters of the blends.

Samples	T_i (°C)	T_b (°C)	DTG_{max1} (%min)	DTG_{max2} (%min)	T_{max1} (°C)	T_{max2} (°C)	C (*105)	S (*107)
COAL	401	557		−15.4		465	9.58	8.12
20%CS	257	543	−3.39	−13.57	298	459	20.55	15.59
40%CS	254	527	−6.47	−11.82	300	453	18.32	14.04
60%CS	244	514	−8.32	−10.44	297	451	17.54	12.90
80%CS	243	499	−12.08	−17.43	294	437	29.52	25.26
CS	241	486	14.62	−15.04	292	438	25.90	23.12
20%RS	265	553	−3.65	−13.22	298	457	18.83	15.11
40%RS	263	544	−6.46	−11.97	293	454	17.31	11.71
60%RS	261	538	−9.41	−9.24	295	438	13.81	9.32
80%RS	257	528	−12.93	−7.47	293	439	19.58	14.05
RS	256	481	−15.66	−5.26	297	455	23.90	19.18
20%RH	278	546	−3.12	−13.02	314	461	16.85	13.82
40%RH	265	535	−5.9	−11.36	310	451	16.18	13.09
60%RH	272	535	−8.15	−8.7	311	449	11.76	8.902
80%RH	270	504	−10.4	−6.68	308	438	14.27	10.33
RH	270	479	−14.68	−5.64	306	421	20.14	16.90

changed the physicochemical properties of the char produced after the burnout of volatiles, and the combustion performance in the char combustion process significantly varied. Liu et al. (2015) pointed out that the formation or the structure of char differed greatly during the carbonization process, directly affecting the DTG peaks.

Co-Combustion Properties of the Biomass and Coal Blends

The mass loss and DTG profiles of coal and biomass blends are presented in **Figure 3**. The combustion process of the blends also contained three stages: moisture evaporation, the decomposition and combustion of volatile matters, and the oxidation of char. It can be seen that for RS and RH, the DTG curves of their blends were located between individual fuels, but for CS, there existed obvious overlapping in its DTG curve, corresponding to the evident decline in the TG curve at approximately 430 °C for CS and 80% CS samples. It was easy to interpret that the intensity of the third DTG peak for CS varied distinctly with RS and RH owing to the higher fixed carbon content and the significantly lower ash content within CS in **Table 1**, generating a higher amount of combustible char, that is, more flammable substances would be produced and combusted in Stage C. Besides, the higher carbon and lower oxygen content required more oxygen during combustion, so the combustion of certain matters in Stage B was delayed, contributing to a higher DTG value in Stage C. When 20% of coal was added to the biomass sample, the combustion performance of the mixed sample improved. This was owing to the fact that the large amount of heat generated during the combustion of biomass volatiles would facilitate the combustion of coal and biomass char. While more coal was mixed with CS, the combustion of char needed more heat, but the combustion of biomass char could not provide sufficient heat; thus, the third DTG peak moved forward to a higher-temperature range. In a similar case in corn and wheat straw, Li et al. (2014) and Wang et al. (2019) identified the same phenomenon.

To compare combustion characteristics and quantitatively analyze, various combustion parameters are shown in **Table 3**. The main observation was that when the percentage of biomass in the blends increased, the ignition temperature immediately decreased, but a relatively slow reduction in the burnout temperature was found. It was noteworthy that the ignition temperature of the blends was extremely close to that of individual biomass samples, revealing that the ignition of two fuels occurred independently, and biomass played a predominant role at low temperatures. A possible explanation for this might be that many volatile matters were obtained and rapidly ignited. The combustion of the volatiles was an exothermic reaction, giving off a large amount of heat and increasing the surface temperature (Liu et al., 2015) and thereby the reaction rate of blends. In contrast, when the percentage of biomass was within 60%, the burnout temperature for blends was closer to that of the coal sample. This result suggested that the coal dominated the burnout process for the blends, which was probably related to the higher carbon content in coal, requiring a high temperature to burn out.

Another important index obtained for the curves was the maximum DTG value; DTG_{max} was deemed to be proportionate to sample reactivity. DTG_{max1} and DTG_{max2} represented the maximum loss rates for Stages B and C, respectively. In the blends, DTG_{max1} increased with the percentage of biomass contained in the blends, which suggested that the higher the amount of biomass in the mixtures, the faster the rate of mass loss for the second stage or in other words, the higher the reactivity of the sample in this stage. This result may be explained by the fact that the biomass had a lower ignition temperature and almost all volatiles generated in Stage B would be combusted, contributing to the higher DTG value for the first mass loss peak. In stage C, this was not the case due to the addition of coal, and DTG_{max2} increased with the rising percentage of coal in the blends, suggesting that coal could improve the reactivity of the samples in the later stage of combustion. It was easy to understand that the higher the ratio of coal, the higher the fixed carbon in the blends, and the combustion of flammable

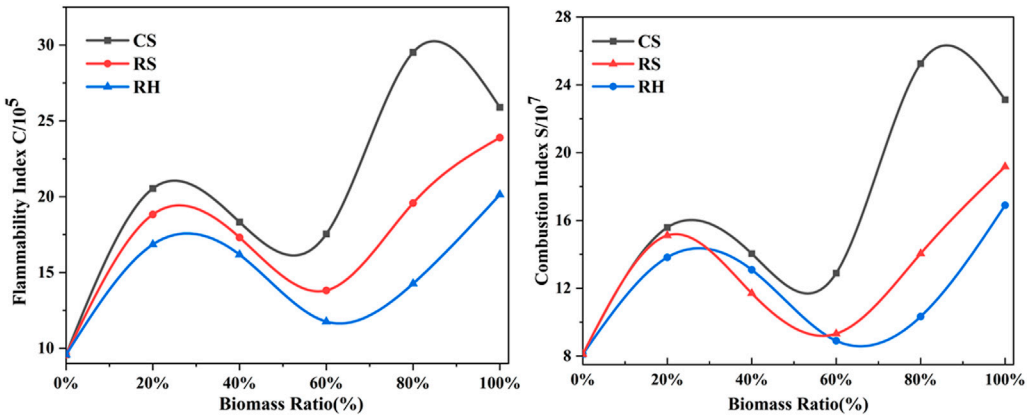

FIGURE 4 | C and S curves with increasing biomass ratio.

substances including char enhanced the sample's reactivity. Interestingly, there was a turning point for blends where DTG_{max2} was bigger than DTG_{max1} when 40% of coal was mixed with biomass. This observation may support the hypothesis that biomass controlled the second combustion stage (Stage B), while coal dominated the third stage (Stage C).

Finally, to achieve a comprehensive evaluation of ignition and combustion performance of coal and biomass blends, two combustion indices as a function of biomass blending ratio are shown in **Figure 4**. The trend of S and C increased first, then declined, and rose again when the percentage of biomass exceeded 80%, overall exhibiting an "N" curve shape. What stands out in the figure is the marked value of C and S for 20% biomass mixed in blends, implying the improvement of combustion performance by the addition of biomass. Considering the stability of boiler operation and the limitation of the feeding system, the amount of biomass in the blends is suggested to be kept at around 20%, according to the results in this study. Previous research (Zhou et al., 2016) had confirmed that the blending proportion of 20% was regarded as the optimum blend for the co-combustion of corn stalk and bituminous coal. This conclusion was consistent with the review by Sahu et al. (2014), which reported that a biomass content of 20% favored the best additive effects.

Synergistic Effect Analysis

To identify whether interactions between coal and biomass happened during the co-combustion process, the calculated TG curves of the blends based on the experimental curves of individual fuels were compared with experimental curves. Assuming that there were no interactions between the two components, the calculated TG curves could be expressed as follows (Wang et al., 2019; Guo et al., 2020):

$$TG_{cal} = x_{bio}TG_{bio} + x_{coaI}TG_{coal}, \tag{10}$$

where TG_{bio} and TG_{coal} are the mass losses of individual fuels and x_{bio} and x_{coaI} are the percentages of biomass and coal, respectively.

The calculated TG curves of three blends are shown in **Figure 5**. To further elucidate the differences between the two curves of the mixed samples, the deviation was introduced as follows (Wang et al., 2019):

$$\Delta w = TG_{exp} - TG_{cal}, \tag{11}$$

where Δw was defined to explicitly demonstrate the interaction between biomass and coal during the co-fire process. **Figure 6** exhibits the deviation value between TG_{cal} and TG_{exp}, and $\Delta w > 0$ and <0 represented the synergetic and suppressive interactions, respectively. It could be found that calculated and experimental curves were similar in the early stage, but deviation occurred with the proceeding co-combustion process. This implied that synergetic interactions existed between coal and biomass.

As shown in **Figure 5** and **Figure 6**, CS and RS exhibited similar patterns for calculated and experimental curves. From the initial stage to around 250 °C (the ignition temperature of biomass), good agreement was observed between TG_{cal} and TG_{exp} for the biomass ratios of 20, 40, and 60% in the blends, which suggested that no interactions happened. With the increase of conversion, when the temperature rose to 300 °C, the Δw curve slightly dropped for all blends.

This may be attributed to the thermal resistance effect, in which the biomass component of the blends softened, flowed, and then adhered to the burning surface. Besides, a higher temperature was needed for the devolatilization of the high coalification degree of coal, and the heat released by biomass combustion after ignition was used for the endothermic reaction of the coal's ignition process. However, when the temperature was over 350 °C, it can be seen from **Figure 6** that TG_{exp} markedly excessed TG_{cal}, which indicated that the inhibition turned into a promoting effect. The Δw reached a peak value at around 450–500°C, which was the burnout temperature of individual biomass. It could be explained by the fact that the ignition temperature of biomass char was low, and vast heat generated after combustion heated the fixed carbon in coal. At the same time, the alkaline matters in biomass ash, including oxides of potassium, sodium, and magnesium, catalyzed the

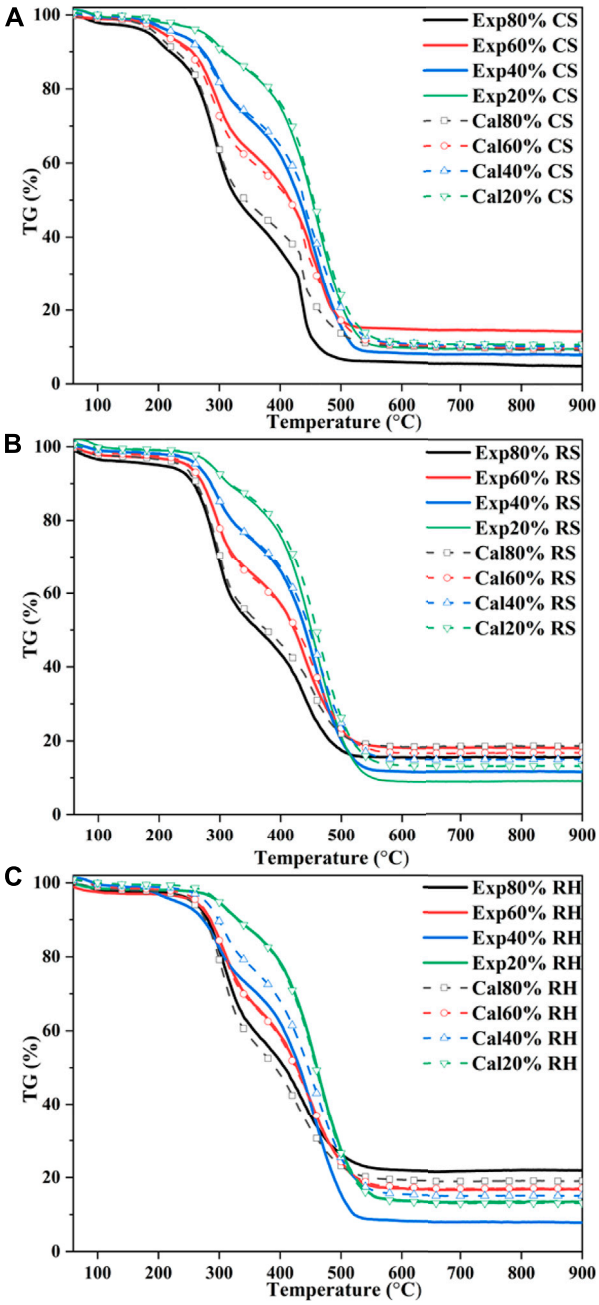

FIGURE 5 | Comparison of calculated and experimental TG values: **(A)** CS, **(B)** RS, and **(C)** RH.

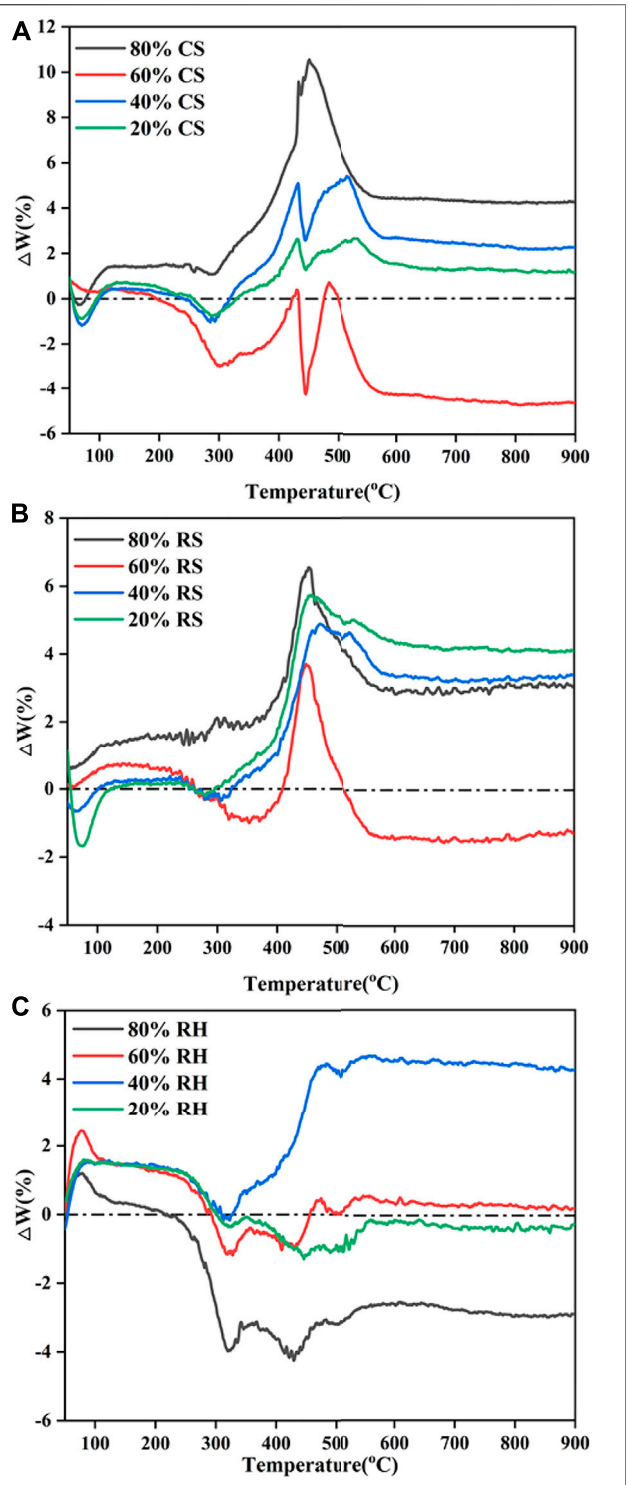

FIGURE 6 | Comparison of deviation between calculated and experimental TG values: **(A)** CS, **(B)** RS, and **(C)** RH.

co-combustion of the blends and then accelerated the reaction rate. This assumption was also confirmed by other researchers (Wang et al., 2016; Wang et al., 2019; Guo et al., 2020), who found the promoting reactions between alkaline and alkaline earth metals in biomass ash and solid carbon in coal.

It was noteworthy that the interaction between 60% biomass and 40% coal lagged behind other group blends; for CS, the interaction functioned as inhibition. This phenomenon may be driven by the fact that the devolatilization of chemical constituents from biomass blocked the pores of coal (Konwar et al., 2019), which could weaken heat-transfer efficiency and oxygen diffusion, therefore hindering the combustion of fixed carbon, inhibiting the devolatilization process and exerting resistance on gas diffusion

TABLE 4 | Combustion characteristic parameters of the blends.

Sample	Stage B				Stage C			
	E (kJ/mol)	A (min^{-1})	N	R^2	E (kJ/mol)	A (min^{-1})	N	R^2
Coal					88.02	4.93 E+05	1	0.995
20%CS	68.25	6.51 E+05	0.6	0.996	92.16	1.16 E+05	1	0.999
40%CS	65.15	3.62 E+05	0.9	0.996	101.51	6.72 E+05	1	0.999
60%CS	62.55	2.27 E+05	0.9	0.995	106.63	2.03 E+06	1.2	0.998
80%CS	58.90	1.01 E+05	0.9	0.995	166.06	1.63 E+12	1.5	0.985
CS	51.89	1.96 E+04	1.2	0.981	292.88	1.72 E+19	2	0.990
20%RS	110.3	1.84 E+10	1	0.981	92.9	1.84 E+06	1	0.998
40%RS	106.8	7.36 E+09	1	0.993	93.82	2.12 E+06	1	0.996
60%RS	104.2	3.37 E+09	1.2	0.993	94.5	2.47 E+06	1.2	0.996
80%RS	95.91	6.77 E+08	1.2	0.993	102.5	1.19 E+08	1.2	0.996
RS	79.42	1.12 E+07	1.2	0.976	176.11	3.71 E+12	1.2	0.997
20%RH	115.12	2.49 E+11	1	0.996	94.06	1.44 E+06	1.2	0.999
40%RH	101.39	7.96 E+08	1.2	0.996	93.83	1.55 E+06	1.2	0.996
60%RH	97.63	2.53 E+08	1.2	0.994	92.84	1.37 E+06	1.5	0.997
80%RH	91.34	7.23 E+07	1.2	0.995	94.38	1.17 E+06	1.5	0.996
RH	83.31	1.43 E+07	1.2	0.992	125.72	1.24 E+09	1.5	0.996

(Chen et al., 2015). Besides, the generated fly ash would hinder the diffusion of the flame during 40% coal char combustion, thereby exhibiting a distinct flame retardant effect. Under such a blending ratio, the catalytic effects of biomass char were dramatically restricted by the blocking pores, while for 80% biomass samples, the reaction of biomass in different stages dominated the whole process due to the higher biomass blending ratio. Cong et al. (2020) confirmed this result in evaluating the performance of semi-coke and corn stover, and such a trend was also observed.

As for RH, which is shown in **Figure 6C**, the calculated and experimental TG profiles almost coincided for 20 and 60% RH blends. It was noted that for 40% RH, the calculated values were higher than experimental values and $\Delta w > 0$, which represented the synergetic interaction between two components in the sample, but inhibiting interactions were detected for 80% RH since an opposite trend was found between the two values. These results showed that the interactions in the blends switched from promotion to suppression, with the biomass ratio increased from 20 to 80%. A probable reason for the change was the highest content of SiO_2 in RH ash compared with straw biomass. Different from the catalytic effects of alkali matters in biomass ash, SiO_2 and Al_2O_3 could hinder the reaction process. According to earlier studies, nearly 80% of RH ash was SiO_2 and this significantly inhibited the combustion process. This assumption corresponded to Wang et al. (2016) and Zhou et al. (2014), who demonstrated that the existence of SiO_2 in rice husk ash had obvious inhibiting effects during the co-combustion process; the experimental data were lower than calculated values in the temperature range of 575–800 K.

Kinetic Analysis

The kinetic parameters were calculated on the assumption that the reaction was separated into a single stage during the thermal conversion (Gil et al., 2010). Thus, two independent reactions were necessary for coal/biomass blends to describe the co-combustion process, and the conversion in each stage was recalculated for each reaction. In this study, several reaction order values (n = 0.3, 0.6, 0.9, 1, 1.2, 1.5, 2, and 3) were applied to the TG data; the n value that gave the highest correlation coefficient represents the kinetic mechanisms for each reaction. **Table 4** shows that in this research, reaction orders of 0.9–1.2 and 1–1.5 were the best fitting models for Stage B and Stage C, respectively. Similarly, Chen et al. (2018) also reported that 1.2 and 1.5 were the most suitable model functions for the two stages during the co-combustion of coal/biomass blends.

Figure 7 shows the curve fitting of CR plots for all samples, which had the best linear results. Most of the resulting correlation coefficients (R2) were higher than 0.99 (**Table 4**), indicating that the calculation profiles were reliable. A decreasing order of activation energy was found in Stage B, followed by RH > RS > CS, and the E values for the three biomasses were 83.31 kJ/mol, 79.42 kJ/mol, and 51.89 kJ/mol, respectively. As the reaction progressed, what stood out in Stage C was the sharp increase for the E values, which were 292.88 kJ/mol, 176.11 kJ/mol, and 125.72 kJ/mol, with the opposite order as RH < RS < CS. The E values were considered to be the minimum energies required for the combustion reactions, with the high value representing that the reaction started slowly. These results meant that CS was easier to ignite in the early stage, but more energy was needed to break down the barriers in the later combustion process. This was due to the difference in the constitution of the three biomasses; the decomposition and burning of volatile matter and fixed carbon greatly influenced the combustion process. A single or overlapping process of manifold reaction mechanisms, including diffusion and interface, also accounted for the different values (Huang et al., 2018). The difference in the E values between the two stages implied that a higher temperature was required for the char-burning stage, revealing that this reaction with higher activation energies was more temperature-dependent (Masnadi et al., 2014; Liu et al., 2015).

It was noted that in Stage B for all blends, the activation energy and pre-exponential factor values increased with increasing biomass ratio in the blends, while a significant opposite trend was observed in Stage C. Besides, when the biomass ratio was under 60%, there was no striking difference in E values between the coal sample and the blends in Stage C; for RH, the blending ratio even reached 80%. This finding also accorded with our earlier observations, which showed that

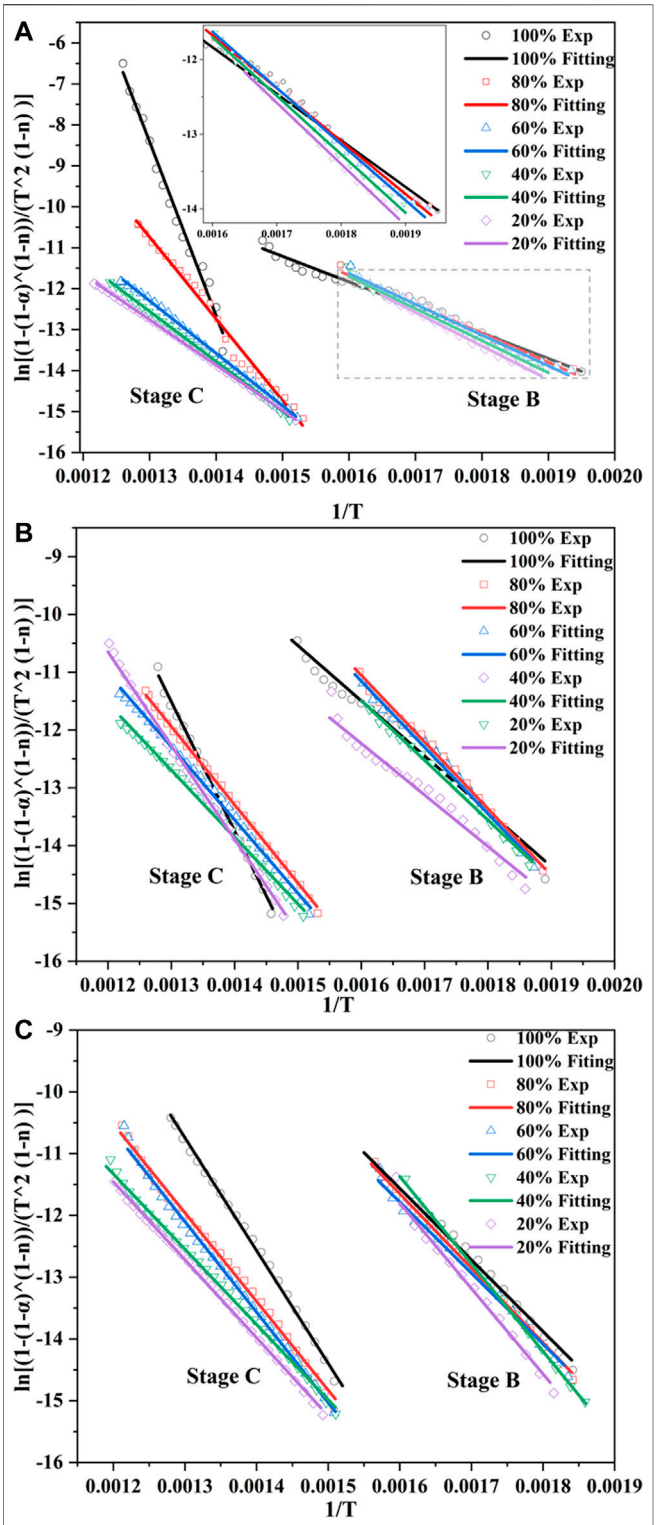

FIGURE 7 | CR plots for coal/biomass blends: **(A)** CS, **(B)** RS, and **(C)** RH.

coal dominated the oxidation of char in the later stage. The activation energy value of coal and biomass blends acquired in this study was comparable to those of previous studies. Zhou et al. (2016) reported that the activation energy of corn stalk/bituminous coal blends was in the range of 64.5–94.8 kJ/mol. Xie and Ma (2013) demonstrated 97 kJ/mol of E value for rice straw using the Friedman method. Wang et al. (2020) specified an activation energy of 83.35 kJ/mol for rice husk with a second-order reaction mechanism.

CONCLUSIONS

In the air atmosphere, the combustion process of biomass and the blends could be portioned into two stages after the initial moisture evaporation compared to a single stage for the coal sample. Considering the pattern of characteristic combustion parameters (T_i, T_b, DTG_{max1}, DTG_{max2}, T_{max1}, T_{max2}, C, and S), as the biomass ratio increased, the combustion performance of the blends was enhanced. Based on the combustion characteristics, 20% biomass was the optimum percentage for the co-combustion process. The synergetic interaction of the co-combustion process for CS and RS blends was observed due to the catalytic effect of the biomass ash. However, an inhibiting effect for RH and coal in a higher biomass ratio was found, attained by a large amount of SiO_2 content in ash, hindering the combustion of fixed carbon. The reaction orders of 1.2 and 1.5 were the best fitting results for Stages B and C and sought to be the reaction mechanisms for biomass and the blends. In Stage B, the activation energy values for three biomasses showed a decreasing order as RH > RS > CS, and the E values were 83.31 kJ/mol, 79.42 kJ/mol, and 51.89 kJ/mol, respectively. However, as the reaction was processed, an opposite trend was reported. Also, the E and A values increased with the increasing biomass percentage in Stage B, while the oxidation of char dominated Stage C and presented a decreasing pattern.

DATA AVAILABILITY STATEMENT

The original contributions presented in the study are included in the article/Supplementary material; further inquiries can be directed to the corresponding author.

AUTHOR CONTRIBUTIONS

YY drafted the work and agreed to be accountable for all aspects of the work in ensuring that questions related to the accuracy or integrity of any part of the work are appropriately investigated and resolved. YH revised it critically for important intellectual content. JT and YW helped the acquisition, analysis, or interpretation of data for the work. ZW and SK provided approval for publication of the content.

FUNDING

This work was supported by the National Natural Science Foundation of China (51776185), the Zhejiang Provincial Natural Science Foundation (LGC19E060001, LY20E060005), and the Fundamental Research Funds for the Central Universities (2021FZZX001-11).

REFERENCES

Chen, J., Mu, L., Cai, J., Yin, H., Song, X., and Li, A. (2015). Thermal Characteristics and Kinetics of Refining and Chemicals Wastewater, lignite and Their Blends during Combustion. *Energ. Convers. Manage.* 100, 201–211. doi:10.1016/j.enconman.2015.05.016

Chen, G.-B., Chatelier, S., Lin, H.-T., Wu, F.-H., and Lin, T.-H. (2018). A Study of Sewage Sludge Co-Combustion with Australian Black Coal and Shiitake Substrate. *Energies* 11 (12), 3436. doi:10.3390/en11123436

Coats, A. W., and Redfern, J. P. (1964). Kinetic Parameters from Thermogravimetric Data. *Nature* 201 (491), 68–69. doi:10.1038/201068a0

Cong, H., Zhao, L., Mašek, O., Yao, Z., Meng, H., Huo, L., et al. (2020). Evaluating the Performance of Honeycomb Briquettes Produced from Semi-Coke and Corn stover Char: Co-Combustion, Emission Characteristics, and a Value-Chain Model for Rural China. *J. Clean. Prod.* 244, 118770. doi:10.1016/j.jclepro.2019.118770

Gil, M. V., Casal, D., Pevida, C., Pis, J. J., and Rubiera, F. (2010). Thermal Behaviour and Kinetics of Coal/Biomass Blends During Co-Combustion. *Bioresour. Technol.* 101 (14), 5601–5608. doi:10.1016/j.biortech.2010.02.008

Guo, S., Han, Y., Wang, L., Che, D., Liu, H., and Sun, B. (2020). Synergistic Effects of Co-Combustion of Sewage Sludge and Corn Stalk and the Resulting Gas Emission Characteristics. *IET Renew. Power Generation* 14 (9), 1596–1605. doi:10.1049/iet-rpg.2020.0104

Haykiri-Acma, H., and Yaman, S. (2008). Effect of Co-Combustion on the Burnout of Lignite/Biomass Blends: A Turkish Case Study. *Waste Manage.* 28 (11), 2077–2084. doi:10.1016/j.wasman.2007.08.028

Hossain, S. S., Mathur, L., and Roy, P. K. (2018). Rice Husk/Rice Husk Ash as an Alternative Source of Silica in Ceramics: A Review. *J. Asian Ceram. Societies* 6 (4), 299–313. doi:10.1080/21870764.2018.1539210

Hu, J., Yan, Y., Evrendilek, F., Buyukada, M., and Liu, J. (2019). Combustion Behaviors of Three Bamboo Residues: Gas Emission, Kinetic, Reaction Mechanism and Optimization Patterns. *J. Clean. Prod.* 235, 549–561. doi:10.1016/j.jclepro.2019.06.324

Huang, L., Xie, C., Liu, J., Zhang, X., Chang, K., Kuo, J., et al. (2018). Influence of Catalysts on Co-Combustion of Sewage Sludge and Water Hyacinth Blends as Determined by TG-MS Analysis. *Bioresour. Technol.* 247, 217–225. doi:10.1016/j.biortech.2017.09.039

Huo, L., Yao, Z., Yao, Z., Jia, J., Zhao, L., Cong, H., et al. (2020). Evaluation of Different Clean Heat Supply Modes Based on Crop Straws in the Rural Area of Northern China. *Int. J. Agric. Biol. Eng.* 13 (5), 209–217. doi:10.25165/j.ijabe.20201305.5600

Jayaraman, K., Kok, M. V., and Gokalp, I. (2017). Thermogravimetric and Mass Spectrometric (TG-MS) Analysis and Kinetics of Coal-Biomass Blends. *Renew. Energ.* 101, 293–300. doi:10.1016/j.renene.2016.08.072

Kastanaki, E., and Vamvuka, D. (2006). A Comparative Reactivity and Kinetic Study on the Combustion of Coal-Biomass Char Blends. *Fuel* 85 (9), 1186–1193. doi:10.1016/j.fuel.2005.11.004

Konwar, K., Nath, H. P., Bhuyan, N., Saikia, B. K., Borah, R. C., Kalita, A. C., et al. (2019). Effect of Biomass Addition on the Devolatilization Kinetics, Mechanisms and Thermodynamics of a Northeast Indian Low Rank Sub-bituminous Coal. *Fuel* 256, 115926. doi:10.1016/j.fuel.2019.115926

Li, L., Ren, Q., Wang, X., Li, S., and Lu, Q. (2014). TG-MS Analysis of thermal Behavior and Gaseous Emissions during Co-Combustion of Straw with Municipal Sewage Sludge. *J. Therm. Anal. Calorim.* 118 (1), 449–460. doi:10.1007/s10973-014-3952-7

Lin, Y., Ma, X., Ning, X., and Yu, Z. (2015). TGA-FTIR Analysis of Co-Combustion Characteristics of Paper Sludge and Oil-Palm Solid Wastes. *Energ. Convers. Manage.* 89, 727–734. doi:10.1016/j.enconman.2014.10.042

Liu, X., Chen, M., and Wei, Y. (2015a). Kinetics Based on Two-Stage Scheme for Co-Combustion of Herbaceous Biomass and Bituminous Coal. *Fuel* 143, 577–585. doi:10.1016/j.fuel.2014.11.085

Liu, Z., Li, W., Zhang, Y., Wang, J., Orndorff, W., and Pan, W.-P. (2015b). Influence of Biomass on Coal Combustion Based on Thermogravimetry and Fourier Transform Infrared Spectroscopy. *J. Therm. Anal. Calorim.* 122 (3), 1289–1298. doi:10.1007/s10973-015-4841-4

Lu, J.-J., and Chen, W.-H. (2015). Investigation on the Ignition and Burnout Temperatures of Bamboo and Sugarcane Bagasse by Thermogravimetric Analysis. *Appl. Energ.* 160, 49–57. doi:10.1016/j.apenergy.2015.09.026

Luo, J., Fang, Z., and Smith, R. L. (2014). Ultrasound-Enhanced Conversion of Biomass to Biofuels. *Prog. Energ. Combustion Sci.* 41, 56–93. doi:10.1016/j.pecs.2013.11.001

Masnadi, M. S., Habibi, R., Kopyscinski, J., Hill, J. M., Bi, X., Lim, C. J., et al. (2014). Fuel Characterization and Co-Pyrolysis Kinetics of Biomass and Fossil Fuels. *Fuel* 117, 1204–1214. doi:10.1016/j.fuel.2013.02.006

Sahu, S. G., Chakraborty, N., and Sarkar, P. (2014). Coal-Biomass Co-Combustion: An Overview. *Renew. Sustain. Energ. Rev.* 39, 575–586. doi:10.1016/j.rser.2014.07.106

Sathitruangsak, P., and Madhiyanon, T. (2017). Effect of Operating Conditions on the Combustion Characteristics of Coal, Rice Husk, and Co-Firing of Coal and Rice Husk in a Circulating Fluidized Bed Combustor. *Energy Fuels* 31 (11), 12741–12755. doi:10.1021/acs.energyfuels.7b01513

Shi, K., Oladejo, J. M., Yan, J., and Wu, T. (2019). Investigation on the Interactions Among Lignocellulosic Constituents and Minerals of Biomass and Their Influences on Co-Firing. *Energy* 179, 129–137. doi:10.1016/j.energy.2019.05.008

Su, W., Ma, H., Wang, Q., Li, J., and Ma, J. (2013). Thermal Behavior and Gaseous Emission Analysis During Co-Combustion of Ethanol Fermentation Residue from Food Waste and Coal Using TG-FTIR. *J. Anal. Appl. Pyrolysis* 99, 79–84. doi:10.1016/j.jaap.2012.10.023

Vamvuka, D., and Sfakiotakis, S. (2011). Combustion Behaviour of Biomass Fuels and Their Blends with lignite. *Thermochim. Acta* 526 (1-2), 192–199. doi:10.1016/j.tca.2011.09.021

Wang, C., Wang, F., Yang, Q., and Liang, R. (2009). Thermogravimetric Studies of the Behavior of Wheat Straw with Added Coal during Combustion. *Biomass and Bioenergy* 33 (1), 50–56. doi:10.1016/j.biombioe.2008.04.013

Wang, J., Zhang, S.-Y., Guo, X., Dong, A.-X., Chen, C., Xiong, S.-W., et al. (2012). Thermal Behaviors and Kinetics of Pingshuo Coal/Biomass Blends During Copyrolysis and Cocombustion. *Energy Fuels* 26 (12), 7120–7126. doi:10.1021/ef301473k

Wang, G., Zhang, J., Shao, J., Liu, Z., Zhang, G., Xu, T., et al. (2016). Thermal Behavior and Kinetic Analysis of Co-Combustion of Waste Biomass/low Rank Coal Blends. *Energ. Convers. Manage.* 124, 414–426. doi:10.1016/j.enconman.2016.07.045

Wang, C., Wang, X., Jiang, X., Li, F., Lei, Y., and Lin, Q. (2019). The thermal Behavior and Kinetics of Co-Combustion between Sewage Sludge and Wheat Straw. *Fuel Process. Technol.* 189, 1–14. doi:10.1016/j.fuproc.2019.02.024

Wang, T., Fu, T., Chen, K., Cheng, R., Chen, S., Liu, J., et al. (2020). Co-combustion Behavior of Dyeing Sludge and rice Husk by Using TG-MS: Thermal Conversion, Gas Evolution, and Kinetic Analyses. *Bioresour. Technol.* 311, 123527. doi:10.1016/j.biortech.2020.123527

Xie, Z., and Ma, X. (2013). The thermal Behaviour of the Co-Combustion between Paper Sludge and Rice Straw. *Bioresour. Technol.* 146, 611–618. doi:10.1016/j.biortech.2013.07.127

Yanfen, L., and Xiaoqian, M. (2010). Thermogravimetric Analysis of the Co-Combustion of Coal and Paper Mill Sludge. *Appl. Energ.* 87 (11), 3526–3532. doi:10.1016/j.apenergy.2010.05.008

Zhou, C., Liu, G., Cheng, S., Fang, T., and Lam, P. K. S. (2014). Thermochemical and Trace Element Behavior of Coal Gangue, Agricultural Biomass and Their Blends during Co-combustion. *Bioresour. Technol.* 166, 243–251. doi:10.1016/j.biortech.2014.05.076

Zhou, C., Liu, G., Wang, X., and Qi, C. (2016). Co-Combustion of Bituminous Coal and Biomass Fuel Blends: Thermochemical Characterization, Potential Utilization and Environmental Advantage. *Bioresour. Technol.* 218, 418–427. doi:10.1016/j.biortech.2016.06.134

Conflict of Interest: The authors declare that the research was conducted in the absence of any commercial or financial relationships that could be construed as a potential conflict of interest.

frontiers in Energy Research

ORIGINAL RESEARCH
published: 11 November 2021
doi: 10.3389/fenrg.2021.772755

Effects of Temperature and Additives on NO_x Emission From Combustion of Fast-Growing Grass

Haili Liu[1], Qingchao Hong[1], Heyun Liu[1], Zhen Huang[2], Xu Zhang[1], Wang Chen[1], Xi Zeng[1] and Shulin Pan[1]*

[1]School of Energy and Mechanical Engineering, Hunan Institute of Humanities, Science and Technology, Loudi, China, [2]Guangzhou Institute of Energy Conversion, Chinese Academy of Sciences, Guangzhou, China

Fast-growing grass, as a popular renewable energy, is low in sulfur content, so NO_x is the major pollutant during its combustion. To study the emission characteristics of NO_x and obtain the data of controlling NO_x emission, the effects of combustion temperature as well as the additive type and mass fraction were investigated on the emission characteristics of NO_x from the combustion of fast-growing grass. Results revealed that the first peak for NO_x emission from this combustion gradually increases with an increase in temperature. Moreover, the additives were found to dramatically impact the amount of NO_x emission and its representative peak. The optimal additives and their optimal mass fractions were determined at various specific temperatures to reduce NO_x emission. At combustion temperatures of 600, 700, 750, 800, and 850°C, the optimal conditions to limit NO_x emissions were 5% SiO_2, 3% Al_2O_3, 3% $Ca(OH)_2$, 15% Al_2O_3, and 3% SiO_2 (or 3% Al_2O_3), respectively; the corresponding emission peaks decreased by 43.59, 44.21, 47.99, 24.18, and 30.60% (or 31.51%), with denitration rates of 63.28, 50.34, 57.44, 27.05, and 27.34% (or 27.28%), respectively.

Keywords: fast-growing grass, NOx emissions, denitration rate, emission peak, the optimal mass fraction

OPEN ACCESS

Edited by:
Noroyuki Kobayashi,
Nagoya University, Japan

Reviewed by:
Jiaqiang E,
Hunan University, China
Zhaosheng Yu,
South China University of Technology, China
Chen Chunxiang,
Guangxi University, China

****Correspondence:***
Zhen Huang
huangzhen@ms.giec.ac.cn

Specialty section:
This article was submitted to Advanced Clean Fuel Technologies, a section of the journal Frontiers in Energy Research

Received: *08 September 2021*
Accepted: *25 October 2021*
Published: *11 November 2021*

Citation:
Liu H, Hong Q, Liu H, Huang Z, Zhang X, Chen W, Zeng X and Pan S (2021) Effects of Temperature and Additives on NO_x Emission From Combustion of Fast-Growing Grass. Front. Energy Res. 9:772755. doi: 10.3389/fenrg.2021.772755

INTRODUCTION

Scientific and technological advances along with evolving industrialization, have been continuously improving people's living standards. However, energy consumption for this industrial development has had its own drawbacks, with the extensive use of traditional fossil fuels leading to serious environmental problems, such as air pollution and global warming. Consumption of coal, petroleum, and other traditional energy sources produces lots of SO_2 and NO_x that eventually cause acid rain, thereby corroding houses, bridges and other constructions. Meanwhile, the emitted NO_x increases the content of fine particulate matters (PM2.5) in the atmosphere. The environmental monitoring data in China has revealed that the nitrate content has exceeded the sulfate content in some cities. For instance at the Beijing-Tianjin-Hebei Urban Agglomeration, the absolute concentration and proportion of nitrate exceeded those of sulfate by a large margin during the summers between 2017 and 2018, making it the leading secondary inorganic component in PM2.5 (National Joint Center for air pollution control, 2019). Xu et al. (2019) measured water-soluble inorganic ions (WSI) in PM2.5 in Beijing between February 5 and November 15, 2017. The results showed that nitrate was the major component of WSI in PM2.5 that exacerbated the rapid growth of PM2.5 concentrations in the Fangshan District during heavy pollution. Therefore, more efforts are required to reduce NO_x emission.

Developing clean and efficient renewable energy sources are urgently required. Biomass fuels are considered the best renewable organic alternative to fossil fuels because of their extremely low sulfur content and renewable characteristics (Recalde et al., 2019; Wang et al., 2021). Lvxin fast-growing grass (hereafter referred to as the "fast-growing grass") is a fast-growing plant developed by Prof. Lei Xuejun (Lei, 2015) by hybridizing seven different varieties Lvxin grass. This fast-growing grass requires intensive farming yielding wide leaves with a shape similar to sugarcane and sorghum, a height of up to 4–5 m, diameters up to 50–60 mm, and a normal yield of 5–8 tons of dried grass per mu (1 mu = 0.0667 ha). This fast-growing grass is not only resistant to high temperatures and drought, but also resilient and easy to grow. Most importantly, it can absorb heavy metal ions which makes it suitable to be applied for the remediation of heavy metal-contaminated soil (Lei, 2017). Among its various uses, an important one is as a fuel for biomass power plants. However, characteristics of NO_x emission from the combustion of this fast-growing grass have not been publicly reported.

Extensive research has demonstrated the benefits of oxides, alkali salt, and other additives on NO_x removal from biomass combustion products (RotaZanoelo, 2003; Lee et al., 2005; Sun et al., 2019; Wang et al., 2020; Xiaorui et al., 2021). Many studies have also been conducted on the wet denitration reaction along with additives (Bae et al., 2006; Niu et al., 2010; Gasnot et al., 2011; Wang et al., 2014). Hao (Hao et al., 2015) revealed a significantly positive influence of Na/K additives on the reduction of NO (with the following order: Na_2CO_3 > KCl > NaCl), which also expanded the temperature range of the elective non-catalytic reduction (SNCR) process. Cai et al. (2021) showed that adding hydrogen peroxide, sodium carbonate, ethanol, and other additives to urea-based SNCR increases the OH groups, thereby enhancing the NO*x* removal efficiency and widening the SNCR "temperature window". Chen et al. (2016) showed that adding urea to hydrazine hydrate solution promotes hydrazine decomposition and produces NO-reducing H free radical, thereby achieving NO_x removal. Qi (QiGe et al., 2020) demonstrated NO_x removal by gradually oxidizing NO to HNO_3 in an atmosphere of H_2O_2, OH, and HO_2 using an additive-aided H_2O_2 solution and denitration process. Incorporating additives during the combustion process is simple, convenient, cost-efficient, and spatially efficient. Chen et al. (2017) showed that adding 5% additives to microalgae during a mixed combustion efficiently removes NO_x; the additives reduced the amount of NO_x emission in the following order: $CuCl_2$ > SiC > $ZnCl_2$ > MgO. Ren et al. (2010) has shown a reduction in straw-N conversion into NH_3 and inhibition of N-conversion into HCN and HNCO by adding an iron additive, thereby reducing NO_x emission. During biomass combustion, the reduction in NO_x emissions can be influenced by the type and amount of additives at different temperatures. Therefore, it is important to identify the best additives and their optimal amounts at different temperatures.

This study reports the NO_x emission characteristics of fast-growing grass at different temperatures (600, 700, 750, 800, and 850°C), using varying mass fractions (3, 5, 10, and 15%) of different additives (Al_2O_3, CaO, $Ca(OH)_2$, and SiO_2). These results are expected to function as a reference to ensure the control of NO_x emission during the combustion of the fast-growing grass.

MATERIALS AND METHODS

Materials

The experimental samples were obtained from the fast-growing grass planting base in Yangshi Town, Loudi, Hunan. The industrial and elemental analyses of the grass are shown in **Table 1**. Analytical- and reagent-grade Al_2O_3, CaO, $Ca(OH)_2$, and SiO_2 with the purities of over 99, 98, 95, and 99%, respectively; all these are typical industrial additives that are applied to solid fuels. In this experiment, the following samples were tested: 1) samples of pure fast-growing grass; 2) mixture of fast-growing grass samples and additives at concentrations of 3, 5, 10, and 15%. All samples were pre-treated by drying in an electrothermal drying oven at 106°C for 12 h, followed by grinding and then sieving the particles through an 80-mesh sieve to obtain particles smaller than 200 μm in diameter. Finally, the samples were labelled and stored in dry containers for subsequent use.

Experimental Apparatus and Methods

The experimental system is illustrated in **Figure 1**. The combustion test was performed in a quartz tube reactor of a tube furnace with an inner diameter of 43 mm and a length of 600 mm (OTF-1200X, Hefei Kejing Material Technology Co., Ltd.). The temperature in the furnace was adjustable between room temperature and 1,200°C. NO_x emission was measured using a gas analyzer (Testo 350, Testo in Germany) connected to a computer that monitors and saves the experimental data in real time.

The experiment was performed using the following steps: 1) enter the target temperature into the temperature-control tube furnace and start heating; 2) open the gas cylinder valve and adjust N_2 and O_2 flowmeters such that their flows are 0.8 and 0.2 L/min, respectively; 3) after reaching the target temperature, weigh 0.2 g of each sample and spread it out in a porcelain boat; then, push the boat to the center of the tube furnace quickly; 4) place the probe of the gas analyzer at the gas outlet and observe the collected data on the computer. The combustion reaction was considered complete when the volume concentration of NO_x decreases to 2 ppm. Each set of experiments was repeated 3 times and average values were calculated.

Calculation Method

In this experiment, combustion is considered to be complete when the NO_x emission concentration falls to 2 ppm; the elapsed time is the burnout time *t*. Calculation formula references (Liu et al., 2018; Xu et al., 2021).

① The average concentration (*AC*) is calculated as follows:

$$AC = \frac{\int_0^t C dt}{t} \tag{1}$$

Where, the numerator on the right-hand side refers to the integral of the gas concentration for the reaction time, *t* represents the burnout time, and the *AC* is measured in ppm.

TABLE 1 | Proximate and ultimate analyses and calorific values of fast-growing grass samples (% dry weight).

Fast-growing grass	Ultimate analysis					Proximate analysis			Calorific value (MJ/kg)
Aanalysis item	N	C	H	S	O	Ash content (A_d)	Volatile matter (V_d)	Fixed carbon (FC_d)	High calorific value ($Q_{gr,d}$)
Numerical value	0.730	40.102	5.241	0.260	46.107	7.56	78.88	13.56	18.20

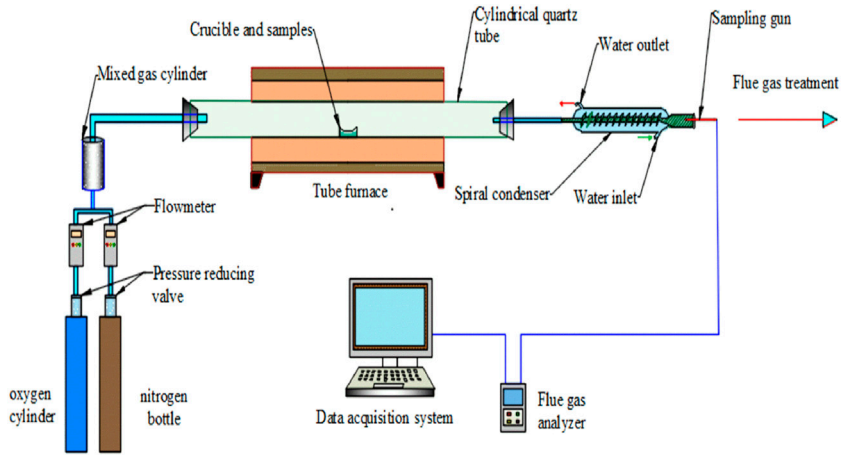

FIGURE 1 | Experimental system.

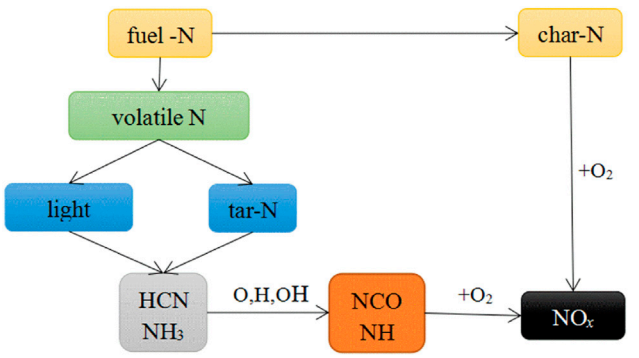

FIGURE 2 | The pathways for conversion of fuel-N into NO_x.

② Calculation of NO_x volume (V)

Considering that the V is negligible compared to the input air volume, the V is approximately calculated as follows:

$$V = Q \times t \times \frac{AC}{10^6} \tag{2}$$

Where, the V is measured in L; Q represents the input air flow in L/s.

③ The mass (M) of produced NO_x is calculated as follows:

$$M = \frac{V \times 273.15}{T \times 22.4} \times M_g \tag{3}$$

Where, the unit of M is g; T(K) represents the temperature of the gas; M_g (g/mol) represents the molar mass of NO_x.

④ The denitration rate (η) is calculated as follows:

$$\eta = \frac{M_0 - M_1}{M_0} \times 100\% \tag{4}$$

Where, M_0 represents the mass of NO_x produced by combustion of samples without additives; M_1 is the mass of NO_x produced by combustion of samples with additives.

RESULTS AND DISCUSSION

The Effect of Temperature on NO_x Emission From Combustion of Fast-Growing Grass

The reaction pathway for NO_x generation by the oxidation of fuel-N (Vermeulen et al., 2012; Shah et al., 2019) shown in **Figure 2** displays that the following two main sources of NO_x in the flue gas: the conversion of volatile-N into volatile-NO_x; and the conversion of char-N into char-NO_x. The conversion of fuel-N mainly occurs at temperatures below 900°C; therefore, the NO_x emission levels were measured and analyzed in the flue gases from combustion of fast-growing grass at different temperatures below 900°C.

As shown in **Figure 3**, NO_x generated from volatile combustion appeared late (at 60s) in the NO_x emission curve at 600°C; the NO_x concentration (peak intensity) was rather low at 19.50 ppm and the combustion reaction lasted for 179 s. At a relatively low temperature of 600°C, not only is the volatilization slow, but the chemical reaction that generates volatile-NO_x from oxidation of volatile-N through intermediate products HCN and NH_3 is also extremely slow; therefore, NO_x concentration is

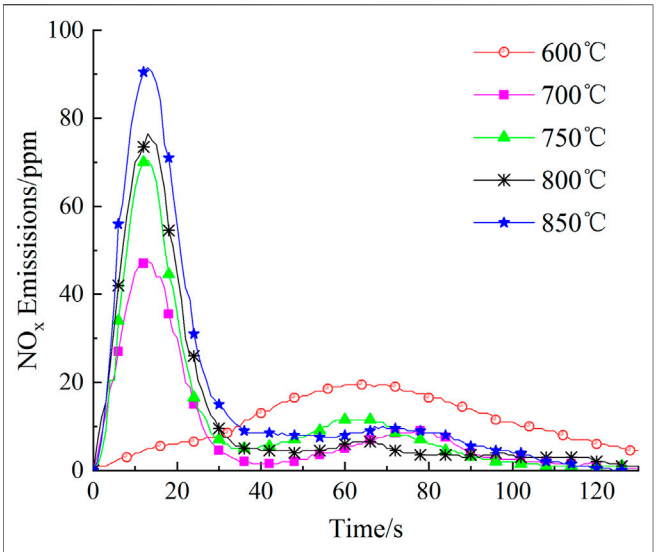

FIGURE 3 | NO_x release curves for fast-growing grass combustion at different temperatures.

relatively low and the time of NO_x emission is rather long (Li et al., 2018; Shah et al., 2018). This is similar to that of microalgae combustion at 600°C (Chen et al., 2017). Unlike at 600°C, two peaks were observed in the NO_x emission curves at 700, 750, 800, and 850°C, corresponding to the volatile and char combustion stages. At temperatures of 700, 750, 800, and 850°C, the first peak was observed much sooner at around 13 s; the peak intensities increased gradually as the temperature increased, reaching 47.50, 70.50, 76.50, and 91.50, respectively. This is similar to results observed for microalgae combustion (Sun et al., 2019; ZhaoSu, 2019), solid biomass combustion (LiChyang, 2020) and the mixed combustion of sewage sludge and rice husk (Xu et al., 2021b). The second peaks were observed in the NO_x emission curves at 77, 58, 62, and 67 s with intensities of 9.00, 11.50, 6.50, and 10.00 ppm, for 700, 750, 800, and 850°C, respectively; the intensities of these peaks were much lower than those of the first peaks. Similar observations have also been reported in previous studies (Lane et al., 2013; Sun et al., 2019). These phenomena were attributed to the generation of char-NO_x from combustion of char-N of the fast-growing grass. The mechanism is shown in **Eq. 5** (Thomas et al., 1993; Molina et al., 2000; LI et al., 2007).

$$\text{char} - \text{N} + \frac{1}{2}\text{O}_2 \rightarrow \text{NO} \tag{5}$$

The Effects of a Additives on the NO_x Ggeneration From Combustion of the Fast-Growing Grass

Currently, NO_x removal is mainly achieved by adding additives to urea or ammonia solutions to introduce SNCR. However, these methods are damaging to the equipment and have high operating costs (Pudasainee et al., 2012); therefore, they are not applicable to small combustion equipment. Consequently, this study focused on mixed combustion of fast-growing grass along with additives to reduce NO_x emission at different combustion temperatures using varying mass fractions of four different additives.

Effects of Additives on Volatile-NO_x Generation

As shown in **Table 2**, the additives have an inhibitory effect on the generation of volatile-NO_x. At 600°C, the first peak of NO_x emission from combustion of fast-growing grass was significantly reduced after the introduction of additives. The peaks were reduced to average values of 34.40, 25.64, 16.01, 21.80% upon addition of SiO_2, Al_2O_3, CaO, and $Ca(OH)_2$, respectively. There are different reasons for the peak reduction for different additives. SiO_2 inhibits N-conversion to NO_x precursors (HCN, HNCO, and NH_3) during combustion (Ren et al., 2010); similarly, Al_2O_3 inhibits NO_x precursors generation

TABLE 2 | The first NO_x emission peaks from the combustion of fast-growing grass using different mass fractions of additives at 600°C.

Temperature (°C)	Type of additive	Mass fraction	The first peak/ppm
600	Al_2O_3	Pure sample	19.50
		3%	13.50
		5%	14.50
		10%	15.00
		15%	15.00
	CaO	3%	16.50
		5%	15.67
		10%	16.67
		15%	16.67
	$Ca(OH)_2$	3%	17.00
		5%	12.50
		10%	15.00
		15%	16.50
	SiO_2	3%	13.00
		5%	11.00
		10%	11.67
		15%	15.50

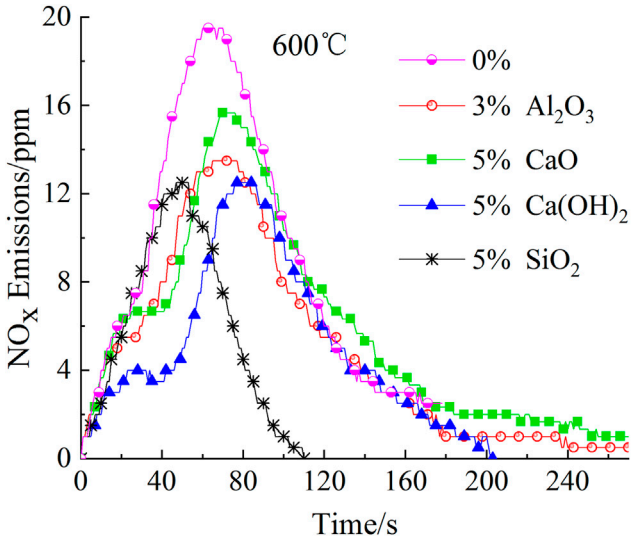

FIGURE 4 | Emission curves for additives at their respective optimal mass fractions at 600°C.

(Ren et al., 2010) and is often used as the carrier of the denitration catalyst (Ma. et al., 2015; Li et al., 2013; Yao et al., 2017; QiShan et al., 2020). On one hand, CaO can catalyze HCN to N_2, as shown in **Eq. 6** (Tan et al., 2009); on the other hand, it can also react with HCN and NH_3 to form N_2 during the pyrolysis stage, as shown in **Eqs. 7–9** (Fu et al., 2014; Liu et al., 2015; Zhang et al., 2017). Similarly, $Ca(OH)_2$ decomposes into CaO and H_2O at high temperatures exhibiting a peak-reducing effect, as shown in **Eq. 10** (Liu et al., 2015).

$$2C_iH_j + 2HCN \rightarrow N_2 + (j + 1 - k)H_2 + 2C_{i+1}H_k \quad (6)$$

$$CaO + 2HCN \rightarrow CaCN_2 + CO + H_2 \quad (7)$$

$$CaC_xN_y \rightarrow CaC_x + \frac{y}{2}N_2 \quad (8)$$

$$CaC_x + yNH_3 \rightarrow CaC_xN_y + \frac{3}{2}yH_2 \quad (9)$$

$$Ca(OH)_2 \rightarrow CaO + H_2O \quad (10)$$

Surprisingly, just adding more additives did not have a better effect on reducing the peak. Optimal mass fractions were determined for the additives. For example, SiO_2, $Ca(OH)_2$, and CaO exhibited the best NO_x removal at a mass fraction of 5% with peak-reducing rates of 43.59, 35.90, and 19.64%, respectively. However, Al_2O_3 obtained the best reduction effect at a mass fraction of 3%, decreasing the peak intensity by 30.77%. These phenomena result from the agglomeration or blanketing of active components on the additive surface when the amount of additives reaches a

TABLE 3 | The first peak for NO_x emission from fast-growing grass combustion using different mass fractions of additives at different temperatures.

Temperature (°C)	Type of additive	Mass fraction	The first peak/ppm	Temperature (°C)	Type of additive	Mass fraction	The first peak/ppm
700	Al_2O_3	Pure sample	47.50	750	Al_2O_3	Pure sample	70.50
		3%	26.50			3%	50.50
		5%	27.50			5%	51.50
		10%	34.00			10%	55.50
		15%	32.00			15%	57.50
	CaO	3%	47.00		CaO	3%	43.50
		5%	41.00			5%	37.00
		10%	47.00			10%	44.00
		15%	43.50			15%	42.00
	$Ca(OH)_2$	3%	27.00		$Ca(OH)_2$	3%	36.67
		5%	29.00			5%	39.00
		10%	33.00			10%	43.00
		15%	28.67			15%	39.33
	SiO_2	3%	34.67		SiO_2	3%	45.00
		5%	31.50			5%	45.50
		10%	39.67			10%	48.67
		15%	38.50			15%	49.00
800	Al_2O_3	Pure sample	76.50	850	Al_2O_3	Pure sample	91.50
		3%	62.00			3%	63.50
		5%	57.50			5%	64.50
		10%	62.67			10%	73.00
		15%	58.00			15%	75.50
	CaO	3%	65.50		CaO	3%	63.00
		5%	63.00			5%	68.50
		10%	66.00			10%	75.33
		15%	63.00			15%	75.50
	$Ca(OH)_2$	3%	64.33		$Ca(OH)_2$	3%	68.00
		5%	55.00			5%	74.50
		10%	57.33			10%	75.00
		15%	56.67			15%	72.00
	SiO_2	3%	62.00		SiO_2	3%	62.67
		5%	58.50			5%	65.50
		10%	64.50			10%	77.50
		15%	64.00			15%	76.00

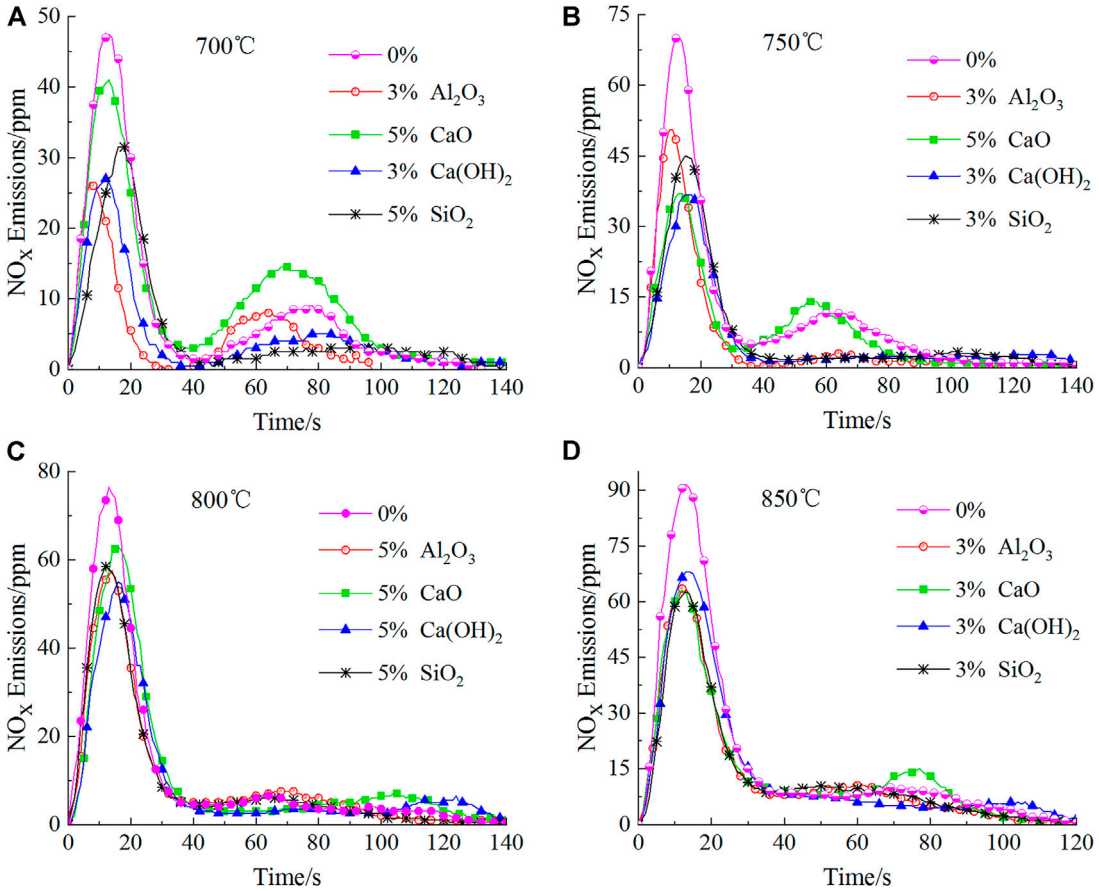

FIGURE 5 | Emission curves for the four additives at their optimal mass fractions at different temperatures.

certain value, which in -turn reduces of the number of active sites. Similar observations have also been reported by previous studies (Yu et al., 2017a; Sun et al., 2019). In order to further study the effects of additives on NO_x emission from the combustion of fast-growing grass at 600°C, the emission curves of the four additives at their optimal mass fractions (see **Figure 4**) were determined.

As shown in **Figure 4**, the additives affected not only the first peak of NO_x emission, but also its appearance time. The peak appeared 13 s sooner upon adding 5% SiO_2, whereas the peak appeared 16, 5, and 9 s later upon adding 5% $Ca(OH)_2$, 3% Al_2O_3, and 3% Al_2O_3, respectively. Similar phenomena have also been reported by Sun's research group (Sun et al., 2019).

As the temperature changes, the effect of additives on lowering the first peak of NO_x emission varied, as shown in **Table 3**. Overall, at 700, 750, and 800°C, $Ca(OH)_2$ casued the most decrease in the first peak, whereas Al_2O_3 exhibited the same effect at 850°C. This is because of the relationship between the catalytic activity of the additives and the temperature (Sun et al., 2019), which caused the efficiency of NH_3 conversion to N_2 to differ at different temperatures.

Similar to the situation at 600°C, additives exhibited different rules to efficiently reduce the first peak at the same temperature, with varying mass fractions. For instance, at 700°C, Al_2O_3 and $Ca(OH)_2$ worked best at 3%, reducing the peak by 44.21 and 43.16%, respectively. At 800°C, however, Al_2O_3 and $Ca(OH)_2$ exhibited the best results at 5%, with the peak intensities dropping by 24.84 and 28.11%, respectively.

The Effects of Additives on the Generation of Char-NO_x

As shown in **Figure 5**, unlike the situation for 600°C, additives had little effect on the appearance time for the first peaks; the time for the peaks to appear was around 15 s after the addition of the four additives. However, the effect of different additives on the second peak varies, indicating that the additives have different effects on the production of char-NO_x. Al_2O_3 and SiO_2 reduced the second peak down to a certain extent, whose effect is unapparent in the high temperature zone (800°C and 850°C); however, it is quite obvious in the low temperature zone (700°C and 750°C). Unlike the two aforementioned additives, CaO increased the second peak to a certain extent, which is the most obvious at 700°C, and raised the second peak by 61.11% compared to that without additives. This may be because CaO can facilitate the conversion of char-N to char-NO_x (Liu et al., 2018b)

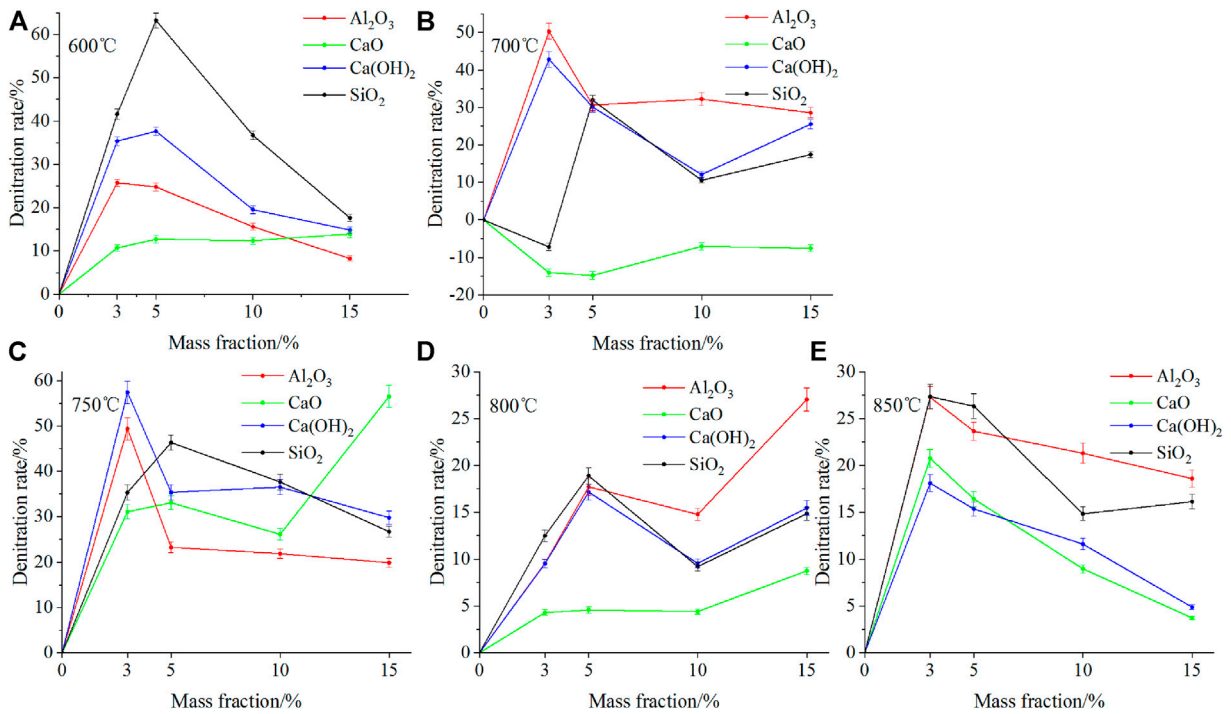

FIGURE 6 | Comparison of denitration rates for different mass fractions of four additives at different temperatures.

and function most efficiently at 700°C (HayhurstLawrence, 1996). These phenomena will be further investigated in subsequent studies. Interestingly, the situation of $Ca(OH)_2$ is opposite to that of CaO. It all depends on whether the H_2O generated after decomposition of $Ca(OH)_2$ reacts with the HCN and char-C to produce CO, the reaction mechanism for which is shown in **Eq. 11** (Liu et al., 2017; SchäferBonn, 2002) and **Eq. 12** (Heikkilä et al., 2021; HermannHüttinger, 1986; MoulijnKapteijn, 1995); it also matters whether CO can convert NO to N_2, whose reaction mechanism is shown in **Eq. 13**, **14** (Chan et al., 1983; Thomas et al., 1993; AarnaSuuberg, 1997; Dong et al., 2007; Gong et al., 2021).

$$HCN + H_2O \rightarrow NH_3 + CO \quad (11)$$

$$char - C + H_2O \rightarrow CO + H_2 \quad (12)$$

$$CO + C(O) \rightarrow CO_2 + C_f \quad (13)$$

$$C_f + NO \rightarrow C(O) + \frac{1}{2}N_2 \quad (14)$$

The Effect of Additives on the Denitration Rate for Combustion of the Fast-Growing Grass

Figure 6 presents the denitration rate for the combustion of fast-growing grass with four mass fractions of four different additives at different temperatures. As shown in **Figure 6**, at different temperatures, four additives exhibited different NO_x removal effects. At 600 and 750°C, SiO_2 and CaO displayed the best denitration effects with average denitration rates of 39.80 and 42.69%, respectively. At 700, 800, and 850°C, Al_2O_3 demonstrated the best denitration effect with average denitration rates of 34.56, 17.27, and 22.71%, respectively, The denitrification effect is better than $CaCO_3$ (Qi et al., 2017)and calcium and Ca-Fe oxides additives (Yu et al., 2017b; Qi et al., 2017). The addition of CaO at 700°C showed no denitrification effect and the average yield of NO_x increased by 10.86%, this is because it promotes the production of char-NO_x.

As shown in **Figure 6**, at the same temperature, the same additive displayed different NO_x removal effects (η) for different mass fractions. At 600 °C, $Ca(OH)_2$ worked best (η = 63.28%) at a mass fraction of 5%; at 700°C, Al_2O_3 showed the best effect (η = 50.34%) at 3%, whereas CaO failed to make any difference but rather increased NO_x emission; at 750°C, $Ca(OH)_2$ worked (η = 57.44%) the best at a mass fraction of 3%; at 800°C, Al_2O_3 worked best (η = 27.05%) at a mass fraction of 15%; at 850°C, Al_2O_3 worked best (η = 27.28%) at a mass fraction of 3%.

According to the peak-reducing effect and NO_x removal effect of the additives on NO_x emission from the combustion of fast-growing grass, the optimal control conditions at different temperatures are as follows: 1) at 600°C, 5% SiO_2 is the best, with the highest peak-reducing rate and NO_x removal efficiency; 2) at 700 and 750°C, 3% Al_2O_3 and 3% $Ca(OH)_2$ are the best, respectively; 3) at 800°C, 5% $Ca(OH)_2$ has the best peak-reducing effect; however, it has a much lower (9.89% lower) NO_x removal efficiency than that of 15% Al_2O_3; 15% Al_2O_3 has the highest NO_x removal efficiency with a slightly lower (3.92% lower) peak-reducing effect than that of 5% $Ca(OH)_2$; therefore, at 800°C, 15% Al_2O_3 is the best; 4) at 850°C, 3% SiO_2 and

3% Al_2O_3 are better and acceptable, with a gap of only 0.91% in the peak-reducing effect and only 0.06% in the NO_x removal efficiency.

CONCLUSIONS

The temperature one of the most critical influences on NO_x emission from the fast-growing grass combustion. As the combustion temperature rises, the average concentration of NO_x emission from the combustion of fast-growing grass increases. which agrees with the law of NO_x emission in biomass combustion. Moreover, at 700, 750, 800, and 850°C, the second peaks were found to be much lower than the first peaks of NO_x emission.

The type and mass fraction of additives also have an important impact on the NO_x emission. Additives can inhibit the formation of volatile-NO_x and also influence the production of char-NO_x to varying degrees. In particular, different from the other three additives, CaO can promote the production of char-NO_x. At the same temperature, different additives have their respective optimal mass fractions to reduce NO_x emission.

In addition, the type and mass fraction of additives affect the denitration rate of combustion of the fast-growing grass. The best additive and its optimal mass fraction vary at different temperatures. Considering both the peaks of NO_x emission and NO_x removal efficiencies at experimental temperatures, the optimal controlling conditions for NO_x emission were obtained. The research results can serve as data reference for NO_x emission control during the combustion of the fast-growing grass.

DATA AVAILABILITY STATEMENT

The original contributions presented in the study are included in the article/**Supplementary Material**, further inquiries can be directed to the corresponding author.

AUTHOR CONTRIBUTIONS

HL: paper writing. QH: experiments. HL: supervisor. ZH: evaluation of results. XZ: experiments. WC: technical support. XZ: evaluation of results. SP: technical support. All authors: contributed to the article and approved the submitted version.

FUNDING

This work was supported by the Hunan Provincial Natural Science Foundation of China (2021JJ50132) and the Hunan Province Graduate Scientific Research and Innovation Project of China (CX20201189)

SUPPLEMENTARY MATERIAL

The Supplementary Material for this article can be found online at: https://www.frontiersin.org/articles/10.3389/fenrg.2021.772755/full#supplementary-material.

REFERENCES

Aarna, I., and Suuberg, E. M. (1997). A Review of the Kinetics of the Nitric Oxide-Carbon Reaction. *Fuel.* 76 (6), 475–491. doi:10.1016/S0016-2361(96)00212-8

Bae, S. W., Roh, S. A., and Kim, S. D. (2006). NO Removal by Reducing Agents and Additives in the Selective Non-Catalytic Reduction (SNCR) Process. *Chemosphere.* 65 (1), 170–175. doi:10.1016/j.chemosphere.2006.02.040

Cai, J., Zheng, W., and Wang, Q. (2021). Effects of Hydrogen Peroxide, Sodium Carbonate, and Ethanol Additives on the Urea-Based SNCR Process. *Sci. Total Environ.* 772, 145551. doi:10.1016/j.scitotenv.2021.145551

Chan, L. K., Sarofim, A. F., and Beér, J. M. (1983). Kinetics of the NO carbon Reaction at Fluidized Bed Combustor Conditions. *Combustion and Flame* 52, 37–45. doi:10.1016/0010-2180(83)90119-0

Chen, C., Chen, F., Cheng, Z., Chan, Q. N., Kook, S., and Yeoh, G. H. (2017). Emissions Characteristics of NO_X and SO_2 in the Combustion of Microalgae Biomass Using a Tube Furnace. *J. Energ. Inst.* 90 (5), 806–812. doi:10.1016/j.joei.2016.06.003

Chen, H., Chen, D. Z., Fan, S., Hong, L., and Wang, D. (2016). SNCR De-NO X Within a Moderate Temperature Range Using Urea-Spiked Hydrazine Hydrate as Reductant. *Chemosphere.* 161, 208–218. doi:10.1016/j.chemosphere.2016.07.010

Dong, L., Gao, S., Song, W., and Xu, G. (2007). Experimental Study of NO Reduction Over Biomass Char. *Fuel Process. Technol.* 88 (7), 707–715. doi:10.1016/j.fuproc.2007.02.005

Fu, S.-l., Song, Q., Tang, J.-s., and Yao, Q. (2014). Effect of CaO on the Selective Non-Catalytic Reduction DeNO Process: Experimental and Kinetic Study. *Chem. Eng. J.* 249, 252–259. doi:10.1016/j.cej.2014.03.102

Gasnot, L., Dao, D. Q., and Pauwels, J. F. (2012). Experimental and Kinetic Study of the Effect of Additives on the Ammonia Based SNCR Process in Low Temperature Conditions. *Energy Fuels.* 26 (5), 2837–2849. doi:10.1021/ef300310c

Gong, Q.-C., He, L.-Q., Zhang, L.-H., and Duan, F. (2021). Comparison of the NO Heterogeneous Reduction Characteristics Using Biochars Derived from Three Biomass With Different Lignin Types. *J. Environ. Chem. Eng.* 9 (1), 105020. doi:10.1016/j.jece.2020.105020

Hao, J., Yu, W., Lu, P., Zhang, Y., and Zhu, X. (2015). The Effects of Na/K Additives and Flyash on NO Reduction in a SNCR Process. *Chemosphere.* 122, 213–218. doi:10.1016/j.chemosphere.2014.11.055

Hayhurst, A. N., and Lawrence, A. D. (1996). The Effect of Solid CaO on the Production of NO_x and N_2O in Fluidized Bed Combustors: Studies Using Pyridine as a Prototypical Nitrogenous Fuel. *Combustion and Flame.* 105 (4), 511–527. doi:10.1016/0010-2180(95)00219-7

Heikkilä, A. M., Koskela, A. M., Iljana, M. O., Lin, R., Bartusch, H., Heikkinen, E.-P., et al. (2021). Coke Gasification in Blast Furnace Shaft Conditions With H_2 and H_2O Containing Atmospheres. *Steel Research Int.* 92 (3), 2000456. doi:10.1002/srin.202000456

Hermann, G., and Hüttinger, K. J. (1986). Mechanisms of Non-Catalysed and Iron-Catalysed Water Vapour Gasification of Carbon. *Fuel.* 65 (10), 1410–1418. doi:10.1016/0016-2361(86)90115-8

Lane, D. J., Ashman, P. J., Zevenhoven, M., Hupa, M., van Eyk, P. J., de Nys, R., et al. (2013). Combustion Behavior of Algal Biomass: Carbon Release, Nitrogen Release, and Char Reactivity. *Energy Fuels.* 28 (1), 41–51. doi:10.1021/ef4014983

Lee, S., Park, K., Park, J., and Kim, B. (2005). Characteristics of Reducing NO Using Urea and Alkaline Additives. *Combustion and flame.* 141 (3), 200–203. doi:10.1016/j.combustflame.2005.01.004

Lei, X. (2015). Carbon Sink Grass and its Carbon Sink Mechanism. *Agric. Eng. (Chinese)* 5 (5), 38–43. doi:10.3969/j.issn.2095-1795.2015.05.014

Lei, X. (2017). Comprehensively Carry Out General Secretary Xi Jinping's Important Strategic Thought on Ecological Civilization Construction. *Energy China (Chinese)* 39 (7), 4–11. doi:10.3969/j.issn.1003-2355.2017.07.001

Li, P.-W., and Chyang, C.-S. (2020). A Comprehensive Study on NOx Emission and Fuel Nitrogen Conversion of Solid Biomass in Bubbling Fluidized Beds Under Staged Combustion. *J. Energ. Inst.* 93 (1), 324–334. doi:10.1016/j.joei.2019.02.007

Li, P.-W., Chyang, C.-S., and Ni, H.-W. (2018). An Experimental Study of the Effect of Nitrogen Origin on the Formation and Reduction of NOx in Fluidized-Bed Combustion. *Energy.* 154, 319–327. doi:10.1016/j.energy.2018.04.141

Li, P., Li, J., Hu, Y., Wan, Y., Yue, Y., Jing, Z., Hu, N., Yang, J., and Yang, G. (2007). "*Research On NO_X Emission Characteaistics And Mechanism during Sewage Sludge/Coal Mixtures Combustion*," in Proceeding of the International symposium on coal combustion, Wuhan(CN).

Li, R. H., Zhou, S., Li, C. L., Wang, Z. Y., and Zhu, Y. Q. (2013). A Study on SCR Catalyst Support. *Adv. Mater. Res.* 726-731, 17–20. doi:10.4028/www.scientific.net/AMR.726-731.17

Liu, H., Yi, L., Hu, H., Xu, K., Zhang, Q., Lu, G., et al. (2017). Emission Control of NO_X Precursors During Sewage Sludge Pyrolysis Using an Integrated Pretreatment of Fenton Peroxidation and CaO Conditioning. *Fuel.* 195, 208–216. doi:10.1016/j.fuel.2017.01.067

Liu, H., Zhang, Q., Hu, H., Liu, P., Hu, X., Li, A., et al. (2015). Catalytic Role of Conditioner CaO in Nitrogen Transformation During Sewage Sludge Pyrolysis. *Proc. Combustion Inst.* 35 (3), 2759–2766. doi:10.1016/j.proci.2014.06.034

Liu, X., Luo, Z., and Yu, C. (2018a). Effect of limestone on the Emission of NO during Petroleum Coke Combustion. *Fuel.* 224, 1–9. doi:10.1016/j.fuel.2018.03.066

Liu, X., Luo, Z., and Yu, C. (2018b). Effect of limestone on the Emission of NO During Petroleum Coke Combustion. *Fuel.* 224, 1–9. doi:10.1016/j.fuel.2018.03.066

Ma, L., Qi, Y. F., Wang, M. T., and Li, Z. M. (2015). "Investigation of Micro-characteristics on Manganese-Basis Catalysts for Denitration Prepared by Different Carriers," in International conference on computer science and environmental engineering(CSEE 2015), Beijing, China, May-2015, 172–178.

Molina, A., Eddings, E. G., Pershing, D. W., and Sarofim, A. F. (2000). Char Nitrogen Conversion: Implications to Emissions from Coal-Fired Utility Boilers. *Prog. Energ. combustion Sci.* 26 (4), 507–531. doi:10.1016/S0360-1285(00)00010-1

Moulijn, J. A., and Kapteijn, F. (1995). Towards a Unified Theory of Reactions of Carbon with Oxygen-Containing Molecules. *Carbon.* 33 (8), 1155–1165. doi:10.1016/0008-6223(95)00070-T

National Joint Center for air pollution control (2019). Nitrate Has Become the Most Important Secondary Inorganic Component in PM2.5 in Beijing, Tianjin and Hebei 03/15, 2021. Available at: https://huanbao.bjx.com.cn/news/20190313/968481.shtml.

Niu, S., Han, K., and Lu, C. (2010). Experimental Study on the Effect of Urea and Additive Injection for Controlling Nitrogen Oxides Emissions. *Environ. Eng. Sci.* 27 (1), 47–53. doi:10.1089/ees.2008.0181

Pudasainee, D., Kim, J.-H., Yoon, Y.-S., and Seo, Y.-C. (2012). Oxidation, Reemission and Mass Distribution of Mercury in Bituminous Coal-Fired Power Plants With SCR, CS-ESP and Wet FGD. *Fuel.* 93, 312–318. doi:10.1016/j.fuel.2011.10.012

Qi, J., Han, K., Wang, Q., and Gao, J. (2017). Carbonization of Biomass: Effect of Additives on Alkali Metals Residue, SO 2 and NO Emission of Chars during Combustion. *Energy* 130, 560–569. doi:10.1016/j.energy.2017.04.109

Qi, Y., Ge, P., Wang, M., Shan, X., Ma, R., Huang, J., et al. (2020a). Experimental Investigation and Numerical Simulation of Simultaneous Desulfurization and Denitrification by H_2O_2 Solution Assisted With Microwave and Additive. *Chem. Eng. J.* 391, 123559. doi:10.1016/j.cej.2019.123559

Qi, Y., Shan, X., Wang, M., Hu, D., Song, Y., Ge, P., et al. (2020b). Study on Low-Temperature SCR Denitration Mechanisms of Manganese-Based Catalysts With Different Carriers. *Water Air Soil Pollut.* 231 (6), 289. doi:10.1007/s11270-020-04644-5

Recalde, M., Woudstra, T., and Aravind, P. V. (2019). Gasifier, Solid Oxide Fuel Cell Integrated Systems for Energy Production From Wet Biomass. *Front. Energ. Res.* 7, 129. doi:10.3389/fenrg.2019.00129

Ren, Q., Zhao, C., Wu, X., Liang, C., Chen, X., Shen, J., et al. (2010). Catalytic Effects of Fe, Al and Si on the Formation of NOX Precursors and HCl during Straw Pyrolysis. *J. Therm. Anal. Calorim.* 99 (1), 301–306. doi:10.1007/s10973-009-0150-0

Rota, R., and Zanoelo, E. F. (2003). Influence of Oxygenated Additives on the NOxOUT Process Efficiency☆. *Fuel.* 82 (7), 765–770. doi:10.1016/S0016-2361(02)00365-4

Schäfer, S., and Bonn, B. (2002). Hydrolysis of HCN as an Important Step in Nitrogen Oxide Formation in Fluidised Combustion. Part II: Heterogeneous Reactions Involving limestone. *Fuel.* 81 (13), 1641–1646. doi:10.1016/S0016-2361(02)00096-0

Shah, I. A., Gou, X., and Wu, J. (2019). Simulation Study of an Oxy-Biomass-Based Boiler for Nearly Zero Emission Using Aspen Plus. *Energies.* 12 (10), 1949. doi:10.3390/en12101949

Shah, I. A., Gou, X., Zhang, Q., Wu, J., Wang, E., and Liu, Y. (2018). Experimental Study on NOx Emission Characteristics of Oxy-Biomass Combustion. *J. Clean. Prod.* 199, 400–410. doi:10.1016/j.jclepro.2018.07.022

Sun, J., Zhao, B., and Su, Y. (2019). Advanced Control of NO Emission from Algal Biomass Combustion Using Loaded Iron-Based Additives. *Energy.* 185, 229–238. doi:10.1016/j.energy.2019.07.042

Tan, H., Wang, X., Wang, C., and Xu, T. (2009). Characteristics of HCN Removal Using CaO at High Temperatures. *Energy Fuels.* 23 (2), 1545–1550. doi:10.1021/ef800935u

Thomas, K. M., Grant, K., and Tate, K. (1993). Nitrogen-Doped Carbon-13 Materials as Models for the Release of NOx and N_2O during Coal Char Combustion. *Fuel.* 72 (7), 941–947. doi:10.1016/0016-2361(93)90291-9

Vermeulen, I., Block, C., and Vandecasteele, C. (2012). Estimation of Fuel-Nitrogen Oxide Emissions from the Element Composition of the Solid or Waste Fuel. *Fuel.* 94, 75–80. doi:10.1016/j.fuel.2011.11.071

Wang, F., Chen, T., Jin, M., and Lu, P. (2014). Simultaneous Desulfurization and Denitrification from Flue Gas Using Urea/Piperazine Solution. *Adv. Mater. Res.* 881-883 (1764), 641–644. doi:10.4028/www.scientific.net/AMR.881-883.641

Wang, K., Khoo, K. S., Chew, K. W., Selvarajoo, A., Chen, W.-H., Chang, J.-S., et al. (2021). Microalgae: The Future Supply House of Biohydrogen and Biogas. *Front. Energ. Res.* 9, 660399. doi:10.3389/fenrg.2021.660399

Wang, Q., Han, K., Wang, P., Li, S., and Zhang, M. (2020). Influence of Additive on Ash and Combustion Characteristics During Biomass Combustion under O2/CO2 Atmosphere. *Energy.* 195, 116987. doi:10.1016/j.energy.2020.116987

Xiaorui, L., Xudong, Y., Guilin, X., and Yiming, Y. (2021). NO Emission Characteristic During Fluidized Combustion of Biomass With Limestone Addition. *Fuel.* 291, 120264. doi:10.1016/j.fuel.2021.120264

Xu, G., Ou, J., Fang, B., Wei, H., Hu, T., and Wang, H. (2021a). NO Emission From the Combustion of Mixed Fuel Pellets of Fenton/CaO-Conditioned Municipal Sludge and Rice Husk. *Environ. Pollut.* 281, 117018. doi:10.1016/j.envpol.2021.117018

Xu, G., Ou, J., Fang, B., Wei, H., Hu, T., and Wang, H. (2021b). NO Emission From the Combustion of Mixed Fuel Pellets of Fenton/CaO-Conditioned Municipal Sludge and rice Husk. *Environ. Pollut.* 281, 117018. doi:10.1016/j.envpol.2021.117018

Xu, Q., Wang, S., Jiang, J., Bhattarai, N., Li, X., Chang, X., et al. (2019). Nitrate Dominates the Chemical Composition of PM2.5 during Haze Event in Beijing, China. *Sci. Total Environ.* 689, 1293–1303. doi:10.1016/j.scitotenv.2019.06.294

Yao, X., Kong, T., Yu, S., Li, L., Yang, F., and Dong, L. (2017). Influence of Different Supports on the Physicochemical Properties and Denitration Performance of the Supported Mn-Based Catalysts for NH3-SCR at Low Temperature. *Appl. Surf. Sci.* 402, 208–217. doi:10.1016/j.apsusc.2017.01.081

Yu, Z.-y., Fan, X.-h., Gan, M., and Chen, X.-l. (2017a). Effect of Ca-Fe Oxides Additives on NOx Reduction in Iron Ore Sintering. *J. Iron Steel Res. Int.* 24 (12), 1184–1189. doi:10.1016/S1006-706X(18)30016-5

Yu, Z.-y., Fan, X.-h., Gan, M., and Chen, X.-l. (2017b). Effect of Ca-Fe Oxides Additives on NOx Reduction in Iron Ore Sintering. *J. Iron Steel Res. Int.* 24 (12), 1184–1189. doi:10.1016/S1006-706X(18)30016-5

Zhang, Q., Liu, H., Lu, G., Yi, L., Hu, H., Chi, H., et al. (2017). Mechanism of Conditioner CaO on NOx Precursors Evolution During Sludge Steam Gasification. *Proc. Combustion Inst.* 36 (3), 4003–4010. doi:10.1016/j.proci.2016.09.006

Zhao, B., and Su, Y. (2019). Emission and Conversion of NO From Algal Biomass Combustion in O2/CO2 Atmosphere. *J. Environ. Manage.* 250, 109419. doi:10.1016/j.jenvman.2019.109419

Conflict of Interest: The authors declare that the research was conducted in the absence of any commercial or financial relationships that could be construed as a potential conflict of interest.

Publisher's Note: All claims expressed in this article are solely those of the authors and do not necessarily represent those of their affiliated organizations, or those of the publisher, the editors and the reviewers. Any product that may be evaluated in this article, or claim that may be made by its manufacturer, is not guaranteed or endorsed by the publisher.

frontiers in Energy Research

ORIGINAL RESEARCH
published: 28 January 2022
doi: 10.3389/fenrg.2022.828836

Exploring NH_3 and NO_x Interaction Chemistry With CH_4 and C_2H_4 at Moderate Temperatures and Various Pressures

Yuwen Deng[1], Zijian Sun[1], Wenhao Yuan[1], Jiuzhong Yang[2], Zhongyue Zhou[1] and Fei Qi[1]*

[1]School of Mechanical Engineering, Shanghai Jiao Tong University, Shanghai, China, [2]National Synchrotron Radiation Laboratory, University of Science and Technology of China, Hefei, China

The oxidation of $CH_4/C_2H_4/NH_3/NO/NO_2$ gas mixtures was studied aiming to explore the homogenous chemistry of exhaust gas from lean-operated natural gas engine. With respect to this goal, experiments were carried out with a laminar flow reactor under engine-relevant (diluted and lean) conditions over the temperature range of 600–1400 K. Four gas mixtures were designed to evaluate the effects of NO/NO_2 ratio (1, 4) and pressure (0.04 and 1.0 atm) on the interaction chemistry of NH_3/NO_x with CH_4 and C_2H_4. By using synchrotron vacuum ultraviolet photoionization mass spectrometry, fingerprint products for revealing interaction chemistry were identified and quantified, e.g., nitrogenous and oxygenated intermediates. The experimental results show that the NO concentrations are significantly affected by adding CH_4/C_2H_4, changing NO/NO_2 ratio and pressure. Besides, the promotion of $DeNO_x$ reactions and narrower temperature windows of NO reduction are unexpectedly observed in the presence of CH_4/C_2H_4. To interpret the experimental observations, a detailed kinetic model was developed by integrating hydrocarbons/NH_3/NO_x interaction chemistry. Rate of production and sensitivity analyses indicate that the active radical pool is enriched and additional chain-branching pathways regarding NO/NO_2 interconversion are activated with the addition of hydrocarbons. In the presence of both CH_4 and C_2H_4, reaction $C_2H_3 + O_2 = CH_2CHO + O$ was demonstrated as a crucial reaction that drives the reactivity of $CH_4/C_2H_4/NH_3/NO/NO_2$ mixture. This is explained by the production of CH_2CHO, whose dissociation generates CH_2O and ultimately leads to the abundant production of active OH *via* the reaction sequence $CH_2O \rightarrow HCO \rightarrow HO_2 \rightarrow OH$. The conversion kinetics of hydrocarbons, NO and NH_3 under different NO/NO_2 ratios and pressure, as well as the formation kinetics of oxygenated and nitrogenous intermediates was also analyzed in this work.

Keywords: nitrogenous oxides, ammonia, hydrocarbons, flow reactor oxidation, kinetic modeling

OPEN ACCESS

Edited by:
Zhihua Wang,
Zhejiang University, China

Reviewed by:
Bin Yang,
Tsinghua University, China
Yingjia Zhang,
Xi'an Jiaotong University, China

****Correspondence:***
Wenhao Yuan
yuanwh@sjtu.edu.cn

Specialty section:
This article was submitted to Advanced Clean Fuel Technologies, a section of the journal Frontiers in Energy Research

Received: *04 December 2021*
Accepted: *11 January 2022*
Published: *28 January 2022*

Citation:
Deng Y, Sun Z, Yuan W, Yang J, Zhou Z and Qi F (2022) Exploring NH_3 and NO_x Interaction Chemistry With CH_4 and C_2H_4 at Moderate Temperatures and Various Pressures. Front. Energy Res. 10:828836. doi: 10.3389/fenrg.2022.828836

1 INTRODUCTION

Modern combustion engine technologies have increasingly focused on the reduction of carbon dioxide emissions owing to the globally tightening legislation (Johnson, 2015; Börnhorst and Deutschmann, 2021), whereas the highly optimized engine structures and emission control measures render it extremely difficult to further make a breakthrough on decreasing raw

emissions. Meanwhile, lean-operated natural gas engines are considered as a promising technology because of their high thermo-efficiency and comparably low pollutant emissions (Lott and Deutschmann, 2021). Alternative concepts like biomethane and power-to-gas technologies will endow gas engines with outstanding potential on the way towards carbon neutrality (Schmitt et al., 2021). Nevertheless, the excessive engine-out emissions of methane, known with potent greenhouse potential and liable to produce carcinogenic formaldehyde by partial oxidation, bring new challenges to natural gas engines (Hutter et al., 2018). Also, the presence of nitrogen oxides (NO_x) in exhaust gas deserves special attention given its particular environmental hazard in engendering photochemical smog and acid rain (Gasnot et al., 2012; Piumetti et al., 2016). Hence, a highly efficient and durable exhaust gas abatement system, commonly containing both catalytic oxidation of unburned hydrocarbons (UHC) and NO_x reduction sections, was considered imperative (Lott and Deutschmann, 2021). The ammonia-based selective catalytic reduction (SCR) technology is currently widely applied for NO_x removal from gas engines benefiting from its higher $DeNO_x$ efficiency and relatively moderate cost. However, it must be pointed out that despite the whole $DeNO_x$ process integrating simultaneously complex gas-phase and surface chemistry (Vassallo et al., 1995; Tamm et al., 2009), the probability of the gas-phase reactions between hydrocarbons, NO_x and NH_3 in SCR was exclusively ignored among most of the studies regarding exhaust gas abatement (Mejía-Centeno et al., 2013; Wang et al., 2019; Lee et al., 2020; Jia et al., 2021; Savva et al., 2021), especially given the recently proposed post-treatment measures allowing the catalytic converters to be positioned closer to the engine thus featuring much higher pressure and temperatures (Lott and Deutschmann, 2021).

To the best of our knowledge, only limited studies have been reported to date in terms of the homogeneous reactivities of NH_3 and NO_x in the presence of multiple other typical exhaust gas constituents, mainly C_1-C_2 hydrocarbons like methane and ethylene, etc. Hemberger et al. (Hemberger et al., 1994) investigated the selective non-catalytic reduction (SNCR) of NO by ammonia with the addition of methane and ethane in a flow reactor over the temperature range 800–1300 K. Gasnot et al. (Gasnot et al., 2012) performed an experimental and kinetic study of the effect of several additives such as CH_4, C_2H_4, C_2H_6, C_2H_2, CH_3OH, C_2H_5OH and CO on ammonia-based SNCR process at temperatures of 900–1200 K. Torkashvand et al. (Torkashvand et al., 2019) investigated hydrocarbon abatement from the exhaust of lean-burn gas engines under ambient pressure and pre-turbine conditions. Most recently, Schmitt et al. (Schmitt et al., 2021) conducted flow reactor experiments in the temperature range of 700–1200 K at atmospheric pressure to reveal influences of individual components by adding NO_2, CH_4, CO, and C_2H_4 sequentially to a highly argon-diluted NO/NH_3 base mixture.

The aim of the present work is to explore the impact of methane and ethylene on the homogeneous conversion chemistry of NO_x and NH_3 under near-real exhaust conditions. With respect to this goal, the oxidation experiments of $CH_4/C_2H_4/NH_3/NO/NO_2$ gas mixtures were firstly carried out in a laminar flow reactor at lean conditions, at temperatures of 600–1400 K and pressures of 0.04–1.0 atm. Different gas mixtures were designed to investigate the impact of NO/NO_2 ratio and pressure on the conversion kinetics of NH_3, NO and hydrocarbons. Mole fraction profiles of reactants, products, hydrocarbon, nitrogenous and oxygenated intermediates were evaluated by using synchrotron vacuum ultraviolet photoionization mass spectrometry (SVUV-PIMS). On the basis of these experiments, a detailed kinetic model was developed to interpret the experimental results and reveal the conversion kinetics of NH_3 and NO_x in the presence of CH_4 and C_2H_4 under different conditions.

2 EXPERIMENTAL METHODS

The experimental work was conducted at the National Synchrotron Radiation Laboratory, China. Details about the experimental setup have been introduced in our previous work (Qi, 2013; Zhou et al., 2016). Four experimental conditions were selected to cover the pressure ranges from 0.04 to 1 atm, the temperature ranges from 600 to 1400 K, and different NO/NO_2 ratios. Detailed experimental conditions are listed in **Table 1**. Furthermore, two gas mixture conditions in the absence and presence of methane (Sun et al., 2021), which were reported previously, are also summarized in **Table 1** and will be discussed in the following sections to clarify the impact of individual gas additives on the conversion chemistry of NH_3/NO_x. The gas mixtures were highly diluted in carrier gas argon with a total flow rate of 250 standard cubic centimeters per minute (sccm) and an average residence time of 0.6–1.4 s. Gas mixtures were fed into a quartz flow reactor with 0.7 cm inner diameter and 40 cm heating length. The identification and quantification of intermediate species were achieved by using SVUV-PIMS. The calculated uncertainties of mole fractions for species with known photoionization cross sections (PICSs) were estimated to be ±25% and a factor of 2 for those with estimated PICSs.

3 KINETIC MODELING

The kinetic model used for the simulation was developed based on AramcoMech 3.0 (Zhou et al., 2018), which contains a well-established C_0-C_2 base mechanism. The sub-mechanism describing NH_3 oxidation as well as interaction kinetics between C_0-C_2 species and NO_x was taken from the work of Glarborg et al. (Glarborg et al., 2018). In addition, rate constants of several key reactions in the sub-mechanism of NH_3, which are mainly related to the production of NH_2 and NO, have been updated from the theoretical studies of Stagni et al. (Stagni et al., 2020). These reactions include the dissociation of HNO and H-abstraction reactions of NH_3 by H, O, OH and HO_2 radicals. The newly proposed reactions pathways of NH radicals by Duynslaegher et al. (Duynslaegher et al., 2012), namely the reactions of NH with O or N_2O to produce N + OH or N_2 + HNO, and the reaction of NH_2 with NO yielding

TABLE 1 | Experimental conditions.

Gas mixture	P/atm	CH_4/ppm	C_2H_4/ppm	NH_3/ppm	NO/ppm	NO_2/ppm	O_2	Ar
GM1	0.04	6,000	6,000	1,000	500	500	0.06	0.926
GM2	1	6,000	6,000	1,000	500	500	0.06	0.926
GM3 (Sun et al., 2021)	1	6,000	0	1,000	500	500	0.06	0.932
GM4 (Sun et al., 2021)	1	0	0	1,000	500	500	0.06	0.938
GM5	0.04	6,000	6,000	1,000	800	200	0.06	0.926
GM6	1	6,000	6,000	1,000	800	200	0.06	0.926

$N_2O + H_2$, etc., were also implemented in the present kinetic model. The rate constant of $NH_2 + O = HNO + H$ calculated by Sumathi et al. (Sumathi et al., 1998) was also adopted to improve the prediction results of NO_x. The detailed updating list of the rate constants involved in the C_1-C_2/NO_x/NH_3 sub-mechanism has been summarized in our recent work on CH_4/NH_3/NO_x (Sun et al., 2021), thus not outlined here.

Meanwhile, the C_1-C_2/NO_x/NH_3 sub-mechanism has also been further improved in the present work to describe the interaction kinetics among hydrocarbon species, NH species and NO_x. The reaction pathways of carbonyl species such as acrolein, acetaldehyde and ketene with NO_x, and the $C_2H_4 + NO_2$ channel laid out by Deng et al. (Deng et al., 2019) were included in the present model. Also, the recombination reactions of CH_3 and NH_2, together with C_2H_3 and NO/NO_2/CN, are implemented from the calculation results of Deng et al. (Deng et al., 2019) or by analogy with similar reactions when available. The reaction pathways describing the interaction chemistry between C_2H_2 and NO_x were taken from the recent studies of Marshall et al. (Marshall et al., 2019). Thermodynamic parameters of newly added species such as $CH_3NH2CH_3NO_2$, $C_2H_3NO_2$ and C_2H_3CN, etc. in the present model were taken from Glarborg et al. (Glarborg et al., 2018) and the theoretical calculations of Deng et al. (Deng et al., 2019). The simulation of flow reactor was carried out by using the Plug Flow Reactor module in Chemkin-Pro software (ReactionDesign, 2009) with the measured centerline temperatures of flow reactor as input parameters.

4 RESULTS AND DISCUSSION

Dozens of species were detected in the oxidation of CH_4/C_2H_4/NH_3/NO/NO_2 gas mixtures and their mole fractions were evaluated as functions of temperatures. Specifically, major nitrogenous intermediates detected and identified in this work include nitromethane (CH_3NO_2), nitroethylene ($C_2H_3NO_2$), methylamine (CH_3NH_2), nitrous acid (HONO) and cyanides (HCNO). Major oxygenated intermediates detected include formaldehyde (CH_2O), methanol (CH_3OH) and acetaldehyde (CH_3CHO). In the following sections, effect of CH_4/C_2H_4 on the NO_x/NH_3 homogeneous conversion chemistry will be discussed first. Subsequently, the impacts of pressure and NO/NO_2 ratio on the kinetics of HCs/NO_x/NH_3 mixture will be analyzed. Finally, the formation kinetics of nitrogenous and oxygenated intermediates will be analyzed to reveal the unique interactive reactions among hydrocarbons, NH_3 and NO_x.

4.1 Effect of CH_4 and C_2H_4 Addition on NO_x/NH_3 Conversion

Figure 1 shows the experimental and predicted mole fraction profiles of reactants (NH_3, NO, NO_2 and O_2) in the oxidation of gas mixtures 1–6 (GM1-6), **Figure 2** shows the experimental and simulated mole fraction profiles of major products (N_2O, N_2, H_2O, CO and CO_2) in the oxidation of GM1-3 and GM5-6. For all the investigated gas mixtures, the model is capable of predicting the temperature-dependent decomposition profiles of reactants except for the discrepancy observed for NO in GM1 and GM4. Regarding the major products, the model is able to reproduce the formation of most products except that the under-estimation of equilibrium concentration of N_2 at 0.04 atm. Rate of production (ROP) analyses have been carried out to reveal the conversion kinetics of NO_x and NH_3 under different conditions. The selected temperatures for the ROP analyses, i.e., 1239 K (GM1), 886 K (GM2), 911 K (GM3), 1060 K (GM4) and 1239 K (GM5), correspond to the temperature at which the conversion rate of ammonia reaches about 50%.

Numerous previous studies (Miller and Bowman, 1989; Glarborg et al., 2018; Okafor et al., 2018; Schmitt et al., 2021) have concluded that reactions R1-R5 are the major reactions in the oxidation of NH_3/NO_x. **Figure 3** summarizes the reaction pathways of NH_3 in the oxidation of GM1-5. The results show that regardless of whether there is the addition of hydrocarbons, over 90% of NH_3 is converted to NH_2 *via* H-abstraction reaction by OH. In the oxidation of NH_3/NO_x (GM4), reactions R2 and R4 contribute to a major part of NH_2 consumption, producing N_2 and nitroxide (H_2NO), respectively. The remaining two reactions R1 and R5 produce NNH and N_2O, respectively. NNH and N_2O are eventually converted to N_2 through single-step collision reactions. H_2NO produced from R4 is eventually converted to NO *via* nitroxyl (HNO) through stepwise dehydrogenation reactions.

$$NH_2 + NO = NNH + OH \quad (R1)$$

$$NH_2 + NO = N_2 + H_2O \quad (R2)$$

$$NO + HO_2 = NO_2 + OH \quad (R3)$$

$$NH_2 + NO_2 = H_2NO + NO \quad (R4)$$

$$NH_2 + NO_2 = N_2O + H_2O \quad (R5)$$

By examining **Figure 3** one can see that the profile of NO with temperature in GM4 has a distinct difference from that in other mixtures, and is also different from the result observed in the work of Schmitt et al. (Schmitt et al., 2021). To clarify the kinetics

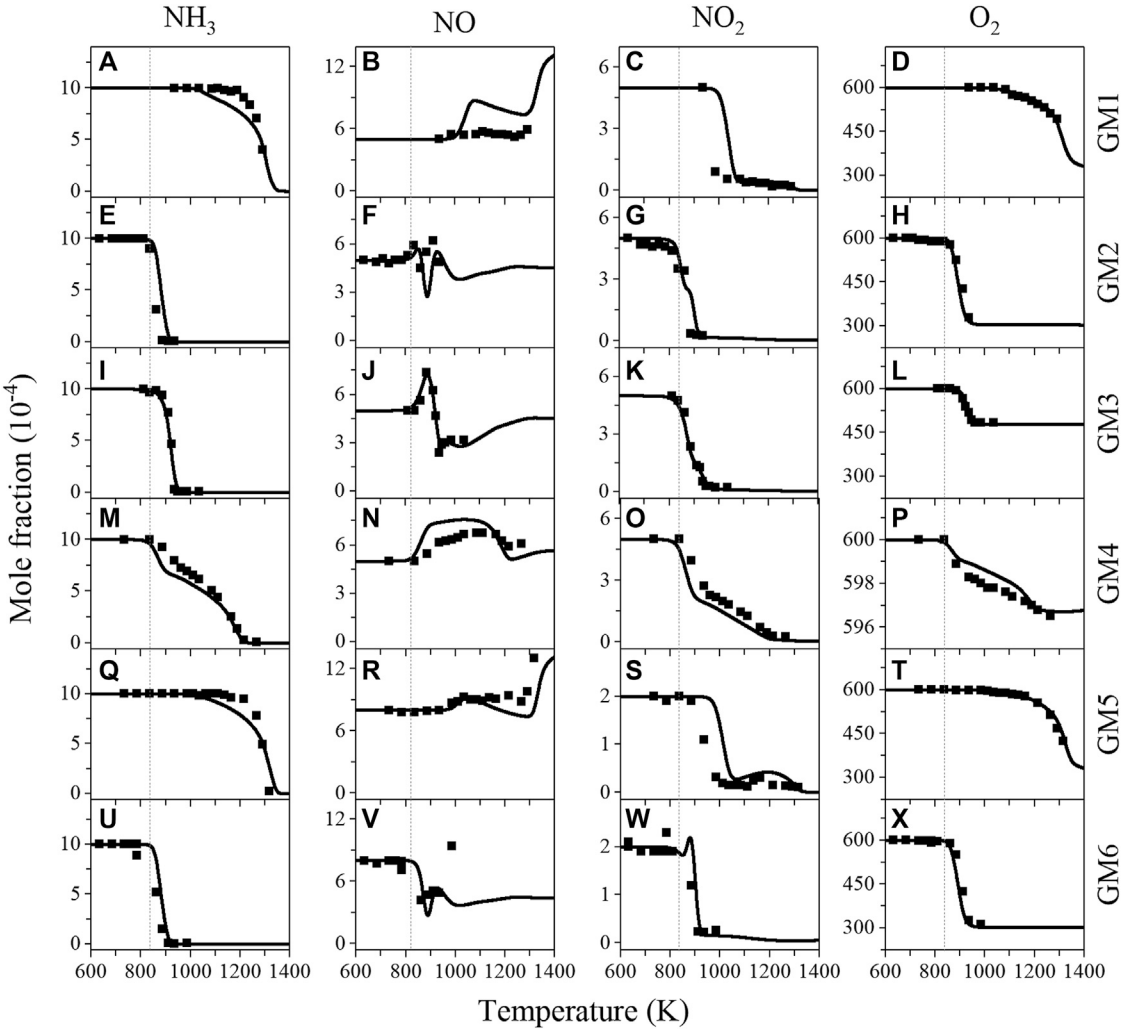

FIGURE 1 | Experimental (symbols) and simulated (lines) mole fraction profiles of ammonia (NH_3), nitric oxide (NO), nitrogen dioxide (NO_2) and oxygen (O_2) from the oxidation of GM1-6. Experimental data of GM3-4 are taken from the work of Sun et al. (Sun et al., 2021).

behind it, ROP analyses were performed at low- to high-temperatures (860, 1,162 and 1316 K). The results indicate that the initial increase of NO at the temperature of 863 K is mainly caused by the decomposition of nitrous acid (HONO), followed by the interconversion reaction R4. HONO is produced through the reaction sequence $NH_2 \rightarrow H_2NO \rightarrow HNO\ (+NO_2) \rightarrow HONO$. Over the temperature range of 900–1100 K, the concentration of NO has only a slight change, generally because the thermal $DeNO_x$ reactions R1 and R2 proceed rather slow over this temperature range. When the temperature increases above 1100 K, NO is quickly consumed *via* the thermal $DeNO_x$ reactions R1 and R2. As the temperature increases up to 1300 K, a second rise of NO concentration with temperature is observed. ROP analysis results show that reaction R6 is the dominant reaction that contributes to the formation of NO at temperatures above 1300 K.

$$NO_2 + H = NO + OH \quad \text{(R6)}$$

In comparison with the oxidation of NH_3/NO_x (GM4), no noticeable change was observed for the initial conversion temperatures of NH_3 and NO_x in the oxidation of $CH_4/NH_3/NO_x$ (GM3). However, in the presence of both CH_4 and C_2H_4 (GM2), the initial conversion temperatures of NH_3 and NO_x are found around 50 K lower than those in the oxidation of NH_3/NO_x, as seen in GM2, 3, 4 in **Figure 1**. By comparing GM2, GM3, GM4 and GM6, it can be also concluded that the addition of hydrocarbons promotes the consumption rate of NH_3, NO_2 and O_2, i.e., for GM2, GM3 and GM6, NH_3, NO_2 and O_2 are quickly consumed over a narrow temperature range, while for GM4, the temperature regime is much wider.

The comparison of experimental and simulated mole fraction profiles of CH_4 and C_2H_4 in GM1-3 and GM5-6 is illustrated in **Figure 4**. As expected, the initial conversion temperatures, as well as reaction temperature regime of CH_4 and C_2H_4 are noticeably affected by the NO/NO_2 ratio and the pressure. To elucidate the effect of CH_4/C_2H_4 addition on NO reduction, sensitivity analysis

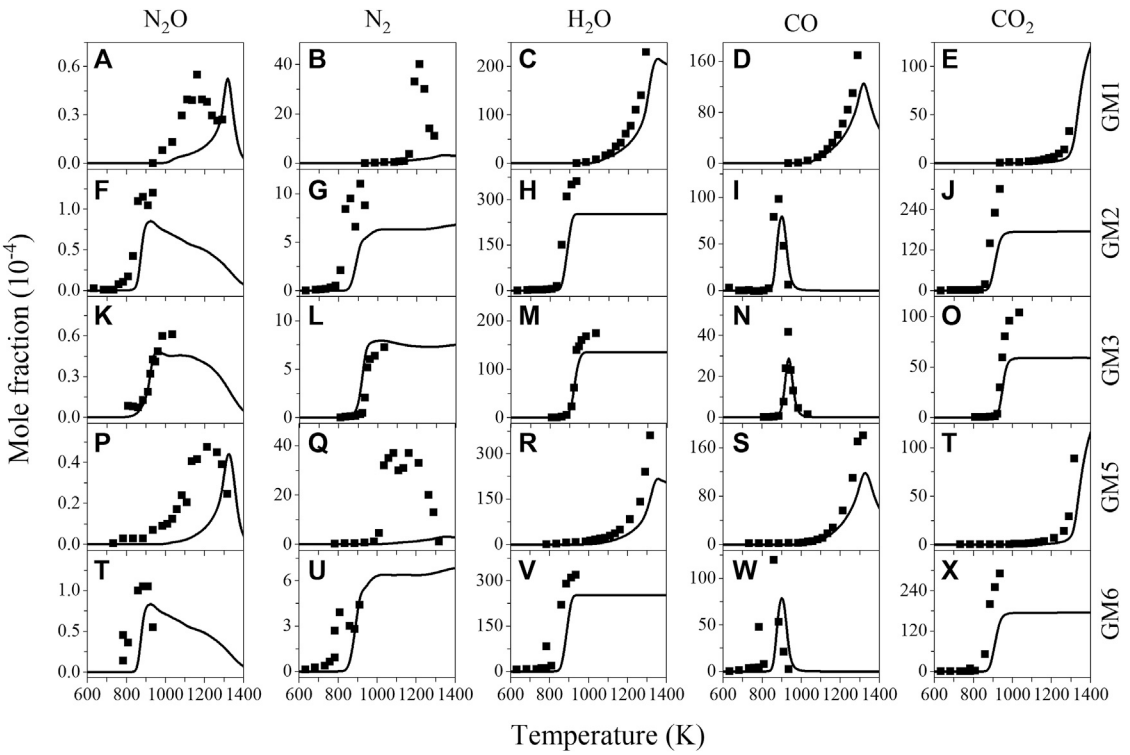

FIGURE 2 | Experimental (symbols) and simulated (lines) mole fraction profiles of nitrous oxide (N_2O), nitrogen (N_2), water (H_2O), carbon monoxide (CO) and carbon dioxide (CO_2) from the oxidation of GM1-3, GM5 and GM6. Experimental data of GM3 are taken from the work of Sun et al. (Sun et al., 2021).

on NO was also performed for GM1-4 and the results are summarized in **Figure 5**, a negative sensitivity coefficient indicates the promoting effect on NO consumption. As seen in **Figure 5D**, the competing reactions R1 and R2 show considerable sensitivity to NO consumption in GM4. Other sensitive reactions include chain-branching reactions promoting the formation of active radical pool along with those related to NO/NO_2 interconversion.

In the oxidation of $CH_4/NH_3/NO_x$ mixture (GM3), the concentration of NO has a first rise at a lower temperature (~ 860 K), and then it quickly decreases at the temperature around 911 K (**Figure 1J**). As the temperature increases to 1080 K, the concentration of NO has a second rise. According to the ROP analyses, the first rise of NO concentration is attributed by the reaction of CH_3 and NO_2 (R7). The reduction of NO between 911–1080 K is attributed by the thermal $DeNO_x$ reactions (R1 and R2), the interaction between NO and HO_2 (R3), and the reaction of CH_3O with NO (R8). The second rise of NO at higher temperatures is attributed by the reaction R6, which is the same as that in the oxidation of GM4. The sensitivity analyses shown in **Figure 5C** again illustrate the crucial role of reactions R7 and R8, i.e., converting the relatively inactive CH_3 and CH_3O_2 into highly active and unstable CH_3O radicals. The decomposition of CH_3O radical initiates the chain-branching reaction by replenishing the active radical pool to a major extent *via* the reactions $CH_3O(+M) = CH_2O + H(+M)$ and $H + O_2 = OH + O$. In addition, another consumption pathway of CH_3O, i.e., $CH_3O + O_2 = CH_2O + HO_2$, produces HO_2 of lower reactivity and competes with the above-mentioned direct dehydrogenation channel, thus exhibiting negative sensitivity to the reduction of NO.

$$CH_3 + NO_2 = CH_3O + NO \quad (R7)$$

$$CH_3O_2 + NO = CH_3O + NO_2 \quad (R8)$$

In the presence of both CH_4 and C_2H_4 (GM1-2, GM5-6), the reaction network becomes more complex. Base on the ROP analysis, the reaction scheme is summarized in **Figure 6**. It should be noted that for all the four gas mixtures the major reaction pathways are similar, while the reaction flux is different. In the case of CH_4/C_2H_4 addition, the mole fraction profiles of NO in GM2 also show multiple extreme points. ROP analyses at 835, 860, 911, and 985 K suggests that the occurrence of the first maximum and minimum points of NO mole fraction is the same as GM3 in terms of the kinetic interpretation, while the following attenuation of NO is dominated by the oxidation reaction with HO_2 (R3), while other reactions have little impacts on it. Additionally, for the low pressure case of GM1 (0.04 atm), the reduction of NO is not sensitive to the recombination of methyl or vinyl group with NO_2, which is in clear contrast to GM2.

According to the ROP analyses, CH_4 mainly proceeds the H-abstraction reaction initiated by OH to produce CH_3, which is further oxidized by NO_2 or HO_2 producing methoxyl, or undergoes the recombination reactions with NO_2, O_2 and CH_3. Particularly, the recombination reaction of CH_3 and NO_2

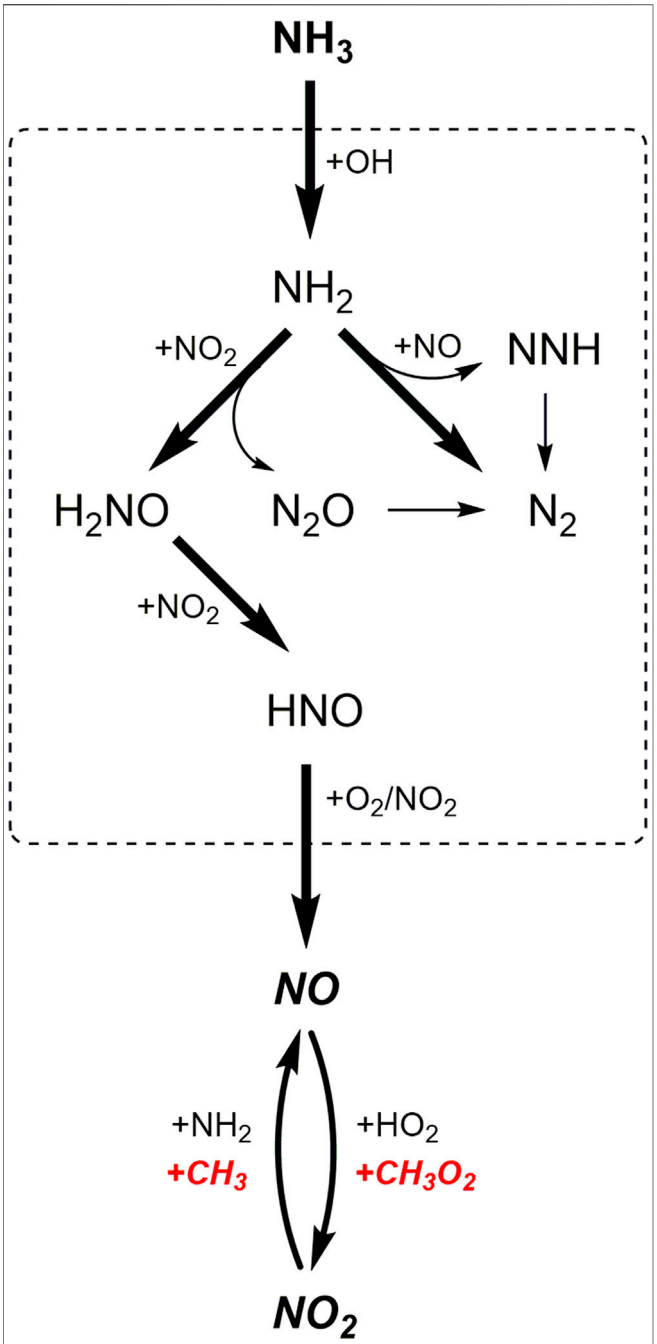

FIGURE 3 | Major reaction paths of NH_3 in the oxidation of GM1, GM2, GM3, GM4, GM5 and GM6.

(R9) is a major reaction that inhibits the reduction of NO, as can be seen in **Figure 5B**, while the competing oxidizing reaction R7 is the dominant reaction that promotes the consumption of NO. CH_3O subsequently decomposes to CO through CH_2O and HCO *via* the stepwise H-elimination process, CO is mainly converted to CO_2 *via* the reaction CO + OH = CO_2+H.

$$CH_3NO_2\,(+M) = CH_3 + NO_2\,(+M) \qquad (R9)$$

At low pressure, the consumption of C_2H_4 mainly undergoes the H-abstraction reaction by OH, giving vinyl radical (C_2H_3). At atmospheric pressure, OH-addition reaction producing 2-hydroxyethyl (PC_2H_4OH) also becomes important. PC_2H_4OH prefers to add O_2 to form $O_2C_2H_4OH$, which further dissociates into two formaldehyde molecules *via* the C-C bond fission reaction. The consumption pathways of C_2H_3 are more complex than those of PC_2H_4OH. On one hand, C_2H_3 can add O_2 or NO, followed by β-C-C scission reaction and finally produce formaldehyde. On the other hand, it can take an O atom from O_2 (R10) or NO_2 (R11) to form vinoxy (CH_2CHO). Besides, part of C_2H_3 undergoes recombination reaction with NO_2 (R12) and this reaction is the most sensitive reaction that promotes the reduction of NO at 1 atm, as shown in **Figure 5B**. Reaction R12 is a typical competitive reaction of R7 (CH_3 + NO_2 = CH_3O + NO), which is the most sensitive reaction that inhibits the reduction of NO. Therefore, in the presence of both CH_4 and C_2H_4, the role of CH_4 and C_2H_4 on the reduction of NO is opposite. This can be also proved by the extremely slight change of NO reduction ratios as well as the $DeNO_x$ temperature windows of GM2 and GM3 shown in **Figure 1**. Although the subsequent reaction of ethylene also involves interaction reactions with NO_x, the proportion of this interaction is not appreciable (mostly less than 5%).

$$C_2H_3 + O_2 = CH_2CHO + O \qquad (R10)$$

$$C_2H_3 + NO_2 = CH_2CHO + NO \qquad (R11)$$

$$C_2H_3NO_2 = C_2H_3 + NO_2 \qquad (R12)$$

As a key intermediate produced from the interaction between C_2H_4 and NO_x, CH_2CHO can either react with O_2 to produce CH_2O, or produce ketene (CH_2CO) *via* H-abstraction reaction by NO_2. It is noteworthy that CH_2O is also a major decomposition product of CH_3O. As a result, CH_2O is an abundant product in the oxidation of $CH_4/C_2H_4/NO_x/NH_3$ mixtures at atmospheric pressure The decomposition of CH_2O eventually produces active OH *via* the reaction sequence CH_2O $_{(+OH/H/O)}$ → HCO $_{(+O2)}$ → HO_2 $_{(+NO)}$ → OH and thereby promote the reactivity. The ketenyl (HCCO) radical produced by CH_2CO can either be directly converted to CO and CO_2, or proceed the reactions with NO/NO_2 leading to the formation of HCNO. A majority of HCNO undergoes the reaction with OH yielding CO, the remaining part decomposes to CO *via* the HCO as intermediate.

In general, the addition of CH_4/C_2H_4 at lean conditions promotes the formation of reactive radicals, thereby enhancing the global reaction reactivity. In addition, additional chain-branching pathways that consume NO are introduced due to the formation of CH- or CHO- type radicals such as CH_3O. As a result, in the presence of CH_4/C_2H_4, the NO conversion temperature regime is narrower than that in the oxidation of NH_3/NO_x, which is in agreement with the conclusions of Glarborg et al. (Glarborg et al., 2018).

4.2 Effects of NO/NO_2 Ratio and Pressure on $HCs/NO_x/NH_3$ Kinetics

4.2.1 CH_4 and C_2H_4

As can be observed in **Figure 4**, when NO/NO_2 ratio increases from 1 to 4, the initial decomposition temperature of C_2H_4 is only

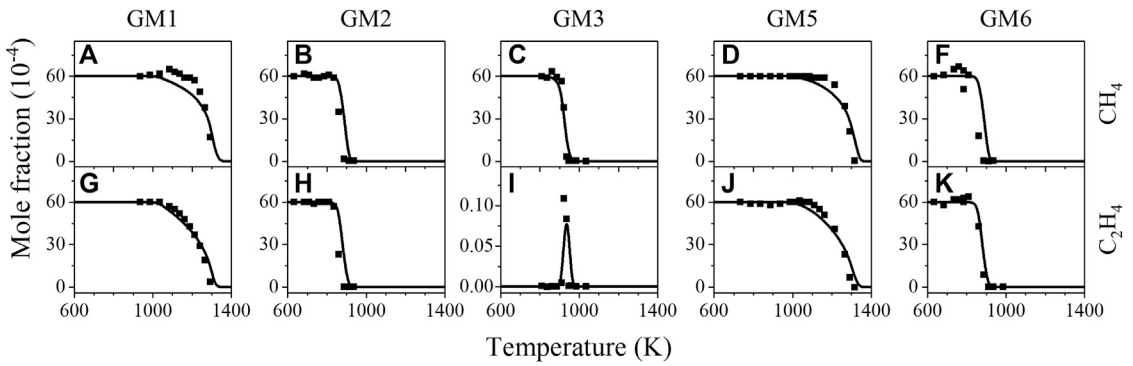

FIGURE 4 | Experimental (symbols) and simulated (lines) mole fraction profiles of methane (CH_4) and ethylene (C_2H_4) in the oxidation GM1, GM2, GM5 and GM6.

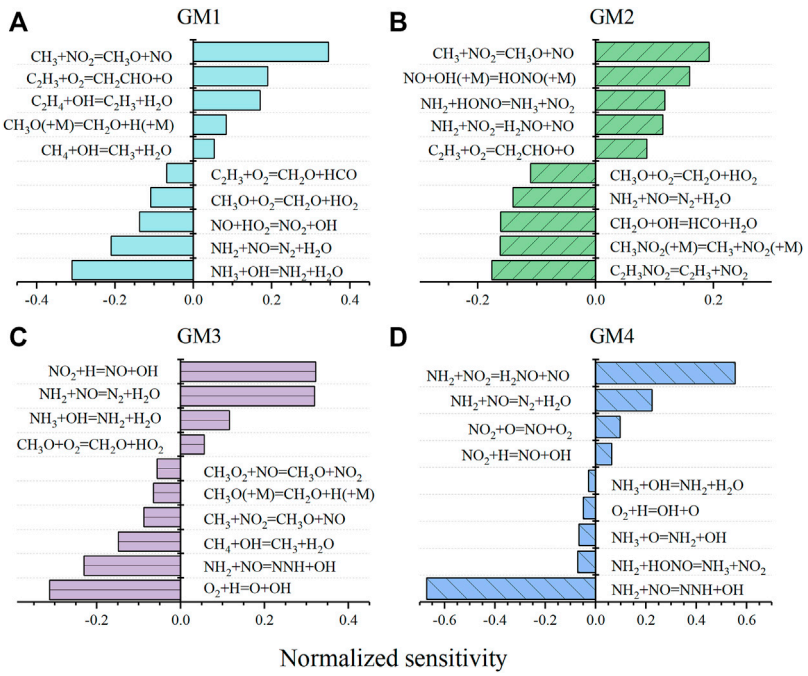

FIGURE 5 | Sensitivity analysis of NO during the flow reactor oxidation of GM1, GM2, GM3 and GM4 at 1213, 860, 911, and 1188 K, respectively. Negative sensitivity coefficients indicate promotion to NO consumption.

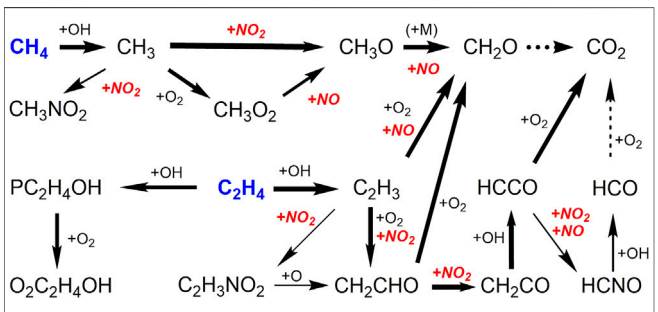

FIGURE 6 | Major reaction paths of CH_4 and C_2H_4 in the oxidation of GM1, GM2, GM5 and GM6 at 1239, 886, 1239, and 886 K, respectively.

slightly changed, while the initial decomposition temperature of CH_4 is decreased by around 50 K. As pressure increases from 0.04 to 1 atm, the initial decomposition temperatures of CH_4 and C_2H_4 are decreased by around 150–400 K. ROP and sensitivity analyses have been performed to clarify the influence of NO/NO_2 ratio and pressure on the conversion kinetics of CH_4 and C_2H_4. **Figure 7** displays the sensitivity analysis results of CH_4 and C_2H_4 in the flow reactor oxidation of GM1, GM2, GM5 and GM6 at 1239, 886, 1239, and 886 K, respectively. It can be seen that the dominant reactions have not changed significantly as the NO/NO_2 ratio increases from 1 to 4, indicating that the NO/NO_2 ratio has little effect on the conversion kinetics of CH_4 and C_2H_4.

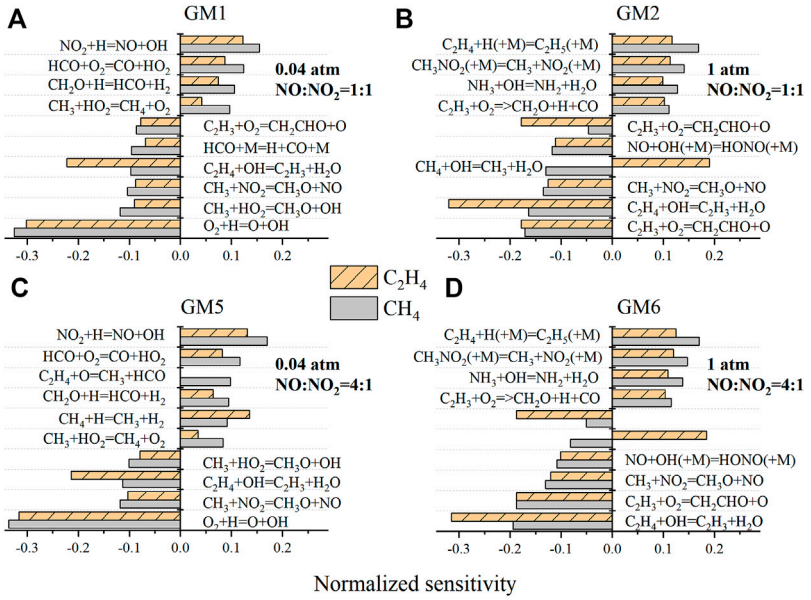

FIGURE 7 | Sensitivity analysis on CH_4 and C_2H_4 consumption during the flow reactor oxidation of GM1, GM2, GM5 and GM6 at 1239, 886, 1239, and 886 K, respectively.

In contrast to NO/NO_2 ratio, the change of pressure has significant effect on the dominant reactions of CH_4 and C_2H_4 consumption. As seen in **Figure 7**, at low pressure, the typical chain-branching reaction H + O_2 = OH + O is the most sensitive reaction promoting the consumption of CH_4 and C_2H_4. The reaction CH_3+NO_2 = CH_3O + NO is also identified as a sensitive promoting reaction. This does not seem surprising since this reaction and the following decomposition reactions of CH_3O have been already identified as one of the most important reactions that initiate the production of radical pool. At atmospheric pressure, H-abstraction reaction of C_2H_4 by OH is identified as the dominant reaction responsible for the consumption of both CH_4 and C_2H_4. H-abstraction reaction of CH_4 by OH is observed as a promoting reaction for CH_4 consumption but an inhibiting reaction for C_2H_4 consumption. This indicates that OH plays a key role in controlling the global reactivity. The O_2-addition reaction of C_2H_3 is also a sensitive promoting reaction for CH_4 and C_2H_4 consumption. As discussed above, the decomposition of CH_2CHO produced from this reaction readily generates CH_2O, whose further decomposition reaction produces HCO as major products.

4.2.2 NH_3 and NO

Figure 8 depicts the sensitivity analysis results of NH_3 during the flow reactor oxidation of GM1, GM2, GM5, and GM6 at 1239, 886, 1239, and 886 K, respectively. Similar to CH_4 and C_2H_4, the dominant reactions for NH_3 consumption are almost identical at different NO/NO_2 ratios. At low pressure (0.04 atm), the most sensitive reaction for NH_3 conversion is H + O_2 = O + OH owing to the relatively higher temperatures. At atmospheric pressure, H-abstraction reaction by OH controls the decomposition of NH_3. Reaction C_2H_4 + OH = C_2H_3 + H_2O and reaction C_2H_3 + O_2 = CH_2CHO also play a key role in the conversion of NH_3 regardless of low and atmospheric pressure, the latter reaction is closely related to the abundant production of CH_2O which ultimately dominates the yield of OH. Under both low and atmospheric pressure, the H-abstraction reaction of CH_4 by OH always plays the role that inhibits the conversion of NH_3, since CH_4 and its decomposition products strongly compete for the active radical pool (OH/O/H).

As can be observed in **Figure 1**, the maximum conversion ratio of NO increases as NO/NO_2 ratio increases. Besides, the impact of pressure on the conversion of NO is also significant. At atmospheric pressure the conversion ratio of NO increases (from 9% in GM2 increased to 45% in GM6) as NO/NO_2 ratio increases from 1 to 4. However, at low pressure (0.04 atm) the concentration of NO is found to go up with increasing temperature, i.e., at the same NO/NO_2 ratio, the fall of pressure directly inhibits the reduction of NO. In the oxidation experiment on $CH_4/NO/NO_2$ carried out by Sahu et al. (Sahu et al., 2021), it is also found that the initial NO fraction needs to approach a certain level to enhance the reactivity of the mixture, or else the low level of NO would act as an inhibitor. This non-monotonous sensitization impact of NO is attributed to the antagonism between chain-terminating reaction CH_3 + NO_2 (+M) = CH_3NO_2 (+M) and chain-branching process CH_2O + HO_2 = HCO + H_2O_2, H_2O_2(+M) = OH + OH(+M). Sahu et al. pointed out that when the initial concentration of NO is high, more CH_2O and HO_2 are produced, thus leading to the transition to chain-branching process.

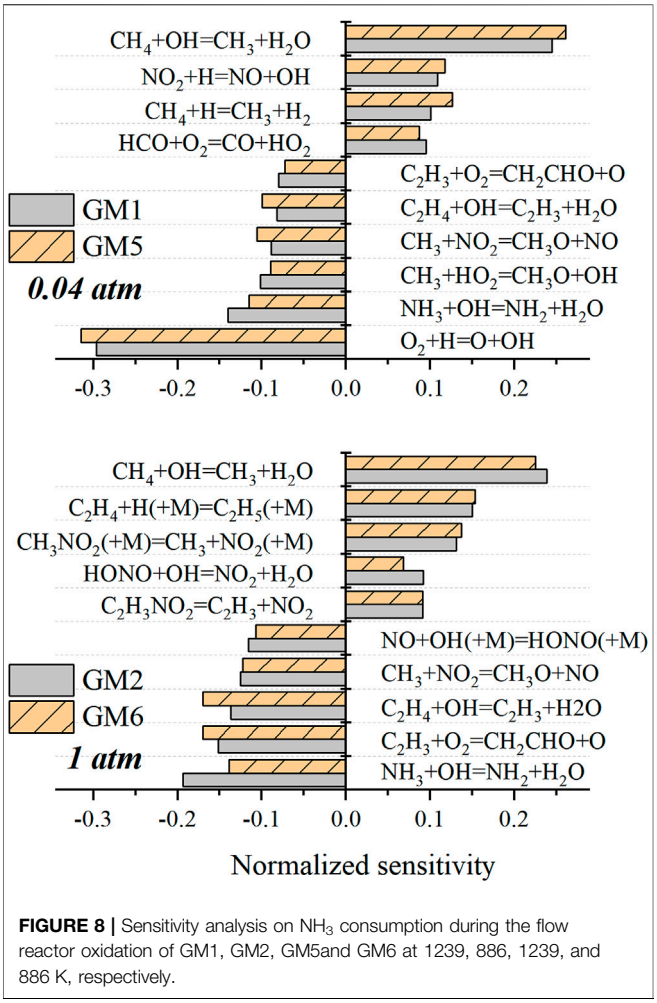

FIGURE 8 | Sensitivity analysis on NH_3 consumption during the flow reactor oxidation of GM1, GM2, GM5and GM6 at 1239, 886, 1239, and 886 K, respectively.

4.3 Formation of Major Products and Intermediates

N_2 and N_2O are two major nitrogenous products observed in the present work. As seen in **Figure 2**, the present model can capture the profiles of N_2 at atmospheric pressure, while highly under-predicts its formation at low pressure. Base on the sensitivity analysis, the formation of N_2 is controlled by reaction R7 (CH_3 + NO_2 = CH_3O + NO). However, the kinetics of CH_3 + NO_2 under low pressure remains controversial despite certain studies available in the literature (Yamaguchi et al., 1999; Srinivasan et al., 2005; Glarborg et al., 2018). Therefore, the under-estimation of N_2 at low-pressure may be attributed to the under-estimation of the rate constant of R7 at higher temperatures.

Glarborg et al. (Glarborg et al., 2018) mentioned that one of the disadvantages of SNCR with urea lies in the formation and possible emission of N_2O, which is a harmful gas destroying ozone layer. In the present experiments, N_2O has been observed to form in the order of tens of ppm on average over a wide temperature range. ROP analysis shows that almost all of N_2O is produced from reaction R5 (NH_2 + NO_2 = N_2O + H_2O) at atmospheric pressure, while at low pressure the reaction NH + NO = N_2O + H controls the formation of N_2O. In the work of Alzueta et al. (Alzueta et al., 2021), few ppm of N_2O formation was also detected in the flow reactor oxidation experiment of NH_3/NO, and the reaction N_2H_2 + NO = NH_2 + N_2O was considered as dominant reaction for N_2O formation. However, in the present work the contribution of this pathway is found almost negligible (<1%) for N_2O formation.

Figure 9 illustrates the experimental and simulated mole fraction profiles of CH_3OH, CH_2O and CH_3CHO in the oxidation of GM1, GM2, GM5 and GM6. Among them, CH_2O is the most abundantly produced. ROP analysis shows that the reaction $CH_3O(+M) = CH_2O + H(+M)$ dominates CH_2O formation independent of pressure and NO/NO_2 ratio. The production of CH_2O is derived from either methane- or ethylene-related oxidation steps. At atmospheric pressure, these two parts account for almost half of each, while at low pressure due to the activation of the additional formaldehyde generation path, $CH_3 + O = CH_2O + H$, the part derived from methane occupies about 70%. The concentration of CH_2O at low pressure peaks at a relatively high temperature of 1200 K, demonstrating that at this temperature it is sufficient to overcome the energy barrier of the reaction between CH_3 and O.

In regard to acetaldehyde (CH_3CHO), its production is closely related to ethenol (C_2H_3OH). At atmospheric pressure a majority of CH_3CHO is produced *via* the reaction $C_2H_3OH + NO/NO_2 = CH_3CHO + NO/NO_2$. At low pressure, most of CH_3CHO is formed from the isomerization of ethenol. As an unstable reactive intermediates, C_2H_3OH is primarily generated from the reaction $C_2H_4 + OH = C_2H_3OH + H$, and partly from the reaction $C_2H_4 + OH = CH_3CHO + H$. As for methanol, the yield observed in the experiment is not notable, mainly deriving from the H-abstraction of CH_3O from HO_2 or CH_2O, or through the recombination of CH_3 and OH.

Figure 10 displays the experimental and simulated mole fraction profiles of HCNO and HONO in gas mixtures of GM1, GM2, GM5 and GM6. HCNO is a key nitrogenous intermediate produced from the interaction of hydrocarbons and NO_x under high temperature and reducing conditions in reburning chemistry, where nitric oxides are converted into cyanides and isocyanides by reactions with multiple hydrocarbon-derived radicals such as CH_3, $^3CH_2$, and HCCO. Under the excess oxygen condition investigated in this work, part of the contribution of hydrocarbon derivatives to NO reduction is found mainly through the reactions R13-R15.

$$C_2H_3 + NO = HCN + CH_2O \quad (R13)$$

$$CHCHO + NO = HCNO + CO + H \quad (R14)$$

$$HCCO + NO = HCNO + CO \quad (R15)$$

The above reactions contribute less than 1% to NO reduction at atmospheric pressure, but at low pressure, it approaches around 9%. Consequently, although the addition of CH_4/C_2H_4 enriches the free radical pool and promotes the reactivity of the NH_3/NO/NO_2 mixture, its direct contribution to NO reduction is still negligible compared to the thermal $DeNO_x$ reactions (R1-R5). Furthermore, R13-R15 mostly feed into the cyanide pool (HCN,

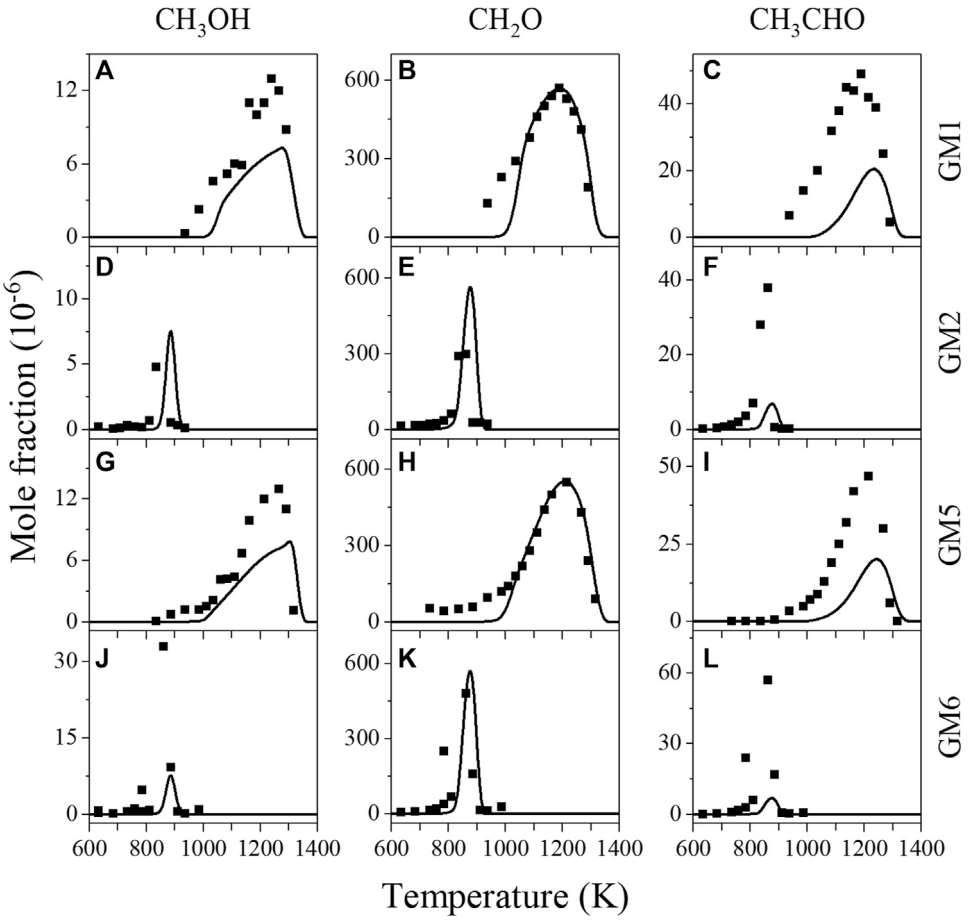

FIGURE 9 | Experimental (symbols) and simulated (lines) mole fraction profiles of methanol (CH_3OH), formaldehyde (CH_2O) and acetaldehyde (CH_3CHO) in the oxidation of GM1, GM2, GM5 and GM6.

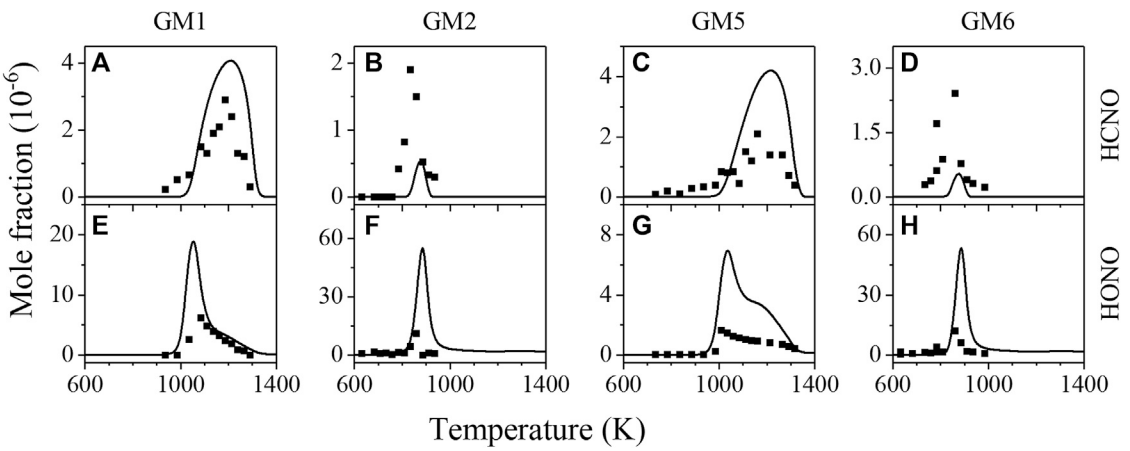

FIGURE 10 | Experimental (symbols) and simulated (lines) mole fraction profiles of HCNO and nitrous acid (HONO) in the oxidation of GM1, GM2, GM5 and GM6.

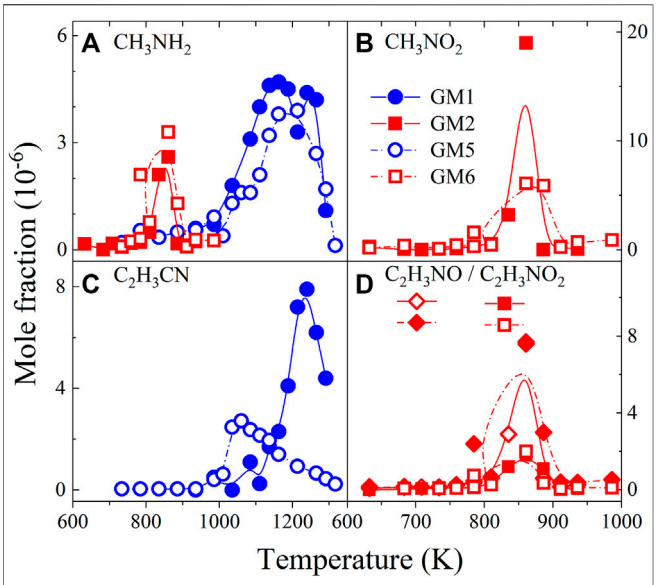

FIGURE 11 | Experimental mole fraction profiles of methylamine (CH_3NH_2), nitromethane (CH_3NO_2), vinyl cyanide (C_2H_3CN)nitrosoethylene (C_2H_3NO) and nitroethylene ($C_2H_3NO_2$) in the oxidation of GM1, GM2, GM5 and GM6.

HCNO), while the subsequent consumption of HCNO through R16 and R17 recycle NO with the dissociation of H_2NO/HNO, which complicates the process of HCNO kinetics on NO reduction.

$$HCNO + OH = H_2NO + CO \quad (R16)$$

$$HCNO + OH = HNO + HCO \quad (R17)$$

Apart from HCNO, nitrous acid (HONO) was also detected in the experiment, as seen in **Figure 10**. HONO is mainly produced from the H-abstraction reactions of CH_2CHO and H_2NO by NO_2. HONO majorly undergoes N-O bond fission to yield NO and OH, thus the HONO participated reactions belong to sensitivity reactions for the consumption of NH_3, NO, CH_4 and C_2H_4.

Figure 11 shows the measured mole fractions of CH_3NH_2, CH_3NO_2, C_2H_3CN, C_2H_3NO and $C_2H_3NO_2$ in the oxidation of GM1, GM2, GM5 and GM6. The identification of these species provides key evidence for the direct recombination reactions of CH_3, C_2H_3 with NH_2, NO_x, CN, i.e., CH_3NO_2 is the product from the reaction of CH_3 with NO_2, while C_2H_3CN is produced from the reaction of C_2H_3 with CN. Nevertheless, these species are beyond the focus of the present study, thus only a brief description is given herein.

As can be observed in **Figure 11B**, CH_3NO_2 is the most abundantly produced nitrogenous intermediates at 1 atm. CH_3NO_2 mainly decomposes to CH_2O and NO *via* CH_2NO_2 as intermediate. CH_3NH_2 can be observed at both 0.04 and 1 atm and it is mainly formed from the recombination of CH_3 with NH_2. The decomposition of CH_3NH_2 finally gives HCN *via* sequential dehydrogenation reactions $CH_3NH_2 \rightarrow CH_2NH_2 \rightarrow CH_2NH \rightarrow HCNH/H_2CN \rightarrow HCN$. The oxidation of HCN produces NO, N_2 and CO as major products under fuel-lean conditions. The decomposition of species produced from the reactions of C_2H_3, such as C_2H_3CN, C_2H_3NO and $C_2H_3NO_2$, also proceed through the stepwise H-elimination reaction, leading to the production of C_2H_2, CN and NO. C_2H_2 and CN are finally converted into CO and NO through sequential oxidation reactions. Because the consumption pathways of these nitrogenous intermediates are still not well understood, the present model is not able to reproduce their mole fraction profiles. More experimental and theoretical studies are deserved to achieve a better interpretation of the interaction kinetics between hydrocarbon radicals with NH, CN radicals and NO_x.

5 CONCLUSION

The present work has focused on two aspects with the aim to reveal the NH_3 and NO_x interaction chemistry with CH_4 and C_2H_4 at moderate temperatures and various pressures. First, speciation profiles of reactants, products, nitrogenous and oxygenated intermediates were obtained by using synchrotron vacuum ultraviolet photoionization mass spectrometry. Second, a detailed kinetic model integrating HCs/NH_3/NO_x interaction chemistry was developed and applied to interpret the experimental observations. Rate of production and sensitivity analyses were performed to analyze the conversion chemistry of NO_x and NH_3 in the presence of hydrocarbons.

The experimental results show that the addition of CH_4 and C_2H_4 promotes the conversion of NO and NH_3 at atmospheric pressure in terms of decreasing the initial conversion temperature and narrowing the reaction temperature range. The analysis results indicate that CH_4/C_2H_4 addition at atmospheric pressure promotes DeNO_x-related reactions mainly by enriching the radical pool. Besides, additional chain-branching pathways that convert NO_2 to NO are introduced due to the production of CH_3O radical. Reaction $C_2H_3 + O_2 = CH_2CHO + O$ is found to play a key role in driving the reactivity of CH_4/C_2H_4/NH_3/NO/NO_2 mixture at all the investigated conditions, generally because the further decomposition of CH_2CHO generates CH_2O, which eventually produce OH abundantly *via* the reaction sequence $CH_2O \rightarrow HCO \rightarrow HO_2 \rightarrow OH$.

The NO/NO_2 ratio is found to have only a slight impact on the conversion of CH_4, C_2H_4, NH_3 and NO from the experimental observations, while the change of pressure has significant impacts. Regarding the oxygenated and nitrogenous intermediates, formaldehyde and nitromethane are observed as the most abundantly produced oxygenated and nitrogenous intermediates, respectively. The identification of nitrogenous intermediates such as methylamine, nitromethane, vinyl cyanide, nitrosoethylene and nitroethylene provides key evidence for the direct recombination reactions of hydrocarbon or hydrocarbon radicals with NO_x, NH_2 or CN. The new data and corresponding analyses are expected to provide valuable information for understanding the complex gas phase reactions in the exhaust gas as well as an extension of the kinetic model of HCs/NH_3/NO_x reaction systems.

DATA AVAILABILITY STATEMENT

The raw data supporting the conclusions of this article will be made available by the authors, without undue reservation.

AUTHOR CONTRIBUTIONS

YD: Methodology, Investigation, Data curation, Writing- original draft. ZS: Methodology, Investigation, Data curation. WY: Conceptualization, Methodology, Writing -review and editing, Funding acquisition. JY: Methodology, investigation. ZZ: Methodology, Writing - review and editing. FQ: Funding acquisition, Writing - review and editing.

FUNDING

The authors are grateful for the funding support from the National Natural Science Foundation of China (51706137, 51761135111) and the National Key R&D Program of China (2019YFA0405602).

ACKNOWLEDGMENTS

The authors wish to acknowledge the financial support provided by the National Natural Science Foundation of China.

REFERENCES

Alzueta, M., Ara, L., Mercader, V., Delogu, M., and Bilbao, R. (2021). Interaction of NH_3 and NO under Combustion Conditions. Experimental Flow Reactor Study and Kinetic Modeling Simulation. *Combustion and Flame* 235, 111691. doi:10.1016/j.combustflame.2021.111691

Börnhorst, M., and Deutschmann, O. (2021). Advances and Challenges of Ammonia Delivery by Urea-Water Sprays in SCR Systems. *Prog. Energ. Combustion Sci.* 87, 100949. doi:10.1016/j.pecs.2021.100949

Deng, F., Zhang, Y., Sun, W., Huang, W., Zhao, Q., Qin, X., et al. (2019). Towards a Kinetic Understanding of the NOx Sensitization Effect on Unsaturation Hydrocarbons: A Case Study of Ethylene/nitrogen Dioxide Mixtures. *Proc. Combustion Inst.* 37 (1), 719–726. doi:10.1016/j.proci.2018.07.115

Duynslaegher, C., Contino, F., Vandooren, J., and Jeanmart, H. (2012). Modeling of Ammonia Combustion at Low Pressure. *Combustion and Flame* 159 (9), 2799–2805. doi:10.1016/j.combustflame.2012.06.003

Gasnot, L., Dao, D. Q., and Pauwels, J. F. (2012). Experimental and Kinetic Study of the Effect of Additives on the Ammonia Based SNCR Process in Low Temperature Conditions. *Energy Fuels* 26 (5), 2837–2849. doi:10.1021/ef300310c

Glarborg, P., Miller, J. A., Ruscic, B., and Klippenstein, S. J. (2018). Modeling Nitrogen Chemistry in Combustion. *Prog. Energ. Combustion Sci.* 67, 31–68. doi:10.1016/j.pecs.2018.01.002

Hemberger, R., Muris, S., Pleban, K.-U., and Wolfrum, J. (1994). An Experimental and Modeling Study of the Selective Noncatalytic Reduction of NO by Ammonia in the Presence of Hydrocarbons. *Combustion and Flame* 99 (3-4), 660–668. doi:10.1016/0010-2180(94)90060-4

Hutter, R., De Libero, L., Elbert, P., and Onder, C. H. (2018). Catalytic Methane Oxidation in the Exhaust Gas Aftertreatment of a Lean-Burn Natural Gas Engine. *Chem. Eng. J.* 349, 156–167. doi:10.1016/j.cej.2018.05.054

Jia, Y., Jiang, J., Zheng, R., Guo, L., Yuan, J., Zhang, S., et al. (2021). Insight into the Reaction Mechanism over PMoA for Low Temperature NH3-SCR: A Combined *In-Situ* DRIFTs and DFT Transition State Calculations. *J. Hazard. Mater.* 412, 125258. doi:10.1016/j.jhazmat.2021.125258

Johnson, T. V. (2015). Review of Vehicular Emissions Trends. *SAE Int. J. Engines* 8 (3), 1152–1167. doi:10.4271/2015-01-0993

Lee, K., Choi, B., Lee, C., and Oh, K. (2020). Effects of SiO2/Al2O3 Ratio, Reaction Atmosphere and Metal Additive on De-NOx Performance of HC-SCR over Cu-Based ZSM-5. *J. Ind. Eng. Chem.* 90, 132–144. doi:10.1016/j.jiec.2020.07.005

Lott, P., and Deutschmann, O. (2021). Lean-Burn Natural Gas Engines: Challenges and Concepts for an Efficient Exhaust Gas Aftertreatment System. *Emiss. Control. Sci. Technol.* 7 (1), 1–6. doi:10.1007/s40825-020-00176-w

Marshall, P., Leung, C., Gimenez-Lopez, J., Rasmussen, C. T., Hashemi, H., Glarborg, P., et al. (2019). The C2H2 + NO2 Reaction: Implications for High Pressure Oxidation of C2H2/NOx Mixtures. *Proc. Combustion Inst.* 37 (1), 469–476. doi:10.1016/j.proci.2018.06.202

Mejía-Centeno, I., Castillo, S., Camposeco, R., and Fuentes, G. A. (2013). SCR of NOx by NH3 over Model Catalysts: The Kinetic Data-Linear Free Energy Relation. *Catal. Commun.* 31, 11–15. doi:10.1016/j.catcom.2012.10.022

Miller, J. A., and Bowman, C. T. (1989). Mechanism and Modeling of Nitrogen Chemistry in Combustion. *Prog. Energ. Combustion Sci.* 15 (4), 287–338. doi:10.1016/0360-1285(89)90017-8

Okafor, E. C., Naito, Y., Colson, S., Ichikawa, A., Kudo, T., Hayakawa, A., et al. (2018). Experimental and Numerical Study of the Laminar Burning Velocity of CH4-NH3-air Premixed Flames. *Combustion and flame* 187, 185–198. doi:10.1016/j.combustflame.2017.09.002

Piumetti, M., Bensaid, S., Fino, D., and Russo, N. (2016). Catalysis in Diesel Engine NOxaftertreatment: a Review. *Catal. Struct. Reactivity* 1 (4), 155–173. doi:10.1080/2055074x.2015.1105615

Qi, F. (2013). Combustion Chemistry Probed by Synchrotron VUV Photoionization Mass Spectrometry. *Proc. Combustion Inst.* 34 (1), 33–63. doi:10.1016/j.proci.2012.09.002

ReactionDesign (2009). *CHEMKIN-PRO 15092 Reaction Design*. San Diego 2009.

Sahu, A. B., Mohamed, A. A. E.-S., Panigrahy, S., Saggese, C., Patel, V., Bourque, G., et al. (2021). An Experimental and Kinetic Modeling Study of NO_x Sensitization on Methane Autoignition and Oxidation. *Combustion and Flame*, 111746. doi:10.1016/j.combustflame.2021.111746

Savva, Z., Petallidou, K. C., Damaskinos, C. M., Olympiou, G. G., Stathopoulos, V. N., and Efstathiou, A. M. (2021). H_2-SCR of NO_x on Low-SSA CeO_2-Supported Pd: The Effect of Pd Particle Size. *Appl. Catal. A: Gen.* 615, 118062. doi:10.1016/j.apcata.2021.118062

Schmitt, S., Schwarz, S., Ruwe, L., Horstmann, J., Sabath, F., Maier, L., et al. (2021). Homogeneous Conversion of NO X and NH 3 with CH 4 , CO, and C 2 H 4 at the Diluted Conditions of Exhaust-gases of Lean Operated Natural Gas Engines. *Int. J. Chem. Kinet.* 53 (2), 213–229. doi:10.1002/kin.21435

Srinivasan, N. K., Su, M.-C., Sutherland, J. W., and Michael, J. V. (2005). Reflected Shock Tube Studies of High-Temperature Rate Constants for OH + CH4 → CH3 + H2O and CH3 + NO2 → CH3O + NO. *J. Phys. Chem. A.* 109 (9), 1857–1863. doi:10.1021/jp040679j

Stagni, A., Cavallotti, C., Arunthanayothin, S., Song, Y., Herbinet, O., Battin-Leclerc, F., et al. (2020). An Experimental, Theoretical and Kinetic-Modeling Study of the Gas-phase Oxidation of Ammonia. *React. Chem. Eng.* 5 (4), 696–711. doi:10.1039/C9RE00429G

Sumathi, R., Sengupta, D., and Nguyen, M. T. (1998). Theoretical Study of the H2 + NO and Related Reactions of [H2NO] Isomers. *J. Phys. Chem. A.* 102 (18), 3175–3183. doi:10.1021/jp9804953

Sun, Z., Deng, Y., Song, S., Yang, J., Yuan, W., and Qi, F. (2021). Experimental and Kinetic Modeling Study of the Homogeneous Chemistry of NH_3 and NO_x with CH_4 at the Diluted Conditions. *Combustion and Flame, submitted*.

Tamm, S., Ingelsten, H. H., Skoglundh, M., and Palmqvist, A. E. C. (2009). The Influence of Gas Phase Reactions on the Design Criteria for Catalysts for Lean NO_x Reduction with Dimethyl Ether. *Appl. Catal. B: Environ.* 91 (1-2), 234–241. doi:10.1016/j.apcatb.2009.05.030

Torkashvand, B., Lott, P., Zengel, D., Maier, L., Hettel, M., Grunwaldt, J.-D., et al. (2019). Homogeneous Oxidation of Light Alkanes in the Exhaust of Turbocharged Lean-Burn Gas Engines. *Chem. Eng. J.* 377, 119800. doi:10.1016/j.cej.2018.08.186

Vassallo, J., Miró, E., and Petunchi, J. (1995). On the Role of Gas-phase Reactions in the Mechanism of the Selective Reduction of NO_x. *Appl. Catal. B: Environ.* 7 (1-2), 65–78. doi:10.1016/0926-3373(95)00032-1

Wang, D., Peng, Y., Yang, Q., Hu, F., Li, J., and Crittenden, J. (2019). NH3-SCR Performance of WO3 Blanketed CeO2 with Different Morphology: Balance of Surface Reducibility and Acidity. *Catal. Today* 332, 42–48. doi:10.1016/j.cattod.2018.07.048

Yamaguchi, Y., Teng, Y., Shimomura, S., Tabata, K., and Suzuki, E. (1999). Ab Initio Study for Selective Oxidation of Methane with NOx (X = 1, 2). *J. Phys. Chem. A.* 103 (41), 8272–8278. doi:10.1021/jp990985a

Zhou, C.-W., Li, Y., Burke, U., Banyon, C., Somers, K. P., Ding, S., et al. (2018). An Experimental and Chemical Kinetic Modeling Study of 1,3-butadiene Combustion: Ignition Delay Time and Laminar Flame Speed Measurements. *Combustion and Flame* 197, 423–438. doi:10.1016/j.combustflame.2018.08.006

Zhou, Z., Du, X., Yang, J., Wang, Y., Li, C., Wei, S., et al. (2016). The Vacuum Ultraviolet Beamline/endstations at NSRL Dedicated to Combustion Research. *J. Synchrotron Radiat.* 23 (4), 1035–1045. doi:10.1107/S1600577516005816

Conflict of Interest: The authors declare that the research was conducted in the absence of any commercial or financial relationships that could be construed as a potential conflict of interest.

Publisher's Note: All claims expressed in this article are solely those of the authors and do not necessarily represent those of their affiliated organizations, or those of the publisher, the editors and the reviewers. Any product that may be evaluated in this article, orclaim that may be made by its manufacturer, is not guaranteed or endorsed by the publisher.

frontiers in Energy Research

ORIGINAL RESEARCH
published: 17 February 2022
doi: 10.3389/fenrg.2022.847947

Experimental and Numerical Study on the Combustion Characteristics of a Laminar Non-Premixed Methane Jet Flame in Oxygen/Carbon Dioxide Coflow

Fan Zhang[1], Xing Li[2,3,4], Shengrong Xie[2,5], Junxiong Wang[2] and Xiaohan Wang[2]*

[1]School of Mechanical and Electric Engineering, Guangzhou University, Guangzhou, China, [2]Guangzhou Institute of Energy Conversion, Chinese Academy of Sciences, Guangzhou, China, [3]Dalian National Laboratory for Clean Energy, Dalian, China, [4]Department of Energy and Mechanical Engineering, Hunan Institute of Humanities, Science and Technology, Loudi, China, [5]University of Chinese Academy of Sciences, Beijing, China

OPEN ACCESS

Edited by:
Zhihua Wang,
Zhejiang University, China

Reviewed by:
Yu Wang,
Wuhan University of Technology, China
Lei Zhou,
Harbin Institute of Technology, Shenzhen, China
Jinhua Wang,
Xi'an Jiaotong University, China

***Correspondence:**
Xing Li
lixing@ms.giec.ac.cn
inspirationlee@hotmail.com

Specialty section:
This article was submitted to Advanced Clean Fuel Technologies, a section of the journal Frontiers in Energy Research

Received: *03 January 2022*
Accepted: *24 January 2022*
Published: *17 February 2022*

Citation:
Zhang F, Li X, Xie S, Wang J and Wang X (2022) Experimental and Numerical Study on the Combustion Characteristics of a Laminar Non-Premixed Methane Jet Flame in Oxygen/Carbon Dioxide Coflow. Front. Energy Res. 10:847947. doi: 10.3389/fenrg.2022.847947

The combustion characteristics of laminar non-premixed CH_4 jet flame in an O_2/CO_2 coflows with different oxygen mole fractions were studied experimentally. The flame heights at different oxygen concentrations and fuel jet velocity were obtained. The experimental observation shows that the luminosity of the CH_4 jet flame in O_2/CO_2 coflow is different from that of the flame in air stream. A two-dimensional numerical study of a laminar non-premixed CH_4 jet flame in the O_2/CO_2 coflow with the O_2 mole fraction of 0.35 was conducted to analyze the effects of CO_2 dilution on the flame. The distribution of OH radicals in the flame was measured experimentally using planar laser-induced fluorescence (PLIF) to validate the computational method adopted in this work, and the computational and experimental results of the OH distributions showed good consistency at various fuel flow velocities. Three artificial species were created in the numerical experiment to analyze the effects of the chemical reactions, third-body collisions, and transport properties of CO_2 on the height, width, and temperature distribution of the flame. The results showed that CO_2 participation in chemical reactions exerts significant effects on the flame. However, the influences of the third-body effects and transport properties of CO_2 on the jet flame are unremarkable. The global reaction pathways and distributions of important species in the laminar non-premixed CH_4 jet flame were analyzed in detail to investigate the influence mechanisms of CO_2 on the flame height and temperature. The entire flame can be divided into two oxidation parts, which separated by the boundary of the HCCO. The H, O, and OH concentrations and distributions in different parts of the flame were influenced by CO_2 dilution, resulting in different flame heights and temperature distributions.

Keywords: non-premixed laminar jet flame, O_2/CO_2 coflow, chemical effect, third-body effect, transport property

INTRODUCTION

The reduction of CO_2 emissions during fossil fuel utilization is an important task for human society. The injection of purified CO_2 from flue gas into underground reservoirs is believed to help achieve this goal (Buhre et al., 2005; Wall, 2007). However, CO_2-rich flue gas is required to increase the efficiency and economy during carbon capture and storage. Several new advanced combustion technologies that use O_2/CO_2 as an oxidizer, such as oxy-fuel combustion technology (Buhre et al., 2005; Wall, 2007; Hjärtstam et al., 2009; Rathnam et al., 2009; Scheffknecht et al., 2011; Taniguchi et al., 2011; Chen et al., 2012; Dhaneswar and Pisupati, 2012; Luo et al., 2015; Moroń and Rybak, 2015; Liu et al., 2016; Ge et al., 2017; Seddighi, 2017; Menage et al., 2018; Zhang et al., 2018), moderate or intense low-oxygen dilution (MILD) oxy-combustion (Li et al., 2013; Tu et al., 2015; Mardani and FazlollahiGhomshi, 2016; Mao et al., 2017; Gładysz et al., 2018), gaseous fuel-fired oxy-fuel combustion technology (Yin et al., 2011; Seepana and Jayanti, 2012a; Seepana and Jayanti, 2012b; Oh et al., 2013a; Oh et al., 2013b; Oh and Noh, 2013; Oh and Noh, 2014; Giménez-López et al., 2015; Oh and Noh, 2015; Oh and Hong, 2016; Bürkle et al., 2018), and high-temperature oxygen combustion technology (Li et al., 2014; Li et al., 2015; Li et al., 2016), have been developed to meet this requirement. However, many other challenges must be solved before these combustion technologies can be widely adopted in the industry, since the differences in the physical properties and chemical characteristics of CO_2 and N_2 can lead to important distinctions in flame structure. More information on the combustion characteristics of different fuels in various O_2/CO_2 environments must be obtained for the development of new combustion approaches.

Experimental and numerical studies on the fundamental combustion characteristics of O_2/CO_2-fired flames have been conducted previously. The effect of CO_2 on the free-propagation speed of laminar premixed $CH_4/O_2/CO_2$ flames was investigated numerically (Liu et al., 2003). The speeds of laminar $CH_4/O_2/CO_2$ flames at different equivalence ratios and pressures were measured and computed (Xie et al., 2013). The CH_4 oxidation under CO_2-rich conditions has also been investigated using an atmospheric pressure flow reactor (Glarborg and Bentzen, 2008). The effects of environmental pressure (Maruta et al., 2007) and oxidizer temperature (Li et al., 2014) on the stretch extinction characteristics of CH_4/CO_2 versus O_2/CO_2 counterflow non-premixed flames have been studied through experiments and numerical computations. The ignition temperature of a stoichiometric $CH_4/O_2/CO_2$ mixture was examined by using a micro flow reactor with a controlled temperature profile (Li et al., 2015). The fundamental studies (Liu et al., 2003; Maruta et al., 2007; Glarborg and Bentzen, 2008; Xie et al., 2013; Li et al., 2014; Li et al., 2015; Li et al., 2016) show that CO_2 exerts an inhibitory effect on flames. Consequently, a higher oxygen concentration is recommended for the O_2/CO_2-fired flames to achieve a comparable combustion characteristics as the air flames.

The previous fundamental studies have provided an essential understanding of flames in O_2/CO_2 environments (Liu et al., 2003; Maruta et al., 2007; Glarborg and Bentzen, 2008; Xie et al., 2013; Li et al., 2014; Li et al., 2015; Li et al., 2016). However, the three-dimensional structures of flames in O_2/CO_2, which are important for the development of industrial burner, deserves more attention. The combustion characteristics of turbulent premixed CH_4/air/CO_2 and $CO/H_2/CO_2/O_2$ flames was investigated experimentally (Kobayashi et al., 2007; Kobayashi et al., 2009; Wang et al., 2013). And it was observed that local wrinkled structures become sharp and propagate deeply into the burned mixture with addition of CO_2. It was also proposed that CO_2 addition is effective for restraining combustion oscillation (Kobayashi et al., 2007). Experimental studies of the swirl-stabilized turbulent CH_4/air and $CH_4/O_2/CO_2$ flames show that the average length of air flames is longer than that of oxy-flames. Moreover, it was found that one-dimensional laminar flame properties could not be used to explain the intense burning of turbulent oxy-flames (Watanabe et al., 2016).

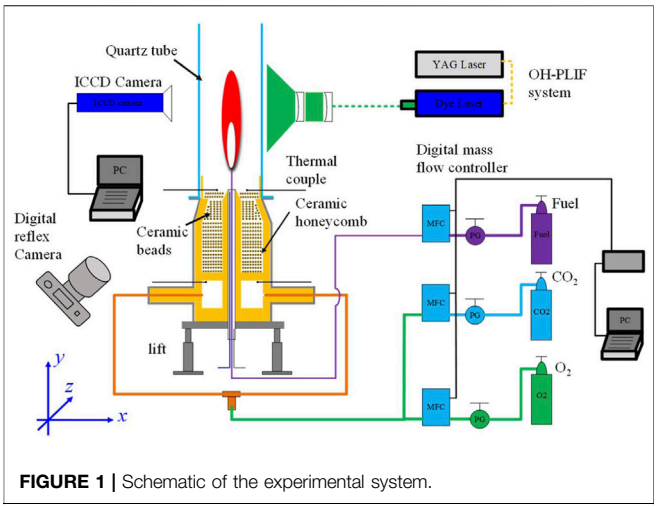

FIGURE 1 | Schematic of the experimental system.

Recently, the influences of CO_2 on the combustion characteristics of multidimensional flames has been studied in detail. The physical and chemical effects of CO_2 dilution on a CH_4/H_2 jet flame in the MILD oxy-combustion regime have been investigated using two-dimensional numerical computations with a detailed kinetic mechanism (Tu et al., 2016; Tu et al., 2017). It was found that the chemical effects of CO_2 play a comparable role in the suppression of temperature rise to the physical effects (Tu et al., 2016). The influences of CO_2 dilution on the shape and structure of laminar CO/H_2 diffusion flames in an $O_2/N_2/CO_2$ coflow was examined (Xu et al., 2017), and the chemical effects of the thermal and transport properties of CO_2 on the flames were discussed in detail. The previous numerical studies provide important information on the effects of CO_2 under MILD (Tu et al., 2016; Tu et al., 2017) and syngas (Xu et al., 2017) combustion regimes. However, the effects of CO_2 on the flame shape and temperature distribution of gaseous-fuel-fired flames in an O_2/CO_2 environment with a high O_2 concentration needs special attention and was not clarified.

The target of the present work is to study on the combustion characteristics of laminar non-premixed methane jet flames in oxygen/carbon dioxide coflows. The laminar flame heights at

different oxygen concentrations were measured by experiments. The OH distributions of typical laminar methane jet flames in a O_2/CO_2 coflow were measured by OH-PLIF technique. Two-dimensional numerical computations with a detailed kinetic mechanism were conducted, and three artificial species modified from CO_2 were employed in the numerical experiment to clarify the effects of CO_2. The influences through the chemical reactions, third-body collisions, and transport properties of CO_2 on the combustion characteristics of a laminar non-premixed CH_4 jet flame in an O_2/CO_2 environment with a high O_2 concentration was distinguished in detail.

EXPERIMENT

Experimental Setup and Method

Figure 1 shows a schematic diagram of the experimental system. The jet-flame experimental apparatus includes three parts, namely, a quartz tube, a fuel tube, and a stainless-steel chamber. The length and height of the rectangular quartz tube are 10 and 60 cm, respectively, and the wall thickness is 4 mm. The fuel stream was supplied through a stainless-steel tube with an inner diameter (d) of 1 mm and a length of 15 cm. The fuel tube was installed at the center of a rectangular quartz tube. The rectangular quartz tube and the stainless-steel chamber were connected together, and a ceramic honeycomb (diameter, 12 cm; height, 10 cm) and ceramic beads (diameter, 2 mm) were arranged in the stainless-steel chamber to achieve a uniform coflow velocity. A well-mixed O_2/CO_2 stream was fed into the rectangular quartz tube from the bottom of the chamber. Three MKS digital mass flow controllers were employed to control the volumetric flow rates of gases, and a wet gas meter (Shinagawa, W-NK-2) was used to calibrate the digital mass flow controllers. The rectangular quartz tube was adopted in the experiment because it is convenient for optical measurements. In addition, the similarity of non-premixed laminar CH_4 jet flames in a circular tube with an inner diameter of 9.2 cm to those in a rectangular quartz tube has been confirmed by preliminary experiment. The laminar CH_4 jet flames in O_2/CO_2 colfows with different oxygen mole fractions (X_{O2} = 0.30, 0.35 and 0.40) were tested by the present experimental system.

A single-lens reflex digital camera (Nikon D-610, f/4) was fixed in front of the flame to record the flame images. The ISO and exposure time were set as 1,250 and 1/40 s, respectively. The qualitative distribution of OH radicals in laminar non-premixed CH_4 jet flames in an O_2/CO_2 coflow was measured using the OH-PLIF technique. The experimental apparatus was fixed on a lifter with a scale which can adjust the position of the flame. Consequently, the OH distribution of the different parts of the flame can be measured. The distribution of OH radicals at the center plane of the flame was measured by the OH-PLIF system. A beam with a wavelength of 355 nm was provided by a Nd:YAG laser (Quanta-Ray Pro-230). This beam was then transformed into a new laser beam by a dye laser (Sirah PSCAN-G-30) to excite the OH radicals in the flame. The wavelength of the dye laser beam was around 283.565 nm for the present OH-PLIF system. And the height of the laser sheet was about 40 mm and the thickness was less than 100 μm at the location of the flame. An ICCD camera (LAVISION VC-IRO and VC-Imager Pro X 4M) with an OH filter was used to obtain the OH image of the flame. The finest pixel resolution of the ICCD camera at the flame position was approximately 50 μm. A detailed description of the OH-PLIF system and the selected wavelength is provided elsewhere (Li et al., 2017). Raw OH-PLIF images were directly used for qualitative comparison with the numerical results because the measured OH intensity is proportional to the computational OH molar concentration within a 10% error (Yamamoto et al., 2009). The OH-PLIF results at each fuel flow velocity were averaged from every 100 OH-PLIF images. As the length of the laser sheet at the location of the flame was approximately 40 mm, which cannot cover the overall scope of the flame, the OH distributions in different parts of the flame were measured by adjusting the height of the experimental apparatus. The overall OH distribution of a jet flame was assembled from the OH distributions at different parts of the flame.

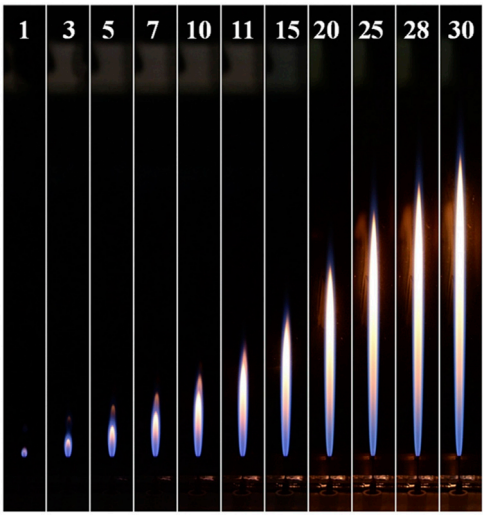

FIGURE 2 | The images of CH_4-jet-flames in O_2/CO_2 coflows with an oxygen mole fraction of 0.35. (The number on the top denotes the corresponding fuel flow velocity in the unit of m/s).

Experimental Results

The flame height and width which are determined by oxygen concentration and fuel flow rate are important parameter for the design of the industrial burner. Consequently, the laminar CH_4 jet flames in O_2/CO_2 coflows with oxygen mole fractions (X_{O2}) of 0.30, 0.35 and 0.40 were studied experimentally. The coflow velocity was kept at 0.1 m/s for different cases. The laminar CH_4 jet flames in the air coflow were also tested for the comparison. The images of CH_4 laminar jet flames in the O_2/CO_2 coflow (X_{O2} = 0.35) with different fuel jet velocities are shown in **Figure 2**. It can be seen that the flame height of the laminar CH_4 jet flame increase linearly with the fuel velocity when the O_2/CO_2 is used as the oxidizer.

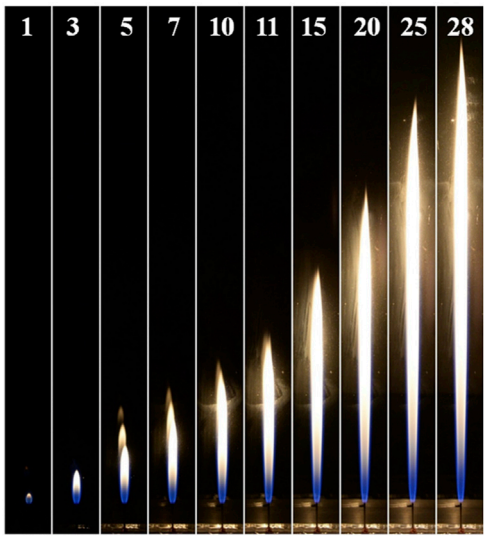

FIGURE 3 | The images of CH_4-jet-flames in air coflow. (The number on the top denotes the corresponding fuel flow velocity in the unit of m/s).

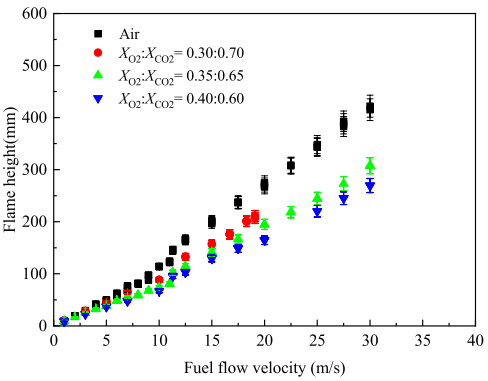

FIGURE 4 | Measured flame heights of CH_4-jet-flames in O_2/CO_2 and air coflows with 5% error bars.

The experimental results in **Figures 2**, **3** show that the luminosity of the flame in the O_2/CO_2 coflow is different from that of the laminar CH_4 jet flame in air. Both the laminar CH_4 jet flames in the air and O_2/CO_2 coflows can be divided into two sections, bottom and top partitions, based on the flame luminosity. The bottom section of the flame is dominated by the blue color luminosity, while the top partition of flame shows orange and yellow colors for the flame in O_2/CO_2 and air respectively. It can be seen that the bottom section of the flame with O_2/CO_2 coflow show dark blue color, however, the flame in air is more bright. The luminosities of the laminar CH_4 jet flames in O_2/CO_2 and air coflows suggests that the effect of CO_2 on the flame structure is remarkable, which needs further investigation.

The flame height of laminar CH_4 jet flames in O_2/CO_2 (X_{O2} = 0.30, 0.35 and 0.40) and air coflows were measured, as shown in

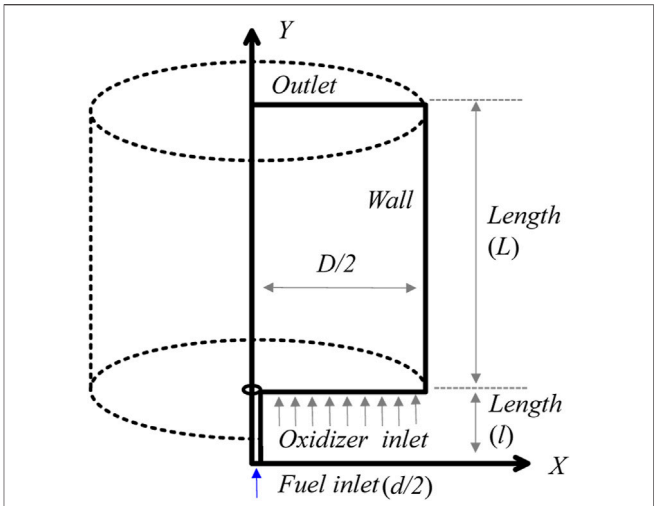

FIGURE 5 | Physical model and boundary conditions.

Figure 4. It can be seen that the flame height is smoothly decreased as the increase of oxygen mole fraction. The flame in air is taller than those of the flames in O_2/CO_2 coflows. The theoretical study on the flame length of non-premixed laminar jet flame was conducted in the early studies (Roper, 1977; Roper et al., 1977), and the formula of the flame length for circular port burner was obtained and shown as follows,

$$L_f = \frac{Q\left(T_0/T_F\right)}{4\pi D_0 \ln\left(1+\frac{1}{S}\right)}\left(T_0/T_f\right)^{0.67} \quad (1)$$

Where T_0, T_F and T_f are the ambient temperature, the fuel flow temperature and the average temperature of the flame respectively. Q is the volumetric flow rate of fuel stream, S is the stoichiometric molar ratio of oxidizer to fuel. D_0 is the diffusion coefficient at T_0. The increase of oxygen concertation leads a decrease of the stoichiometric molar ratio of oxidizer to fuel and an increase of the flame temperature. Consequently the laminar flame height in the O_2/CO_2 coflow with a higher oxygen concentration is lower.

NUMERICAL COMPUTATION AND ANALYSIS

Physical Model and Computation Method

Numerical computation with a detailed reaction mechanism was conducted to clarify the effects of CO_2 on the combustion characteristics of the laminar CH_4 jet flame in O_2/CO_2 colfow. **Figure 5** illustrates the physical model and boundary conditions. A CH_4 stream was injected into the O_2/CO_2 coflow through a tube with an inner diameter (d) of 1 mm and a length (L) of 15 cm. The length (L) and width ($D/2$) of the computation domain are 50 and 4.6 cm, respectively. An O_2/CO_2 mixture with an O_2 mole fraction (X_O) of 0.35 was used in the study, since the previous work has shown that the counterflow non-premixed CH_4 flame in an O_2/CO_2 coflow with X_O = 0.35 has a combustion

TABLE 1 | Properties of artificial species.

	KCO_2	XCO_2	DCO_2
Chemical effect as CO_2	×	×	√
Third-body effects as CO_2	√	×	√
Thermal properties as CO_2	√	√	√
Transport properties as CO_2	√	√	×

intensity comparable with that of an air flame (Maruta et al., 2007; Li et al., 2014). The pressure in the system was 1 atm, and the inlet temperature of the oxidizer and fuel streams was 300 K. Laminar non-premixed CH_4 jet flames with two different fuel jet velocities (V_F = 5 and 10 m/s, Re = 293 and 586) were investigated. The inlet flow velocity of the oxidizer stream was fixed at 0.1 m/s. The laminar non-premixed jet flame was simplified to a two-dimensional axisymmetric swirl model. All walls were considered to be in a no-slip state. A convective heat transfer boundary (ambient temperature, 300 K; convective heat transfer coefficient, 6 W/m^2·K) based on the experimental conditions was used for the wall of the computational domain, and an adiabatic wall condition was applied to the fuel tube wall. While the velocity inlet boundary was used at the fuel and oxidizer inlets, the pressure outlet boundary was applied at the outlet.

The governing equations included the mass, momentum, energy, and species-conservation equations, as well as the ideal gas equation of state. A detailed description of the governing equations can be found elsewhere (Li et al., 2017). The governing equations were discretized based on the finite-volume method, and the open-source framework, OpenFOAM (OpenFOAM, 2016) was employed to conduct the numerical study. The SIMPLE algorithm was used. The finite rate chemistry model and the GRI-Mech 3.0 mechanism (Smith et al., 2020) were also used to compute the chemical reactions. Previous studies on CO_2-diluted flames (Liu et al., 2003; Maruta et al., 2007; Xie et al., 2013; Li et al., 2014; Li et al., 2015) have shown satisfactory performance of the mechanism. The diffusion coefficient was calculated using the Maxwell–Stefan equations. The thermal diffusion effect was also included in the calculations. Mesh independence was confirmed by preliminary numerical computations. Grids with 136320 cells were used, and the finest grid size was 45 μm. The values of 1.0×10^{-6} and 1.0×10^{-8} were used as convergence criteria for the mass and energy conservation equations and chemical reactions, respectively. Radiation heat transfer from the gases was not included in the computation, since the present work primarily focuses on comparisons of the effects of the chemical reactions, third-body collisions, and transport properties of CO_2. A discussion on the radiation of CO_2 on non-premixed flames can be found elsewhere (Maruta et al., 2007).

Additional computations using three artificial species modified from CO_2 were conducted to analyze the effects of the chemical reactions, third-body reactions, and transport properties of CO_2 on the combustion characteristics of the laminar non-premixed jet flame. The properties of the artificial species are listed in **Table 1**. The first artificial species is KCO_2, which does not participate in chemical reactions but participates in third-body collisions and has thermal and transport properties identical to those of CO_2. The second artificial species is XCO_2, which has the same thermal and transport properties as CO_2 but does not participate in chemical reactions and third-body collisions. The third artificial species is DCO_2, which has the same chemical reactions, third-body effects, and thermal properties as CO_2 but transport properties (i.e., thermal conductivities, viscosities, diffusion coefficients,

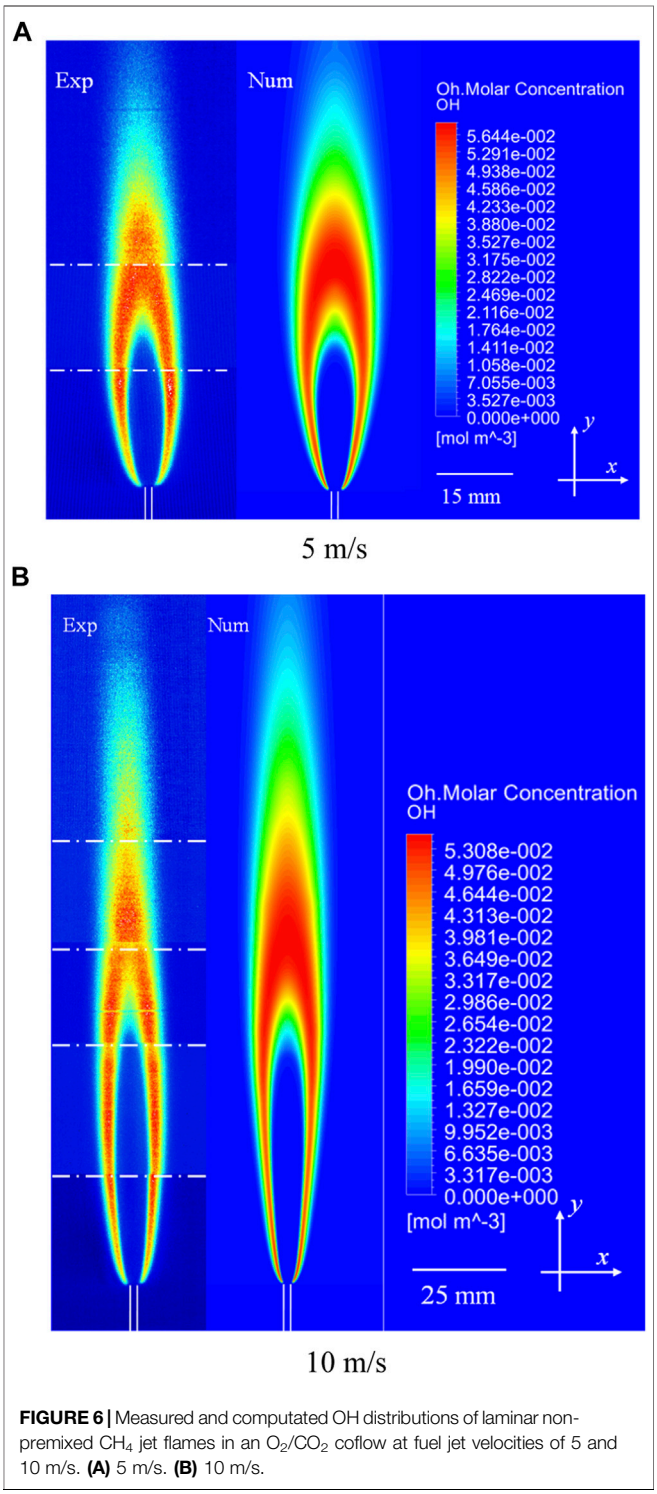

FIGURE 6 | Measured and computated OH distributions of laminar non-premixed CH_4 jet flames in an O_2/CO_2 coflow at fuel jet velocities of 5 and 10 m/s. **(A)** 5 m/s. **(B)** 10 m/s.

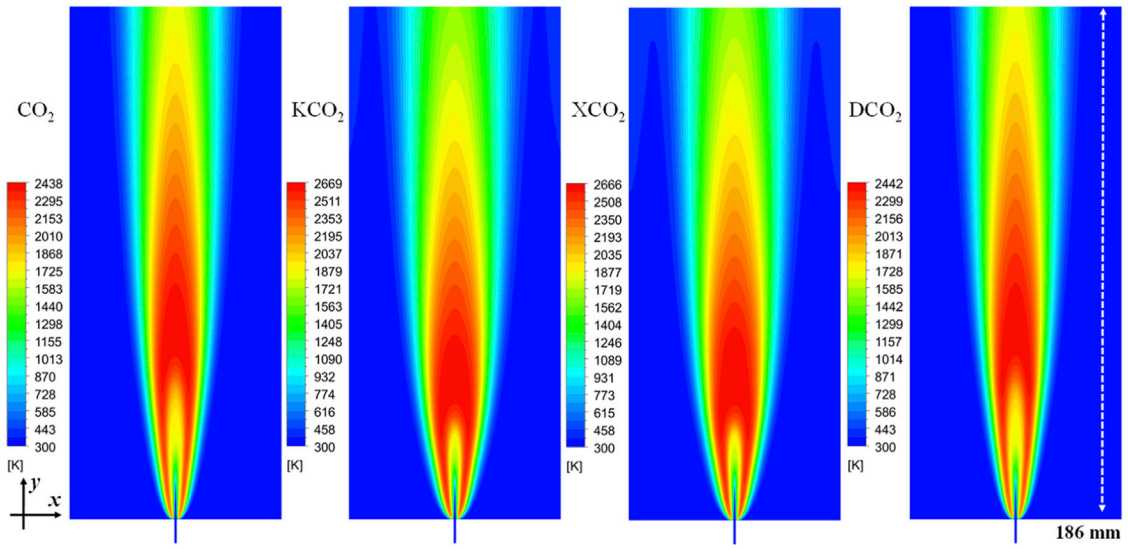

FIGURE 7 | Computational temperature distributions in flames in different oxidizers (V_F = 10 m/s).

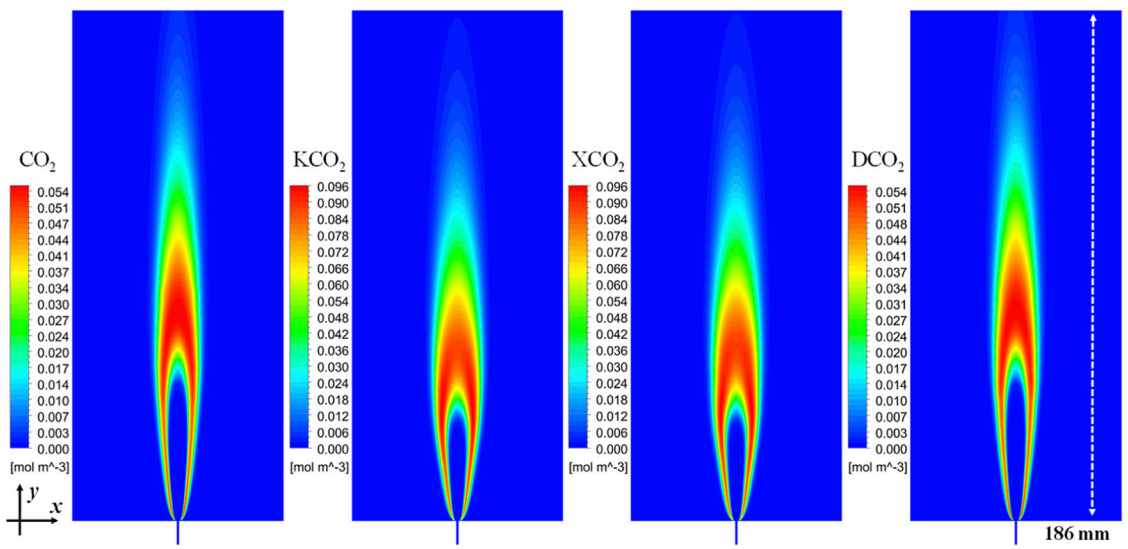

FIGURE 8 | Computational OH radical distributions in flames in different oxidizers (V_F = 10 m/s).

and thermal diffusion coefficients) identical to those of N_2. The participation or not of CO_2 in the chemical reactions can lead to differences in the computational results between the CO_2 and KCO_2 conditions. Differences in the combustion characteristics between KCO_2 and XCO_2 can be attributed to the third-body effects of CO_2. The effects of the transport properties of CO_2 on the jet flame can be attributed to differences in the computational results between the DCO_2 and CO_2 cases.

Validation of the Computational Method

The computational OH distributions of laminar non-premixed CH_4 jet flames at V_F = 5 and 10 m/s were compared with the experimental results, as shown in **Figure 6**. The total OH distributions in the flames at fuel jet velocities of 5 and 10 m/s consist of three and five parts, respectively. It can be seen that the shape and height determined from the computational OH distributions are consistent with the results obtained from the experiment. The small difference between the computational and experimental OH distributions may be attributed to two reasons: the laser sheet is not perfectly set at the center of the flame and is slightly inclined and the computational method assumes a two-dimensional physical model and neglects radiation heat loss. Despite minor differences can be observed between the measured and computational OH distributions, the

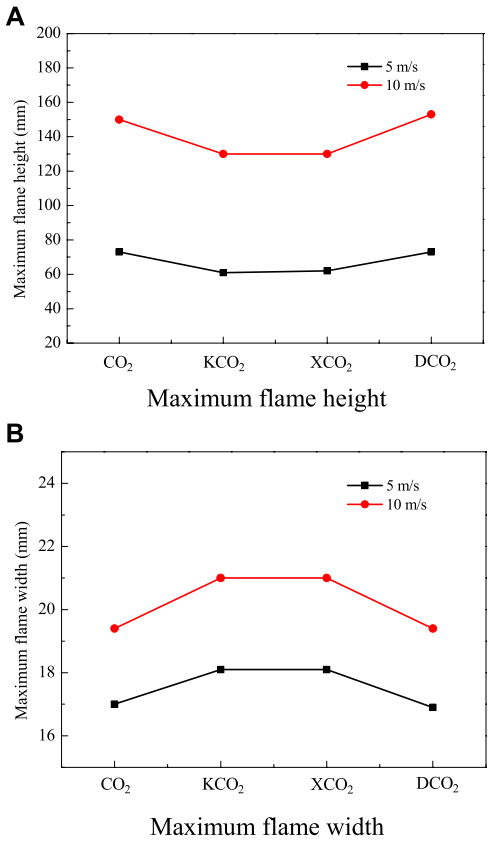

FIGURE 9 | Computational flame height and width based on OH distributions in laminar non-premixed CH_4 jet flames in different oxidizers. **(A)** Maximum flame height. **(B)** Maximum flame width.

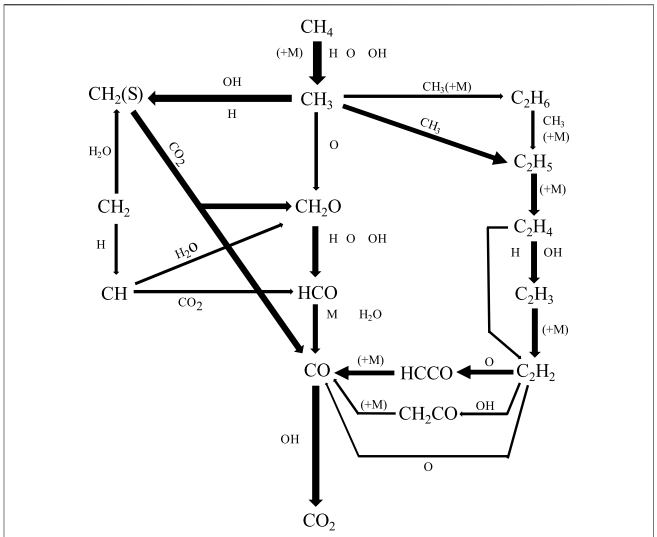

FIGURE 10 | Integral reaction flow in a laminar non-premixed CH_4 jet flame in an O_2/CO_2 coflow at V_F = 10 m/s (thick lines show the major reactions).

comparison of the overall results indicates that the present computational method and kinetic mechanism are reasonable for the study of the effects of CO_2 on the combustion characteristics of laminar non-premixed CH_4 jet flames in an O_2/CO_2 coflow with a high O_2 concentration.

Effects of CO_2 on Flame Temperature and Shape

The computational results of jet flames in O_2/CO_2, O_2/KCO_2, O_2/XCO_2, and O_2/DCO_2 coflows were obtained and compared. **Figures 7**, **8** respectively show the temperature and OH distributions in laminar non-premixed jet flames at V_F = 10 m/s. The flames in the O_2/CO_2 and O_2/DCO_2 coflows are nearly identical, and the flames in O_2/KCO_2 and O_2/XCO_2 coflows are almost the same. Comparison of flames in the O_2/KCO_2 and O_2/XCO_2 coflows indicates that the contribution of the third-body effects of CO_2 on the shape and temperature distribution of the laminar jet flame is insignificant. The results of flames in the O_2/CO_2 and O_2/DCO_2 coflows reveal that the difference in transport properties between CO_2 and N_2 also does not lead to a significant change in the flames. However, the difference between the flames in the O_2/CO_2 and O_2/KCO_2 coflows suggests that the flame shape and temperature distribution of laminar non-premixed jet flames are significantly changed by the chemical effects of CO_2. Specifically, the flame height is decreased, whereas the maximum flame width is increased, when the chemical effects of CO_2 are excluded from consideration. The decrease in the maximum flame temperature by the chemical effect of CO_2 is approximately 230 K.

The detailed computational results of laminar non-premixed CH_4 jet flames in O_2/CO_2, O_2/KCO_2, O_2/XCO_2, and O_2/DCO_2 coflows at a fuel flow velocities of 5 and 10 m/s were analyzed. The flame heights and widths based on the OH distribution in flames in different oxidizers at V_F = 5 and 10 m/s are illustrated in **Figures 9A,B**, respectively. The flame boundaries are judged by 99% decrease of the maximum OH molar concentration. The variations in the flame height and width of laminar non-premixed CH_4 jet flames at V_F = 5 m/s in different oxidizer coflows are similar to those of flames at V_F = 10 m/s. Although not shown here, the numerical results indicate that the maximum flame temperatures at V_F = 5 m/s in O_2/CO_2 and O_2/DCO_2 are nearly identical, i.e., 2470 K, and the maximum flame temperatures in O_2/KCO_2 and O_2/XCO_2 are similar, i.e., approximately 2670 K. The computational OH distributions show that flame height decreases, whereas flame width increases, when the chemical effect of CO_2 is suspended.

Mechanism of CO_2 on the Laminar Non-Premixed CH_4 Jet Flames

The reaction pathways and flame structures in O_2/CO_2, O_2/KCO_2, O_2/XCO_2 and O_2/DCO_2 were analyzed to interpret the mechanism of the chemical effect of CO_2 on laminar non-premixed CH_4 jet flames. The primary reaction pathways of flames in the O_2/KCO_2, O_2/XCO_2, and O_2/DCO_2 coflows are nearly identical to those of flames in the O_2/CO_2 coflow.

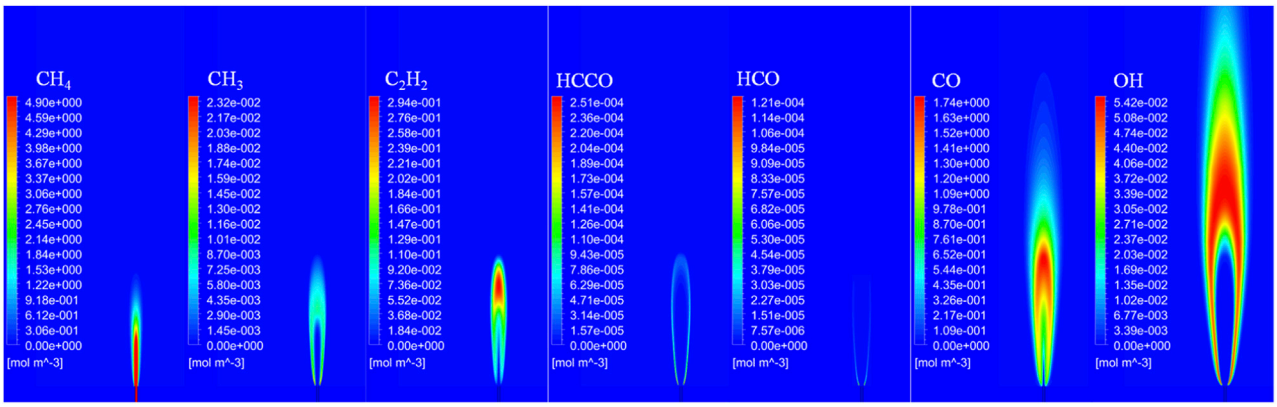

FIGURE 11 | Molar concentrations of important species in a laminar non-premixed CH_4 jet flame in an O_2/CO_2 coflow (V_F = 10 m/s).

Figure 10 shows the global reaction pathways of laminar non-premixed flames in the O_2/CO_2 coflow at V_F = 10 m/s. CH_4 is transformed into CH_3 through H abstraction by H, O, and OH. Most of the CH_3 radicals are transformed into C_2H_5, $CH_2(S)$, and C_2H_6, and only a small amount of the CH_3 radicals react with O atoms to produce CH_2O. Most of the C_2H_6 generated is transformed into C_2H_5 through third-body reactions. C_2H_5 radicals decompose rapidly into C_2H_4, and H abstraction by H and OH, which are important sources of C_2H_4 consumption, produces C_2H_3 radicals. The reaction $C_2H_3(+M) = C_2H_2 + H (+M)$ consumes C_2H_3 radicals to produce C_2H_2. Most of the C_2H_2 is consumed by reaction with O to produce HCCO. The HCCO radicals generate CH and CO via the third-body reaction $HCCO(+M) = CH + CO(+M)$. Finally, CO is oxidized to CO_2 by the reaction $OH + CO = H + CO_2$.

Figure 11 shows the distribution of important species in a laminar non-premixed jet flame in an O_2/CO_2 environment at V_F = 10 m/s. The CH_4-rich region can be observed near the exit of the tube, and the CH_3-rich region can be observed around the region with a high CH_4 concentration. The C_2H_2-rich concentration region is located at nearly the same area as the CH_3-rich region. The HCCO is found on the margins of the C_2H_2-rich region, and theHCO only exists at the two sides of the CH_3-rich region. The molar concentration of the HCCO is higher than that of the HCO. The CO-rich region is located downstream of the HCCO-rich region.

The analysis of the computational results of flames in the O_2/KCO_2, O_2/XCO_2, and O_2/DCO_2 coflows shows that the distributions of important species are similar to those of flames in O_2/CO_2. Moreover, laminar non-premixed CH_4 jet flames in different oxidizers can be divided into two parts based on the global oxidation process. The results of flames in the O_2/CO_2 coflow at V_F = 10 m/s are illustrated in **Figure 12**; here, the white dotted line indicates the boundary between the first and second parts of the flame. The first part of the flame includes the oxidation process from CH_4 to CO through the reaction pathway $CH_4 \rightarrow CH_3 \rightarrow C_2H_6 \rightarrow C_2H_5 \rightarrow C_2H_4 \rightarrow C_2H_3 \rightarrow C_2H_2 \rightarrow HCCO \rightarrow CO$, while the primary reaction in the second part is the oxidation of CO to CO_2. Consequently, the top of the HCCO

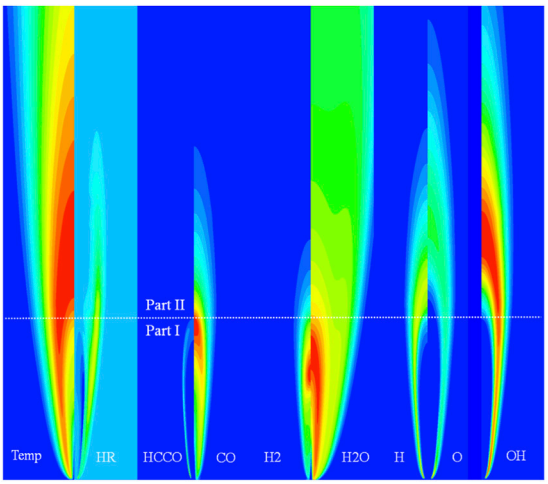

FIGURE 12 | The structure of the laminar non-premixed CH_4 jet flame (V_F = 10 m/s) in an O_2/CO_2 coflow. (Temp: temperature; HR: heat of reaction).

region is used as the boundary separating the first and second parts of the flame. Generation of H_2 and H_2O is mainly completed in the first part of the flame. The distribution of the heats of reaction indicates that the first and second parts of the flame make remarkable contributions to heat generation. A distinct endothermic region is located in the first part of the flame. The effects of CO_2 on the first and second typical parts of non-premixed laminar jet flames result in different combustion characteristics.

The distributions of important species of flames in the O_2/CO_2 and O_2/KCO_2 coflows were compared to enable interpretation of the chemical effect of CO_2 on the laminar non-premixed CH_4 jet flame, since the effect of third-body collisions with CO_2 on the laminar non-premixed jet flame has been confirmed to be negligible. The distributions of the molar concentrations of HCCO, CO, O, and H in the flames in O_2/CO_2 and O_2/KCO_2 coflows are shown in **Figures 13A–D**. The heights of the HCCO-, CO-, O-, and H-rich regions in the flame in the O_2/KCO_2 coflow

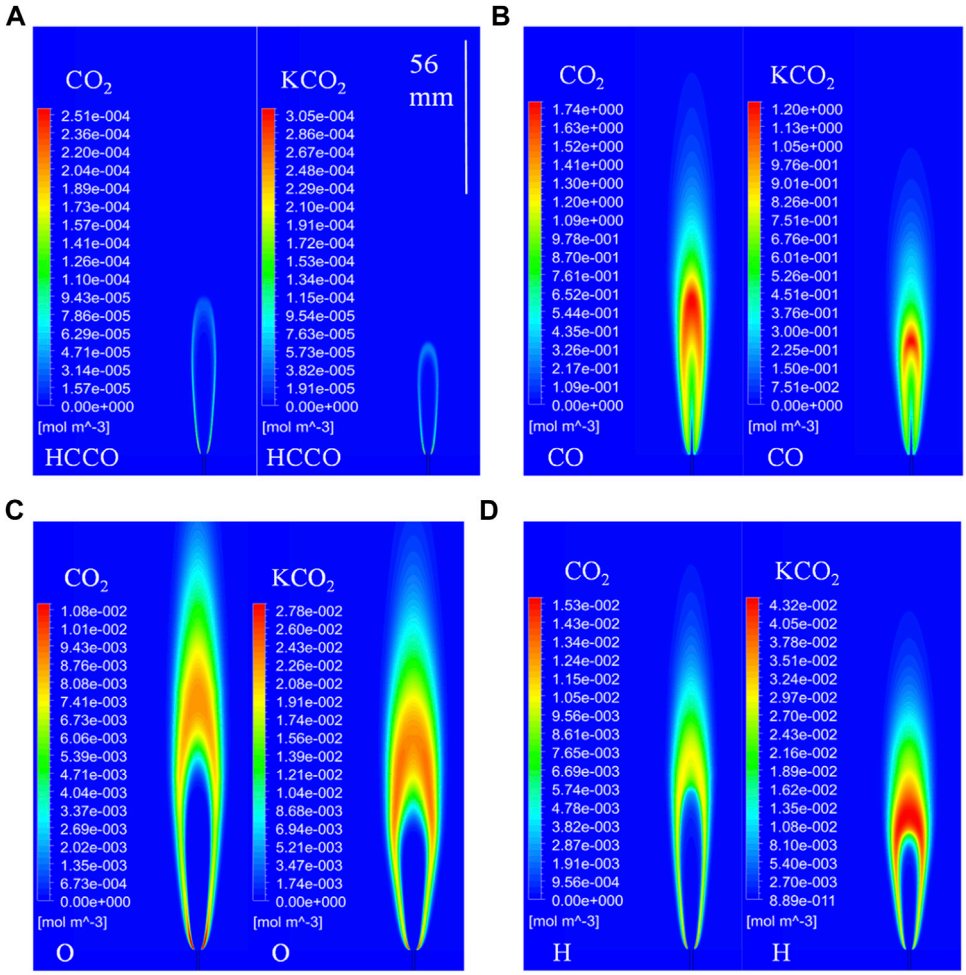

FIGURE 13 | Distributions of the molar concentration of important species in flames in O_2/CO_2 and O_2/KCO_2: **(A)** HCCO, **(B)** CO, **(C)** O, and **(D)** H.

are shorter than those in the flame in the O_2/CO_2 coflow. Interestingly, the difference between the heights of the HCCO-rich region in the flames in the O_2/CO_2 and O_2/KCO_2 coflows is nearly identical to that between the heights of the OH-rich regions (as shown in **Figure 8**). The difference between the flame heights based on the OH distribution is related to differences in HCCO distribution in the first part of the flame. The analysis of the reaction pathways shows that HCCO is primarily produced by the reaction $O + C_2H_2 = H + HCCO$. As O atoms are mainly generated by the reaction $H + O_2 = O + OH$, the flame height essentially depends on the H distribution. The contours of the H molar concentration shown in **Figure 13D** indicate that the concentration of H atoms of the flame in O_2/KCO_2 is significantly higher than that of the flame in O_2/CO_2. Pathway analysis of the entire flame region shows that the reaction $OH + CO = H + CO_2$ is an important source of H atoms. This finding suggests that the chemical effect of CO_2 on H formation and distribution ultimately leads to a difference in flame heights.

The results shown in **Figure 12** indicate that the high-temperature region and the OH-rich region are coincident, this finding can also be observed from the results shown in **Figures 7**, **8**. This phenomena is attributed to the fact that the high-temperature region is located in the second part of the laminar non-premixed flame, where the reaction $OH + CO = H + CO_2$ is the primary exothermic reaction. The results shown in **Figure 7** indicate that the maximum temperature of the laminar non-premixed flame in the O_2/CO_2 coflow is approximately 230 K lower than that of the flame in the O_2/KCO_2 coflow. Although not shown here, analysis of the computational results shows that the net reaction rates of $OH + CO = H + CO_2$ and $H + O_2 = O + OH$ of the flame in the O_2/CO_2 coflow are lower than those of the flame in the O_2/KCO_2 coflow. The net reaction rate of $OH + CO = H + CO_2$ in the second part of the flame is significantly reduced by the chemical effect of CO_2, which results in a low flame temperature.

CONCLUSION

The heights of the laminar CH_4 jet flames in O_2/CO_2 coflows with different oxygen mole fractions of 0.30, 0.35 and 0.40 were obtained by experimental study. The height of the flame in

O_2/CO_2 coflow decreases as the increase of oxygen mole fraction. And the height of the laminar CH_4 jet flame in O_2/CO_2 coflow with oxygen mole fraction of 0.30 is shorter than that of the laminar CH_4 jet flame in air. Moreover, the luminosity of the CH_4 jet flame in O_2/CO_2 coflow is totally different from that of the flame in air stream.

The chemical reactions, third-body effects, and transport properties of CO_2 on the combustion characteristics of a laminar non-premixed CH_4 jet flame in an O_2/CO_2 coflow with a high O_2 concentration (X_O = 0.35) were investigated using a two-dimensional numerical computational method with a detailed kinetic mechanism. The computational OH distributions showed good consistency with the results obtained from the experiments. Whereas the third-body effect and transport properties of CO_2 do not exert remarkable effects on the laminar non-premixed flame, the chemical effect of CO_2 on the laminar non-premixed jet flame is significant. The chemical effect of CO_2 increases the flame height but decreases the maximum flame temperature. The primary oxidation pathway in the jet flame is $CH_4 \rightarrow CH_3 \rightarrow C_2H_6 \rightarrow C_2H_5 \rightarrow C_2H_4 \rightarrow C_2H_3 \rightarrow C_2H_2 \rightarrow HCCO \rightarrow CO \rightarrow CO_2$. The CH_4 non-premixed laminar jet flame can be divided into two parts based on the global oxidization process; here, the top of the HCCO-rich region is the boundary between these parts. The decrease in the concentration of O atoms by the chemical effect of CO_2 in the first part of the flame can explain the observed decrease in flame height, and the inhibitory effect of CO_2 on the reaction rate of OH + CO = H + CO_2 in the second part of the flame induces a decrease in maximum flame temperature.

DATA AVAILABILITY STATEMENT

The original contributions presented in the study are included in the article/supplementary material, further inquiries can be directed to the corresponding author.

AUTHOR CONTRIBUTIONS

FZ: Laser diagnostic, Data analysis, Reviewing and editing. XL: Conceptualization, Supervision, Methodology, Investigation, Reviewing and editing, Funding acquisition. SX: Data Curation, Reviewing and editing. JW: Data Curation, Reviewing and editing. XW: Reviewing and editing.

FUNDING

The supports of National Natural Science Foundation of China (No. 52176139) and the DNL Cooperation Fund, CAS (DNL202006) are gratefully acknowledged.

REFERENCES

Buhre, B. J. P., Elliott, L. K., Sheng, C. D., Gupta, R. P., and Wall, T. F. (2005). Oxy-fuel Combustion Technology for Coal-Fired Power Generation. *Prog. Energ. Combustion Sci.* 31, 283–307. doi:10.1016/j.pecs.2005.07.001

Bürkle, S., Dreizler, A., Ebert, V., and Wagner, S. (2018). Experimental Comparison of a 2D Laminar Diffusion Flame under Oxy-Fuel and Air Atmosphere. *Fuel* 212, 302–308. doi:10.1016/j.fuel.2017.10.067

Chen, L., Yong, S. Z., and Ghoniem, A. F. (2012). Oxy-fuel Combustion of Pulverized Coal: Characterization, Fundamentals, Stabilization and CFD Modeling. *Prog. Energ. Combustion Sci.* 38, 156–214. doi:10.1016/j.pecs.2011.09.003

Dhaneswar, S. R., and Pisupati, S. V. (2012). Oxy-fuel Combustion: The Effect of Coal Rank and the Role of char-CO2 Reaction. *Fuel Process. Technol.* 102, 156–165. doi:10.1016/j.fuproc.2012.04.029

Ge, X., Dong, J., Fan, H., Zhang, Z., Shang, X., Hu, X., et al. (2017). Numerical Investigation of Oxy-Fuel Combustion in 700°C-Ultra-Supercritical Boiler. *Fuel* 207, 602–614. doi:10.1016/j.fuel.2017.06.119

Giménez-López, J., Millera, A., Bilbao, R., and Alzueta, M. U. (2015). Experimental and Kinetic Modeling Study of the Oxy-Fuel Oxidation of Natural Gas, CH_4 and C_2H_6. *Fuel* 160, 404–412. doi:10.1016/j.fuel.2015.07.087

Gładysz, P., Stanek, W., Czarnowska, L., Sładek, S., and Szlęk, A. (2018). Thermo-ecological Evaluation of an Integrated MILD Oxy-Fuel Combustion Power Plant with CO_2 Capture, Utilisation, and Storage – A Case Study in Poland. *Energy* 144, 379–392. doi:10.1016/j.energy.2017.11.133

Glarborg, P., and Bentzen, L. L. B. (2008). Chemical Effects of a High CO_2 Concentration in Oxy-Fuel Combustion of Methane. *Energy Fuels* 22, 291–296. doi:10.1021/ef7005854

Hjärtstam, S., Andersson, K., Johnsson, F., and Leckner, B. (2009). Combustion Characteristics of lignite-fired Oxy-Fuel Flames. *Fuel* 88, 2216–2224. doi:10.1016/j.fuel.2009.05.011

Kobayashi, H., Hagiwara, H., Kaneko, H., and Ogami, Y. (2007). Effects of CO_2 Dilution on Turbulent Premixed Flames at High Pressure and High Temperature. *Proc. Combust. Inst.* 31, 1451–1458. doi:10.1016/j.proci.2006.07.159

Kobayashi, H., Yata, S., Ichikawa, Y., and Ogami, Y. (2009). Dilution Effects of Superheated Water Vapor on Turbulent Premixed Flames at High Pressure and High Temperature. *Proc. Combust. Inst.* 32, 2607–2614. doi:10.1016/j.proci.2008.05.078

Li, P., Dally, B. B., Mi, J., and Wang, F. (2013). MILD Oxy-Combustion of Gaseous Fuels in a Laboratory-Scale Furnace. *Combust. Flame* 160, 933–946. doi:10.1016/j.combustflame.2013.01.024

Li, X., Jia, L., Nakamura, H., Tezuka, T., Hasegawa, S., and Maruta, K. (2015). Study on Flame Responses and Ignition Characteristics of $CH_4/O_2/CO_2$ Mixture in a Micro Flow Reactor with a Controlled Temperature Profile. *Appl. Therm. Eng.* 84, 360–367. doi:10.1016/j.applthermaleng.2015.03.022

Li, X., Jia, L., Onishi, T., Grajetzki, P., Nakamura, H., Tezuka, T., et al. (2014). Study on Stretch Extinction Limits of CH_4/CO_2 versus High Temperature O_2/CO_2 Counterflow Non-premixed Flames. *Combust. Flame* 161, 1526–1536. doi:10.1016/j.combustflame.2013.12.004

Li, X., Yang, H., Jiang, L., Wang, X., and Zhao, D. (2016). Stretch Extinction Characteristics of CH_4/CO_2 versus $O_2/H_2O/CO_2$ and O_2/H_2O Counterflow Non-premixed Flames at Different Oxidizer Temperatures. *Fuel* 186, 648–655. doi:10.1016/j.fuel.2016.09.017

Li, X., Zhang, J., Yang, H., Jiang, L., Wang, X., and Zhao, D. (2017). Combustion Characteristics of Non-premixed Methane Micro-jet Flame in Coflow Air and thermal Interaction between Flame and Micro Tube. *Appl. Therm. Eng.* 112, 296–303. doi:10.1016/j.applthermaleng.2016.10.082

Liu, D., Wall, T., and Stanger, R. (2016). CO_2 Quality Control in Oxy-Fuel Technology for CCS: SO_2 Removal by the Caustic Scrubber in Callide Oxy-Fuel Project. *Int. J. Greenhouse Gas Control.* 51, 207–217. doi:10.1016/j.ijggc.2016.05.026

Liu, F., Guo, H., and Smallwood, G. J. (2003). The Chemical Effect of CO_2 Replacement of N_2 in Air on the Burning Velocity of CH_4 and H_2 Premixed Flames. *Combust. Flame* 133, 495–497. doi:10.1016/s0010-2180(03)00019-1

Luo, W., Wang, Q., Huang, X., Liu, Z., and Zheng, C. (2015). Dynamic Simulation and Transient Analysis of a 3MWth Oxy-Fuel Combustion System. *Int. J. Greenhouse Gas Control.* 35, 138–149. doi:10.1016/j.ijggc.2015.02.003

Mao, Z., Zhang, L., Zhu, X., and Zheng, C. (2017). Experiment Investigation of Coal MILD-Oxy Combustion Integrated with Flue Gas Recirculation at a 0.3MWth Furnace. *Fuel Process. Technol.* 162, 126–134. doi:10.1016/j.fuproc.2017.04.002

Mardani, A., and Fazlollahi Ghomshi, A. (2016). Numerical Study of Oxy-Fuel MILD (Moderate or Intense Low-Oxygen Dilution Combustion) Combustion for CH_4–H_2 Fuel. *Energy* 99, 136–151. doi:10.1016/j.energy.2016.01.016

Maruta, K., Abe, K., Hasegawa, S., Maruyama, S., and Sato, J. (2007). Extinction Characteristics of CH_4/CO_2 versus O_2/CO_2 Counterflow Non-premixed Flames at Elevated Pressures up to 0.7MPa. *Proc. Combust. Inst.* 31, 1223–1230. doi:10.1016/j.proci.2006.08.013

Menage, D., Lemaire, R., and Seers, P. (2018). Experimental Study and Chemical Reactor Network Modeling of the High Heating Rate Devolatilization and Oxidation of Pulverized Bituminous Coals under Air, Oxygen-Enriched Combustion (OEC) and Oxy-Fuel Combustion (OFC). *Fuel Process. Technol.* 177, 179–193. doi:10.1016/j.fuproc.2018.04.025

Moroń, W., and Rybak, W. (2015). Ignition Behaviour and Flame Stability of Different Ranks Coals in Oxy Fuel Atmosphere. *Fuel* 161, 174–181. doi:10.1016/j.fuel.2015.08.065

Oh, J., and Hong, S. (2016). Oxygen Temperature Variation of a Non-premixed Oxy-Methane Flame in a Lab-Scale Slot Burner. *Appl. Therm. Eng.* 104, 804–817. doi:10.1016/j.applthermaleng.2016.05.112

Oh, J., and Noh, D. (2015). Flame Characteristics of a Non-premixed Oxy-Fuel Jet in a Lab-Scale Furnace. *Energy* 81, 328–343. doi:10.1016/j.energy.2014.12.046

Oh, J., Noh, D., and Ko, C. (2013). The Effect of Hydrogen Addition on the Flame Behavior of a Non-premixed Oxy-Methane Jet in a Lab-Scale Furnace. *Energy* 62, 362–369. doi:10.1016/j.energy.2013.09.049

Oh, J., Noh, D., and Lee, E. (2013). The Effect of CO Addition on the Flame Behavior of a Non-premixed Oxy-Methane Jet in a Lab-Scale Furnace. *Appl. Energ.* 112, 350–357. doi:10.1016/j.apenergy.2013.06.033

Oh, J., and Noh, D. (2013). Lifted Flame Behavior of a Non-premixed Oxy-Methane Jet in a Lab-Scale Slot Burner. *Fuel* 103, 862–868. doi:10.1016/j.fuel.2012.09.055

Oh, J., and Noh, D. (2014). The Effect of CO_2 Addition on the Flame Behavior of a Non-premixed Oxy-Methane Jet in a Lab-Scale Furnace. *Fuel* 117, 79–86. doi:10.1016/j.fuel.2013.08.065

OpenFOAM The Open Source CFD Toolbox. 2016 Available at: http://www.openfoam.org.

Rathnam, R. K., Elliott, L. K., Wall, T. F., Liu, Y., and Moghtaderi, B. (2009). Differences in Reactivity of Pulverised Coal in Air (O2/N2) and Oxy-Fuel (O2/CO2) Conditions. *Fuel Process. Technol.* 90, 797–802. doi:10.1016/j.fuproc.2009.02.009

Roper, F. G., Smith, C., and Cunningham, A. C. (1977). The Prediction of Laminar Jet Diffusion Flame Sizes: Part II. Experimental Verification. *Combust. Flame* 29, 227–234. doi:10.1016/0010-2180(77)90113-4

Roper, F. G. (1977). The Prediction of Laminar Jet Diffusion Flame Sizes: Part I.Theoretical Model. *Combust. Flame.* 29, 219–226. doi:10.1016/0010-2180(77)90112-2

Scheffknecht, G., Al-Makhadmeh, L., Schnell, U., and Maier, J. (2011). Oxy-fuel Coal Combustion-A Review of the Current State-Of-The-Art. *Int. J. Greenhouse Gas Control.* 5, S16–S35. doi:10.1016/j.ijggc.2011.05.020

Seddighi, S. (2017). Design of Large Scale Oxy-Fuel Fluidized Bed Boilers: Constant thermal Power and Constant Furnace Size Scenarios. *Energy* 118, 1286–1294. doi:10.1016/j.energy.2016.11.004

Seepana, S., and Jayanti, S. (2012). Experimental Studies of Flame Extinction in a Swirl-Stabilized Oxy-Fuel Burner. *Fuel* 93, 75–81. doi:10.1016/j.fuel.2011.10.065

Seepana, S., and Jayanti, S. (2012). Flame Structure Investigations of Oxy-Fuel Combustion. *Fuel* 93, 52–58. doi:10.1016/j.fuel.2011.07.033

Smith, G. P., Golden, D. M., Frenklach, M., Moriarty, N. W., Eiteneer, B., Goldenberg, M., et al. 2020 Berkeley Mechanical Engineering. Available at: http://www.me.berkeley.edu/gri_mech/.

Taniguchi, M., Yamamoto, K., Okazaki, T., Rehfeldt, S., and Kuhr, C. (2011). Application of Lean Flammability Limit Study and Large Eddy Simulation to Burner Development for an Oxy-Fuel Combustion System. *Int. J. Greenhouse Gas Control.* 5, S111–S119. doi:10.1016/j.ijggc.2011.05.008

Tu, Y., Liu, H., Chen, S., Liu, Z., Zhao, H., and Zheng, C. (2015). Numerical Study of Combustion Characteristics for Pulverized Coal under Oxy-MILD Operation. *Fuel Process. Technol.* 135, 80–90. doi:10.1016/j.fuproc.2014.10.025

Tu, Y., Liu, H., and Yang, W. (2017). Flame Characteristics of CH4/H2 on a Jet-In-Hot-Coflow Burner Diluted by N_2, CO_2, and H_2O. *Energy Fuels* 31, 3270–3280. doi:10.1021/acs.energyfuels.6b03246

Tu, Y., Su, K., Liu, H., Chen, S., Liu, Z., and Zheng, C. (2016). Physical and Chemical Effects of CO_2 Addition on CH_4/H_2 Flames on a Jet in Hot Coflow (JHC) Burner. *Energy Fuels* 30, 1390–1399. doi:10.1021/acs.energyfuels.5b02499

Wall, T. F. (2007). Combustion Processes for Carbon Capture. *Proc. Combustion Inst.* 31, 31–47. doi:10.1016/j.proci.2006.08.123

Wang, J., Matsuno, F., Okuyama, M., Ogami, Y., Kobayashi, H., and Huang, Z. (2013). Flame Front Characteristics of Turbulent Premixed Flames Diluted with CO_2 and H_2O at High Pressure and High Temperature. *Proc. Combust. Inst.* 34, 1429–1436. doi:10.1016/j.proci.2012.06.154

Watanabe, H., Shanbhogue, S. J., Taamallah, S., Chakroun, N. W., and Ghoniem, A. F. (2016). The Structure of Swirl-Stabilized Turbulent Premixed CH_4/air and $CH_4/O_2/CO_2$ Flames and Mechanisms of Intense Burning of Oxy-Flames. *Combust. Flame.* 174, 111–119. doi:10.1016/j.combustflame.2016.09.015

Xie, Y., Wang, J., Zhang, M., Gong, J., Jin, W., and Huang, Z. (2013). Experimental and Numerical Study on Laminar Flame Characteristics of Methane Oxy-Fuel Mixtures Highly Diluted with CO_2. *Energy Fuels* 27, 6231–6237. doi:10.1021/ef401220h

Xu, H., Liu, F., Sun, S., Zhao, Y., Meng, S., and Tang, W. (2017). Effects of H_2O and CO_2 Diluted Oxidizer on the Structure and Shape of Laminar Coflow Syngas Diffusion Flames. *Combust. Flame* 177, 67–78. doi:10.1016/j.combustflame.2016.12.001

Yamamoto, K., Ozeki, M., Hayashi, N., and Yamashita, H. (2009). Burning Velocity and OH Concentration in Premixed Combustion. *Proc. Combust. Inst.* 32, 1227–1235. doi:10.1016/j.proci.2008.06.077

Yin, C., Rosendahl, L. A., and Kær, S. K. (2011). Chemistry and Radiation in Oxy-Fuel Combustion: A Computational Fluid Dynamics Modeling Study. *Fuel* 90, 2519–2529. doi:10.1016/j.fuel.2011.03.023

Zhang, Z., Li, X., Luo, C., Zhang, L., Xu, Y., Wu, Y., et al. (2018). Investigation on the Thermodynamic Calculation of a 35 MWth Oxy-Fuel Combustion Coal-Fired Boiler. *Int. J. Green. Gas Control.* 71, 36–45. doi:10.1016/j.ijggc.2018.02.004

Conflict of Interest: The authors declare that the research was conducted in the absence of any commercial or financial relationships that could be construed as a potential conflict of interest.

Publisher's Note: All claims expressed in this article are solely those of the authors and do not necessarily represent those of their affiliated organizations, or those of the publisher, the editors, and the reviewers. Any product that may be evaluated in this article, or claim that may be made by its manufacturer, is not guaranteed or endorsed by the publisher.

frontiers in Energy Research

ORIGINAL RESEARCH
published: 23 February 2022
doi: 10.3389/fenrg.2022.828167

Numerical Investigations of Injection Timing Effects on a Gasoline Direct Injection Engine Performance: Part A, In-Cylinder Combustion Process

Yuchao Yan[1], *Ruomiao Yang*[1], *Xiaoxia Sun*[2], *Ruijie Li*[3] *and Zhentao Liu*[1]*

[1]Power Machinery and Vehicular Engineering Institute, Zhejiang University, Hangzhou, China, [2]Beijing Power Machinery Research Institute, Beijing, China, [3]Technical Institute of Physics and Chemistry, Chinese Academy of Sciences, Beijing, China

Gasoline direct injection (GDI) engine are widely adopted in the automobile industry since its advantage in the fuel economy. Injection Timing (IT) is an important parameter for the GDI engine, having a great impact on the spray atomization, mixture evenness, combustion characteristics, and therefore performance of the GDI engine. With the motive of IT optimization, a three-dimensional CFD model of a single cylinder 4-stroke spark ignition GDI engine with bore of 84 mm and compression ratio of 10.3 was utilized to analyze the detailed process at different IT (270, 280, 290, 300-degree CA BTDC), while the other conditions were invariant like rotate speed at 2000 RPM. The spray, turbulence, G-equation combustion were included. The result indicated that delayed IT tended to reduce drop-wall impingement significantly but still intensified unevenness of mixture concertation severely, resulting in fuel-rich region appeared around cylinder. Because the duration available for mixing was shortened, which dominantly intensified the unevenness of the mixture. The combustion was deteriorated as the IT delayed because the excessive equivalence ratio region severely slowed flame propagation and frozen at the most uneven region, which finally degraded thermal efficiency and engine performance. In conclusion, this paper demonstrated the whole process from injection to combustion, revealing that droplet-wall impingement and available duration for mixing are dominant trade-off factors for mixture formation and following combustion process, as the IT changes.

Keywords: GDI engine, injection timing, in-cylinder combustion, CFD, mixture formation

OPEN ACCESS

Edited by:
Jun Li,
Guangzhou Institute of Energy Conversion (CAS), China

Reviewed by:
Sheng Huang,
East China University of Science and Technology, China
Hua Xiao,
Guangzhou Maritime College, China
Haifeng Liu,
Tianjin University, China

****Correspondence:***
Zhentao Liu
liuzt@zju.edu.cn

Specialty section:
This article was submitted to Advanced Clean Fuel Technologies, a section of the journal Frontiers in Energy Research

Received: *03 December 2021*
Accepted: *13 January 2022*
Published: *23 February 2022*

Citation:
Yan Y, Yang R, Sun X, Li R and Liu Z (2022) Numerical Investigations of Injection Timing Effects on a Gasoline Direct Injection Engine Performance: Part A, In-Cylinder Combustion Process. Front. Energy Res. 10:828167. doi: 10.3389/fenrg.2022.828167

INTRODUCTION

As acknowledged the Paris Agreement sets out arrangements for global action to address climate change after 2020 (Liobikienė and Butkus, 2017). Its long-term goal is to limit the increase in global average temperature to less than 2 degrees Celsius compared to the pre-industrial period and to work towards limiting temperature increases to less than 1.5 degrees Celsius (Huang et al., 2021).

Abbreviations: 3D, three-dimensional; ATDC, after top dead center; BTDC, before top dead center; CAD, crank angle degree; CFD, computational fluid dynamics; CHRR, chemical heat release rate; GDI, gasoline direct injection; GPI, gasoline port injection; ICE, internal combustion engine; IT, injection timing.

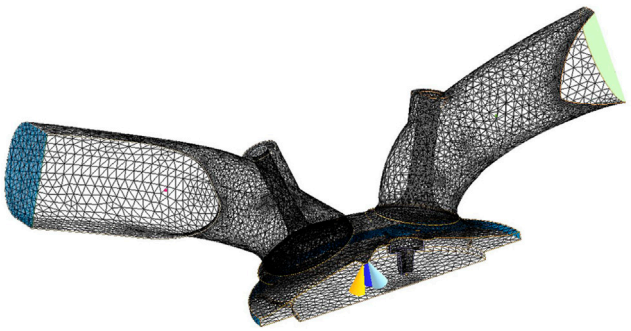

FIGURE 1 | Three-dimensional grid of the GDI engine at top dead center.

TABLE 1 | Engine specifications.

Engine type	Single cylinder
Cycle	4-stroke SI GDI
Valve per cylinder	4
Cylinder bore [mm]	84
Piston stroke [mm]	90
Displacement [L]	2.0
Connecting rod length [mm]	14.43
Compression ratio	10.3:1
Nozzle numbers	3
Nozzle diameter [μm]	300
Intake valve open	50 CAD BTDC exhaust
Intake valve close	143 CAD BTDC compression
Exhaust valve open	145 CAD ATDC compression
Exhaust valve close	58 CAD ATDC exhaust

TABLE 2 | Simulated operating conditions at various injection timings.

Injection type	Pulsed
Start of injection (SOI)	270, 280, 290, 300 CAD BTDC compression
Inflow droplet temperature [K]	400
Inlet pressure [Mpa]	0.08
Outlet pressure [Mpa]	0.1
Mean cone angle [deg]	14
Injection duration [CAD]	18.4
Total injected mass [mg]	27
Engine speed [r/min]	2000
Spark timing	15 CAD BTDC compression

TABLE 3 | Computational models.

Turbulence model	Realizable k-ε model
Nozzle flow model	Solid-cone model
Droplet collision and coalescence Model	O'Rourke model
Wall film model	O'Rourke and Amsden model
Droplet breakup model	RT/KH hybrid breakup model
Turbulence flame propagation model	G-equation and DPIK model

The transportation sector accounts for a large share of the problem of greenhouse emissions (Fridstrøm, 2017; Liu et al., 2022). While the trend towards switching to electric vehicles is clear, internal combustion engines will continue to play an important and irreplaceable role in the transportation industry in the next decades (Gasbarro et al., 2019; Stocchi et al., 2019). However, it also brings about the energy crisis and environmental problems caused by millions of vehicles powered with internal combustion engines (Ambrogi et al., 2019; Liu and Wang, 2022). Moreover, the government proposed a series of requirements and standards (China Phase VI) to restrict emissions for improving energy efficiency and beautifying the environment (Liu et al., 2018a; Liu and Liu, 2021a). The rules are much more stringent than the previous ones and are moving towards higher standards in the foreseeable future (Fennell et al., 2014; Potenza et al., 2019). Strict regulations for exhaust gas emissions and the need to improve fuel efficiency have promoted the development of GDI technology due to its high horsepower output and better fuel economy (Storey et al., 2014; Zhang et al., 2020). Therefore, a lot of researchers have investigated various related technologies to improve GDI engine performance and reduce emissions (Zhang et al., 2017; Feng et al., 2021). It is generally accepted that injection strategies have a great impact on the formation of homogeneous gas mixture and in-cylinder combustion processes (Splitter et al., 2017; Zhu et al., 2018). Various injection methods are investigated to improve GDI performance. Kim et al. (2018) investigated the effects of fuel injection timings on combustion and emission characteristics of a direct-injection spark-ignition gasoline engine with a 50 MPa fuel injection system. The results indicated that when the injection pressure is up to 50 MPa and the injection timing is late, the thermal efficiency can be improved without reducing exhaust gas emissions. Zhuang et al. (2019) studied the effect of ethanol direct injection plus gasoline port injection (EDI + GPI) on engine performance. To further understand the experimental results, CFD simulations were performed. And the results can be a reference for understanding the combustion process based on EDI + GDI. Zhang et al. (2018) investigated the effects of control parameters (spark advance, injection pressure, excess air ratio, and EGR) on the combustion, performance and emissions of a GDI engine. The results indicated that the most important factor affecting NOx emissions and BSFC is the EGR mode. Injection timing has the highest level of contribution to PN emissions, especially in lean combustion conditions. Miganakallu et al. (2020) studied the impact of water-methanol injection on the GDI engines. Different performance indicators were used to evaluate the engine efficiency with water-methanol blends, pure water or pure methanol. Marseglia et al. (2017) investigated an optically accessible multi-cylinder engine performance under single and double injections based on synergic experimental and numerical analysis. Wen et al. (2020) researched the effects

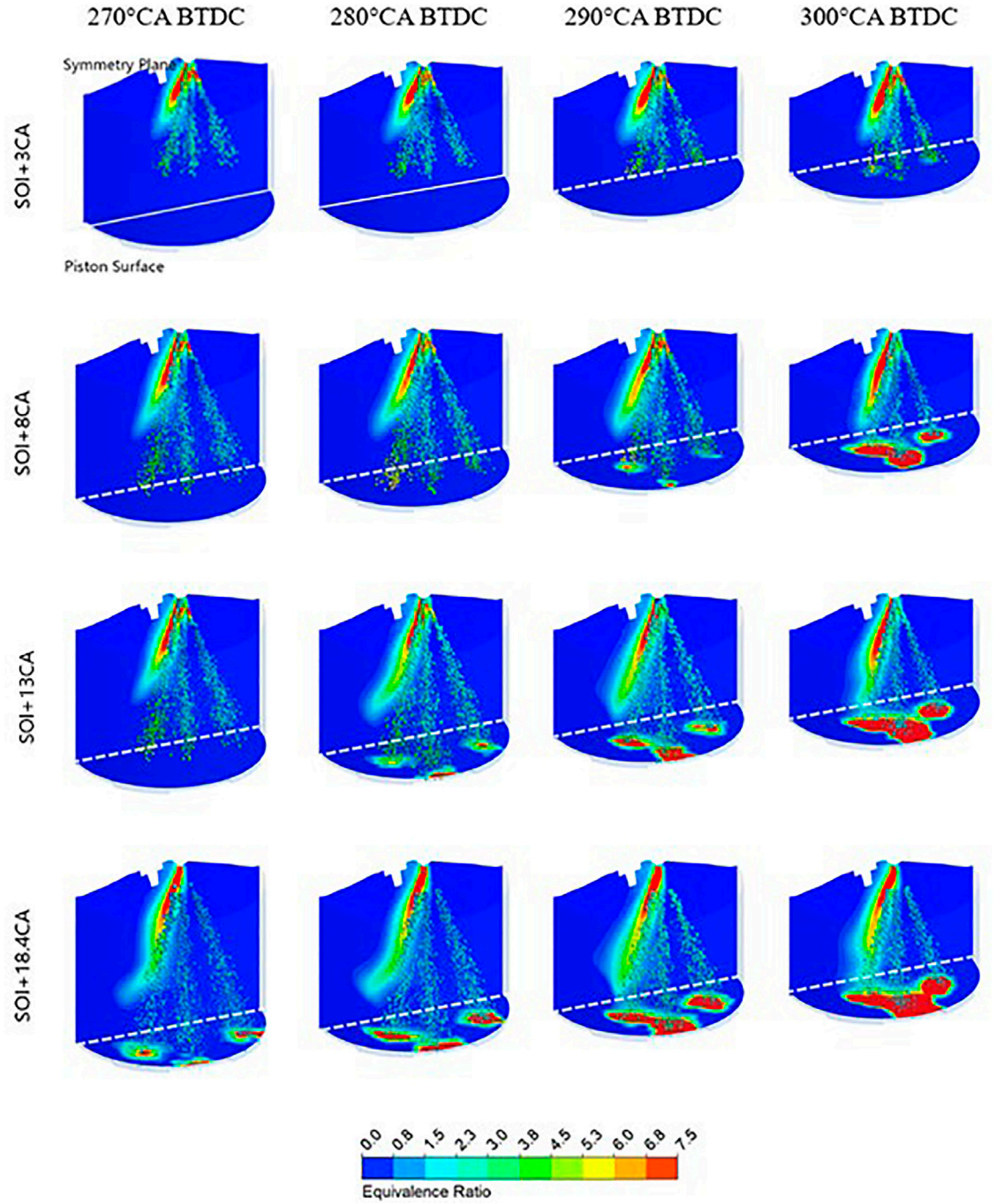

FIGURE 2 | In-cylinder mixture formation during the injection process at different injection timings.

of gasoline octane number on fuel consumption and emissions in two vehicles equipped with GDI and PFI spark-ignition engine. The results indicated that the early split injection strategy reduced the CO mass fraction and so on (Liu et al., 2019). Many studies have investigated the influence of injection parameters on in-cylinder evaluation indicators of mixture formation and combustion (Duronio et al., 2020a; Duronio et al., 2020b). The relevant researches focused more on the macro parameters of the in-cylinder combustion process (Cavicchi et al., 2019; Gong et al., 2021). Moreover, the literature of interaction of influence factors are limited. It's hard to point out the dominant factor in effect of IT, while there exists several trade-off factors like level of droplet-wall impingement, duration for mixing, flow motion intensity as

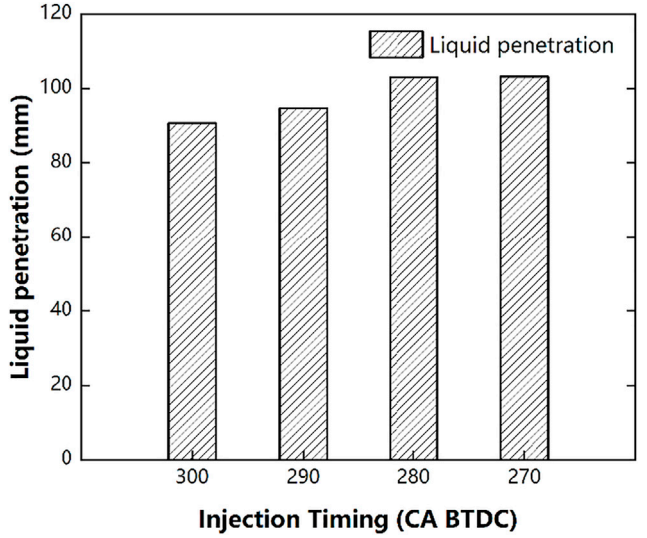

FIGURE 3 | The effect of IT on the maximum droplet penetration distance.

well as temperature, and pressure. Therefore, this research attempted to reveal the dominant factor of IT effect so that it can serve as a reference of IT selection. An already calibrated three-dimensional model was used to investigate the effects of injection timings on in-cylinder mixture formation and combustion processes. The goal of this study was to find out why the internal phenomenon of in-cylinder combustion occurs and propose suggestions for improving the in-cylinder combustion environment. Admittedly, the effect of injection timing on engine performance and emission can be imagined according the engine combustion laws. However, existing literature lacks the documented information about its effects in details. Moreover, the optically accessible engines have limited visualizations of the activities took place inside the chamber due to the difficulties or high costs in design. The 3D CFD simulation results present in this study can help readers to better visualize in-cylinder activities occurred inside the chamber from all directions rather than solely based on imaginations. It is also important to note that researchers may only guess one or two effects that are reasonable when changing the injection timing. But it is essential to show the combined effects caused by the variation of injection timings. Accordingly, the investigation of IT effects on engine combustion is request if wishing to provide a more direct understanding of the interaction between fuel spray, kernel inception and flame propagation, especially for their co-optimizations with the chamber shape. It is also important to note that their interactions and the IT effects would change with engine types and conditions. Consequently, the results of the study can serve as a reference for selecting a proper injection timing of the cylinder to improve combustion performance.

NUMERICAL MODEL

The model used in this study is a four-stroke spray-guided gasoline direct injection (GDI) engine. Since the 3D CFD model was already calibrated against the experimental data (Yan, 2021), with the detailed information shown in reference (Yan, 2021), only the most important information will be shown here. The compression ratio was 14.3 and three nozzles with a diameter of 300 microns were specified since this was a half-symmetry model. The injection timings were selected from 270 to 300 CAD (degree Crank Angle) BTDC (before top dead center) compression with an increment of 10 CAD at a fixed engine speed = 2000 r/min. The simulation was performed by commercial software ANSYS FORTE, a 3D CFD simulation software specialized for internal combustion engine. The three-dimensional CFD grid model is shown in **Figure 1**, consisting of 360,557 cells. The size of mesh was controlled within 1~2 mm, which was the recommended mesh size to precisely capture combustion characteristics according to reference (O'Rourke and Amsden, 1987). The engine specifications are shown in **Table 1** and the detailed information can be found in literature (Yan, 2021). In addition, all simulation tests were performed at a fixed spark ignition advance angle = 15 CAD BTDC compression. More detailed simulation parameters are shown in **Table 2**.

The turbulence model used in this study was the RNG k-ε model (Han and Reitz, 1995; Liu and Dumitrescu, 2019a). The basic governing equations include species conservation equation, fluid continuity equation, momentum conservation equation and energy conservation equation, and gas-phase mixture equation of state (Verma et al., 2016a; Verma et al., 2016b). The G-equation model together with the discrete particle ignition kernel (DPIK) flame model characterized the turbulent flame inception and propagation (Liu et al., 2018b; Liu and Dumitrescu, 2019b). The G-equation model was employed to track the propagation of fully developed, premixed, or partially premixed turbulent flames (Peters, 2000; Liu and Dumitrescu, 2019c). When the flame was initiated by the spark, the ignition-kernel flame had a structure that was typically smaller than the average grid size in the computational mesh (Tan and Reitz, 2006; Liu and Dumitrescu, 2019d). The spray models simulated sub-processes including nozzle flow, spray atomization, droplet breakup, droplet collision and coalescence, droplet vaporization, and wall impingement (Fan et al., 1999; Liu and Liu, 2021b). The nozzle flow model was solid-cone and the droplet Collision and Coalescence Model is the O'Rourke model (O'Rourke and Amsden, 1987). More detailed model settings are shown in **Table 3**. In addition, the chemistry mechanism for gasoline that consisted of 59 species and 437 reactions (ANSYS Forte). The main reactions include pyrolysis and oxidation, example of which are as following showed.

$$n - C_7H_{16} + O_2 = CO + H_2O \quad (1)$$

$$CO + OH = CO_2 + H \quad (2)$$

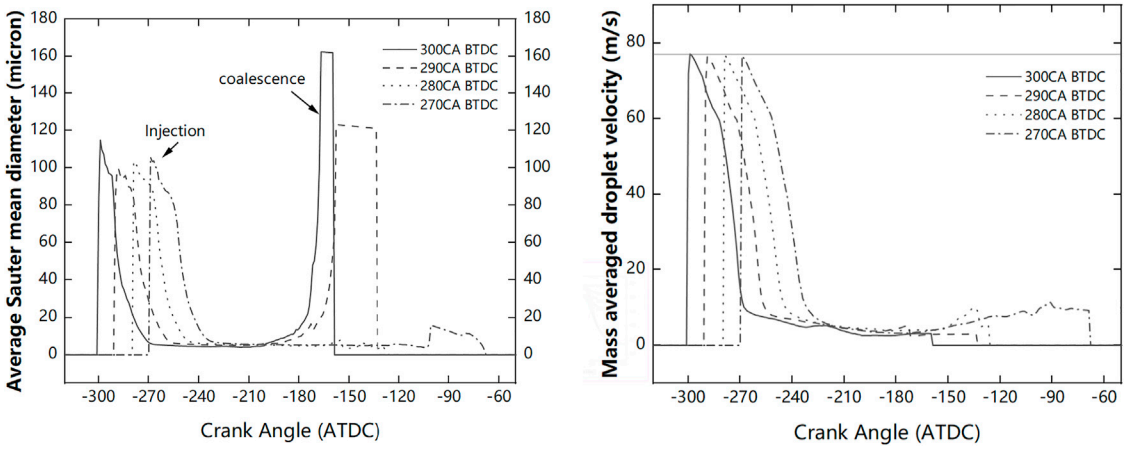

FIGURE 4 | The effect of IT on the mass averaged droplet velocity and the SMD.

Figure 2 shows the highly coincident pressure and apparent heat release rate (HRR) of experimental and simulation data, of in-cylinder combustion simulation, because the pressure and HRR are determined by combustion phase.

RESULTS AND DISCUSSIONS

Injection Timing Effects on In-Cylinder Mixture Formation

In this section, the in-cylinder mixture equivalence ratio and velocity vector image are presented to analyze the effects of IT on the mixture formation process. Some results are selected to show at several CAD of interest. It is also important to mention that the CFD results shown in this section are displayed on the vertical cut-plane combined with the upper surface of the piston, superimposed by the 3D profiles of spray development.

The variation of the injection droplets and in-cylinder equivalence ratio during the injection process is shown in **Figure 2**. As expected, advanced IT corresponded to upper piston position and therefore shorter distance between injector and piston surface during injection, resulting in considerable difference levels of droplet-wall impingement shown in **Figure 2**, which is essential to spray atomization and soot emission. Together with **Figure 3**, which indicates the injection penetration distance was extended by 4.5, 13.6, 13.7%, respectively, as the IT delayed, it can be inferred that the droplet-wall impingement was much intensified at IT of 300, 290 CA BTDC and slight at IT of 270, 280 CA BTDC.

The droplet velocity and Sauter mean diameter (SMD) which is defined as the ratio of total volume to the total surface area of droplet, as commonly used indicators of spray atomization (Liu et al., 2021), are shown in **Figure 4**. During the intake stroke, the droplet velocity initialized with approximately 77 m/s at IT, then decreased to nearly zero due to air friction. By the way, the slope difference was because of the continuous droplet with initial velocity during injection of 18.4-degree CA. The droplet velocity of different IT was similar except for CA offset during the intake stroke, because it was mainly determined by injection pressure which was kept same. It is also of interest to note that the droplet velocity was slightly raised at the beginning of compression stroke, which was probably due to the flow motion driven by the upward piston. The velocity difference during compression stroke echoed the diversity of the remaining droplet and evenness of mixture at various IT.

The SMD is influenced by the interaction of multifactor like nozzle diameter, injection pressure as well as backpressure (Biswal et al., 2019). As shown in **Figure 4**, the SMD of different IT decreased as the droplet breakup. Despite CA offset and slight difference during the breakup process, the SMD dropped to a similar value at the end of the intake stroke. What's outstanding in **Figure 4** is the rapid increment of SMD at IT of 300, 290 CA BTDC. This was mainly because of the severe droplet-wall impingement, contributing to droplet coalescence and therefore large SMD.

In conclusion, advanced IT tended to intensify droplet-wall impingement, but the level of spray atomization at the end of intake stroke was similar.

As shown in **Figure 5**, the equivalence ratio of the in-cylinder mixture at several CA during the compression stroke was utilized to investigate the fuel-gas mixture formation. The courter of symmetry plane and piston surface are colored by equivalence ratio. At the beginning of the compression stroke, the fuel was gathered around the piston surface near the cylinder, which was mainly due to the interaction of different levels of droplet-wall impingement as well as the duration of spray atomization. According to equivalence ratio distribution at 220 CA BTDC shown in **Figure 5**, it can be inferred that despite intensified droplet-wall impingement at advanced IT, the duration of spray atomization outperformed and affected spray atomization dominantly, resulting in more even distribution of mixture concentration around piston surface.

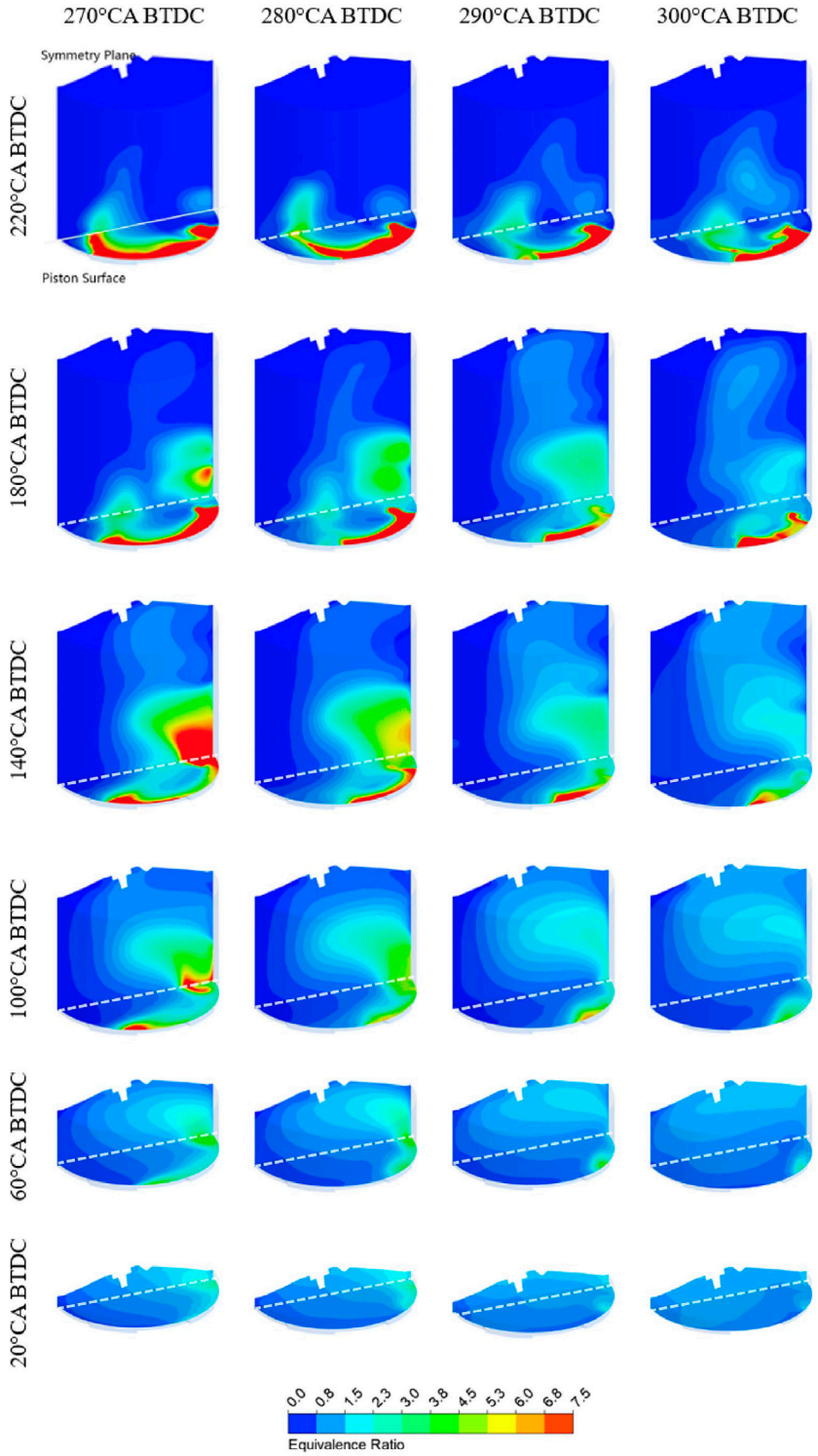

FIGURE 5 | Effect of injection timing on the in-cylinder mixture formation during compression.

As the piston moved toward TDC, the fuel was carried counterclockwise and mixed more evenly but delayed IT corresponded different evenness at TDC.

The mixture equivalence ratio distribution at spark timing (ST), as **Figure 6** shows, had a crucial influence on flame propagation and therefore comprehensive performance of the GDI engine. The

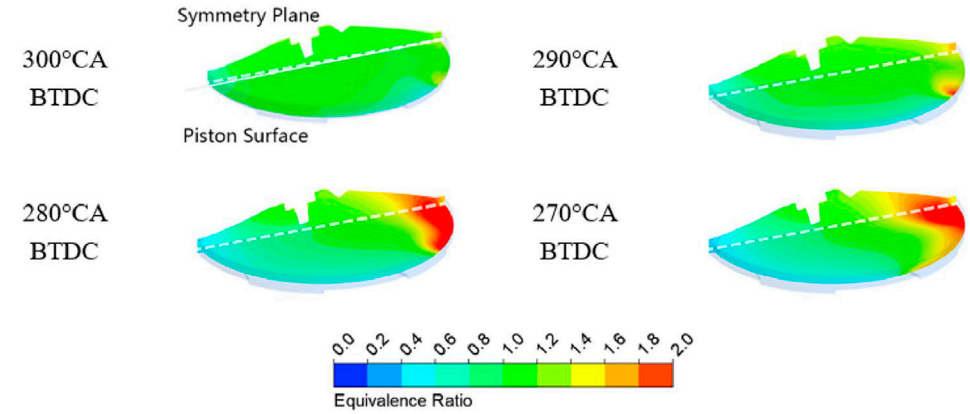

FIGURE 6 | In-cylinder mixture formation at the spark timing with different injection timings.

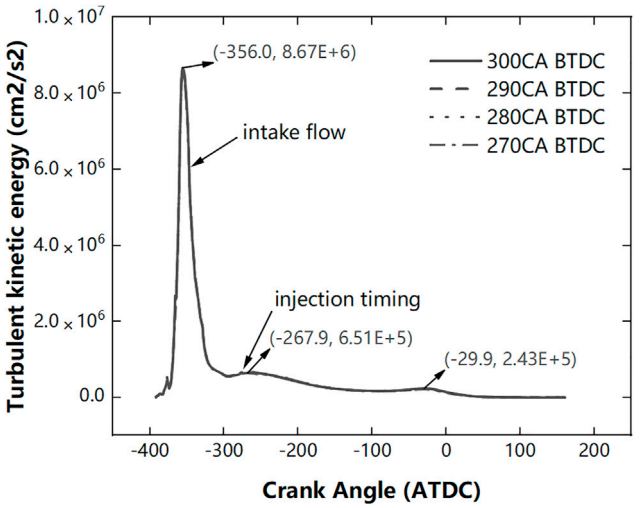

FIGURE 7 | Turbulent kinetic energy at different IT.

mixture of stoichiometric ratio was the ideal condition for ignition and combustion efficiency. **Figure 6** indicated the obvious different evenness of the mixture, suggesting that the fuel and gas had fully mixed evenly at IT of 300 CA BTDC, but with the IT retarding, the evenness of the mixture degraded. At delayed IT, especially at IT of 270, 280 CA BTDC, the fuel was gathered around intake port side of cylinder seriously, resulting in slower flame propagation and therefore contributing to the level of incomplete combustion that will be analyzed next.

The mixture formation process is influenced by the interaction of intake flow, piston movement as well as combustion chamber shape. To investigate the in-cylinder flow motion during the mixture formation process, the turbulent kinetic energy, indicating the intensity of the in-cylinder flow motion, is shown in **Figure 7**. The first peak outstanding the curve echoed the intake flow, and the second one between 300 and 270 CA BTDC was probably due to the injection which slightly enhanced in-cylinder flow motion. Then the turbulent kinetic energy was decreased slowly as the turbulence dissipation, until the spark timing when the combustion produced some kinetic energy of flow motion and thus arose a slight peak. Concerning the effect of IT, the turbulent kinetic energy of different IT was highly coincident, suggesting similar flow motion despite different IT.

To further investigate the flow motion during mixture formation, **Figure 8** shows the velocity field during compression stroke at different IT, corresponding with the equivalence ratio distribution mentioned in **Figure 5**. As shown in **Figure 8**, at the start of the compression stroke the flow from the intake valve to piston surface was predominant in in-cylinder flow motion because of intake flow inertia. As the piston moved upward, the flow around the piston was carried upward and interacted with intake flow inertia, contributing to a counterclockwise tumble flow formation, which could intensify the fuel-gas mixture significantly. Thus, the gathered fuel around the piston surface was carried along with tumble flow and further mixed evenly, echoing fuel movement displayed in **Figure 5**.

As can be seen in **Figure 8** the in-cylinder flow motion was highly similar regardless of delayed IT. **Figure 9** shows the tumble ratio of in-cylinder flow to assess the tumble flow intensity at different IT. The intake flow generated a fierce tumble with some vibration, until the start of injection when injected droplets brought a certain degree of disturbance. During the beginning of compression stroke, the tumble flow continually intensified thanks to the piston movement. Then the tumble ratio achieved maximal value at approximately -66 CA ATDC. After that it was a quicker decrement because the compressed volume of the combustion chamber dominated the flow motion, making the tumble flow degraded and enlarged dissipation of kinetic energy, which could be inferred from **Figure 8**. Besides, it was essential to note that the disturbance of injection at different IT was expanded obviously and directly affected mixture formation. The peak values of the tumble ratio were decreased by 8.3, 14.9, 24.9%, respectively, as the IT delayed. As the IT was delayed, the tumble ratio decreased.

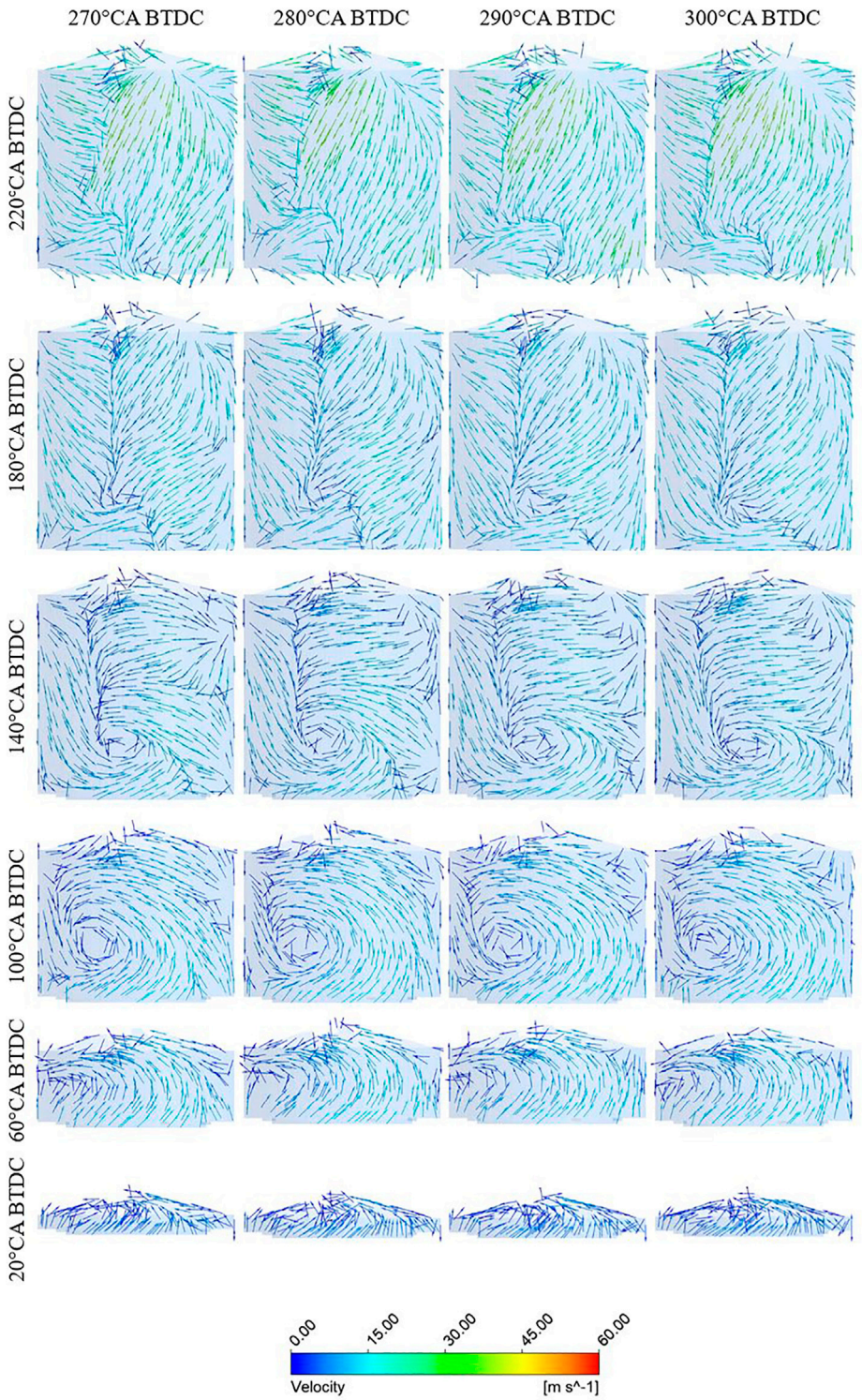

FIGURE 8 | In-cylinder velocity vector before spark timing at different injection timings.

Considering the analysis above comprehensively, it can be concluded that delayed IT significantly degrades the evenness of the mixture. Although delayed IT contributed to the reduction of droplet-wall impingement and slightly enhancing spray atomization, the less available time for mixture formation as well as the tumble flow motion

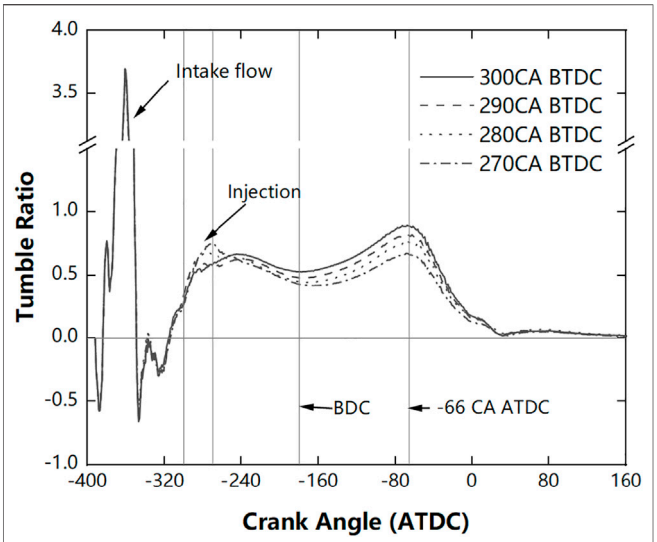

FIGURE 9 | Tumble ratio of in-cylinder flow at different IT.

degradation were dominant factors for deterioration of the mixture evenness.

Injection Timing Effect on In-Cylinder Combustion Characteristics

To assess the combustion process with different injection timing, the flame front colored by turbulent flame speed was displayed of several interested CA in **Figure 10**. The flame front in the numerical simulation is defined as the position of G = 0 in the G-equation turbulent combustion model. In the earlier combustion process before the flame front reached the cylinder, as can be seen in **Figure 10**, the flame front started from the spark plug and had similar shapes of different IT.

The corrugation of the flame front indicated turbulent flame propagation, which could intensify combustion. As can be seen in **Figures 10**, **11A** that an advanced IT tended to enhance turbulent and laminar flame speed. It was worth noting that the flame front propagation speed and front shape at the start of combustion were similar because the equivalence ratio around the spark plug was analogous, according to the corresponding image in **Figure 5**. The flame propagation speed of delayed IT was slowed when the flame front reached the fuel-rich region, resulting in the difference of laminar and turbulent flame speed between 0~40 CA ATDC in **Figure 11A**.

The in-cylinder pressure is shown in **Figure 11B**. The pressure was raised at compression stroke and suddenly increased at spark time when combustion started. The pressure at different IT was coincident before spark timing and separated after ignition due to different combustion performance. The peak combustion pressure and its location (location of peak pressure, LPP) are important indicators of combustion characteristics. **Figure 11B** suggests that LPP at IT of 300 CA BTDC was 26 ATDC. As the IT delayed the LPP advanced by 1.9, 7.0, 9.0 degrees CA, respectively, and peak pressure decreased by 4.2, 12.5, 14.6%, respectively, suggesting a deteriorated combustion efficiency as well as thermal efficiency due to the lower level of constant volume combustion.

The flame propagation and combustion characteristics were also reflected in the apparent heat release rate shown in **Figure 11C**. The duration of combustion (DOC) was defined as the duration from SOC and EOC (End of combustion) when the apparent heat release rate decreased to zero, indicating the combustion speed and affecting thermal efficiency. As the IT delayed from 300 CA BTDC to 270 CA BTDC, the DOC was extended by 4.1, 15.1, 21.9%, respectively, suggesting slower flame speed and degraded combustion efficiency, which is shown in **Figure 12**. The lower and retarded peak heat release rate also indicated the combustion performance deteriorated.

The flame thickness indicates the region of combustion reacted, as shown in **Figure 11D**. As expected the flame thickness raised immediately after ignition as the flame kernel grew fast. Then the flame kept a relatively larger thickness corresponding to the flame propagation process before the following sudden decrement, which echoed the flame propagated to the cylinder. It's of interest that flame thickness of different IT was coincident before the sudden drop, indicating the combustion in the stoichiometric ratio region displayed in **Figure 6** was similar. The flame thickness separated at a sudden drop at approximately 40 CA ATDC because of various levels of incomplete combustion. As **Figure 10** shows, the majority of the flame front of IT of 290, 300 CA BTDC was terminated at the cylinder at 45 CA ATDC, echoing the earlier sharp decrement, followed by the IT of 270, 280 CA BTDC that propagated slower. The gentle growth of flame thickness after approximately 50 CA BTDC was probably due to slowly combustion of the excessive equivalence ratio region, which had a thicker but deteriorated reaction zone.

The excessive equivalence ratio, indicating lack of oxygen, tended to slower the flame propagation speed and even not on fire. That explained the decrease of flame speed with IT delaying as **Figure 10** showed, because the unevenness of mixture was intensified and thus excessive fuel-rich region existed around the intake side of the combustion chamber.

Furthermore, it's important to point out that some extremely excessive fuel regions didn't on fire as the IT delayed. The excessive equivalence ratio, indicating lack of oxygen, tended to slower the flame propagation speed, and even not on fire. That explained the decrease of flame speed with IT delaying as **Figure 10** showed, because the unevenness of mixture was intensified and thus excessive fuel-rich region existed around the intake side of the combustion chamber, as mentioned in **Figure 6**. The flame front propagation speed was vastly decreased when reaching the excessive fuel-rich region and even terminated in extreme equivalence ratio region at IT of 270, 280 CA BTDC, as shown in **Figure 10**. The fuel-rich region that remained unburnt reduced the chemical energy released and therefore decreased the combustion and thermal efficiency. Besides, the unburnt region sharply raised the unburnt hydrocarbon (UHC) by 3.2, 109, 122 times as IT delayed as shown in **Figure 12**.

The flame speed and combustion characteristics analyzed above dominantly determined the combustion efficiency and

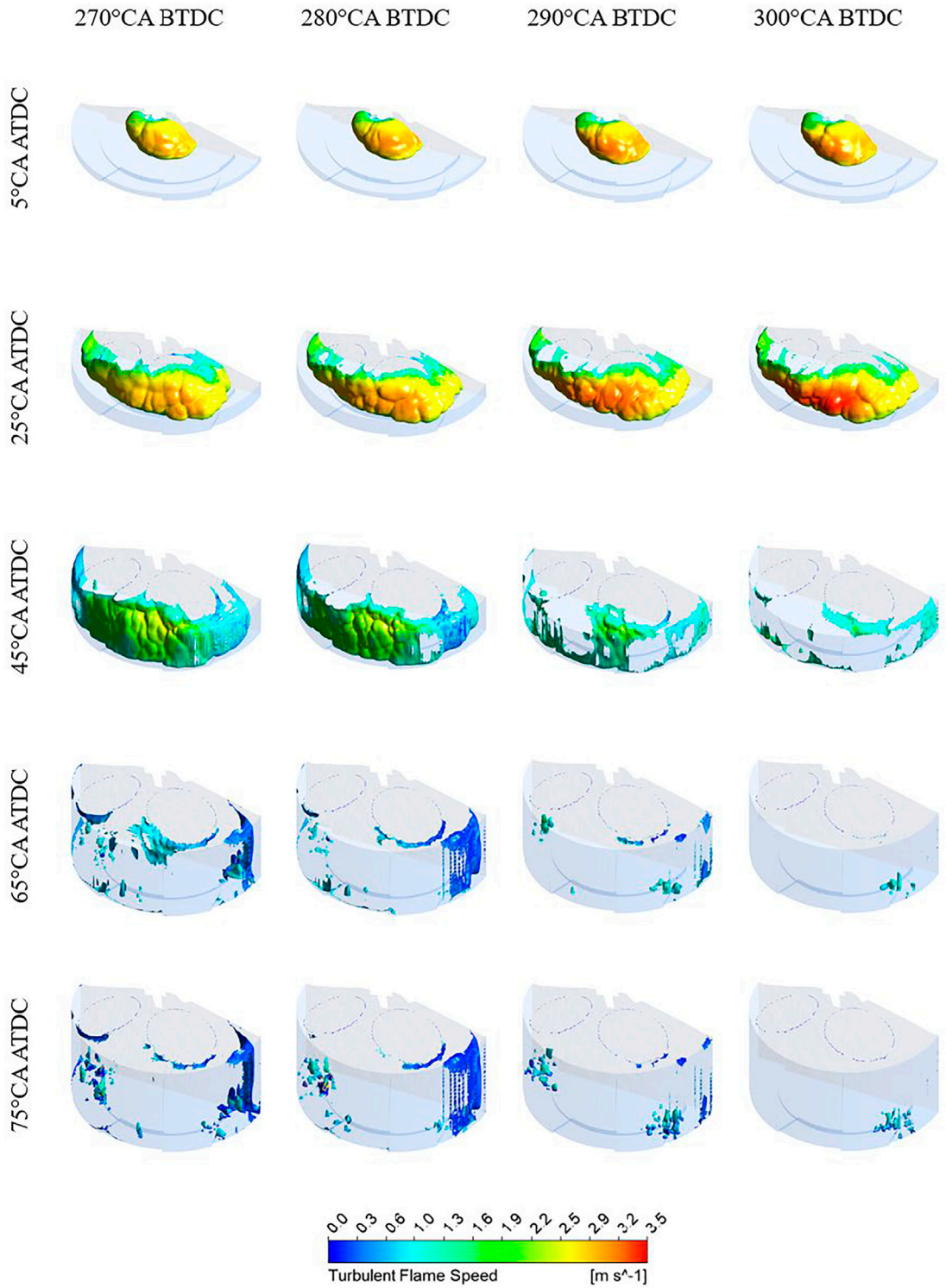

FIGURE 10 | Effect of injection timing on the distribution of turbulent flame speed at the flame front (i.e., G = 0) at several CAD of interest after SOC.

therefore thermal efficiency, as **Figure 12** showed. With IT delaying from 300 to 270 CA BTDC, the combustion efficiency decreased by 3.9, 10.8, 13.6% and thermal efficiency by 4.1, 13.3, 16.5%, respectively. It suggested an optimized IT of 300 CA BTDC in this research with combustion and thermal efficiency of 97.7 and 37.6%, respectively.

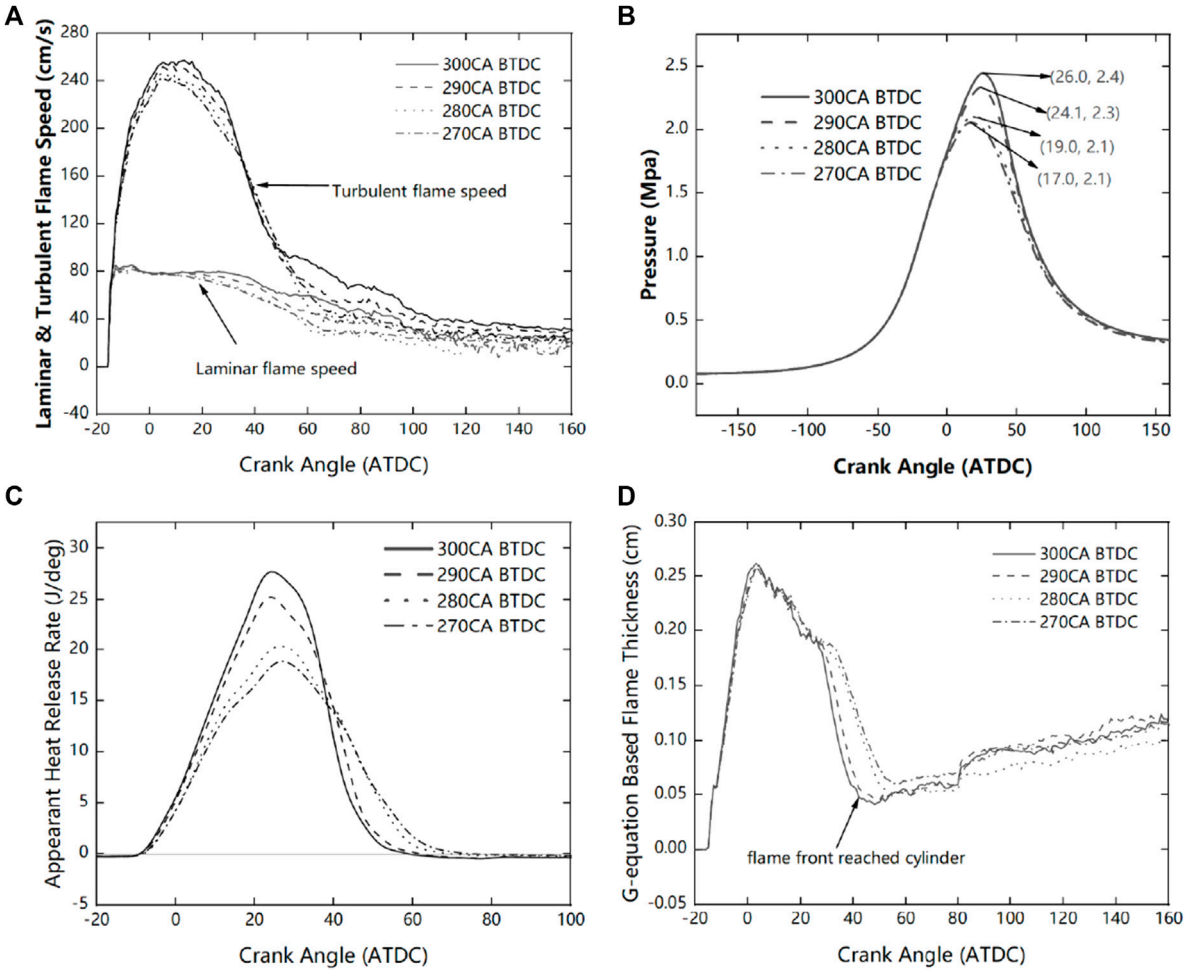

FIGURE 11 | (A) Effect of injection timing on laminar and turbulent flame speed. **(B)** In-cylinder average pressure at different IT. **(C)** Apparent heat release rate at different IT. **(D)** G-equation based flame thickness at different IT.

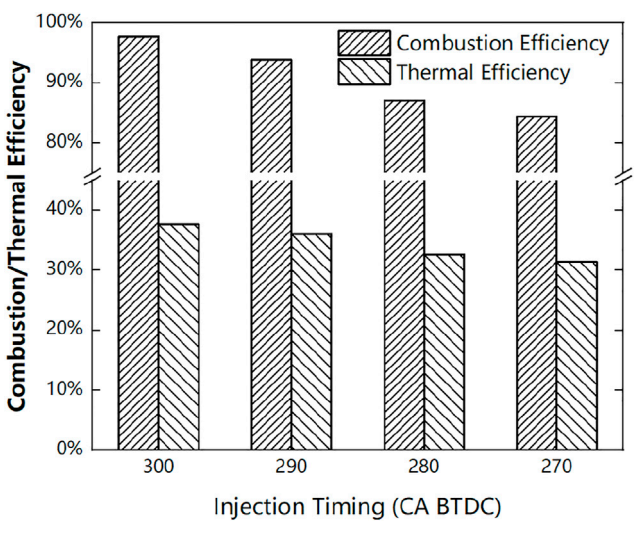

FIGURE 12 | Combustion efficiency and Thermal efficient at different IT.

CONCLUSION

This research investigated the effects of different IT (270, 280, 290, 300-degree CA BTDC) on mixture formation and combustion characteristics in a GDI engine. A three-dimensional CFD model concluding spray, turbulence, G-equation combustion models were utilized to analyze the detailed process of spray atomization, mixture formation and flame propagation comprehensively at different IT. The results are summarized as follows:

1) Delayed IT tended to reduce drop-wall impingement significantly but had a slight impact on droplet breakup and spray atomization.
2) Delayed IT intensified unevenness of mixture concertation, contributing to fuel-rich region extended at the intake port side of cylinder. The fuel-gas mixing process was dominantly driven by the tumble flow motion. Albeit delayed IT generated less droplet-wall impingement, the shorter duration of the mixing process and degraded tumble flow motion enlarged the unevenness of mixture at spark timing.

3) The combustion was deteriorated as the IT delayed because the excessive equivalence ratio region severely slowed flame propagation and terminated at the most uneven region.

In conclusion, this paper demonstrated the whole process from injection to combustion, revealing that level of droplet-wall impingement and available duration for the mixing process is a pair of trade-off factors for mixture formation and following combustion process, as the IT changes. In this research, the positive effect of mixing duration defeated the negative influences of droplet-wall impingement as the IT advanced. But considering the more advanced IT, it's recommended to assess the interaction of these factors since the dominant influence factor is uncertain with too earlier IT. Thus, this research has a positive effect to guide the IT optimization for various models of the GDI engine.

DATA AVAILABILITY STATEMENT

The raw data supporting the conclusion of this article will be made available by the authors, without undue reservation.

AUTHOR CONTRIBUTIONS

YY: Conceptualization, methodology, simulation, and writing—draft preparation. RY: Validation, writing—draft preparation, writing—review and editing. XS: Analysis, supervision, Validation. LR: writing review and editing. ZL: Analysis, supervision. All authors have read and agreed to the published version of the manuscript.

REFERENCES

Ambrogi, L., Liu, J., Battistoni, M., Dumitrescu, C., and Gasbarro, L. (2019). CFD Investigation of the Effects of Gas' Methane Number on the Performance of a Heavy-Duty Natural-Gas Spark-Ignition Engine. SAE International,Technical Paper 2019-24-0008. doi:10.4271/2019-24-0008

ANSYS Forte *Forte Theory*. San diego: Ansys, Inc. Release 17.2, 2017.

Biswal, A., Kale, R., Balusamy, S., Banerjee, R., and Kolhe, P. (2019). Lemon Peel Oil as an Alternative Fuel for GDI Engines: A spray Characterization Perspective. *Renew. Energ.* 142, 249–263. doi:10.1016/j.renene.2019.04.087

Cavicchi, A., Postrioti, L., and Scarponi, E. (2019). Hydraulic Analysis of a GDI Injector Operation with Close Multi-Injection Strategies. *Fuel* 235, 1114–1122. doi:10.1016/j.fuel.2018.08.089

Duronio, F., De Vita, A., Allocca, L., and Anatone, M. (2020). Gasoline Direct Injection Engines - A Review of Latest Technologies and Trends. Part 1: Spray Breakup Process. *Fuel* 265, 116948. doi:10.1016/j.fuel.2019.116948

Duronio, F., De Vita, A., Montanaro, A., and Villante, C. (2020). Gasoline Direct Injection Engines - A Review of Latest Technologies and Trends. Part 2. *Fuel* 265, 116947. doi:10.1016/j.fuel.2019.116947

Fan, L., Li, G., Han, Z., and Reitz, R. D. (1999). Modeling Fuel Preparation and Stratified Combustion in a Gasoline Direct Injection Engine. SAE International, Technical paper 1999-01-0175. doi:10.4271/1999-01-0175

Feng, L., Sun, X., Pan, X., Yi, W., Cui, Y., Wang, Y., et al. (2021). Gasoline spray Characteristics Using a High Pressure Common Rail Diesel Injection System by the Method of Laser Induced Exciplex Fluorescence. *Fuel* 302, 121174. doi:10.1016/j.fuel.2021.121174

Fennell, D., Herreros, J., and Tsolakis, A. (2014). Improving Gasoline Direct Injection (GDI) Engine Efficiency and Emissions with Hydrogen from Exhaust Gas Fuel Reforming. *Int. J. Hydrogen Energ.* 39 (10), 5153–5162. doi:10.1016/j.ijhydene.2014.01.065

Fridstrøm, L. (2017). From Innovation to Penetration: Calculating the Energy Transition Time Lag for Motor Vehicles. *Energy Policy* 108, 487–502. doi:10.1016/j.enpol.2017.06.026

Gasbarro, L., Liu, J., Dumitrescu, C., Ulishney, C., Battistoni, M., and Ambrogi, L. (2019). Heavy-duty Compression-Ignition Engines Retrofitted to Spark-Ignition Operation Fueled with Natural Gas. SAE International, Technical Paper 2019-24-0030. doi:10.4271/2019-24-0030

Gong, C., Si, X., and Liu, F. (2021). Effects of Injection Timing and CO2 Dilution on Combustion and Emissions Behaviors of a Stoichiometric GDI Engine under Medium Load Conditions. *Fuel* 303, 121262. doi:10.1016/j.fuel.2021.121262

Han, Z., and Reitz, R. D. (1995). Turbulence Modeling of Internal Combustion Engines Using RNG κ-ε Models. *Combustion Sci. Technol.* 106 (4-6), 267–295. doi:10.1080/00102209508907782

Huang, Q., Liu, J., Ulishney, C., and Dumitrescu, C. E. (2021). On the Use of Artificial Neural Networks to Model the Performance and Emissions of a Heavy-Duty Natural Gas Spark Ignition Engine. *Int. J. Engine Res.*, 1–20. doi:10.1177/14680874211034409

Kim, T., Song, J., Park, J., and Park, S. (2018). Numerical and Experimental Study on Effects of Fuel Injection Timings on Combustion and Emission Characteristics of a Direct-Injection Spark-Ignition Gasoline Engine with a 50 MPa Fuel Injection System. *Appl. Therm. Eng.* 144, 890–900. doi:10.1016/j.applthermaleng.2018.09.007

Liobikienė, G., and Butkus, M. (2017). The European Union Possibilities to Achieve Targets of Europe 2020 and Paris Agreement Climate Policy. *Renew. Energ.* 106, 298–309. doi:10.1016/j.renene.2017.01.036

Liu, H., Mao, B., Liu, J., Zheng, Z., and Yao, M. (2018). Pilot Injection Strategy Management of Gasoline Compression Ignition (GCI) Combustion in a Multi-cylinder Diesel Engine. *Fuel* 221, 116–127. doi:10.1016/j.fuel.2018.01.073

Liu, H., Wang, X., Zhang, D., Dong, F., Liu, X., Yang, Y., et al. (2019). Investigation on Blending Effects of Gasoline Fuel with N-Butanol, DMF, and Ethanol on the Fuel Consumption and Harmful Emissions in a GDI Vehicle. *Energies* 12 (10), 1845. doi:10.3390/en12101845

Liu, J., and Dumitrescu, C. E. (2019). Lean-burn Characteristics of a Heavy-Duty Diesel Engine Retrofitted to Natural-Gas Spark Ignition. *J. Eng. Gas Turbines Power* 141071013 (7). doi:10.1115/1.4042501

Liu, J., Huang, Q., Ulishney, C., and Dumitrescu, C. E. (2022). Comparison of Random forest and Neural Network in Modelling the Performance and Emissions of a Natural Gas Spark Ignition Engine. *J. Energ. Resour. Technol.* 144 (3), 032310. doi:10.1115/1.4053301

Liu, J., Szybist, J., and Dumitrescu, C. (2018). Choice of Tuning Parameters on 3D IC Engine Simulations Using G-Equation. SAE International, Technical Paper 2018-01-0183. doi:10.4271/2018-01-0183

Liu, J., and Dumitrescu, C. E. (2019). Combustion Partitioning inside a Natural Gas Spark Ignition Engine with a Bowl-In-Piston Geometry. *Energ. Convers. Manage.* 183, 73–83. doi:10.1016/j.enconman.2018.12.118

Liu, J., and Dumitrescu, C. E. (2019). Methodology to Separate the Two Burn Stages of Natural-Gas Lean Premixed-Combustion inside a Diesel Geometry. *Energ. Convers. Manage.* 195, 21–31. doi:10.1016/j.enconman.2019.04.091

Liu, J., and Dumitrescu, C. E. (2019). Numerical Investigation of Methane Number and Wobbe index Effects in Lean-Burn Natural Gas Spark-Ignition Combustion. *Energy Fuels* 33 (5), 4564–4574. doi:10.1021/acs.energyfuels.8b04463

Liu, J., and Wang, H. (2022). Machine Learning Assisted Modeling of Mixing Timescale for LES/PDF of High-Karlovitz Turbulent Premixed Combustion. *Combustion and Flame* 238, 111895. doi:10.1016/j.combustflame.2021.111895

Liu, Z., and Liu, J. (2021). Effect of Altitude Conditions on Combustion and Performance of a Turbocharged Direct-Injection Diesel Engine. *Proc. Inst. Mech. Eng. D: J. Automobile Eng.* 236 (4), 09544070211026204. doi:10.1177/09544070211026204

Liu, Z., and Liu, J. (2021). Experimental Investigation of Combustion Characteristics of a Single cylinder Diesel Engine at Altitude. *J. Energ. Resour. Technol.* 143 (10), 102306. doi:10.1115/1.4050575

Liu, Z., Zhang, Y., Fu, J., and Liu, J. (2021). "Three-dimensional Fluid Dynamics Modeling of a 6V150 Diesel Engine," in American Society of Mechanical Engineers International Mechanical Engineering Congress and Exposition. IMECE2021-67711, November 1-5, 2021.

Marseglia, G., Costa, M., Catapano, F., Sementa, P., and Vaglieco, B. M. (2017). Study about the Link between Injection Strategy and Knock Onset in an Optically Accessible Multi-cylinder GDI Engine. *Energ. Convers. Manage.* 134, 1–19. doi:10.1016/j.enconman.2016.12.012

Miganakallu, N., Yang, Z., Rogóż, R., Kapusta, Ł. J., Christensen, C., Barros, S., et al. (2020). Effect of Water - Methanol Blends on Engine Performance at Borderline Knock Conditions in Gasoline Direct Injection Engines. *Appl. Energ.* 264, 114750. doi:10.1016/j.apenergy.2020.114750

O'Rourke, P. J., and Amsden, A. A. (1987). The TAB Method for Numerical Calculation of spray Droplet Breakup. SAE International, Technical Paper 872089. doi:10.4271/872089

Peters, N. (2000). *Turbulent Combustion*. Cambridge, United Kingdom: Cambridge University Press.

Potenza, M., Milanese, M., and de Risi, A. (2019). Effect of Injection Strategies on Particulate Matter Structures of a Turbocharged GDI Engine. *Fuel* 237, 413–428. doi:10.1016/j.fuel.2018.09.130

Splitter, D., Kaul, B., Szybist, J., and Jatana, G. (2017). Engine Operating Conditions and Fuel Properties on Pre-spark Heat Release and SPI Promotion in SI Engines. *SAE Int. J. Engines* 10 (3), 1036–1050. doi:10.4271/2017-01-0688

Stocchi, I., Liu, J., Dumitrescu, C. E., Battistoni, M., and Grimaldi, C. N. (2019). Effect of Piston Crevices on the Numerical Simulation of a Heavy-Duty Diesel Engine Retrofitted to Natural-Gas Spark-Ignition Operation. *J. Energ. Resour. Technol.* 141 (11), 112204. doi:10.1115/1.4043709

Storey, J. M., Lewis, S., Szybist, J., Thomas, J., Barone, T., Eibl, M., et al. (2014). Novel Characterization of GDI Engine Exhaust for Gasoline and Mid-level Gasoline-Alcohol Blends. *SAE Int. J. Fuels Lubr.* 7 (2), 571–579. doi:10.4271/2014-01-1606

Tan, Z., and Reitz, R. D. (2006). An Ignition and Combustion Model Based on the Level-Set Method for Spark Ignition Engine Multidimensional Modeling. *Combustion and Flame* 145 (1-2), 1–5. doi:10.1016/j.combustflame.2005.12.007

Verma, I., Bish, E., Kuntz, M., Meeks, E., Puduppakkam, K., Naik, C., et al. (2016). CFD Modeling of Spark Ignited Gasoline Engines-Part 1: Modeling the Engine under Motored and Premixed-Charge Combustion Mode. SAE International, Technical Paper 2016-01-0591. doi:10.4271/2016-01-0591

Verma, I., Bish, E., Kuntz, M., Meeks, E., Puduppakkam, K., Naik, C., et al. (2016). CFD Modeling of Spark Ignited Gasoline Engines-Part 2: Modeling the Engine in Direct Injection Mode along with spray Validation. SAE International, Technical Paper 2016-01-0579. doi:10.4271/2016-01-0579

Wen, M., Zhang, C., Yue, Z., Liu, X., Yang, Y., Dong, F., et al. (2020). Effects of Gasoline Octane Number on Fuel Consumption and Emissions in Two Vehicles Equipped with GDI and PFI Spark-Ignition Engine. *J. Energ. Eng.* 146 (6), 04020069. doi:10.1061/(asce)ey.1943-7897.0000722

Yan, Y. (2021). The Effect of Injection Timing on the Performance of Direct Injection Gasoline Engines. Bachelor Thesis. Hangzhou (China): Zhejiang University.

Zhang, M., Hong, W., Xie, F., Su, Y., Han, L., and Wu, B. (2017). Influence of Diluents on Combustion and Emission Characteristics of a GDI Engine. *Appl. Therm. Eng.* 124, 746–755. doi:10.1016/j.applthermaleng.2017.06.043

Zhang, M., Hong, W., Xie, F., Su, Y., Liu, H., and Zhou, S. (2018). Combustion, Performance and Particulate Matter Emissions Analysis of Operating Parameters on a GDI Engine by Traditional Experimental Investigation and Taguchi Method. *Energ. Convers. Manage.* 164, 344–352. doi:10.1016/j.enconman.2018.03.017

Zhang, Z., Zhang, W., Ma, X., Awad, O. I., Xu, H., and Shuai, S. (2020). Effects of GDI Injector Deposits on spray and Combustion Characteristics under Different Injection Conditions. *Fuel* 278, 118094. doi:10.1016/j.fuel.2020.118094

Zhu, G., Liu, J., Fu, J., Xu, Z., Guo, Q., and Zhao, H. (2018). Experimental Study on Combustion and Emission Characteristics of Turbocharged Gasoline Direct Injection (GDI) Engine under Cold Start New European Driving Cycle (NEDC). *Fuel* 215, 272–284. doi:10.1016/j.fuel.2017.10.048

Zhuang, Y., Zhu, G., Gong, Z., Wang, C., and Huang, Y. (2019). Experimental and Numerical Investigation of Performance of an Ethanol-Gasoline Dual-Injection Engine. *Energy* 186, 115835. doi:10.1016/j.energy.2019.07.165

Conflict of Interest: The authors declare that the research was conducted in the absence of any commercial or financial relationships that could be construed as a potential conflict of interest.

Publisher's Note: All claims expressed in this article are solely those of the authors and do not necessarily represent those of their affiliated organizations, or those of the publisher, the editors and the reviewers. Any product that may be evaluated in this article, or claim that may be made by its manufacturer, is not guaranteed or endorsed by the publisher.

frontiers in Energy Research

ORIGINAL RESEARCH
published: 23 February 2022
doi: 10.3389/fenrg.2022.828215

Study of In-Cylinder Heat Transfer Boundary Conditions for Diesel Engines Under Variable Altitudes Based on the CHT Model

*Yu Zhang[1], Yuchao Yan[2], Ruomiao Yang[2], Qifan Wang[2], Bowen Zhang[2], Qingliang Gan[2], Zhentao Liu[2] and Jiahong Fu[1]**

[1]Mechanical Engineering Department, Zhejiang University City College, Hangzhou, China, [2]College of Energy Engineering, Power Machinery and Vehicular Engineering Institute, Zhejiang University, Hangzhou, China

The reliability of combustion chamber components is mainly determined by the thermal load of diesel engines. Under the plateau operation condition, diesel engine performance degradation and ablation area appear. Therefore, it is crucial to study the engine heat transfer phenomenon at different altitudes, of which the Woschni formula cannot meet the accuracy requirement. With the motive of modifying and calibrating the Woschni formula at different altitudes, a modified conjugate heat transfer (CHT) model of the combustion chamber and the cooling medium was proposed to analyze the temperature distribution of the cylinder head. The results indicated that relative errors were controlled within 5% under variant altitudes, comparing the temperature field of the numerical simulation with the single-cylinder engine experiment test data. Therefore, the modified in-cylinder conjugate heat transfer model can be used to predict the thermal load of diesel engine combustion chamber components under different altitude operating conditions.

Keywords: variable altitude, diesel engine, conjugate heat transfer, in-cylinder heat transfer model, CFD

OPEN ACCESS

Edited by:
Jun Li,
Guangzhou Institute of Energy Conversion (CAS), China

Reviewed by:
Long Wu,
Tianjin University of Science and Technology, China
Yaojie Tu,
Huazhong University of Science and Technology, China

****Correspondence:***
Jiahong Fu
fujh@zucc.edu.cn

Specialty section:
This article was submitted to Advanced Clean Fuel Technologies, a section of the journal Frontiers in Energy Research

Received: *03 December 2021*
Accepted: *13 January 2022*
Published: *23 February 2022*

Citation:
Zhang Y, Yan Y, Yang R, Wang Q, Zhang B, Gan Q, Liu Z and Fu J (2022) Study of In-Cylinder Heat Transfer Boundary Conditions for Diesel Engines Under Variable Altitudes Based on the CHT Model. Front. Energy Res. 10:828215. doi: 10.3389/fenrg.2022.828215

INTRODUCTION

As a compact, wide power range, and adaptable power system, the internal combustion engine (ICE) is widely used in engineering and agricultural machinery, automobiles, motorcycles, national defense, and other fields (Ambrogi et al., 2019; Liu and Wang, 2022). High-altitude areas can also experience high cold weather (Wang et al., 2013; Yang et al., 2018), which would greatly reduce the performance of batteries (Yu et al., 2014; Zhang et al., 2020). Consequently, internal combustion engines will continue to be used as the primary source of power at high altitudes (Stocchi et al., 2019; Liu et al., 2022). There are many high-altitude roads and vehicles powered by diesel engines for high-altitude operations around the world (Liu and Liu, 2021a; Liu et al., 2021). For example, in China, the area at a high altitude can be as large as 1/4 of the country's land area (Shen et al., 1995; Liu and Liu, 2022). However, it is found that as altitude increases, air density decreases, which causes many problems to the normal operation of the vehicle, such as insufficient power and localized ablation of the cylinder head and piston (Perez and Boehman, 2010; Liu and Liu, 2021b). According to previous literature, these problems are because conventional heat transfer correlations are not well adapted to heat load prediction in high-altitude situations (Zhang et al., 2016; Liu and Liu, 2021c).

The accurate prediction of diesel engine thermal load plays an important role in the whole design process of diesel engines (Shannak and Alhasan, 2002; Sideri et al., 2017). In addition, the

distribution of temperature field and heat flux of combustion chamber components has a decisive influence on diesel engine reliability (Gholinia et al., 2018; Liu et al., 2019). Moreover, it was hard to predict the thermal load of diesel engines precisely due to in-cylinder rapid transient gas changes, extremely inhomogenous distribution of the temperature field, and uncertain initial and boundary conditions (Sroka, 2012; Lu et al., 2013). At the same time, numerical simulation accuracy is greatly affected by the strong coupling relationship between the in-cylinder combustion process, thermal conduction in the combustion chamber walls, and cooling fluid flow (Chen et al., 2017; Lu et al., 2017).

In recent decades, the development of the in-cylinder heat transfer model has roughly gone through three stages: the stage of the pure empirical model (Borman and Nishiwaki, 1987), the semi-empirical model (Woschni, 1967; Hohenberg, 1979; Huber et al., 1990) based on similarity principle and dimensional analysis, and the combination of the turbulence model and heat transfer model (Launder and Spalding, 1974; Han and Reitz, 1997; Broekaert et al., 2016). Nowadays, the experimental correlations proposed by Woschni (1967), Hohenberg (1979), Huber et al. (1990) are the most commonly used formulas. In addition, more research studies made modifications to these heat transfer formulas in detail to improve model precision under different operating conditions. The research team (Launder and Spalding (1974), Han and Reitz (1997)) measured the heat flux density of the premixed spark ignition engines fueled with CH_4, H_2, and CH_3OH under motored and fired operating conditions, analyzed the effects of gas properties on heat flux, and checked and modified the Reynolds analogy modeling approach. The results showed that traditional heat transfer models were not satisfied with precision acquirements due to higher heat flux of the engine fueled with hydrogen rather than hydrocarbon fuels caused by different gas properties. Michl et al. (Broekaert et al., 2016) measured combustion chamber wall heat flux using a rapid response thermocouple and modified the heat transfer model with experimental data, which improved prediction accuracy under various operating conditions. Fagundez et al. (De Cuyper et al., 2016) tested the combustion process of hydrous ethanol fuel and wet ethanol fuel blends with different water volume fractions and established a two-zone combustion model based on Wiebe function. Moreover, the predictive accuracy of the Hohenberg model (Hohenberg, 1979) was the highest by comparing the heat transfer correlations proposed by Woschni (1967), Hohenberg (1979), Sitkei (Michl et al., 2016), and Annand (Fagundez et al., 2017). In addition, the heat transfer model of Hohenberg (1979) was modified with experimental data.

Overall, the model modification was performed to modify the parameters or additional items of the classic formula by considering the impact of the factors on the theory model, predicting the performance using simulation methodology, and checking the applicability of the modified formula. Moreover, lower engine performance and ablation area of the cylinder head and piston with higher altitudes was attributed to a decrement of model predictive accuracy of the traditional heat transfer correlation formula at high altitude (Zhang et al., 2016). In addition, the literature is limited to date on the investigation focused on the applicability of the heat transfer model at variant altitudes. In this study, a collaborative simulation method for solving fluid–solid coupled heat transfer problems is constructed, while the Woschni formula (Woschni, 1967) is modified to obtain a heat transfer model adapted to different altitudes and verified with the experiments. A conjugate heat transfer (CHT) model was calibrated based on single-cylinder experimental data under a simulated plateau environment. Moreover, the diesel engine in-cylinder heat transfer model with higher prediction accuracy at variant altitudes was proposed by modifying the traditional empirical formula, which can be used as a reference for thermal load prediction of combustion chamber components at different altitudes.

METHODOLOGY

It is of significance to revise the Woschni formula (Woschni, 1967) because it can hardly meet the accuracy requirement at a higher altitude. Thus, this study aims to develop a modified heat transfer model for the plateau. The logical idea for modifying the Woschni formula for different altitude conditions is shown in **Figure 1**. The zero-dimensional combustion model and heat transfer model were used to calculate the average heat transfer coefficient and gas temperature, while the three-dimensional numerical simulation model was utilized to solve the temperature field, which was compared with measured data to assess the modified model precision.

Experiments

Experimental Setup

In order to precisely modify the in-cylinder heat transfer model of diesel engines at various attitudes, the experiments on a single-cylinder diesel engine at different operation conditions were carried out. Proper sensors were utilized to measure the relevant parameters, such as pressure and temperature. The diesel engine specifications are shown in **Table 1**.

This study used a four-stroke single-cylinder diesel engine. The engine speed was set to 1500 r/min (MBT), 1900 r/min, and 2200 r/min (rated condition). The different altitude (0, 1000, 2000, 3000, 3700, and 4500 m) environments were simulated by changing the intake pressure. All equipment and sensors have been calibrated precisely to ensure accuracy in the installation. The assembled test bench was equipped with a plateau simulation system that can change ambient pressures from 100 to 57.9 kPa. The ambient pressure at different operation conditions was precalculated in consideration of altitude and aspiration.

The NiCr–NiSi type thermocouples were arranged on the firing surface of the cylinder head in the test engine, and the specific locations of the measurement points are shown in **Figure 2**. A total of 10 measurement points were installed on the fire face located between the inlet and exhaust valves in the nose area and between the two exhaust valves. The sensor calibration revealed that the error is within ±0.1 °C, which can preciously capture the in-cylinder temperature. Moreover, the dynamic response time of this thermocouple is about 50 ~ 100 ms, that meets the quick response requirement of the in-cylinder temperature measure.

An NI data acquisition system that compiles NI-LabVIEW software with temperature measurement was used to collect data.

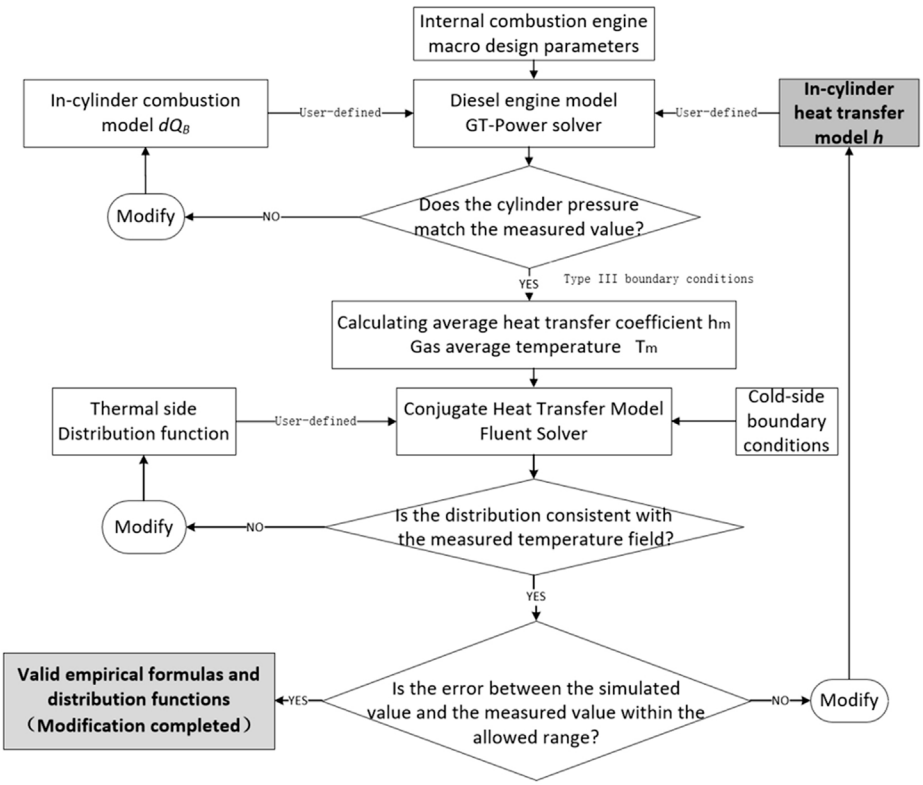

FIGURE 1 | Block diagram of semi-empirical formula correction.

TABLE 1 | Engine specifications.

Research type	Single-cylinder
Cycle	4-stroke DI GDI
Valves per cylinder	4
Bore × stroke	150 × 160 mm
Intake valve open	300 CAD
Intake valve close	−126 CAD
Exhaust valve open	110 CAD
Exhaust valve close	406 CAD
Connecting rod length	300 mm
Compression ratio	13.5
TDC clearance height	2 mm
Valve diameter	46 mm

As the sampling frequency of the temperature and strain data is 5 Hz and 100 kHz, respectively, a pair of independent hardware systems was utilized to ensure the system's reliability and data accuracy.

Experimental Data

To describe the plateau simulation system, first, the pressure and temperature of the intake air were controlled; the parameters such as throttle opening and injection advance angle were adjusted. Once the single-cylinder engine has been stable, the experimental system would collect the temperature data and other engine parameters. The engine performance data, such as excess air coefficient and exhaust gas temperature at different altitudes, are shown in **Figure 3**.

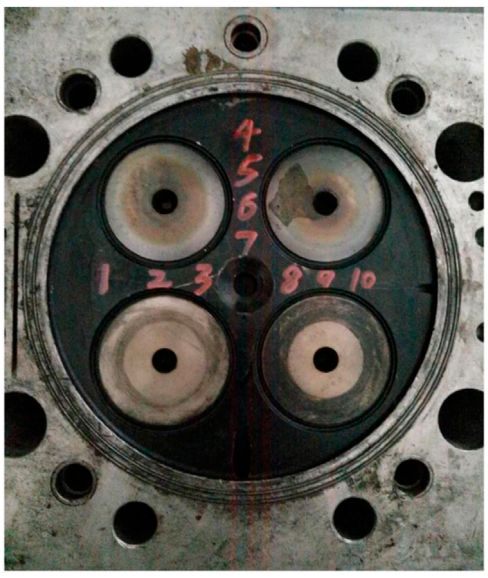

FIGURE 2 | Physical diagram of thermocouples.

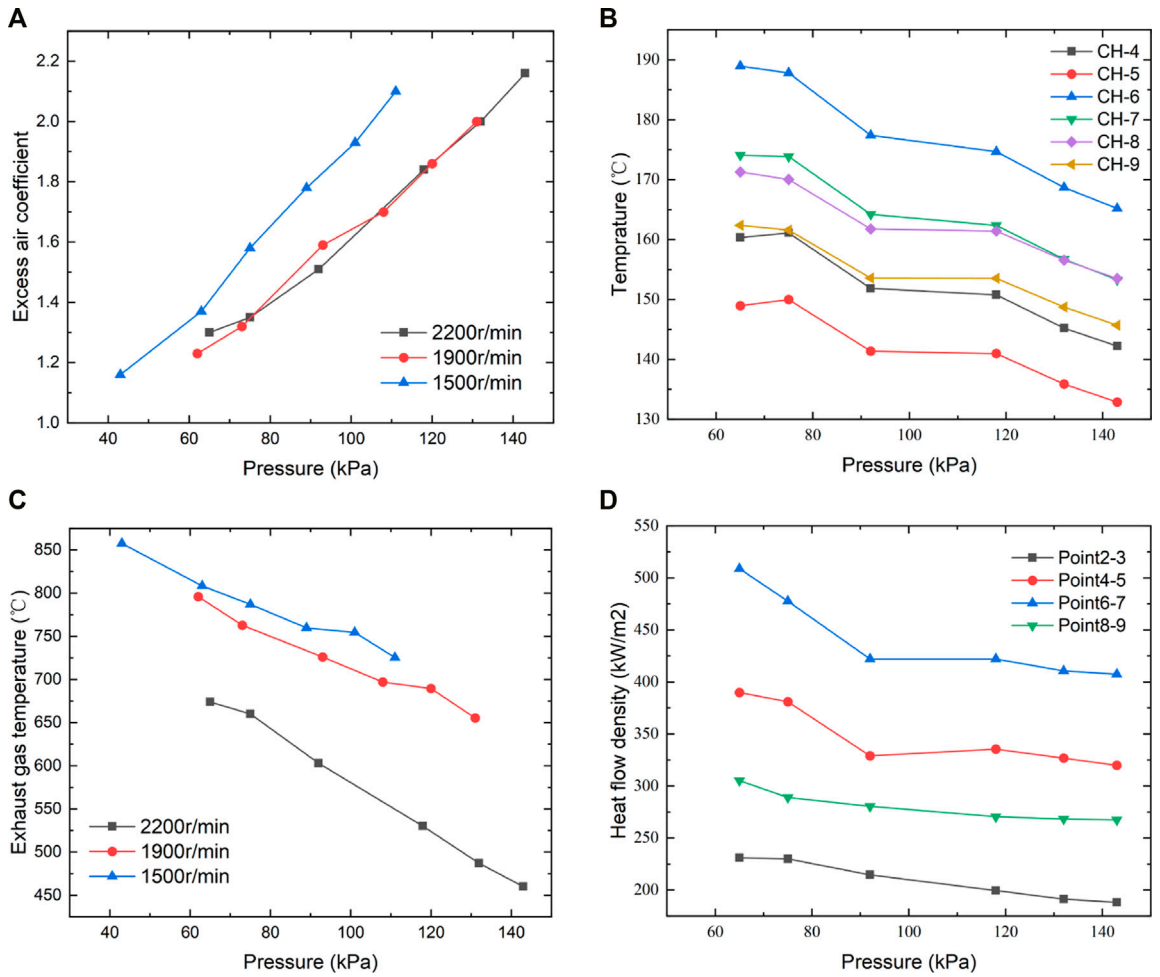

FIGURE 3 | Excessive air coefficient **(A)**, in-cylinder **(B)**, exhaust gas **(C)** temperature, and heat flow density **(D)** with altitude.

It can be inferred from **Figures 3A,B** that with altitude rise, the exhaust air temperature rose while the excess air coefficient dropped, regardless of various engine speeds. As expected, the higher altitude corresponded to lower intake pressure and, therefore, less intake air, echoing the decreased excess air coefficient in **Figure 3A**. The probable reason for the trend of exhaust gas temperature was that the higher equivalence ratio indicated less in-cylinder mass but similar chemical heat released, contributing to exhaust gas temperature according to basic thermal rules. In addition, faster engine speed leads to decreased excess air coefficient and exhaust gas temperature, possibly because of the shortened duration of the air intake process. The deteriorated combustion at higher speed also contributed to lower exhaust gas temperature.

The data relating to the temperature field at the fire face were measured by the experiment. **Figure 3C** shows the temperature at the relevant measurement point on the cylinder head at 2,200 r/min. The heat flow density of the cylinder head, as shown in **Figure 3D**, was measured by the double-layer thermocouples arranged in advance.

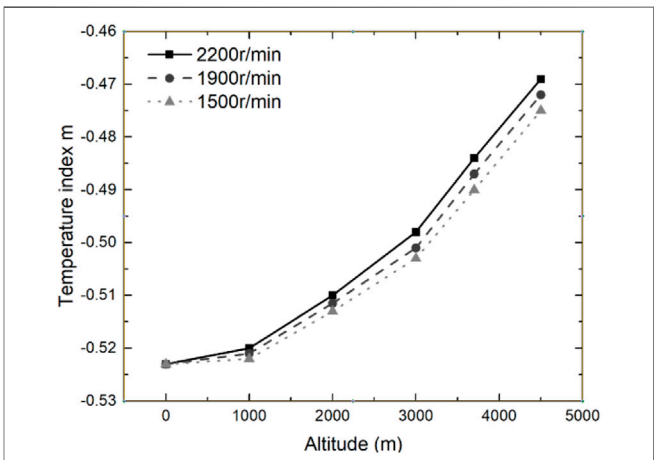

FIGURE 4 | Results of temperature index m under various conditions.

Zero-Dimensional Combustion Model

To further investigate the heat transfer model by simulation, the zero-dimensional combustion model and in-cylinder heat

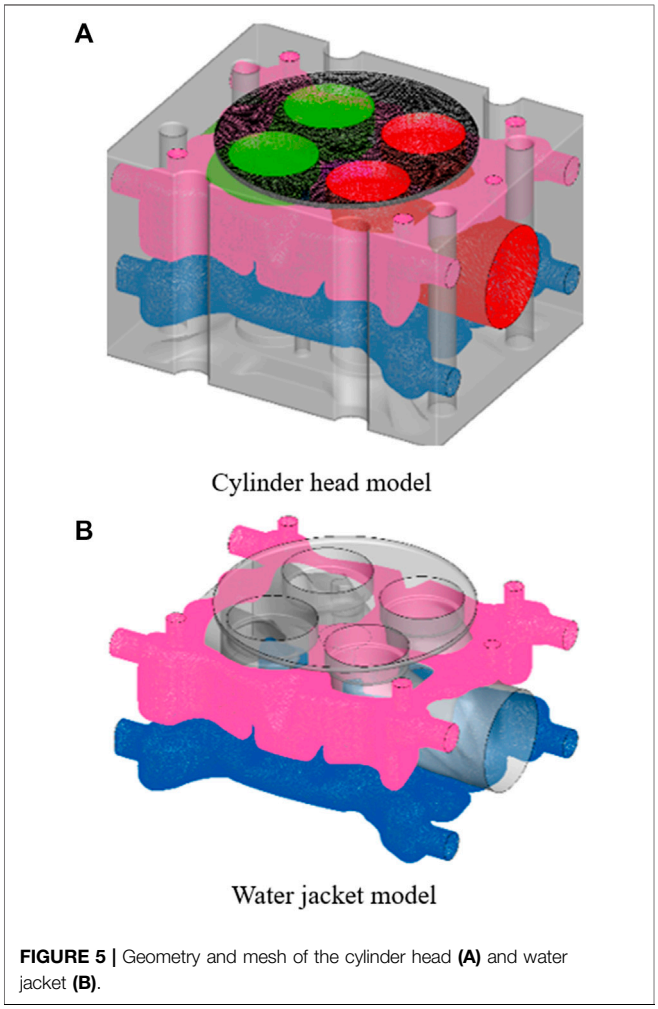

FIGURE 5 | Geometry and mesh of the cylinder head **(A)** and water jacket **(B)**.

TABLE 2 | Macro parameters of the diesel engine at plain.

Parameters	Measured value	Simulated value	Error range (%)
Maximum burst pressure/(bar)	127.6	126.8	0.63
Torque/(N·m)	295	306.8	4.00
Power/(kW)	68.24	70.7	3.61
Exhaust gas temperature/(K)	730.15	745.38	3.33

transfer model, which are the main relevant submodels in GT-POWER, were used to calculate the boundary conditions, such as in-cylinder temperature and heat transfer coefficient, which can be the boundary conditions to a three-dimension numerical simulation model that calculates the temperature field.

A zero-dimensional in-cylinder combustion model (Sitkei and Ramanaiah, 1972) is used in this study; it can be described by the following equation:

$$\frac{dQ_B}{d\varphi} = \eta_f H_u m_f \frac{dY}{d\varphi}, \tag{1}$$

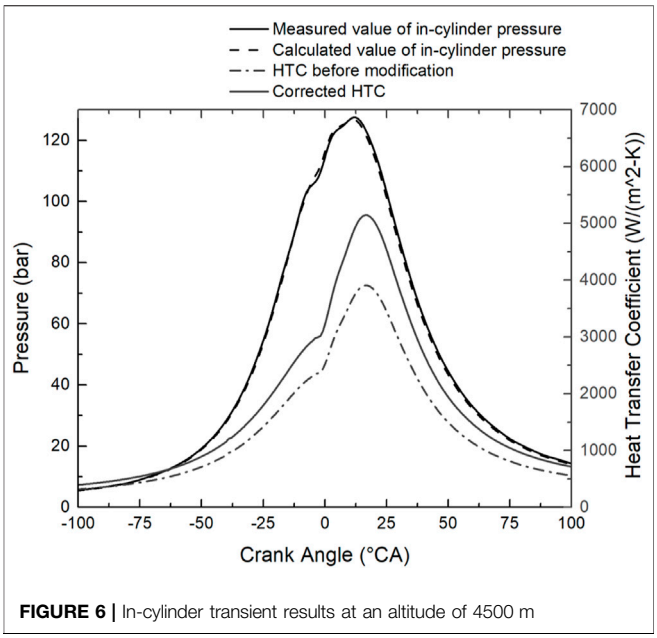

FIGURE 6 | In-cylinder transient results at an altitude of 4500 m

where Q_B is the heat release of the fuel, φ is crankshaft angle, Hu is the lower heating value of a fuel, η_f is combustion efficiency, m_f is the amount of the fuel, and Y is the mass percentage of the burned fuel, which can be described by the equation:

$$Y = \frac{m_B}{m_f} \times 100\%, \tag{2}$$

Wiebe (Annand, 1963) proposed a semi-empirical formula for combustion rate based on the chemical reaction kinetics of a homogenous mixture:

$$Y = 1 - \exp\left(-6.908\tau^{m+1}\right), \tag{3}$$

where m is the combustion quality index, which determines the shape of the combustion heat release curve. The constant 6.908 was obtained if the period between the start of combustion and 99% of the fuel burned is assumed to be the end of combustion, according to the literature (Liu and Dumitrescu, 2019a) and (Wiebe, 1962). τ is dimensionless time, calculated with the following equation:

$$\tau^* = \frac{\varphi - \varphi_B}{\Delta\varphi} = \frac{\varphi - \varphi_B}{\varphi_B - \varphi_C}, \tag{4}$$

where φ_B is combustion initiation angle, φ_C is combustion termination angle, and $\Delta\varphi$ is combustion duration angle.

Thus, substituting **Eq. 3** into **Eqs1**, **5** results in obtaining the calculation model of the combustion heat release rate:

$$\frac{dQ_B}{d\varphi} = 6.908\eta_f H_u m_f \frac{m+1}{\Delta\varphi}\tau^m \exp\left(-6.908\tau^{m+1}\right), \tag{5}$$

In addition, the differential equation for the change of in-cylinder bulk temperature T can be obtained from the first law of thermodynamics (energy conservation equation) as follows:

TABLE 3 | Calculation solution and test data at an altitude of 4500 m

Measurement point number	Measured temperature/K	Calculated temperature/K	Relative error/%
01	474.60	472.48	-1.05
02	487.04	484.19	-1.33
03	481.05	481.13	0.04
04	450.52	458.56	4.53
05	479.57	487.03	3.61
06	502.61	499.68	-1.28
07	480.91	490.24	4.49
08	471.98	481.68	4.88
09	488.01	483.28	-2.20
10	473.26	469.34	-1.96

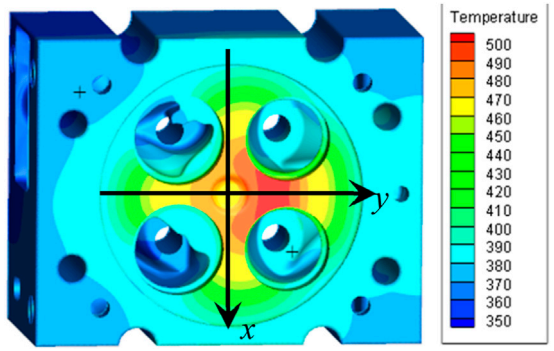

FIGURE 7 | Numerical results of cylinder head temperature.

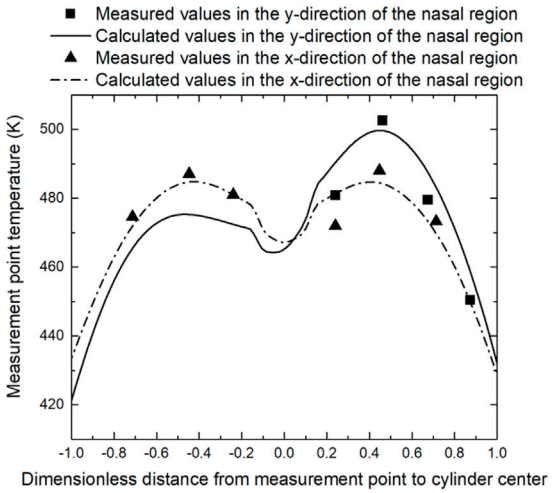

FIGURE 8 | Cylinder head temperature distribution along the path in **Figure 7**.

$$dT = \frac{1}{mc_v}\left(- pdV + \sum_i dQ_i + \sum_j h_j dm_j - udm - m\frac{\partial u}{\partial \Lambda}d\Lambda \right), \tag{6}$$

where pdV is the mechanical work, which is the product of cylinder pressure and cylinder volume change rate; $h_j dm_j$ is the energy, which is brought into the system by mass dm_j; the combustion process can be calculated by Weibe exothermic law, intake and exhaust stroke process can be calculated by the intake and exhaust system energy equation; u is the specific internal energy; c_v is constant volume specific heat; and dQ_i is the wall heat loss of the combustion chamber, which can be calculated by Newton's cooling formula.

In-Cylinder Heat Transfer Model

Heat Transfer Model Without Consideration of Elevation

To establish an in-cylinder head conjugate heat transfer (CHT) model for diesel engines, the main control equations include the coolant turbulence model, solid thermal conductivity model, fluid–solid interface treatment, and in-cylinder transient heat transfer boundary conditions.

As mentioned in *Experiments*, the experiment can obtain the temperature, heat flow density, and other parameters. However, the heat transfer coefficient and gas temperature cannot be measured directly, which requires building a proper model. The main equations are briefly sorted out below.

The heat transfer of coolant flow in the cylinder head water chamber can be described by the standard k-ε turbulence model, whose main controlling equations are the turbulent pulsation energy equation and the turbulent dissipation rate equation, and the detailed information is shown in the study by Yu et al. (2014). Moreover, the thermal conductivity of the solid region of the cylinder head can be described by **Eq. 7**, namely:

$$\rho c_p \frac{\partial T}{\partial t} = \nabla(\lambda \nabla(T)) + S_v, \tag{7}$$

where λ is the thermal conductivity, ρ is the density of the solid, c_p is the specific heat capacity of the solid, S_v is the unit volume of heat generation power, and the non-linear effect with temperature is considered in material properties.

The heat flux and temperature at the fluid–solid interface of the cylinder head are equal and can be described by **Eq. 8**, namely:

$$\begin{aligned} T_{w-solid} &= T_{w-fluid}, \\ q_{w-solid} &= q_{w-fluid}, \\ -\lambda\left(\frac{\partial T}{\partial n}\right)_w &= h(T_w - T_\infty), \end{aligned} \tag{8}$$

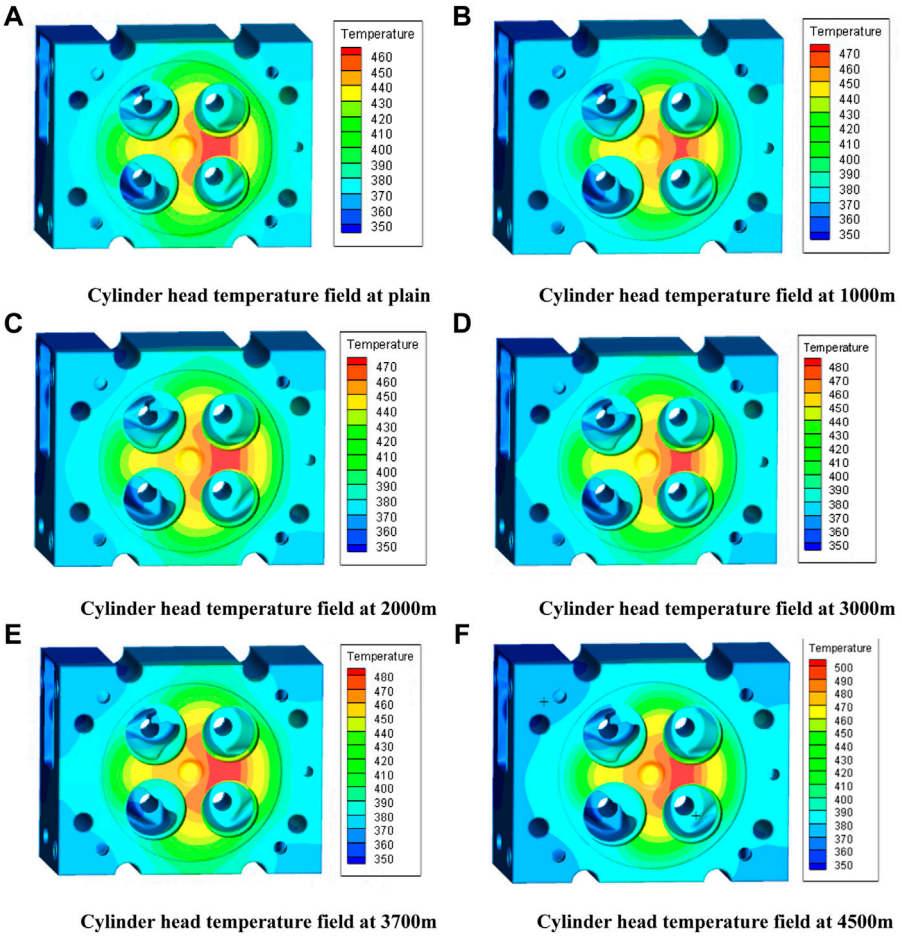

FIGURE 9 | Simulation of the cylinder head temperature field at various altitude from 0 to 4,500 m **(A–F)** at 2,200 r/min.

where q_w is the heat flow density at the interface, n is normal to the outside of the wall, h is the convective heat transfer coefficient, and T_w and T_∞ are the temperatures of the fluid at the interface and the mainstream region, respectively.

The in-cylinder heat transfer coefficient h and gas temperature T are difficult to measure directly by experimental methods; T can be calculated by **Eq. 6**, and the instantaneous average heat transfer coefficient h is the in-cylinder heat transfer boundary model; its semi-empirical formula can be expressed in the following general form according to Liu et al. (2020).

$$h = f(D) \cdot f(p, T) \cdot f(C_m) = cD^{1-n} p^n T^m w^n, \qquad (9)$$

where D is the cylinder bore; p is the instantaneous pressure in the cylinder; T is the instantaneous temperature in the cylinder; w is the function of the piston average speed, and Cm, n, c, and m are constants.

The instantaneous in-cylinder temperature and heat transfer coefficient are obtained from **Eq. 6** and **Eq. 9**, which is based on **Eq. 10** to obtain the corresponding average values.

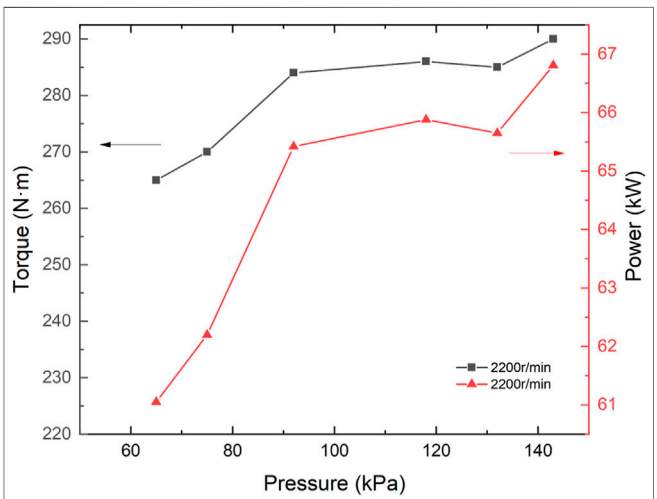

FIGURE 10 | Torque and power with altitude at 2200 r/min.

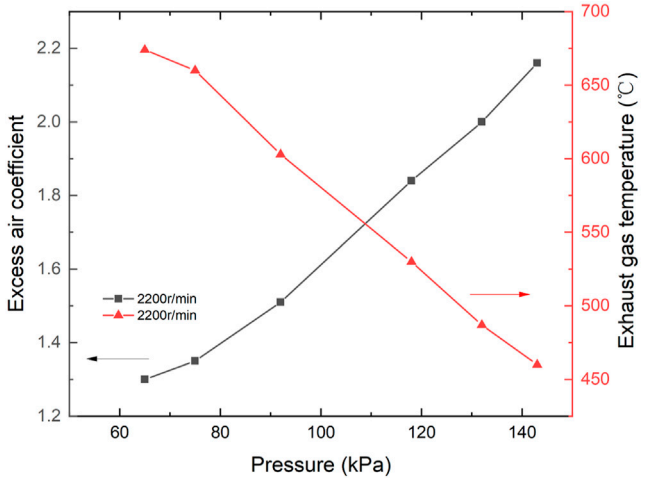

FIGURE 11 | Excess air coefficient and exhaust gas temperature with altitude at 2200 r/min.

$$\begin{cases} h_m = \dfrac{1}{4\pi}\displaystyle\int_0^{4\pi} h d\varphi \\ T_m = \dfrac{1}{4\pi h_m}\displaystyle\int_0^{4\pi} hT d\varphi \end{cases}, \tag{10}$$

where T_m is the integrated average gas temperature and h_m is the cycle average heat transfer coefficient.

To describe the spatial distribution of the average heat transfer coefficient in the cylinder head fire surface, the variation of h_m along the cylinder radial direction is written as a distribution function of the following equation.

$$h_r = h_m\left[a_0 + a_1\left(\frac{r}{r_0}\right) + a_2\left(\frac{r}{r_0}\right)^2\right], \tag{11}$$

where r is the distance from a point P on the fire surface to the cylinder center; r_0 is the cylinder radius; h_r is the heat transfer coefficient at point P; a_0, a_1, a_2, and a_3 are constant coefficients. The values are $a_0 = 0.5$, $a_1 = 3$, and $a_2 = -3$ for the test model in this article.

T_m and h_m is loaded to the cylinder head fire surface as the third type of boundary conditions, which can be used to solve the conjugate heat transfer model.

Heat Transfer Boundary Modification at Variable Altitudes

The semi-empirical equation shown in **Eq. 9** is derived from the in-tube turbulence test correlation and experimental data. The $f(p, T)$ is the part related to the in-cylinder mixture physical parameters. Moreover, mass density ρ, thermal conductivity λ, and viscosity η can be expressed as a function of temperature according to Woschni (1967) as shown in **Eq. 12**.

$$\rho = \frac{pm}{R_g T}, \quad \lambda = k_1 T^a, \quad \eta = k_2 T^b, \tag{12}$$

where the pressure index $n = 0.8$ and the temperature index $m = a\text{-}(b+1)n$.

The in-cylinder components differ with altitude changes due to degradation of combustion and reaction caused by lower intake pressure and, therefore, equivalence ratio. That is the main reason that the temperature index a, b changes and therefore the temperature index m in **Eq. 13**, as Liu and Dumitrescu (2019b supported.

Therefore, it is important to build a correlation formula about the temperature index m and altitude to simulate the heat transfer process at different altitudes.

The most commonly used semi-empirical model is the Woschni formula (Woschni, 1967), which has been modified by Hohenberg (1979), Huber et al. (1990). Comparing the characteristics and applicability of various in-cylinder heat transfer models, the Woschni formula (Woschni, 1967) was used as the basic model in this study, namely,

$$h = 0.013D^{-0.2}p^{0.8}T^m\left[c_1 C_m + c_2\frac{T_1 V_s}{p_1 V_1}(p - p_0)\right]^{0.8}, \tag{13}$$

where h is the convective heat transfer coefficient, W/(m^2·K); C_m is the average piston velocity, m/s; D is the cylinder diameter, m; p and T are the instantaneous pressure (Pa) and temperature (K) of the cylinder gas, respectively; p_1, V_1, and T_1 are the pressure (Pa), volume (m^3), and temperature (K) of the cylinder gas at the moment of IVC, respectively; V_s is the working volume of the cylinder, m^3; p_0 is the cylinder gas pressure(Pa) under the motored condition; c_1 is the airflow velocity coefficient; c_2 is the combustion chamber shape coefficient; m is the temperature index, and the initial value is -0.523.

The structural and operational parameters of the test model were input into the GT-Power model, and the user-defined heat transfer model code was compiled. The Woschni equation (Woschni, 1967) with customizable temperature index term m was loaded into the GT-Power software (Heywood, 2018). Moreover, the temperature index m was adjusted to calculate the average heat transfer coefficient h_m and the average gas temperature T_m in the cylinder under different operating conditions.

In Fluent software, h_m, T_m, and the wall distribution function (shown in **Eq. 11**) are loaded onto the cylinder head fire surface as the third type of boundary conditions by compiling the user-defined function (UDF) (Lefebvre, 2013); the cold side boundary, as well as other boundary conditions, is set up according to the test data. Finally, the conjugate heat transfer model is solved to obtain the cylinder head temperature field.

The measured and calculated results of the temperature field were compared to correct the heat transfer model. If the error between measured and calculated values is unacceptable, then the semi-empirical formula of the temperature index m would be adjusted to reduce the disparity until the model precision could meet the requirement.

All the correction results of the temperature index m at each altitude for engine speed of 1500 r/min, 1900 r/min, and 2200 r/min are summarized, as shown in **Figure 4**.

The effect of altitude on the heat transfer model was carried out by mathematical statistics. The correspondence between

temperature index m and intake pressure can be fitted by the least-squares method, and the fitting results are shown in **Eq. 14**.

$$m = -0.523 + (b_0 + b_1 N)H^2 \times 10^{-9}, \quad (14)$$

where N is the engine speed (r/min), H is the altitude(m), $b_0 = 1.5$, and $b_1 = 5.5 \times$ 10-4.

Numerical Simulation Model

The numerical simulation of the diesel engine thermal state was calculated by the commercial software ANSYS Fluent in this study. The boundary conditions of the heating surface were obtained from the GT-Power model (Serrano et al., 2015), and the boundary conditions on the cooling surface were obtained from the measured data (He et al., 2013). The cylinder head could be divided into two parts: solid and liquid, where the liquid part is a double-layer cooling water jacket. The 3D model shown in **Figure 5** was divided by tetrahedral meshing, and the minimum mesh size is 1~2 mm. The total number of grids is controlled at 9.34 million after grid independence analysis.

The standard k-ε turbulence model (Kim et al., 2008; Liu and Dumitrescu, 2018) was used in this study to describe fluid flow, whose main controlling equations are the turbulent pulsation energy equation k and the turbulent dissipation ε rate equation (Yakhot and Orszag, 1986; Han and Reitz, 1995; Liu and Dumitrescu, 2019c; Liu and Dumitrescu, 2019d) as shown in the following equations:

$$\frac{\partial}{\partial t}(\rho k) + \frac{\partial}{\partial x_i}(\rho k u_i) = \frac{\partial}{\partial x_j}\left[\left(\mu + \frac{\mu_t}{\sigma_k}\right)\frac{\partial k}{\partial x_j}\right] + G_k + G_b - \rho\varepsilon - Y_M + S_k, \quad (15)$$

$$\frac{\partial}{\partial t}(\rho \varepsilon) + \frac{\partial}{\partial x_i}(\rho \varepsilon u_i) = \frac{\partial}{\partial x_j}\left[\left(\mu + \frac{\mu_t}{\sigma_\varepsilon}\right)\frac{\partial \varepsilon}{\partial x_j}\right] + C_{1\varepsilon}\frac{\varepsilon}{k}(G_k + C_{3\varepsilon}G_b) - C_{2\varepsilon}\rho\frac{\varepsilon^2}{k} + S_\varepsilon, \quad (16)$$

where G_k is the turbulent energy caused by the mean velocity gradient, G_b is the turbulent energy due to buoyancy, Y_M represents the effect of fluctuating expansion incompressible turbulence on the total dissipation rate, $C_{1\varepsilon}$, $C_{2\varepsilon}$, and $C_{3\varepsilon}$are constants, σ_k, and σ_ε are the turbulent Prandtl number of k and ε, respectively, and S_k and S_ε are user-defined source terms.

The thermal conductivity controlling equation for the solid side and the heat transfer between the medium can be described by **Eq. 7** and **Eq. 8**.

RESULTS AND DISCUSSION

Numerical Simulation Validation

The result at the engine speed of 2200 r/min under the fixed altitude (4500 m) was chosen as a typical result to analyze. A zero-D calibrated diesel engine model was established that consisted of a combustion chamber module, a camshaft-piston module, a set of intake valves, and a set of exhaust valves. Moreover, the geometric design parameters of the single-cylinder engine as well as the test values of intake pressure, cyclic injection volume, and injection advance angle were input into the GT-Power model for calculation.

Meanwhile, the heat transfer model shown in **Eq. 13** and **Eq. 14** was written as a Fortran code, together with the GT model, to calculate the pressure, temperature, and convective heat transfer coefficient of the in-cylinder gas. The maximum burst pressure, torque, power, and exhaust gas temperature were compared with the measured values as shown in **Table 2**. The errors of each parameter were within 5%, indicating that the model successfully reflected engine performance.

The predicted and measured in-cylinder pressure, together with the heat transfer coefficient calculated by the original and modified model, are shown in **Figure 6**. The highly coincident pressure indicated a satisfied precision of the one-dimensional engine model. In addition, the heat transfer coefficient calculated by the modified model was apparently higher, corresponding to a 45.69% increment of the average value, which also proved the importance of heat transfer model correction.

The simulation results of the cylinder head temperature field are shown in **Figure 6**. To check the accuracy of the simulation results, the simulated and measured temperatures at the same position were compared, as **Table 3** shows, implying that the errors are within 5%. Therefore, it was proven that the convective heat transfer model equation under this working condition is accurate enough.

To further assess the precision of the modified heat transfer model, **Figure 7** shows the simulated temperature distribution at X, Y direction (**Figure 8**) of the cylinder head and the measured data. It is of interest to figure out that the central depression of the temperature profile was probably caused by the central sunk surface, which reduced the local convection motion and, therefore, the heat transfer coefficient. In addition, the heat flow in the exhaust valve nose area was apparently higher, which was mainly due to the strong exhaust flow motion. The high coincidence of measured and calculated data suggested a satisfied accuracy of the corrected model.

Effect of Intake Air Pressure on Temperature Distribution

The distribution of the cylinder head temperature field for each altitude condition is shown in **Figure 9**. The peak temperature was located at the firing surface nose area on the exhaust port side. With the altitude rise, the maximum temperature increased, indicating that the deterioration of combustion also contributed to more severe post-combustion, resulting in a higher heat transfer coefficient. That is the probable reason for the increased peak temperature at the cylinder head.

Effect of Intake Air Pressure on Power Performance

The test data for the 2200 r/min operating condition at the maximum power point are shown in **Figures 10**, **11**. As can

be seen from **Figure 10**, torque and power decreased with altitude rise, probably due to reduced air pressure. The torque dropped from 290 N·m to 265 N·m, and power dropped from 66.81 to 61.05 kW.

Figure 11 shows the excess air coefficient and exhaust gas temperature at each altitude. With the altitude rise, the exhaust gas temperature was gradually rising as analyzed above. In addition, the intake pressure being too low at the last two altitudes, the exhaust temperature exceeded the test safety limits, and the oil supply parameters were adjusted to reduce the torque.

It was also important to point out that there was a sudden change in the exhaust temperature and excess air coefficient as the altitude increased from 2000 to 3000 m because these altitudes corresponded to a sudden drop in intake pressure.

Therefore, it can be concluded that under calibration conditions, as the altitude rises, the temperature field of the cylinder head fire surface, exhaust temperature, excess air coefficient, and other parameters increase, indicating that the engine's combustion deteriorates due to reduced intake volume and decreased excess air coefficient. Therefore, the concentration of soot in the exhaust gas increases, and then the exhaust temperature increases. However, the thermal state of the engine changed abruptly when the altitude rose to 3000 m. When the altitude rose from 0 to 4500 m, the exhaust gas temperature increased by 46.52%, and the excess air coefficient decreased by 39.81%.

SUMMARY AND CONCLUSION

In this study, the in-cylinder heat transfer model has been modified based on simulation analysis and experimental verification. The results indicated that the modified heat transfer model can be used in variable altitude operating conditions, and the main conclusions are as follows.

(1) By comparing different heat transfer correlations, the Woschni formula is selected as the basic model. The temperature index m in the formula is determined as the key correction variable by analyzing the effect of altitude on the model parameters.

(2) A conjugate heat transfer model has been established, and the in-cylinder working process and cylinder head temperature field distribution have been calculated. To obtain the in-cylinder heat transfer model applicable to variable altitudes, the relationship between temperature index m, altitude H, and engine speed N was fitted by the least-squares method. The results indicated that the average heat transfer coefficient hm increased by 45.69% after correction, which also suggests that the traditional model could no longer adapt to the requirements of variable altitudes.

(3) The new modified model is used to calculate the results under different engine speeds at variable altitudes. By comparing the calculation results with the test results, it is found that the errors of the model are less than 5%. Therefore, the new model has good adaptability and precision under various altitudes of operating conditions.

DATA AVAILABILITY STATEMENT

The raw data supporting the conclusion of this article will be made available by the authors, without undue reservation.

AUTHOR CONTRIBUTIONS

YZ: conceptualization, methodology, simulation, and writing-draft preparation; YY: simulation, writing-draft preparation; RY: validation and writing-draft preparation; QW: simulation and writing-draftpreparation; BZ: analysis; QG: analysis; ZL: analysis and supervision; JF: methodology and validation.

FUNDING

The study was jointly funded by the Natural Science Foundation of Zhejiang Province (LQ20E060003), the Project Teacher Research Fund Project (J-202116), and the Projects of Hangzhou Agricultural and Social Development Research Program (20201203B128 and 20212013B04).

REFERENCES

Ambrogi, L., Liu, J., Battistoni, M., Dumitrescu, C. E., and Gasbarro, L. (2019). CFD Investigation of the Effects of Gas' Methane Number on the Performance of a Heavy-Duty Natural-Gas Spark-Ignition Engine. *SAE Tech. Paper* 1, 1. doi:10.4271/2019-24-0008

Annand, W. J. (1963). Heat Transfer in the Cylinders of Reciprocating Internal Combustion Engines. *Proc. Inst. Mech. Eng.* 177 (1), 973–996.

Borman, G., and Nishiwaki, K. (1987). Internal-combustion Engine Heat Transfer. *Prog. Energ. Combustion Sci.* 13 (1), 1–46. doi:10.1016/0360-1285(87)90005-0

Broekaert, S., Demuynck, J., De Cuyper, T., De Paepe, M., and Verhelst, S. (2016). Heat Transfer in Premixed Spark Ignition Engines Part I: Identification of the Factors Influencing Heat Transfer. *Energy* 116, 380–391. doi:10.1016/j.energy.2016.08.065

Chen, X., Yu, X., Lu, Y., Huang, R., Liu, Z., Huang, Y., et al. (2017). Study of Different Cooling Structures on the thermal Status of an Internal Combustion Engine. *Appl. Therm. Eng.* 116, 419–432. doi:10.1016/j.applthermaleng.2017.01.037

De Cuyper, T., Demuynck, J., Broekaert, S., De Paepe, M., and Verhelst, S. (2016). Heat Transfer in Premixed Spark Ignition Engines Part II: Systematic Analysis of the Heat Transfer Phenomena. *Energy* 116, 851–860. doi:10.1016/j.energy.2016.10.032

Fagundez, J. L. S., Sari, R. L., Martins, M. E. S., and Salau, N. P. G. (2017). Comparative Analysis of Different Heat Transfer Correlations in a Two-Zone Combustion Model Applied on a SI Engine Fueled with Wet Ethanol. *Appl. Therm. Eng.* 115, 22–32. doi:10.1016/j.applthermaleng.2016.12.121

Gholinia, M., Pourfallah, M., and Chamani, H. R. (2018). Numerical Investigation of Heat Transfers in the Water Jacket of Heavy Duty Diesel Engine by Considering Boiling Phenomenon. *Case Stud. Therm. Eng.* 12, 497–509. doi:10.1016/j.csite.2018.07.003

Han, Z., and Reitz, R. D. (1995). Turbulence Modeling of Internal Combustion Engines Using RNG κ-ε Models. *Combustion Sci. Technology* 106 (4-6), 267–295. doi:10.1080/00102209508907782

Han, Z., and Reitz, R. D. (1997). A Temperature wall Function Formulation for Variable-Density Turbulent Flows with Application to Engine Convective Heat Transfer Modeling. *Int. J. Heat Mass Transfer* 40 (3), 613–625. doi:10.1016/0017-9310(96)00117-2

He, W. F., Dai, Y. P., Wang, J. F., Li, M. Q., and Ma, Q. Z. (2013). Performance Prediction of an Air-Cooled Steam Condenser Using UDF Method. *Appl. Therm. Eng.* 50 (1), 1339–1350. doi:10.1016/j.applthermaleng.2012.06.020

Heywood, J. B. (2018). *Internal Combustion Engine Fundamentals*. McGraw-Hill Education.

Hohenberg, G. F. (1979). Advanced Approaches for Heat Transfer Calculations. *SAE Tech. Paper* 1, 790825. doi:10.4271/790825

Huber, K., Woschni, G., and Zeilinger, K. (1990). Investigations on Heat Transfer in Internal Combustion Engines under Low Load and Motoring Conditions. *SAE Tech. Paper* 1, 905018.

Kim, H.-M., Park, S.-K., Choi, K.-S., Wang, H.-M., Lee, D.-H., Lee, D.-K., et al. (2008). Investigation on the Flow and Heat Transfer Characteristics of Diesel Engine EGR Coolers. *Int.J Automot. Technol.* 9 (2), 149–153. doi:10.1007/s12239-008-0019-4

Launder, B. E., and Spalding, D. B. (1974). The Numerical Computation of Turbulent Flows. *Computer Methods Appl. Mech. Eng.* 3 (2), 269–289. doi:10.1016/0045-7825(74)90029-2

Lefebvre, A. H. (2013). Ignition Theory and its Application to the Altitude Relighting Performance of Gas Turbine Combustors. *Combustion Heat Transfer Gas Turbine Systems: Proc. Int. Propulsion Symp.* 11, 105.

Liu, J., Dumitrescu, C. E., and Bommisetty, H. (2019). An Experimental Study of the Combustion Process in a Natural-Gas Spark-Ignition Engine. American Society of Mechanical Engineers 2019. *Int. Mech. Eng. Congress Exposition* 1, IMECE2019–11637. doi:10.1115/imece2019-11637

Liu, J., and Dumitrescu, C. E. (2019). Lean-burn Characteristics of a Heavy-Duty Diesel Engine Retrofitted to Natural-Gas Spark Ignition. *J. Eng. Gas Turbines Power* 141 (7), 071013. doi:10.1115/1.4042501

Liu, J., Huang, Q., Ulishney, C., and Dumitrescu, C. E. (2022). Comparison of Random forest and Neural Network in Modelling the Performance and Emissions of a Natural Gas Spark Ignition Engine. *J. Energ. Resour. Technology* 144 (3), 032310. doi:10.1115/1.4053301

Liu, J., Ulishney, C., and Dumitrescu, C. E. (2020). Characterizing Two-Stage Combustion Process in a Natural Gas Spark Ignition Engine Based on Multi-Wiebe Function Model. *J. Energ. Resour. Technology* 142 (10), 102302. doi:10.1115/1.4046793

Liu, J., and Dumitrescu, C. E. (2018). 3D CFD Simulation of a CI Engine Converted to SI Natural Gas Operation Using the G-Equation. *Fuel* 232, 833–844. doi:10.1016/j.fuel.2018.05.159

Liu, J., and Dumitrescu, C. E. (2019). Analysis of Two-Stage Natural-Gas Lean Combustion inside a Diesel Geometry. *Appl. Therm. Eng.* 160, 114116. doi:10.1016/j.applthermaleng.2019.114116

Liu, J., and Dumitrescu, C. E. (2019). Numerical Investigation of Methane Number and Wobbe index Effects in Lean-Burn Natural Gas Spark-Ignition Combustion. *Energy Fuels* 33 (5), 4564–4574. doi:10.1021/acs.energyfuels.8b04463

Liu, J., and Dumitrescu, C. E. (2019). Single and Double Wiebe Function Combustion Model for a Heavy-Duty Diesel Engine Retrofitted to Natural-Gas Spark-Ignition. *Appl. Energ.* 248, 95–103. doi:10.1016/j.apenergy.2019.04.098

Liu, J., and Wang, H. (2022). Machine Learning Assisted Modeling of Mixing Timescale for LES/PDF of High-Karlovitz Turbulent Premixed Combustion. *Combustion and Flame* 238, 111895. doi:10.1016/j.combustflame.2021.111895

Liu, Z., and Liu, J. (2021). Effect of Altitude on in-cylinder Heat Transfer of a Heavy Duty Diesel Engine. American Society of Mechanical Engineers 2021. *Heat Transfer Summer Conf.* 1, HT2021–62351. doi:10.1115/ht2021-62351

Liu, Z., and Liu, J. (2021). "Effects of Increased Altitude on the Diesel Engine Performance," in *The 2nd World Congress on Internal Combustion Engines*, P0387.

Liu, Z., and Liu, J. (2021). Experimental Investigation of Combustion Characteristics of a Single cylinder Diesel Engine at Altitude. *J. Energ. Resour. Technology* 143 (10), 102306. doi:10.1115/1.4050575

Liu, Z., Zhang, Y., Fu, J., and Liu, J. (2021). *Three-dimensional Fluid Dynamics Modeling of a 6V150 Diesel Engine. American Society of Mechanical Engineers 2011*. International Mechanical Engineering Congress and Exposition, IMECE2021–67711.

Liu, Z., and Liu, J. (2022). Effect of Altitude Conditions on Combustion and Performance of a Turbocharged Direct-Injection Diesel Engine. *Proc. Inst. Mech. Eng. D: J. Automobile Eng.* 236 (4), 582–593. doi:10.1177/09544070211026204

Lu, X., Li, Q., Zhang, W., Guo, Y., He, T., and Zou, D. (2013). Thermal Analysis on Piston of marine Diesel Engine. *Appl. Therm. Eng.* 50 (1), 168–176. doi:10.1016/j.applthermaleng.2012.06.021

Lu, Y., Zhang, X., Xiang, P., and Dong, D. (2017). Analysis of thermal Temperature fields and thermal Stress under Steady Temperature Field of Diesel Engine Piston. *Appl. Therm. Eng.* 113, 796–812. doi:10.1016/j.applthermaleng.2016.11.070

Michl, J., Neumann, J., Rottengruber, H., and Wensing, M. (2016). Derivation and Validation of a Heat Transfer Model in a Hydrogen Combustion Engine. *Appl. Therm. Eng.* 98, 502–512. doi:10.1016/j.applthermaleng.2015.12.062

Perez, P. L., and Boehman, A. L. (2010). Performance of a Single-cylinder Diesel Engine Using Oxygen-Enriched Intake Air at Simulated High-Altitude Conditions. *Aerospace Sci. Technology* 14 (2), 83–94. doi:10.1016/j.ast.2009.08.001

Serrano, J., Olmeda, P., Arnau, F., and Dombrovsky, A. (2015). General Procedure for the Determination of Heat Transfer Properties in Small Automotive Turbochargers. *SAE Int. J. Engines* 8 (1), 30–41. doi:10.4271/2014-01-2857

Shannak, B. A., and Alhasan, M. (2002). Effect of Atmospheric Altitude on Engine Performance. *Forschung Im Ingenieurwesen* 67 (4), 157–160. doi:10.1007/s10010-002-0087-y

Shen, L., Shen, Y., Yan, W., and Xu, J. (1995). Combustion Process of Diesel Engines at Regions with Different Altitude. *SAE Tech. Paper* 1, 950857. doi:10.4271/950857

Sideri, M., Berton, A., and D'Orrico, F. (2017). Assessment of the wall Heat Transfer in 3D-CFD in-cylinder Simulations of High Performance Diesel Engines. *Energ. Proced.* 126, 963–970. doi:10.1016/j.egypro.2017.08.187

Sitkei, G., and Ramanaiah, G. V. (1972). A Rational Approach for Calculation of Heat Transfer in Diesel Engines. *SAE Tech. Paper* 1, 720027. doi:10.4271/720027

Sroka, Z. J. (2012). Some Aspects of thermal Load and Operating Indexes after Downsizing for Internal Combustion Engine. *J. Therm. Anal. Calorim.* 110 (1), 51–58. doi:10.1007/s10973-011-2064-x

Stocchi, I., Liu, J., Dumitrescu, C. E., Battistoni, M., and Grimaldi, C. N. (2019). Effect of Piston Crevices on the Numerical Simulation of a Heavy-Duty Diesel Engine Retrofitted to Natural-Gas Spark-Ignition Operation. *J. Energ. Resour. Technology* 141 (11), 112204. doi:10.1115/1.4043709

Wang, X., Ge, Y., Yu, L., and Feng, X. (2013). Effects of Altitude on the thermal Efficiency of a Heavy-Duty Diesel Engine. *Energy* 59, 543–548. doi:10.1016/j.energy.2013.06.050

Wiebe, I. (1962). *Progress in Engine Cycle Analysis: Combustion Rate and Cycle Processes*. Ural-Siberia Branch: Mashgiz, 271.

Woschni, G. (1967). A Universally Applicable Equation for the Instantaneous Heat Transfer Coefficient in the Internal Combustion Engine. *SAE Tech. Paper* 1, 670931. doi:10.4271/670931

Yakhot, V., and Orszag, S. A. (1986). Renormalization Group Analysis of Turbulence. I. Basic Theory. *J. Sci. Comput.* 1 (1), 3–51. doi:10.1007/bf01061452

Yang, M., Gu, Y., Deng, K., Yang, Z., and Zhang, Y. (2018). Analysis on Altitude Adaptability of Turbocharging Systems for a Heavy-Duty Diesel Engine. *Appl. Therm. Eng.* 128, 1196–1207. doi:10.1016/j.applthermaleng.2017.09.065

Yu, L., Ge, Y., Tan, J., He, C., Wang, X., Liu, H., et al. (2014). Experimental Investigation of the Impact of Biodiesel on the Combustion and Emission

Characteristics of a Heavy Duty Diesel Engine at Various Altitudes. *Fuel* 115, 220–226. doi:10.1016/j.fuel.2013.06.056

Zhang, B., Liu, Z., Zhang, Y., Chen, S., and Yu, X. (2016). Changing Regularity of Diesel cylinder Head's thermal State under Variable Altitude Condition. *J. Mech. Electr. Eng.* 33 (10), 1203–1207.

Zhang, H., Shi, L., Deng, K., Liu, S., and Yang, Z. (2020). Experiment investigation on the performance and regulation rule of two-stage turbocharged diesel engine for various altitudes operation. *Energy* 192, 116653. doi:10.1016/j.energy.2019.116653

Conflict of Interest: The authors declare that the research was conducted in the absence of any commercial or financial relationships that could be construed as a potential conflict of interest.

Publisher's Note: All claims expressed in this article are solely those of the authors and do not necessarily represent those of their affiliated organizations, or those of the publisher, the editors, and the reviewers. Any product that may be evaluated in this article, or claim that may be made by its manufacturer, is not guaranteed or endorsed by the publisher.

frontiers in Energy Research

ORIGINAL RESEARCH
published: 25 February 2022
doi: 10.3389/fenrg.2022.823386

Numerical Investigations of Injection Timing Effects on a GDI Engine Performance: Part B, In-Cylinder Emission Formation and Oxidation Process

Yu Zhang[1], Ruomiao Yang[2], Yuchao Yan[2], Ruijie Li[3], Jiahong Fu[1] and Zhentao Liu[2]**

[1]Department of Mechanical Engineering, Zhejiang University City College, Hangzhou, China, [2]Power Machinery and Vehicular Engineering Institute, Zhejiang University, Hangzhou, China, [3]Technical Institute of Physics and Chemistry, Chinese Academy of Sciences, Beijing, China

The emphasis on environmental protection and energy security has promoted automobile engine technology toward low emission and economy. While the traditional port fuel injection engine can hardly meet the latest regulations and requirements, the gasoline direct injection (GDI) engine becomes a hot research topic because of its potential to reduce fuel consumption and emissions. Since injection timing has a determining effect on overall engine performance, this paper aimed to investigate the injection timing effects on mixture formation and emissions. A validated three-dimensional numerical simulation model of a 4-stroke GDI engine combustion chamber was adopted. In a previous work (Part A), the in-cylinder combustion process has been discussed. In this study, the simulation results demonstrate that with the injection timing advancing, the fuel–gas mixture was more uniformly distributed and combusted more completely; the CO, UHC, and soot had decreased sharply by 80.6, 99.2, and 97.5%; the NOx emission increased by 151.7%. The optimized injection timing for this case was 300 CA BTDC. Moreover, this paper studied the in-cylinder views of injection timing effects on mixture formation and emission, providing reference to optimize injection of GDI engine.

Keywords: GDI engine, injection timing, emission, CFD, oxidation

OPEN ACCESS

Edited by:
Jun Li,
Guangzhou Institute of Energy Conversion (CAS), China

Reviewed by:
Haifeng Liu,
Tianjin University, China
Saravanan Balusamy,
Indian Institute of Technology Hyderabad, India

****Correspondence:***
Jiahong Fu
fujh@zucc.edu.cn
Zhentao Liu
liuzt@zju.edu.cn

Specialty section:
This article was submitted to Advanced Clean Fuel Technologies, a section of the journal Frontiers in Energy Research

Received: *27 November 2021*
Accepted: *13 January 2022*
Published: *25 February 2022*

Citation:
Zhang Y, Yang R, Yan Y, Li R, Fu J and Liu Z (2022) Numerical Investigations of Injection Timing Effects on a GDI Engine Performance: Part B, In-Cylinder Emission Formation and Oxidation Process. Front. Energy Res. 10:823386. doi: 10.3389/fenrg.2022.823386

INTRODUCTION

The increasing prominent energy shortage and emission pollution have put forward severe challenges to the automobile power system (Gasbarro et al., 2019; Yang et al., 2021). Therefore, reducing emissions and improving the efficiency of internal combustion engines (ICEs) have become the main targets of research on vehicle engines (Ambrogi et al., 2019; Duronio et al., 2020). Although the electric vehicle is in the ascendant, short driving range (Liu A. et al., 2021; Xu et al., 2021), high cost (Lin and Li, 2019; Wang and Shen, 2021a), and battery safety are the main disadvantages that cannot be ignored (Zhao et al., 1999; Wang and Shen, 2020). Therefore, the ICE will still be the main

Abbreviations: 3D, three-dimensional; AFR, air–fuel ratio; ATDC, after top dead center; BTDC, before top dead center; CAD, crank angle degree; CFD, computational fluid dynamics; CO, carbon monoxide; DMF, dimethylfuran; DPF, diesel particulate filter; GDI, gasoline direct injection; ICE, internal combustion engine; IT, injection timing; NOx, nitrogen oxide; PFI, port fuel injection; RON, research octane number; SI, spark-ignition engine; TWC, three-way catalyst; UHC, unburned hydrocarbon.

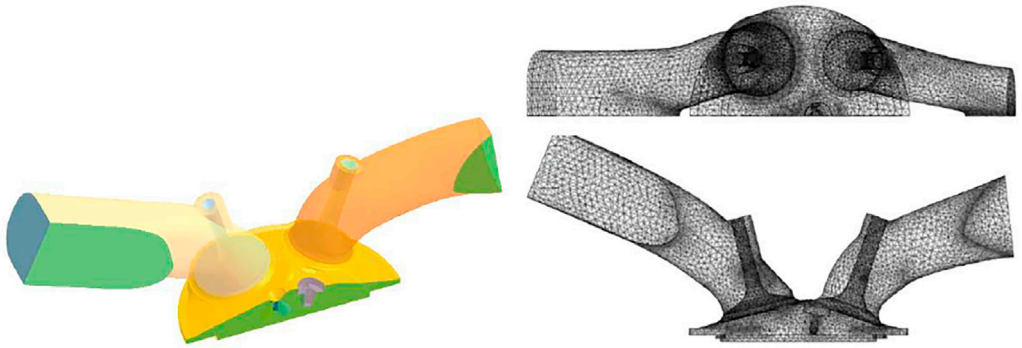

FIGURE 1 | Engine model geometry and mesh.

power resource of the vehicle in the foreseeable future (Heywood, 2018; Li et al., 2019). Also, many researchers have studied combustion models (Keskinen et al., 2016; Shi et al., 2019), heat transfer (Hongliang et al., 2016; Xu et al., 2020a), injection strategies (Shi et al., 2018; Chai et al., 2021), and emissions (Liu and Rigopoulos, 2019; Lin et al., 2021) related to internal combustion engines. While the traditional port fuel injection (PFI) engine has difficulty meeting the requirement of environment protection and economic efficiency, attention is attracted to the gasoline direct injection (GDI) engine (Wang and Shuai, 2011; Liu and Wang, 2022). Also, for GDI engines under partial load conditions, stratified combustion can be achieved through a reasonable injection strategy (Wang and Shen, 2021b; Yu et al., 2022), while under full load conditions, a homogeneous mixture of premixed combustion can be achieved through earlier injection (Yu et al., 2017; Liu et al., 2020). Considering the significant improvement in thermal efficiency and reducing fuel cost, the GDI engine has become a hot research topic (Leduc et al., 2003; Han et al., 2020).

Thanks to the development of accurately controlled injectors like solenoid-actuated and piezo-actuated injectors (Anbari Attar et al., 2014; Lin et al., 2019), the GDI technology can precisely control the injection timing (IT) and quantity, and allows more choice on injection strategies (Lake et al., 2004; Zheng et al., 2021). More importantly, the GDI technology shows great potential in cooperation with engine downsizing, turbocharging, and other technologies (Leduc et al., 2003; Wang and Shen, 2021c). The downsized engine is well known for less fuel consumption in a wide range of work conditions (Hall et al., 2016; Chai et al., 2020). However, downsizing strategy also makes it easier to cause knock combustion and even pre-ignition phenomenon (Ma et al., 2014; d'Adamo et al., 2015). On the other hand, the GDI technology can increase the volumetric efficiency and compression ratio because of the direct injection charge cooling effect, reducing the compression temperature to minimize knock combustion and avoid the pre-ignition phenomenon (Kasseris and Heywood, 2012; Wang et al., 2020). Besides, without port fuel film that troubles the PFI engine, the GDI engine has a better transient response (Li Y. et al., 2021; Awad et al., 2021). Overall, the GDI is crucial to synergy with downsizing and turbocharging to optimize power performance, fuel consumption, and emission performance (Huang et al., 2007; Liu and Dumitrescu, 2019).

IT is an important parameter that influences mixture formation significantly and, therefore, combustion and emission performance (Zeng et al., 2006; Liu J. et al., 2021). Since IT is one of the key roles in optimizing GDI engine performance, many researchers have focused on its effect on engine performance (Huang et al., 2003; Shi et al., 2020). Gong et al. (2021) studied IT and CO_2 dilution on combustion and emissions of a stoichiometric GDI engine. The result shows that peak cylinder pressure, peak heat release rate, and peak cylinder temperature first increased, and then decreased as retarding IT. Their corresponding angle crank had opposite trends. Duan et al. (2020) used an experimental investigation of the single injection strategy and double injection strategy on the combustion phasing, performance, and emissions characteristics in the GDI engine. The result shows that with the increase of second IT, the PCP, Peak combustion pressure; , maximum HRR, Heat release rate, and mean in-cylinder temperature were gradually increased. HC emission gradually increased but much less than the single injection at the same condition. Zhang et al. (2012) experimentally investigated the effect of IT on GDI engine performance. The result shows that IT impacts the charging cooling effect, fuel film, combustion efficiency, and HC emission. Kim et al. (2013) studied the effect of injection strategy on soot emission, revealing that advancing second IT and decreasing second injection fuel mass can reduce soot emission. Li et al. (2021) investigated the spray characteristics, flame propagation, and other indicators of a

TABLE 1 | Engine specifications

Engine type	Single cylinder
Cycle	4-stroke SI GDI
Valve per cylinder	4
Cylinder bore (mm)	84
Piston stroke (mm)	90
Displacement (L)	2.0
Connecting rod length (mm)	144.3
Compression ratio	10.3:1
Intake valve open	50 CAD BTDC exhaust
Intake valve close	143 CAD BTDC compression
Exhaust valve open	145 CAD ATDC compression
Exhaust valve close	58 CAD ATDC exhaust

TABLE 2 | Simulated operating conditions at various injection timings

Injection type	Pulsed
Start of injection (SOI)	270, 280, 290, and 300 CAD BTDC compression
Mean cone angle (°)	14
Injection duration (CAD)	18.4
Total injected mass (mg/cycle)	21.1
Engine speed (r/min)	2,000
Spark timing	15 CAD ATDC compression

GDI optical engine. The results showed that flash boiling injection resulted in lower apparent flame velocity and flame area compared with supercooled injection, which was due to the supercooled combustion conditions. Wen et al. (2020) studied the effects of fuel octane number on the fuel consumption rate and emissions of GDI and PFI spark-ignition (SI) engines. The results indicated that with the increase of research octane number (RON), the fuel consumption rate increases first and then decreases for GDI engines. Liu et al. (2019) investigated the effects of ethanol gasoline, *n*-butanol gasoline, and 2,5-dimethylfuran (DMF) gasoline on the GDI engine efficiency and emissions. The results indicated that *n*-butanol gasoline is the best blended fuel among three kinds of oxygenated fuel blends for reducing harmful emissions and CO_2 emissions.

However, previous research mainly focused on overall engine performance, and the literature about the in-cylinder mixture formation process and distribution of various emissions are limited (Yu et al., 2015; Sun et al., 2021). Moreover, the combustion process in the cylinder has been analyzed (Part A). Therefore, this paper is expected to analyze the in-cylinder view of mixture equivalence ratio, velocity field, and distribution of emissions to understand the effects of IT on engine efficiency and emissions better. A three-dimensional (3D) numerical computational fluid dynamics (CFD) simulation was adopted. It is hoped that this research will provide a more accurate view of how IT influences the mixture formation and then emissions, which contributes to optimizing the IT for better overall GDI engine performance (Zhu, 2019; Liu J. et al., 2021).

NUMERICAL MODEL

A single-cylinder four-stroke SI GDI engine model was studied with 3D engine software and the engine specifications are shown in **Table 1**. As **Figure 1** shows, considering the computational cost, the research model includes half of the combustion chamber due to its symmetry. Computing domain includes intake, exhaust port and valve, spark plug, and combustion chamber that bounded by liner, symmetry, piston, and cylinder head. The computation mesh's global size was set to 0.2 cm and refined around key geometric features like valves and the spark plug.

The chemistry mechanism for gasoline that consists of 59 species and 437 reactions was imported from the software's built-in library (Dumitrescu et al., 2018; ANSYS Forte). The chemistry mechanism can simulate the gas phase and surface reactions and conclude gas-phase input, gas-phase output, thermodynamic input, transport input, transport output, etc. (Li et al., 2019; Liu and Dumitrescu, 2020a). The simulation used the built-in precalculated laminar flame-speed table of ic8h18 to track the laminar flame front. To study the turbulent flame propagation, the Discrete Particle Ignition Kernel Flame model (DPIK) and G-equation were used. DPIK model that uses Lagrangian particles to mark the flame front position was used at the beginning of the spark when the ignition-kernel flame size is smaller than the mesh size (Harshavardhan and Mallikarjuna, 2015; Liu and Dumitrescu, 2020b). The turbulent flame propagation model will switch to G-equation after the flame size grows bigger than the mesh size. The G-equation model consisting of a set of Favre-averaged level-set equations is selected for its balance of time cost and accuracy (Liu and Dumitrescu, 2018; Chai et al., 2019). Reynolds-averaged Navier–Stokes (RANS) is chosen as turbulent transport model, and RNG k-epsilon equation was employed since it has better performance than the k-epsilon model in engine combustion simulation (Lucchini et al., 2012; Stocchi et al., 2019). The G-equation, RANS, and RNG k-epsilon equation establishes a

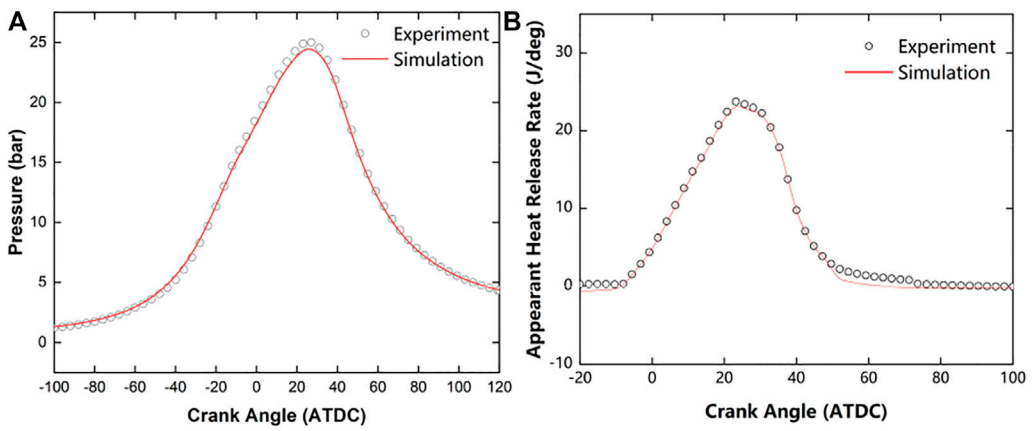

FIGURE 2 | The comparison of simulated data with measured data at the 300 CAD BTDC injection timing: **(A)** pressure trace and **(B)** apparent heat release rate curve.

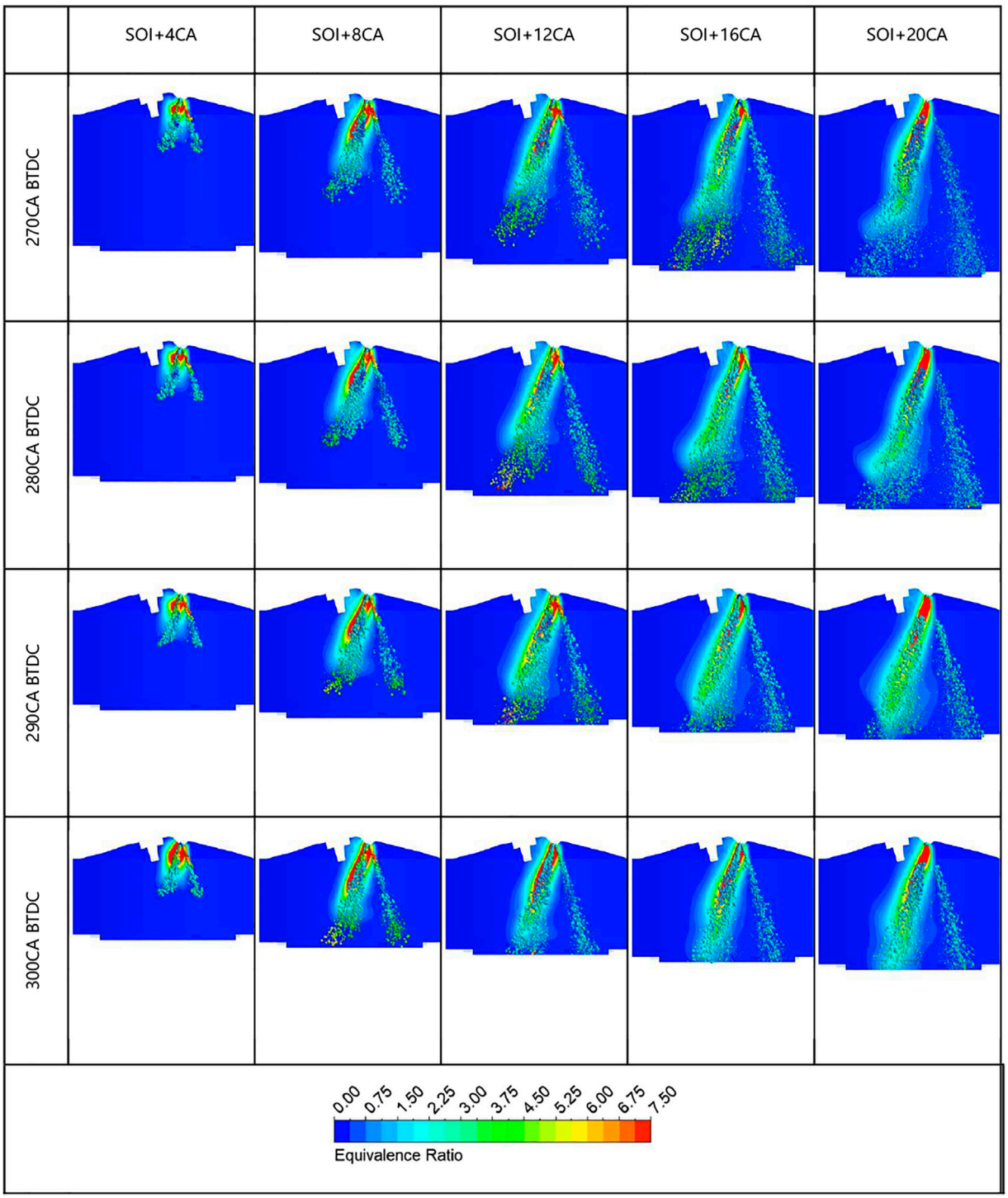

FIGURE 3 | Effect of injection timing on injection process at cylinder symmetry at several CA after SOI.

complete set of equations that describe turbulent flame propagation (Papageorgakis and Assanis, 1998; Bommisetty et al., 2018).

The spray model includes nozzle flow, spray atomization, droplet breakup, collision, coalescence, vaporization, and wall impingement (Zhu, 2019; Feng et al., 2021). The radius of influence model was chosen because of its independence on the CFD mesh size (Costa et al., 2014; Xu et al., 2020b). The model set up three injection nozzles and four ITs to research its effect on GDI engine performance, and **Table 2** shows the detailed simulation operating conditions (Potenza et al., 2019; Liu Z. et al., 2021).

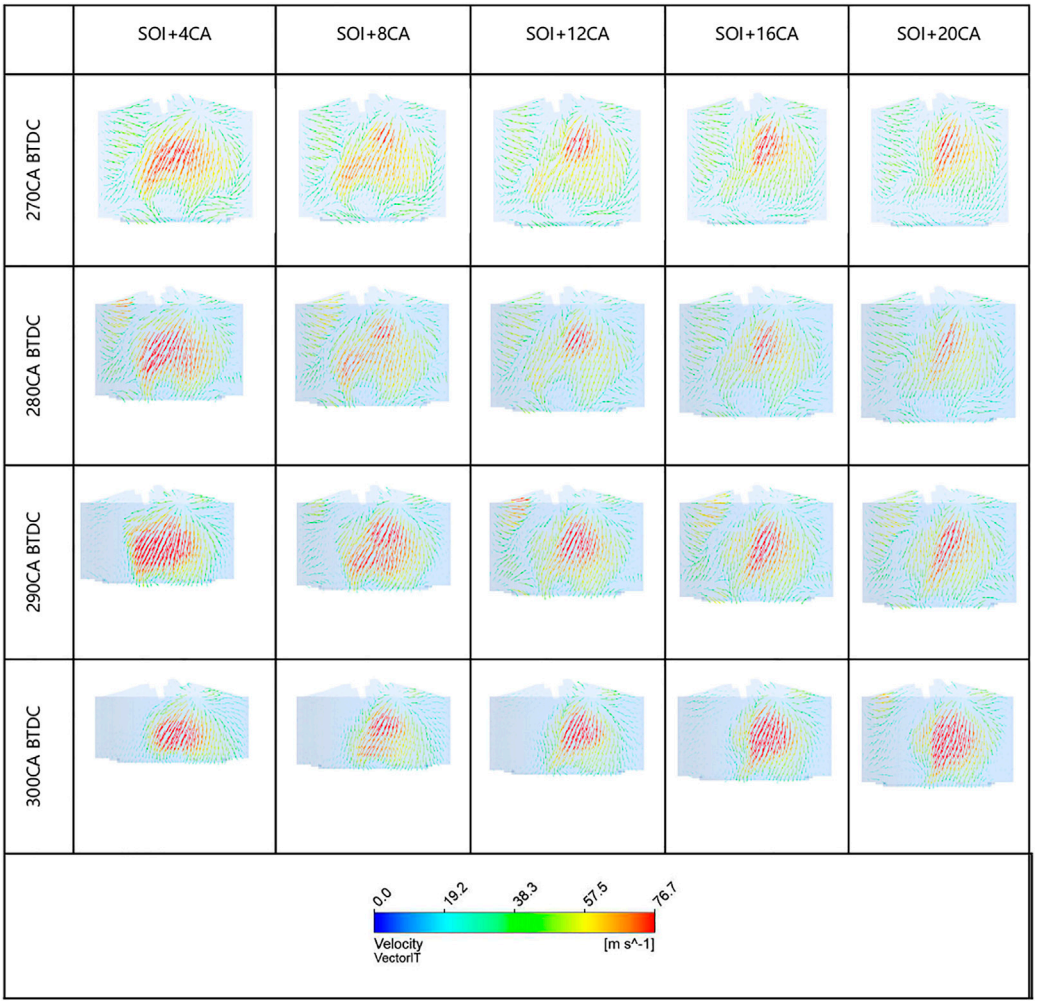

FIGURE 4 | Effect of injection timing on mixture formation at cylinder symmetry at several CA after SOI.

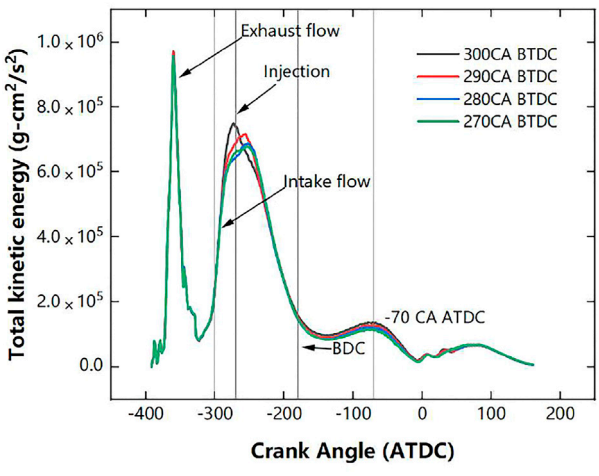

FIGURE 5 | Effect of injection timing on total kinetic energy.

The model was already validated against the experimental data at the condition shown in **Table 2**. Moreover, the comparison of measured cylinder pressure curve with simulated results is shown in **Figure 2**, which indicated that 3D CFD model was validated. The detailed model validation information can be found in Verma et al. (2016a) and Verma et al. (2016b).

RESULTS AND DISCUSSION

Injection Timing Effects on In-Cylinder Mixture Formation

As can be seen in **Figure 3**, the symmetry was colored by the equivalence ratio and the balls, which were colored by velocity and size dependent with droplet diameter, were denoted as droplets. It is obvious that penetration distance of the droplets increased as the IT delayed, which was mainly determined by the difference of the distance between

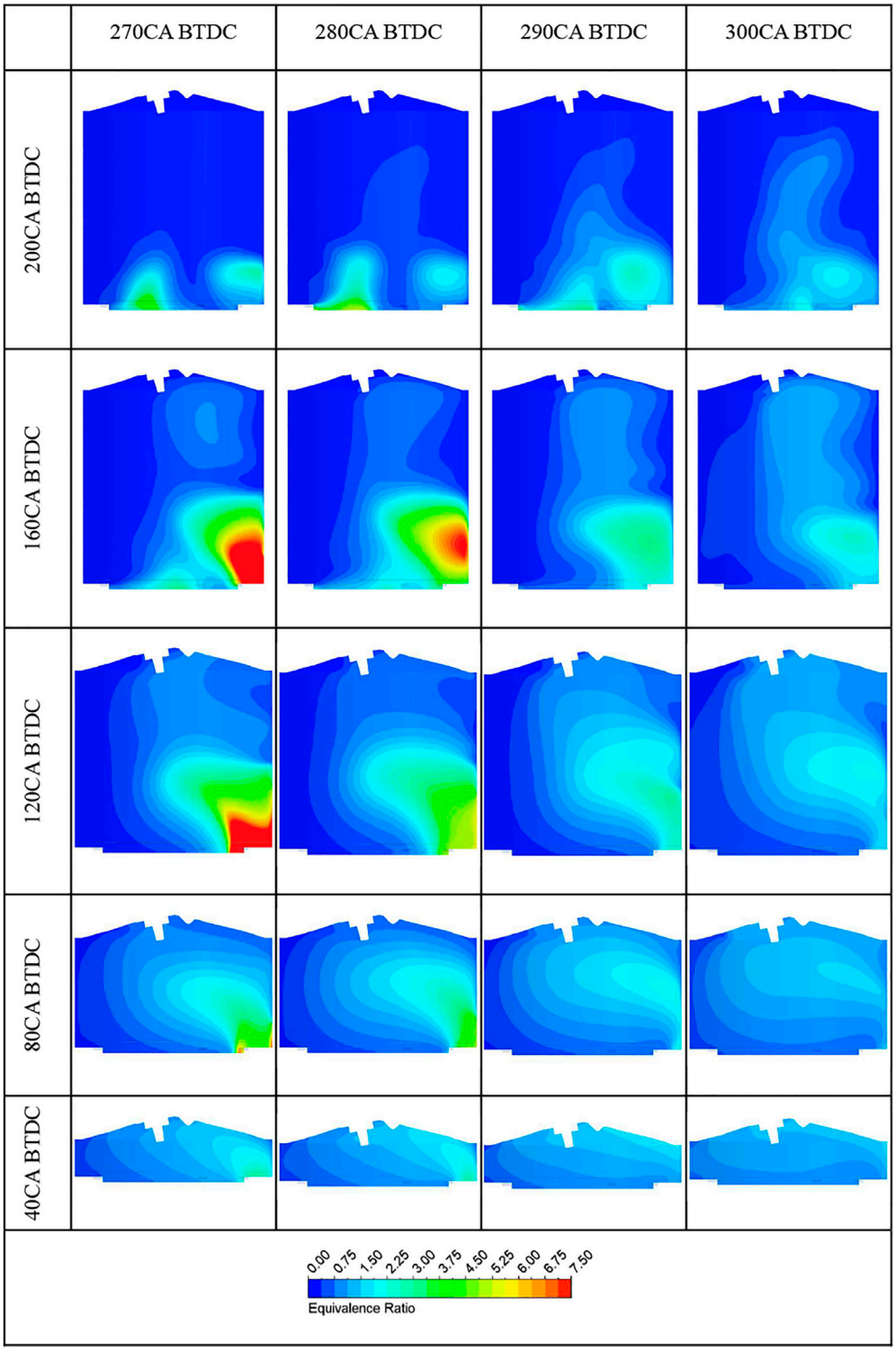

FIGURE 6 | Effect of injection timing on mixture formation at cylinder symmetry at several CAD before spark timing.

nozzles and piston surface. Besides, it was very important to note that the droplet-wall impingement intensified fiercely as the IT advanced, especially at IT of 300 CA BTDC. Also, the maximum equivalence ratio is about 7.5, which is similar with the results in Chen et al. (2019). **Figure 4** compares the velocity field during injection at different ITs. It is apparent

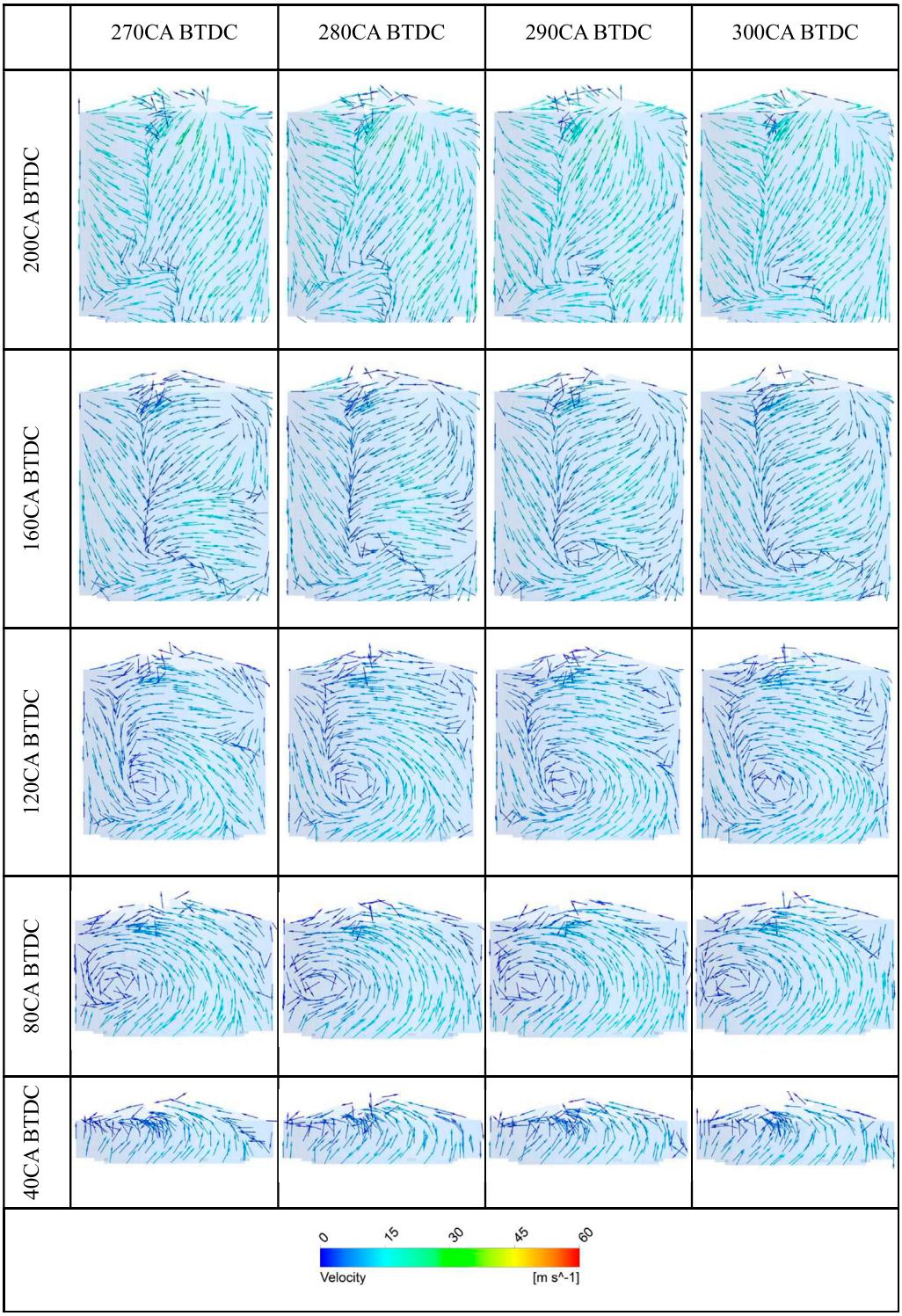

FIGURE 7 | Effect of injection timing on mixture velocity vector diagram at cylinder symmetry at several CAD before spark timing.

in **Figure 4** that advancing IT corresponds to higher velocity and more intensified flow motion, which also can be inferred from **Figure 5**. The main reason for the difference in speed is the intake flow that is stronger at the beginning of intake stroke due to lower pressure. **Figure 5** shows the effect of IT on total kinetic energy as the indicator of intensity of flow motion. The first peak was caused by exhaust flow and the second peak corresponded to intake flow. It was of interest to

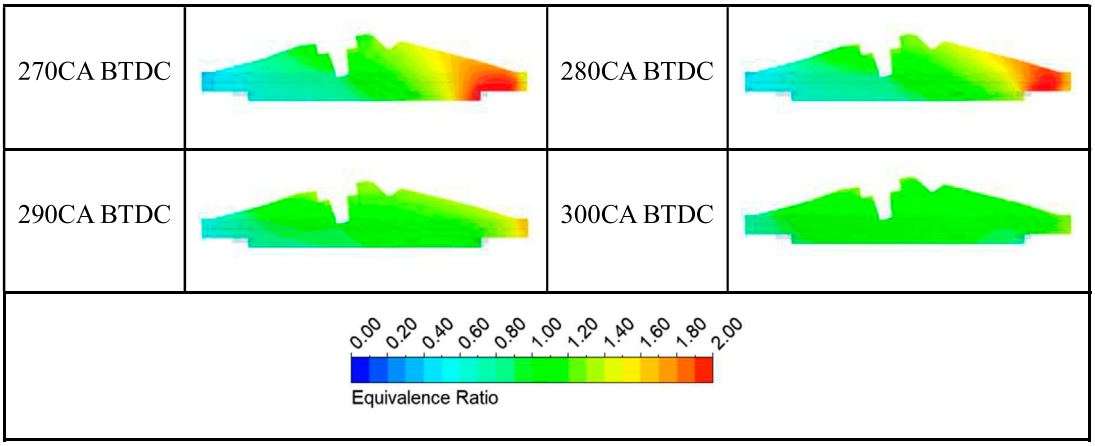

FIGURE 8 | Equivalence ratio and velocity field at cylinder symmetry when sparked at different injection timings.

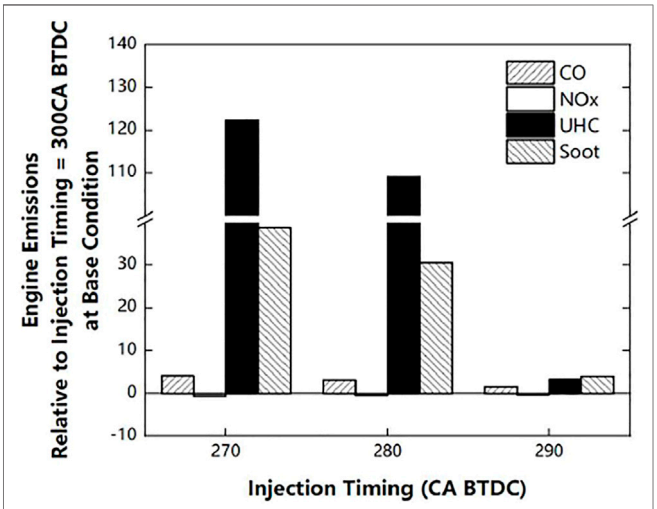

FIGURE 9 | Effect of injection timing on emissions.

point out that disturbance caused by injection at different IT has an apparent effect on the peak value of total kinetic energy. This was probably because the velocity direction of injected fuel was more similar with the in-cylinder flow motion at advanced IT, contributing to decrement of the dissipation of kinetic energy, which was supported by the combination of **Figures 3** and **4**.

To further study the fuel–gas mixture formation, the cylinder symmetry colored by equivalence ratio and velocity field is shown in **Figures 6**, **7**. Different columns represent the in-cylinder fuel–gas mixture formation at various ITs and each row showed the results of different crank angles. At the beginning, the fuel–gas mixture accumulated on the piston surface, as expected, because of a collision phenomenon during the injection process. Significantly, an anticlockwise tumbling flow was formatted during the compression stroke. This tumbling flow drove the fuel-rich mixture near the piston to the intake side and head of the cylinder. Comparing the mixture formation at different ITs, advancing IT made the mixture more uniform, regardless of likely tumbling flow. The time spent on mixing seems to be the main reason for the difference between mixture uniformity. Because the earlier IT corresponds to longer in-cylinder mixing process, it also corresponds to a stronger degree of turbulence, which widens the gap in the mixing level, as shown in **Figure 5**. For example, the fuel-rich mixture of 300 CA BTDC injection timing had moved to the center of the cylinder at 160 CA BTDC; meanwhile, the fuel-rich region of 270 CA BTDC was still gathered around the surface of the piston.

From **Figure 7**, it can be found that the velocity distribution for different ITs were similar, indicating the little effect of IT on in-cylinder flow motion, which corresponded to the overlapping area of **Figure 5**. A clear anticlockwise tumbling flow was formed in the cylinder by the combined action of the piston and intake flow. Comparing **Figures 6**, **7**, it can be found that the tumbling flow dominated in-cylinder mixture formation process. Consequently, as **Figure 8** shows, the in-cylinder mixture formation results were colored by equivalence ratio. Also, the results at the IT of 300 CA BTDC were satisfactory, while delayed IT corresponds to the fuel-rich region, especially at the IT of 270 and 280. The gathered fuel mixture region was located at the intake side near the cylinder, which influenced combustion performance remarkably. This is because the flame can be ignited easily and propagate at the stoichiometry ratio region and excess equivalence ratio region tends to be slower, even freezing the flame propagation. Besides, it was of interest to note that the eq around spark plug is near stoichiometry ratio.

Injection Timing Effects on Emission

Nowadays, as environmental issues are gaining more attention and emission regulations are becoming stricter,

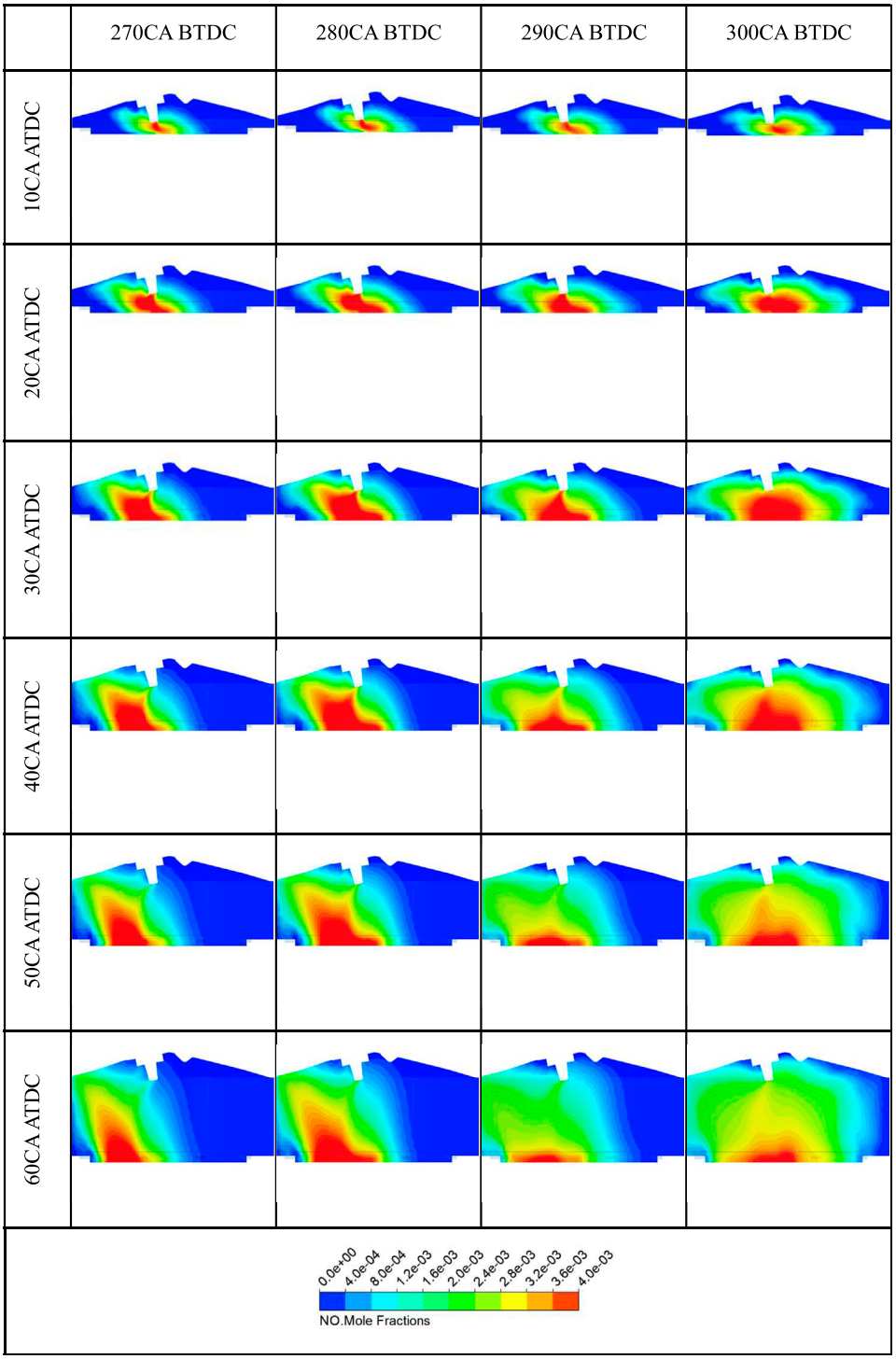

FIGURE 10 | Effect of injection timing on NOx emission at several CAD in combustion duration.

many researchers are exploring methods to improve engine efficiency and reduce emissions. It is a great way to use GDI engines to achieve the purpose of energy saving and emission reduction. However, if the operating parameters of the GDI engine are not well controlled, the GDI engine will have higher emissions than the PFI engine, which is contrary to the original objective. Therefore, it is very important to investigate the in-cylinder emission formation and oxidation process. In this study, the generation of carbon monoxide (CO), unburned hydrocarbons (UHC), nitrogen oxides (NOx), and soot

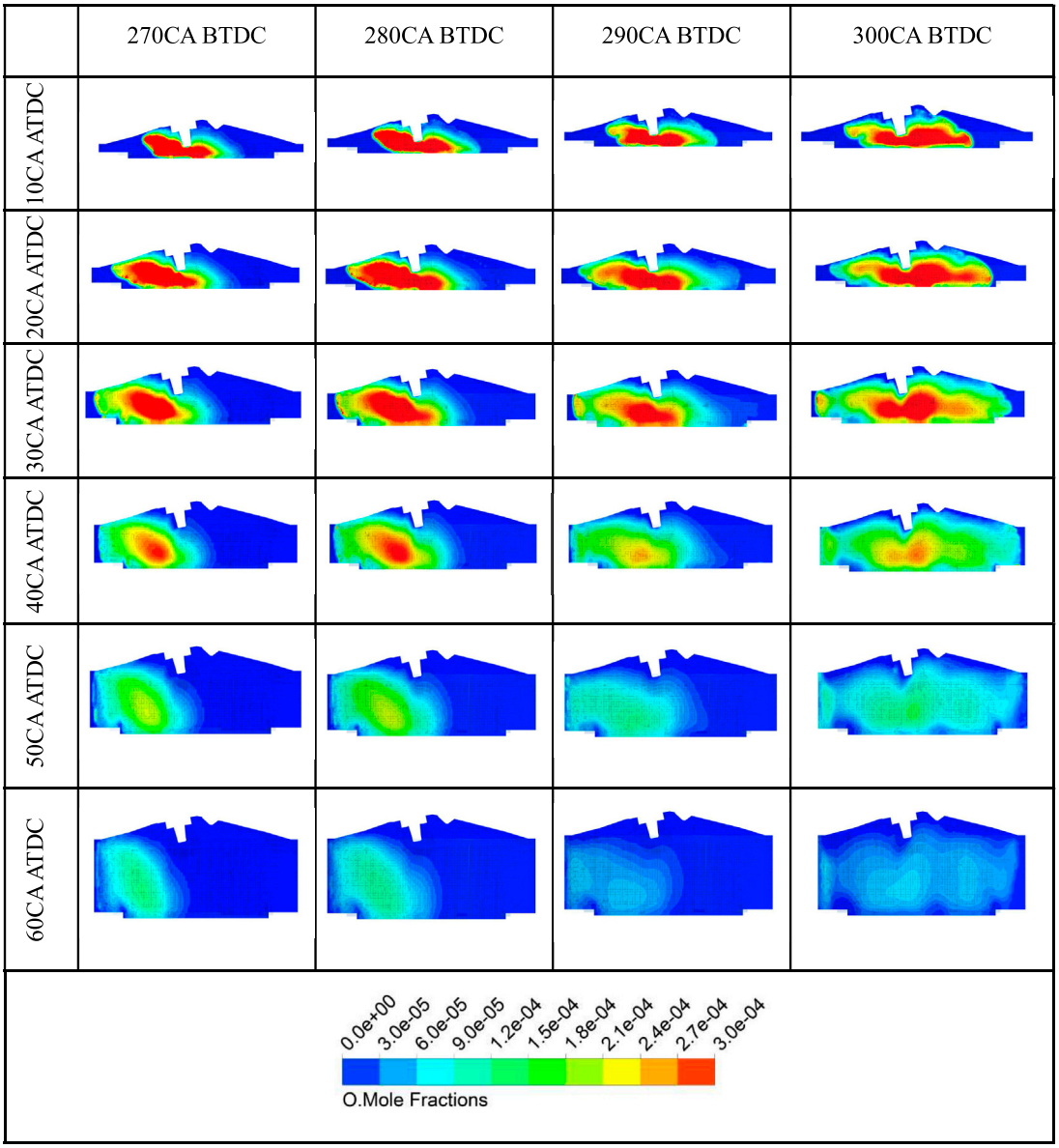

FIGURE 11 | Effect of injection timing on O formation at several CAD in combustion duration.

has been investigated, although soot of gasoline engine is not in the emissions regulation.

Figure 9 shows the various species of emission variation at different ITs. UHC is most sensitive to IT, followed by soot. The UHC, soot, and CO emissions have a significant negative correlation with the advancing of IT, while NOx emission has an insensitive positive correlation. Overall, with the advancing IT from 270 to 300 CA BTDC, the CO emission has decreased by 80.6%, and UHC and soot had been reduced by 99.2% and 97.5%, respectively; NOx emission had increased by 151.7%. The next section will discuss the effect of IT on emissions.

To investigate the effect of IT on NOx generation, the 3D clouds and graphs of NOx and oxygen radicals in the cylinder at different injection angles are as follows. Nitrogen oxides (NOx) and hydrocarbons (HC) under strong sunlight, through a series of chain photochemical reactions, will generate ozone (O_3) and peroxyacetyl nitrate (PAN), that is, the generation of secondary pollutants such as photochemical smog (Duronio et al., 2020). Also, the smog is highly oxidizing and causes stinging eyes, strong respiratory irritation, dizziness, and vomiting. Also, it is very harmful for both plants and the atmosphere. Therefore, it is necessary to study the process of NOx generation at different injection advanced angles.

NOx mainly consists of NO and NO_2, and the engine combustion process mainly produces NO and a small amount

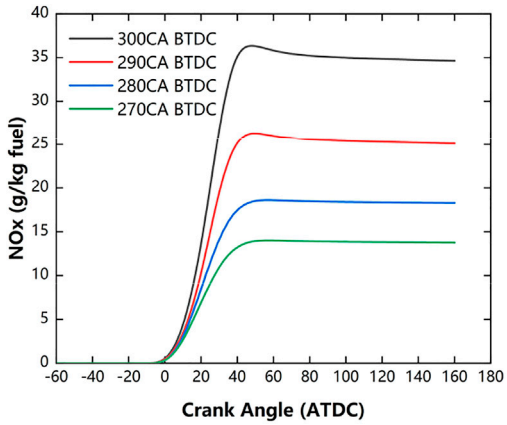

FIGURE 12 | Effect of injection timing on NOx formation.

of NO_2 (Ambrogi et al., 2019). It is generally known that NO accounts for more than 90% of NOx and 3D diagram mainly discusses the NO to replace the NOx. Also, the NO calculation is based on the extended Zeldovich mechanism. The NO oxidation rate, N oxidation rate, and OH reduction rate equations are based on **Eqs 1–3**, respectively.

$$O + N_2 = NO + N \quad (1)$$

$$N + O_2 = NO + O \quad (2)$$

$$N + OH = NO + H \quad (3)$$

The condition of NOx formation includes high temperature, oxygen concentration, and reaction time (Ambrogi et al., 2019; Duronio et al., 2020). **Figure 10** shows that the NOx emission had increased considerably with the IT advancing. Moreover, NOx was first generated around the spark plug and then mainly generated at the exhaust side of the combustion chamber.

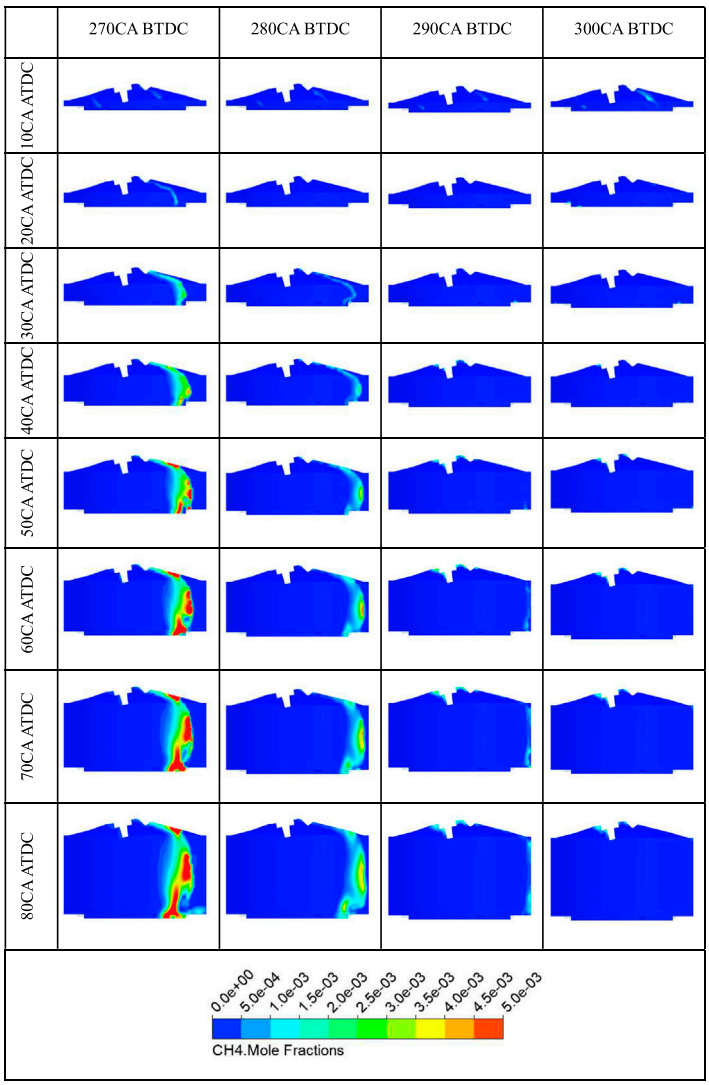

FIGURE 13 | Effect of injection timing on UHC emission.

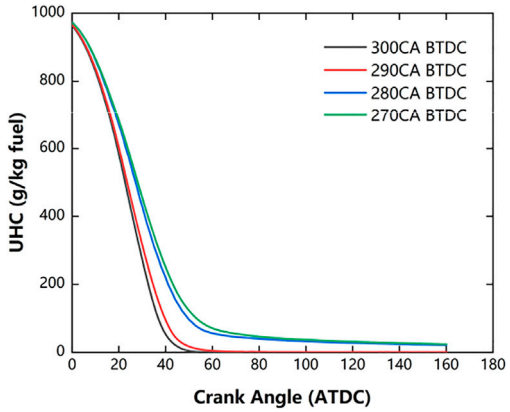

FIGURE 14 | Effect of injection timing on UHC formation.

Considering the conditions of NOx formation, **Figure 11** shows the cylindrical symmetry with O as the color, leading to the conclusion that NOx is mainly produced in the region of high temperature and high oxygen concentration. Comparison with mixture formation and combustion mentioned in the next section reveals that the flame speed variation at different combustion chamber sides resulted in higher temperature. Those regions where the equivalence ratio was close to the stoichiometric ratio have faster combustion speed and higher oxygen concentration than the fuel-rich region, leading to more NOx formation.

To further study the correlation between NOx formation and IT, **Figure 12** is used to show the NOx formation at different ITs. Advanced ITs indicated more uniform in-cylinder mixture, better combustion performance, and higher temperature. As the temperature increased with advanced IT, the NOx rising is mainly caused by increasing in-cylinder temperature with

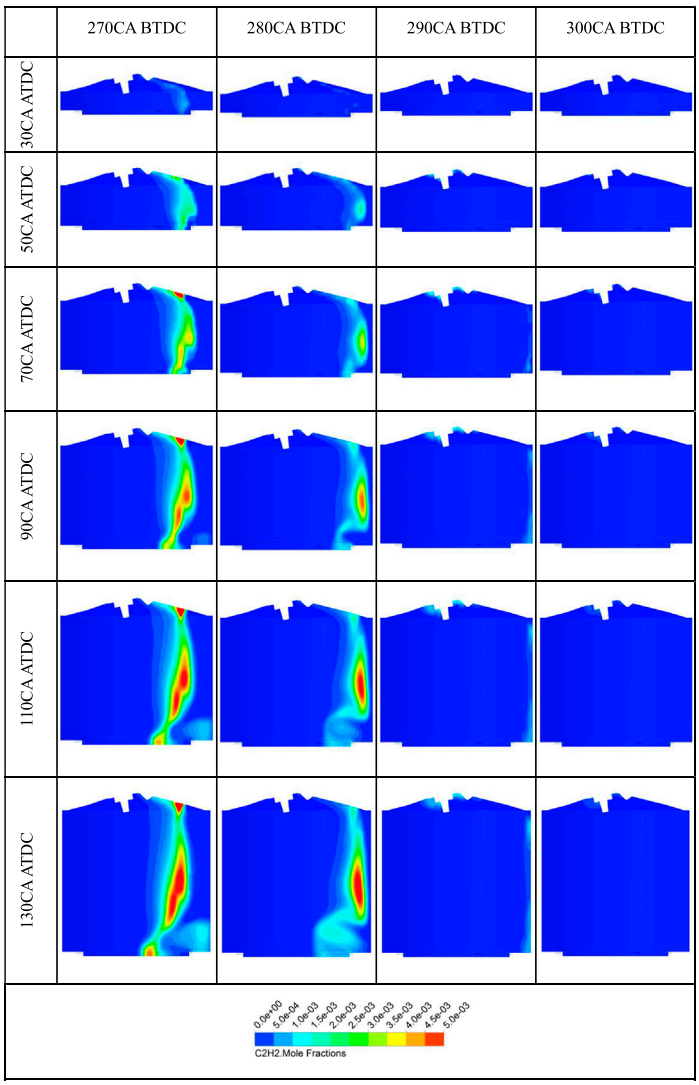

FIGURE 15 | Effect of injection timing on soot generation at several CAD in combustion duration.

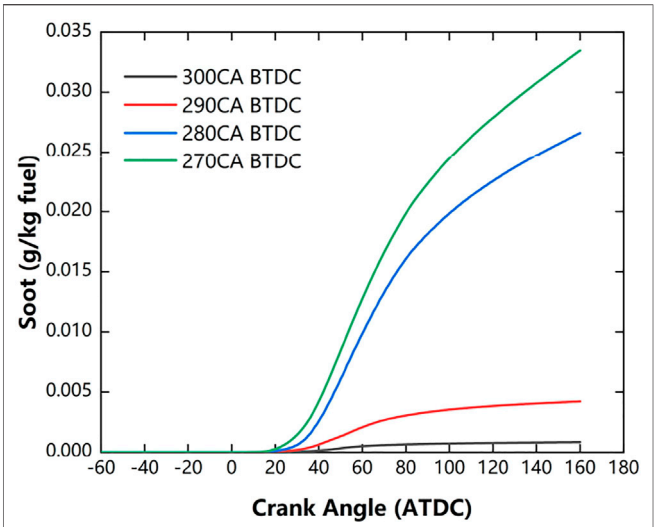

FIGURE 16 | Effect of injection timing on soot formation.

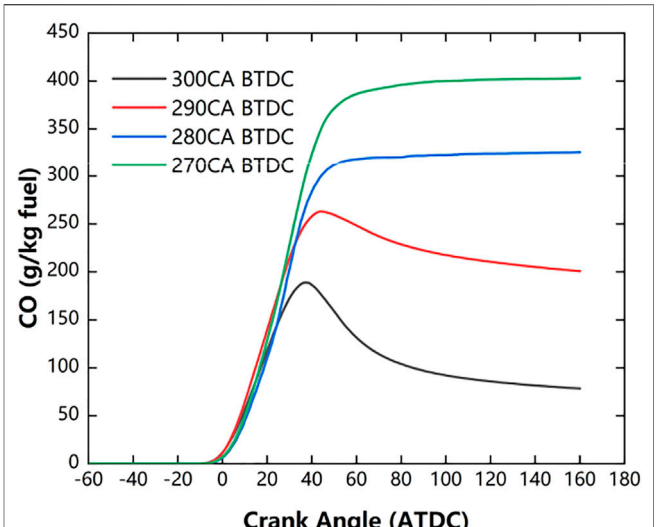

FIGURE 17 | Effect of injection timing on CO emission.

similar generated oxygen radical, as expected. As mentioned previously, advancing IT resulted in more uniform fuel mixture, improved combustion performance, and eventually increased NOx emission.

There are three main pathways for HC generation: incomplete combustion, wall quenching, and wall-moving film adsorption (Ambrogi et al., 2019; Duronio et al., 2020). For incomplete combustion, unburned hydrocarbon (UHC) emissions may be due to uneven oil–gas mixing, misfires, and other phenomena. For wall quenching, it is the major reason for UHC generation. There are various narrow gaps in the combustion chamber, especially the chamber seam between the piston head and the cylinder wall, etc. In the compression stroke, some fuel mixture was compressed into the crevice attributed to the high pressure in the cylinder. Moreover, the quenching effect is very strong due to the crevice with large surface-to-volume ratio. Also, the flame cannot spread into the crevice to continue to burn. Moreover, during the expansion and exhaust stroke, the cylinder pressure drops and the unburned mixture in the gap is exhausted along with the exhaust gas. For oil film adsorption, lubricant oil film on cylinder wall surface and carbon buildup on intake and exhaust valves will absorb the unburned gas mixture during the intake and compression strokes. Also, in the expansion and exhaust stroke, the UHCs will be released in the cylinder. In this study, CH_4 was used to represent UHC due to the fact that CH_4 has a strong chemical bonding.

UHC emission has a significant correlation with IT, as shown in **Figures 13**, **14**. CH_4 as an indicator of UHC is mainly produced at the flame front on the intake side, where the mixture combusted incompletely. With the IT advancing, the UHC has decreased. **Figure 13** indicates that the fuel-rich mixture that did not fire may not be the main reason for the rapid increase of UHC. Considering the previous section, the fuel-rich mixture region, which is especially obvious at 270 and 280 CA BTDC, resulted in an unburnt area. Hence, UHC has a sensitive correlation with IT.

The soot emissions of conventional PFI engines come from fuel combustion. Also, when there are droplets on the wall in the combustion chamber, GDI engines will generate soot due to the fact that the after-treatment system only has a three-way catalyst (TWC), but no DPF (diesel particulate filter). Soot is mainly composed of $PM_{2.5}$ and PM_{10}, of which $PM_{2.5}$ is the most harmful to the human body and environment. Therefore, the soot investigated in this study is mainly $PM_{2.5}$, which is represented by C_2H_2 (Yu et al., 2017). Moreover, the soot is hazardous to human health and reduces atmospheric visibility, which is harmful to the human respiratory system and may cause symptoms such as asthma and cancer. Also, soot will create carbon deposits that decrease the efficiency of the aftertreatment. Hence, the soot needs to be eliminated as much as possible and the study of soot generation is very necessary.

GDI engine has more soot emission than traditional PFI engine due to higher wall temperature (Wang and Shen, 2021b; Yu et al., 2022). Using C_2H_2 as an indicator, **Figure 15** shows the soot formation at different ITs. As can be seen from **Figure 15**, soot emission increased rapidly as IT delayed. Moreover, soot is first formatted around the nozzle and then mainly formatted at the intake side of the flame front, especially at 270 and 280 CA BTDC. As mentioned previously, on the intake side of the combustion chamber, at 270 and 280 CA BTDC, the incomplete combustion of the fuel mixture is severe, even without ignition, causing a significant increase in soot formation. Besides, it can be also found in **Figure 16** that as IT advanced, less soot was generated. This is because the in-cylinder mixture was more uniform at earlier IT, thus improving the combustion performance.

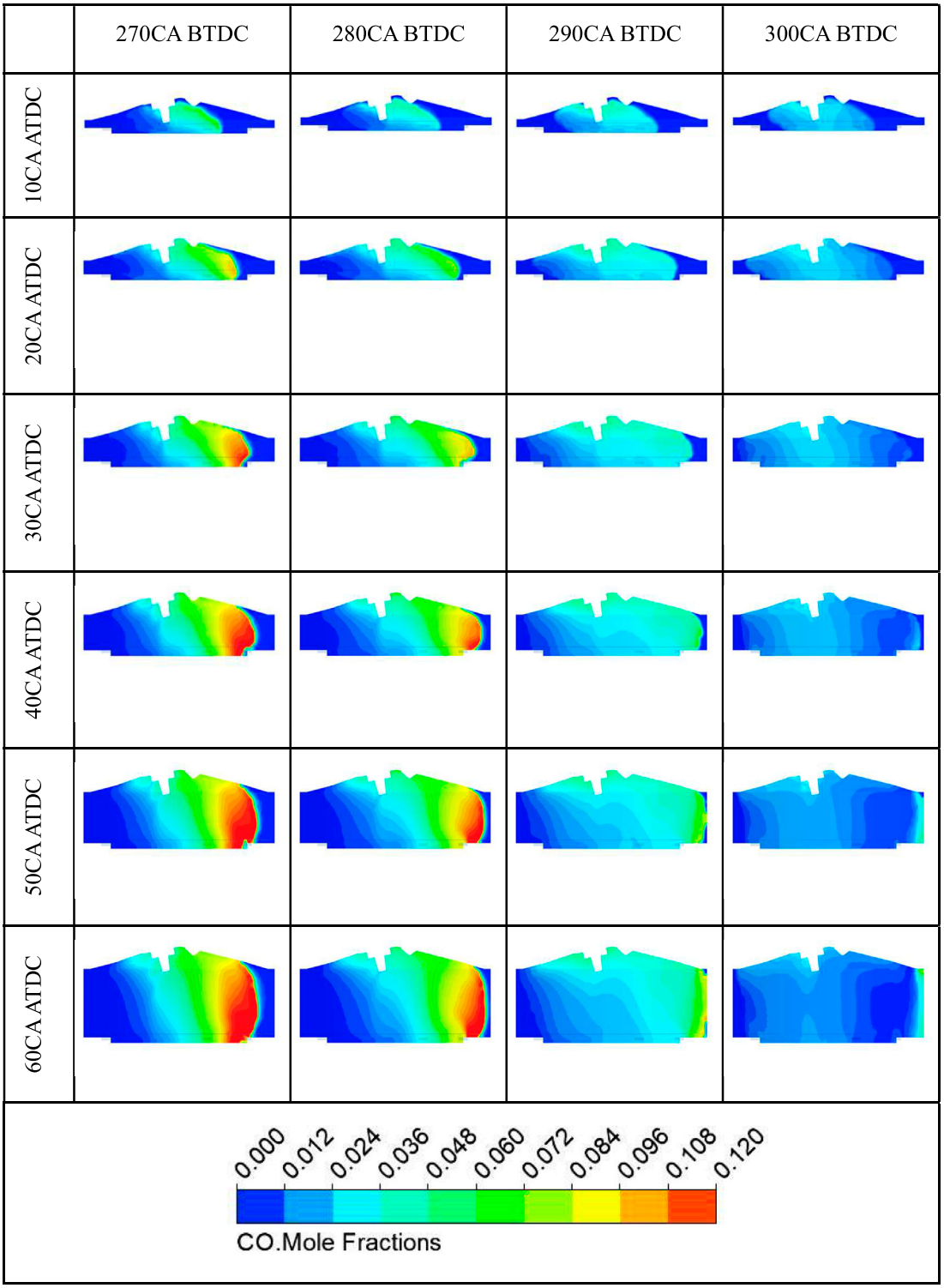

FIGURE 18 | Effect of injection timing on CO generation at several CAD in combustion duration.

It is commonly recognized that the affinity between CO and hemoglobin (Hb), which is the carrier of oxygen delivery in blood, is 200–300 times higher than O_2 (Duronio et al., 2020). Also, it can easily combine Hb to form carboxyhemoglobin (CO-Hb), which greatly reduces the oxygen delivery capacity of blood and leads to serious

oxygen deprivation in the heart, brain, and other vital organs. In addition, CO is a product of incomplete combustion and is produced due to the unevenness of the in-cylinder mixture and wall quenching effect in the crevice of the combustion chamber. Therefore, it is of great significance to investigate the in-cylinder CO concentration distribution at different ITs, which can be used as a reference to explore how to reduce CO emissions from GDI engines.

Figures 17, **18** show the CO formation at different ITs. From **Figure 17**, it can be seen that CO emission was increased with the delayed IT. Furthermore, the results indicated that CO is probably mainly produced at the flame front and severely at the intake side at 270 and 280 CA BTDC injection timing where fuel–gas mixture combusted incompletely. This is because the equivalence ratio of the intake side area at the spark timing was much higher than stoichiometry ratio at 270 and 280 CA BTDC injection timing, as can be seen in **Figure 8**. As mentioned previously, the homogeneity of the mixture varied obviously with advancing IT. Fuel gathered at the intake side of the combustion chamber as IT delayed. As a result, the incomplete combustion was intensified, especially at 270 and 280 CA BTDC injection timing. Eventually, the total CO emission was increased due to non-uniform fuel mixture and incomplete combustion. Consequently, with the delayed injection timing, the CO produced at the intake side was markedly increased and total CO emission was the most at the IT of 270 CA BTDC.

SUMMARY AND CONCLUSION

This paper set out to study the effect of IT on mixture formation and emission performance. By analyzing the numerical CFD simulation results at different ITs, the research showed that advancing IT leads to a more uniform fuel–gas mixture and hence reduces the UHC, soot, and CO emission sharply but gradually increases NOx emission. The results indicated that with the IT advancing, the fuel mixed more uniformly under the effect of tumbling flow, which is hardly influenced by IT. Therefore, the time available for fuel–gas mixed seems to be the main reason for the different uniform mixture. As for emissions, when advancing the IT, and the UHC emission had reduced sharply. The fuel-rich region of the mixture at delayed IT combusted incompletely or even not on fire, resulting in a rapid increase of UHC emission. Moreover, the soot emission decreased by 97.5%, and improvement in combustion efficiency is the main reason. Also, the NOx emission has increased by 151.7%. As the advancing IT, the more uniform mixture was formed, which resulted in better combustion performance and higher in-cylinder temperature, and therefore increased NOx emission. Furthermore, the CO emission decreased by 80.6%. The in-cylinder more uniform fuel mixture is the main reason for the decrement of CO emission.

Overall, this study contributes to understanding how IT influences mixture formation and various species of emissions. As far as this study is concerned, 300 CA BTDC is the optimized IT. Considering the different models and conditions of various GDI engines, the optimized IT cannot be determined simply the same as this investigation. Moreover, this paper provides a reference to optimize the IT of the GDI engine to enhanced power performance and reduced emissions.

DATA AVAILABILITY STATEMENT

The raw data supporting the conclusion of this article will be made available by the authors, without undue reservation.

AUTHOR CONTRIBUTIONS

YZ: conceptualization, methodology, simulation, writing—draft preparation. RY: validation, writing—draft preparation. YY: methodology, simulation. RL: writing—draft preparation. ZL: writing—draft preparation. JF: analysis, supervision.

FUNDING

The work was jointly funded by the Natural Science Foundation of Zhejiang Province (LQ20E060003), the Project Teacher Research Fund Project (J-202116), and Projects of Hangzhou Agricultural and Social Development Research Program (20201203B128, 20212013B04).

REFERENCES

Ambrogi, L., Liu, J., Battistoni, M., Dumitrescu, C., and Gasbarro, L. (2019). *CFD Investigation of the Effects of Gas' Methane Number on the Performance of a Heavy-Duty Natural-Gas Spark-Ignition Engine*. SAE Technical Paper. SAE Technical Paper 2019-24-0008. doi:10.4271/2019-24-0008

Anbari Attar, M., Herfatmanesh, M. R., Zhao, H., and Cairns, A. (2014). Experimental Investigation of Direct Injection Charge Cooling in Optical GDI Engine Using Tracer-Based PLIF Technique. *Exp. Therm. Fluid Sci.* 59, 96–108. doi:10.1016/j.expthermflusci.2014.07.020

ANSYS® Forte. *User Guide*. United States: Ansys, Inc.

Awad, O., Xiao, M., Kamil, M., Bo, Z. H., Ali, O. M., and Shuai, S. (2021). A Review of the Effects of Gasoline Detergent Additives on the Formation of Combustion Chamber Deposits of Gasoline Direct Injection Engines. *SAE Int. J. Fuels Lubricants* 14 (04-14-01-0002), 13–25. doi:10.4271/04-14-01-0002

Bommisetty, H., Liu, J., Kooragayala, R., and Dumitrescu, C. (2018). *Fuel Composition Effects in a CI Engine Converted to SI Natural Gas Operation*. SAE Technical Paper. SAE Technical Paper 2018-01-1137. doi:10.4271/2018-01-1137

Chai, M., Luo, K., Shao, C., Wang, H., and Fan, J. (2020). A Finite Difference Discretization Method for Heat and Mass Transfer with Robin Boundary Conditions on Irregular Domains. *J. Comput. Phys.* 400, 108890. doi:10.1016/j.jcp.2019.108890

Chai, M., Luo, K., Shao, C., Wang, H., and Fan, J. (2019). Interface-resolved Detailed Numerical Simulation of Evaporating Two-phase Flows with Robin Boundary Conditions on Irregular Domains. *Int. J. Heat Mass Transfer* 145, 118774. doi:10.1016/j.ijheatmasstransfer.2019.118774

Chai, M., Luo, K., Wang, H., Zheng, S., and Fan, J. (2021). Imposing Mixed Dirichlet-Neumann-Robin Boundary Conditions on Irregular Domains in a Level Set/ghost Fluid Based Finite Difference Framework. *Comput. Fluids* 214, 104772. doi:10.1016/j.compfluid.2020.104772

Chen, B., Feng, L., Wang, Y., Ma, T., Liu, H., Geng, C., et al. (2019). Spray and Flame Characteristics of wall-impinging Diesel Fuel spray at Different wall Temperatures and Ambient Pressures in a Constant Volume Combustion Vessel. *Fuel* 235, 416–425. doi:10.1016/j.fuel.2018.07.154

Costa, M., Marchitto, L., Merola, S. S., and Sorge, U. (2014). Study of Mixture Formation and Early Flame Development in a Research GDI (Gasoline Direct Injection) Engine through Numerical Simulation and UV-Digital Imaging. *Energy* 77, 88–96. doi:10.1016/j.energy.2014.04.114

d'Adamo, A., Breda, S., Fontanesi, S., and Cantore, G. (2015). LES Modelling of Spark-Ignition Cycle-To-Cycle Variability on a Highly Downsized DISI Engine. *SAE Int. J. Engines* 8 (5), 2029–2041. doi:10.4271/2015-24-2403

Duan, X., Li, Y., Liu, Y., Liu, J., Wang, S., and Guo, G. (2020). Quantitative Investigation the Influences of the Injection Timing under Single and Double Injection Strategies on Performance, Combustion and Emissions Characteristics of a GDI SI Engine Fueled with Gasoline/ethanol Blend. *Fuel* 260, 116363. doi:10.1016/j.fuel.2019.116363

Dumitrescu, C. E., Padmanaban, V., and Liu, J. (2018). An Experimental Investigation of Early Flame Development in an Optical Spark Ignition Engine Fueled with Natural Gas. *J. Eng. Gas Turbines Power* 140 (8), 082802. doi:10.1115/1.4039616

Duronio, F., De Vita, A., Montanaro, A., and Villante, C. (2020). Gasoline Direct Injection Engines - A Review of Latest Technologies and Trends. Part 2. *Fuel* 265, 116947. doi:10.1016/j.fuel.2019.116947

Feng, L., Sun, X., Pan, X., Yi, W., Cui, Y., Wang, Y., et al. (2021). Gasoline spray Characteristics Using a High Pressure Common Rail Diesel Injection System by the Method of Laser Induced Exciplex Fluorescence. *Fuel* 302, 121174. doi:10.1016/j.fuel.2021.121174

Gasbarro, L., Liu, J., Dumitrescu, C., Ulishney, C., Battistoni, M., and Ambrogi, L. (2019). *Heavy-Duty Compression-Ignition Engines Retrofitted to Spark-Ignition Operation Fueled with Natural Gas*. SAE Technical Paper. doi:10.4271/2019-24-0030

Gong, C., Si, X., and Liu, F. (2021). Combined Effects of Excess Air Ratio and EGR Rate on Combustion and Emissions Behaviors of a GDI Engine with CO2 as Simulated EGR (CO2) at Low Load. *Fuel* 293, 120442. doi:10.1016/j.fuel.2021.120442

Hall, J., Bassett, M., Hibberd, B., and Streng, S. (2016). Heavily Downsized Demonstrator Engine Optimised for CNG Operation. *SAE Int. J. Engines* 9 (4), 2250–2261. doi:10.4271/2016-01-2363

Han, D., Fan, Y., Sun, Z., Nour, M., and Li, X. (2020). Combustion and Emissions of Isomeric Butanol/gasoline Surrogates Blends on an Optical GDI Engine. *Fuel* 272, 117690. doi:10.1016/j.fuel.2020.117690

Harshavardhan, B., and Mallikarjuna, J. M. (2015). Effect of Piston Shape on in-cylinder Flows and Air-Fuel Interaction in a Direct Injection Spark Ignition Engine - A CFD Analysis. *Energy* 81, 361–372. doi:10.1016/j.energy.2014.12.049

Heywood, J. B. (2018). *Internal Combustion Engine Fundamentals*. McGraw-Hill Education.

Hongliang, Y., Shulin, D., and Peiting, S. (2016). Effects of Main/pilot Timings on Combustion and Emission Characteristics of marine Dual Fuel Engines. *J. Propulsion Techn.* 37 (9), 1735–1741.

Huang, Z., Shiga, S., Ueda, T., Nakamura, H., Ishima, T., Obokata, T., et al. (2003). Effect of Fuel Injection Timing Relative to Ignition Timing on the Natural-Gas Direct-Injection Combustion. *J. Eng. Gas Turbines Power* 125 (3), 783–790. doi:10.1115/1.1563243

Huang, Z., Wang, J., Liu, B., Zeng, K., Yu, J., and Jiang, D. (2007). Combustion Characteristics of a Direct-Injection Engine Fueled with Natural Gas-Hydrogen Blends under Different Ignition Timings. *Fuel* 86 (3), 381–387. doi:10.1016/j.fuel.2006.07.007

Kasseris, E., and Heywood, J. B. (2012). Charge Cooling Effects on Knock Limits in SI DI Engines Using Gasoline/ethanol Blends: Part 2-effective Octane Numbers. *SAE Int. J. Fuels Lubr.* 5 (2), 844–854. doi:10.4271/2012-01-1284

Keskinen, K., Kaario, O., Nuutinen, M., Vuorinen, V., Künsch, Z., Liavåg, L. O., et al. (2016). Mixture Formation in a Direct Injection Gas Engine: Numerical Study on Nozzle Type, Injection Pressure and Injection Timing Effects. *Energy* 94, 542–556. doi:10.1016/j.energy.2015.09.121

Kim, Y., Kim, Y., Jun, S., Lee, K. H., Rew, S., Lee, D., et al. (2013). Strategies for Particle Emissions Reduction from GDI Engines. *SAE Tech. Pap.* 2. doi:10.4271/2013-01-1556

Lake, T., Stokes, J., Murphy, R., Osborne, R., and Schamel, A. (2004). *Turbocharging Concepts for Downsized DI Gasoline Engines*. SAE Technical Paper.

Leduc, P., Dubar, B., Ranini, A., and Monnier, G. (2003). Downsizing of Gasoline Engine: an Efficient Way to Reduce CO2 Emissions. *Oil Gas Sci. Techn. - Rev. IFP* 58 (1), 115–127. doi:10.2516/ogst:2003008

Li, Y., Duan, X., Liu, Y., Liu, J., Guo, G., and Tang, Y. (2019). Experimental Investigation the Impacts of Injection Strategies Coupled with Gasoline/ethanol Blend on Combustion, Performance and Emissions Characteristics of a GDI Spark-Ignition Engine. *Fuel* 256, 115910. doi:10.1016/j.fuel.2019.115910

Li, Y., Wang, S., Duan, X., Liu, S., Liu, J., and Hu, S. (2021). Multi-objective Energy Management for Atkinson Cycle Engine and Series Hybrid Electric Vehicle Based on Evolutionary NSGA-II Algorithm Using Digital Twins. *Energ. Convers. Manage.* 230, 113788. doi:10.1016/j.enconman.2020.113788

Li, X., Sun, Z., Yang, S., Wang, H., and Nour, M. (2021). Flash Boiling Combustion of Isomeric Butanol and Gasoline Surrogate Blends Using Constant Volume spray Chamber and GDI Optical Engine. *Fuel* 286, 119328. doi:10.1016/j.fuel.2020.119328

Lin, X., Feng, Q., Mo, L., and Li, H. (2019). Optimal Adaptation Equivalent Factor of Energy Management Strategy for Plug-In CVT HEV. *Proc. Inst. Mech. Eng. D: J. Automobile Eng.* 233 (4), 877–889. doi:10.1177/0954407018755612

Lin, X., and Li, H. (2019). Adaptive Control Strategy Extracted from Dynamic Programming and Combined with Driving Pattern Recognition for SPHEB. *Int.J Automot. Technol.* 20 (5), 1009–1022. doi:10.1007/s12239-019-0095-7

Lin, X., Wang, Z., and Wu, J. (2021). Energy Management Strategy Based on Velocity Prediction Using Back Propagation Neural Network for a Plug-in Fuel Cell Electric Vehicle. *Int. J. Energ. Res* 45 (2), 2629–2643. doi:10.1002/er.5956

Liu, A., Garcia, C. E., Sewerin, F., Williams, B. A. O., and Rigopoulos, S. (2020). Population Balance Modelling and Laser Diagnostic Validation of Soot Particle Evolution in Laminar Ethylene Diffusion Flames. *Combustion and Flame* 221, 384–400. doi:10.1016/j.combustflame.2020.06.036

Liu, A., and Rigopoulos, S. (2019). A Conservative Method for Numerical Solution of the Population Balance Equation, and Application to Soot Formation. *Combustion and Flame* 205, 506–521. doi:10.1016/j.combustflame.2019.04.019

Liu, H., Wang, X., Zhang, D., Dong, F., Liu, X., Yang, Y., et al. (2019). Investigation on Blending Effects of Gasoline Fuel with N-Butanol, DMF, and Ethanol on the Fuel Consumption and Harmful Emissions in a GDI Vehicle. *Energies* 12 (10), 1845. doi:10.3390/en12101845

Liu, J., and Dumitrescu, C. E. (2020a). Limitations of Natural Gas Lean Burn Spark Ignition Engines Derived from Compression Ignition Engines. *J. Energ. Resour. Techn.* 142 (12), 122308. doi:10.1115/1.4047404

Liu, J., and Dumitrescu, C. E. (2020b). Improved Thermodynamic Model for Lean Natural Gas Spark Ignition in a Diesel Engine Using a Triple Wiebe Function. *J. Energ. Resour. Techn.* 142 (6), 062303. doi:10.1115/1.4045534

Liu, J., and Dumitrescu, C. E. (2018). 3D CFD Simulation of a CI Engine Converted to SI Natural Gas Operation Using the G-Equation. *Fuel* 232, 833–844. doi:10.1016/j.fuel.2018.05.159

Liu, J., and Dumitrescu, C. E. (2019). Analysis of Two-Stage Natural-Gas Lean Combustion inside a Diesel Geometry. *Appl. Therm. Eng.* 160, 114116. doi:10.1016/j.applthermaleng.2019.114116

Liu, J., and Wang, H. (2022). Machine Learning Assisted Modeling of Mixing Timescale for LES/PDF of High-Karlovitz Turbulent Premixed Combustion. *Combustion and Flame* 238, 111895. doi:10.1016/j.combustflame.2021.111895

Liu, A., Luo, K. H., Rigopoulos, S., and Jones, W. (2021). Effects of the Electric Field on Soot Formation in Combustion: A Coupled Charged Particle PBE-CFD Framework. *Combustion and Flame*, 111796. doi:10.1016/j.combustflame.2021.111796

Liu, J., Huang, Q., Ulishney, C., and Dumitrescu, C. E. (2021). Machine Learning Assisted Prediction of Exhaust Gas Temperature of a Heavy-Duty Natural Gas Spark Ignition Engine. *Appl. Energ.* 300, 117413. doi:10.1016/j.apenergy.2021.117413

Liu, J., Ulishney, C. J., and Dumitrescu, C. E. (2021). Experimental Investigation of a Heavy-Duty Natural Gas Engine Performance Operated at Stoichiometric and Lean Operations. *Energ. Convers. Manage.* 243, 114401. doi:10.1016/j.enconman.2021.114401

Liu, Z., Zhang, Y., Fu, J., and Liu, J. (2021). "Three-dimensional Fluid Dynamics Modeling of a 6V150 Diesel Engine," in *ASME 2021 International Mechanical Engineering Congress and Exposition* (American Society of Mechanical Engineers), IMECE2021–67711.

Lucchini, T., D'Errico, G., Onorati, A., Bonandrini, G., Venturoli, L., and Di Gioia, R. (2012). *Development of a CFD Approach to Model Fuel-Air Mixing in*

Gasoline Direct-Injection Engines. SAE Technical Paper. doi:10.4271/2012-01-0146

Ma, J., Zhao, H., Freeland, P., Hawley, M., and Xia, J. (2014). Numerical Analysis of a Downsized 2-stroke Uniflow Engine. *SAE Int. J. Engines* 7 (4), 2035–2044. doi:10.4271/2014-01-9051

Papageorgakis, G., and Assanis, D. N. (1998). Optimizing Gaseous Fuel-Air Mixing in Direct Injection Engines Using an RNG Based K-ε Model. *SAE Trans.*, 82–107. doi:10.4271/980135

Potenza, M., Milanese, M., and de Risi, A. (2019). Effect of Injection Strategies on Particulate Matter Structures of a Turbocharged GDI Engine. *Fuel* 237, 413–428. doi:10.1016/j.fuel.2018.09.130

Shi, Z., Lee, C.-f., Wu, H., Li, H., Wu, Y., Zhang, L., et al. (2020). Effect of Injection Pressure on the Impinging spray and Ignition Characteristics of the Heavy-Duty Diesel Engine under Low-Temperature Conditions. *Appl. Energ.* 262, 114552. doi:10.1016/j.apenergy.2020.114552

Shi, Z., Lee, C.-f., Wu, H., Wu, Y., Zhang, L., and Liu, F. (2019). Optical Diagnostics of Low-Temperature Ignition and Combustion Characteristics of Diesel/kerosene Blends under Cold-Start Conditions. *Appl. Energ.* 251, 113307. doi:10.1016/j.apenergy.2019.113307

Shi, Z., Zhang, H., Wu, H., and Xu, Y. (2018). Ignition Properties of Lean DME/H2 Mixtures at Low Temperatures and Elevated Pressures. *Fuel* 226, 545–554. doi:10.1016/j.fuel.2018.04.043

Stocchi, I., Liu, J., Dumitrescu, C. E., Battistoni, M., and Grimaldi, C. N. (2019). Effect of Piston Crevices on the Numerical Simulation of a Heavy-Duty Diesel Engine Retrofitted to Natural-Gas Spark-Ignition Operation. *J. Energ. Resour. Technol.* 141 (11), 112204. doi:10.1115/1.4043709

Sun, Z., Cui, M., Ye, C., Yang, S., Li, X., Hung, D., et al. (2021). Split Injection Flash Boiling Spray for High Efficiency and Low Emissions in a GDI Engine under Lean Combustion Condition. *Proc. Combustion Inst.* 38 (4), 5769–5779. doi:10.1016/j.proci.2020.05.037

Verma, I., Bish, E., Kuntz, M., Meeks, E., Puduppakkam, K., Naik, C., et al. (2016). *CFD Modeling of Spark Ignited Gasoline Engines-Part 2: Modeling the Engine in Direct Injection Mode along with spray Validation*. SAE Technical Paper.

Verma, I., Bish, E., Kuntz, M., Meeks, E., Puduppakkam, K., Naik, C., et al. (2016). *CFD Modeling of Spark Ignited Gasoline Engines-Part 1: Modeling the Engine under Motored and Premixed-Charge Combustion Mode*. SAE Technical Paper.

Wang, J., and Shuai, S. (2011). *Principles of Automobile Engines*. [M] Beijing: Tsinghua University Press.

Wang, S., Luo, K., and Fan, J. (2020). CFD-DEM Coupled with Thermochemical Sub-models for Biomass Gasification: Validation and Sensitivity Analysis. *Chem. Eng. Sci.* 217, 115550. doi:10.1016/j.ces.2020.115550

Wang, S., and Shen, Y. (2020). CFD-DEM Study of Biomass Gasification in a Fluidized Bed Reactor: Effects of Key Operating Parameters. *Renew. Energ.* 159, 1146–1164. doi:10.1016/j.renene.2020.06.001

Wang, S., and Shen, Y. (2021a). Particle-scale Modelling of Raceway Dynamics in a Blast Furnace Using a Smoothing Method. *Powder Techn.* 389, 189–203. doi:10.1016/j.powtec.2021.05.020

Wang, S., and Shen, Y. (2021b). Particle-scale Study of Heat and Mass Transfer in a Bubbling Fluidised Bed. *Chem. Eng. Sci.* 240, 116655. doi:10.1016/j.ces.2021.116655

Wang, S., and Shen, Y. (2021c). CFD-DEM Modelling of Raceway Dynamics and Coke Combustion in an Ironmaking Blast Furnace. *Fuel* 302, 121167. doi:10.1016/j.fuel.2021.121167

Wen, M., Zhang, C., Yue, Z., Liu, X., Yang, Y., Dong, F., et al. (2020). Effects of Gasoline Octane Number on Fuel Consumption and Emissions in Two Vehicles Equipped with GDI and PFI Spark-Ignition Engine. *J. Energ. Eng.* 146 (6), 04020069. doi:10.1061/(asce)ey.1943-7897.0000722

Xu, Z., Ji, F., Ding, S., Zhao, Y., Zhang, X., Zhou, Y., et al. (2020a). High-altitude Performance and Improvement Methods of Poppet Valves 2-stroke Aircraft Diesel Engine. *Appl. Energ.* 276, 115471. doi:10.1016/j.apenergy.2020.115471

Xu, Z., Ji, F., Ding, S., Zhao, Y., Wang, Y., Zhang, Q., et al. (2020b). Simulation and Experimental Investigation of Swirl-Loop Scavenging in Two-Stroke Diesel Engine with Two Poppet Valves. *Int. J. Engine Res.*, 1468087420916083. doi:10.1177/1468087420916083

Xu, Z., Ji, F., Ding, S., Zhao, Y., Zhou, Y., Zhang, Q., et al. (2021). Digital Twin-Driven Optimization of Gas Exchange System of 2-stroke Heavy Fuel Aircraft Engine. *J. Manufacturing Syst.* 58, 132–145. doi:10.1016/j.jmsy.2020.08.002

Yang, R., Sun, X., Liu, Z., Zhang, Y., and Fu, J. (2021). A Numerical Analysis of the Effects of Equivalence Ratio Measurement Accuracy on the Engine Efficiency and Emissions at Varied Compression Ratios. *Processes* 9 (8), 1413. doi:10.3390/pr9081413

Yu, H., Duan, S., and Sun, P. (2015). Comparative Analysis between Natural Gas/diesel (Dual Fuel) and Pure Diesel on the marine Diesel Engine. *J. Eng. Res.* 3 (4), 1–5. doi:10.7603/s40632-015-0037-0

Yu, H., Duan, S., and Sun, P. (2017). Numerical Simulation of Combustion Progress on Dual Fuel Engines with Different Turbulence Models. *J. Eng. Res.* 5 (4).

Yu, H., Wang, W., Sheng, D., Li, H., and Duan, S. (2022). Performance of Combustion Process on marine Low Speed Two-Stroke Dual Fuel Engine at Different Fuel Conditions: Full Diesel/diesel Ignited Natural Gas. *Fuel* 310, 122370. doi:10.1016/j.fuel.2021.122370

Zeng, K., Huang, Z., Liu, B., Liu, L., Jiang, D., Ren, Y., et al. (2006). Combustion Characteristics of a Direct-Injection Natural Gas Engine under Various Fuel Injection Timings. *Appl. Therm. Eng.* 26 (8-9), 806–813. doi:10.1016/j.applthermaleng.2005.10.011

Zhang, Y., Zhao, H., Ojapah, M., and Cairns, A. (2012). Effects of Injection Timing on CAI Operation in a 2/4-stroke Switchable GDI Engine. *SAE Int. J. Engines* 5 (2), 67–75. doi:10.4271/2011-01-1773

Zhao, F., Lai, M.-C., and Harrington, D. L. (1999). Automotive Spark-Ignited Direct-Injection Gasoline Engines. *Prog. Energ. combustion Sci.* 25 (5), 437–562. doi:10.1016/s0360-1285(99)00004-0

Zheng, X. U., Fenzhu, J. I., Shuiting, D. I., Yunhai, Z. H., Yu, Z. H., Zhang, Q., et al. (2021). Effect of Scavenge Port Angles on Flow Distribution and Performance of Swirl-Loop Scavenging in 2-stroke Aircraft Diesel Engine. *Chin. J. Aeronautics* 34 (3), 105–117. doi:10.1016/j.cja.2020.07.015

Zhu, Y. X. (2019). *Research on the Effect of Fuel Temperature on Combustion and Emission of GDI Engine [D]*. Jilin University.

Conflict of Interest: The authors declare that the research was conducted in the absence of any commercial or financial relationships that could be construed as a potential conflict of interest.

frontiers in Energy Research

ORIGINAL RESEARCH
published: 04 March 2022
doi: 10.3389/fenrg.2022.847651

Numerical Study on the Effect of Wall Thickness on the Combustion Characteristics of Non-premixed Hydrogen Micro-jet Flame

Xing Li[1,2]*, *Shengrong Xie*[1,3], *Jing Zhang*[1]*, *Daiqing Zhao*[1] and *Xiaohan Wang*[1]

[1]Guangzhou Institute of Energy Conversion, Chinese Academy of Sciences, Guangzhou, China, [2]Dalian National Laboratory for Clean Energy, Dalian, China, [3]University of Chinese Academy of Sciences, Beijing, China

The effect of wall thickness on the combustion characteristics of nonpremixed hydrogen micro-jet flames was studied by two-dimensional numerical computation with a detailed reaction kinetics for the development of hydrogen micro-burner. The hydrogen jet diffusion flames achieved by micro-tubes with the same inner diameter and length but different wall thicknesses were investigated. The heat exchange between solid tube and gases were included in the numerical computation. The distributions of flame temperature, OH radicals, details of thermal interaction, and combustion efficiency were analyzed for comparison. It was found that the temperature distribution, flame shape, and heat recirculation are changed with the fuel flow velocity, and they are affected by wall thickness. The mechanism of wall thickness on the combustion characteristics of hydrogen jet diffusion flame was clarified. Finally, an interesting numerical experiment was conducted to give a further explanation of the effect of heat recirculation and to provide guidance of the thermal management of the micro-burner.

Keywords: hydrogen, micro-jet flame, wall thickness, heat recirculation, combustion characteristics

OPEN ACCESS

Edited by:
Zhihua Wang,
Zhejiang University, China

Reviewed by:
Weijuan Yang,
Zhejiang University, China
Jianlong Wan,
Huazhong University of Science and Technology, China
Huahua Xiao,
University of Science and Technology of China, China

***Correspondence:**
Xing Li
lixing@ms.giec.ac.cn
Jing Zhang
zhangjing@ms.giec.ac.cn

Specialty section:
This article was submitted to Advanced Clean Fuel Technologies, a section of the journal Frontiers in Energy Research

Received: *03 January 2022*
Accepted: *20 January 2022*
Published: *04 March 2022*

Citation:
Li X, Xie S, Zhang J, Zhao D and Wang X (2022) Numerical Study on the Effect of Wall Thickness on the Combustion Characteristics of Non-premixed Hydrogen Micro-jet Flame. Front. Energy Res. 10:847651. doi: 10.3389/fenrg.2022.847651

INTRODUCTION

With the increasing consumption of fossil fuels and the worsening of the environmental issues, the interests on alternative fuels have been significantly increased in the last decade (Alazemi and Andrews, 2015). Among the alternative fuels, hydrogen can be produced from flexible renewable energy sources, such as wind and solar power generation. Moreover, the application of hydrogen combustion also has advantages in emissions, since it has no CO_2 and soot generations (Sharma and Ghoshal, 2015; Dimitriou and Tsujimura, 2017). These advantages make it as one of the promising candidates for future energy system.

Extensive work has been conducted to study the combustion characteristics of hydrogen or hydrogen blend fuels in various power systems. The pure hydrogen-fueled gas turbine burner has been tested (Cappelletti and Martelli, 2017). The results show that low NOx emission can be achieved by using hydrogen flame. The combustion characteristics of jet-A and hydrogen flames in a turbojet engine have been compared based on numerical computation (Kahraman et al., 2018). Comprehensive information on the engine working at hydrogen fueled condition was obtained. The performance of gasoline engine with hydrogen addition has been studied experimentally (Yu et al., 2017). It was found that the power output and thermal efficiency

of the engine can be improved by using hydrogen/gasoline blends. The operating parameters of a gasoline engine using hydrogen/natural gas blend fuel have been obtained by numerical computation (Zareei et al., 2018).

On the other hand, the hydrogen flame can also be directly employed as a heat source by using a porous medium burner (Nozari et al., 2017; Jia et al., 2018) or micro-jet array burner (Kuwana et al., 2016; Li et al., 2018; Rajasegar et al., 2019; Choi et al., 2021). The micro-jet array burner consists of many single micro-jet burners with specific distribution strategy (Kuwana et al., 2016). The management of a single micro-jet flame is important for the whole performance of the micro-jet array burner. Consequently, knowledge on the combustion characteristics of a single micro-jet flame is useful in the design of a micro-jet array burner.

The combustion characteristics of micro-jet flames have been explored for the development of micro energy and power systems in the past (Cheng et al., 2005; Cheng et al., 2008; Fujiwara and Nakamura, 2013; Hossain and Nakamura, 2015; Gao et al., 2016; Zhang et al., 2016; Gao et al., 2017; Li et al., 2017). The species distribution of hydrogen micro-jet flame has been measured by using laser diagnostic techniques (Cheng et al., 2005). The comparisons show that the computational temperature and species distributions agree well with the experimental results. The standoff behavior of laminar methane micro-jet flame was investigated by two-dimensional numerical computation with a detailed reaction mechanism (Cheng et al., 2008).

More effects on the combustion characteristics of micro-jet flame were investigated with the development of computation and experiment methods. The thermal interaction between the H_2 micro-jet flame and the solid tube was included in the numerical study (Hossain and Nakamura, 2015; Gao et al., 2016). It was found that the hydrogen flame can be stabilized at very low fuel flow velocity, and the burner tip is substantially heated up due to the heat transferred from the flame. Meanwhile, the experimental and numerical study of a hydrogen micro-flame also reveals that the micro-burner was heated by the flame, and the thermal interaction between the flame and burner has a significant effect on the combustion characteristics of the flame (Zhang et al., 2016). Generally, the previous studies suggest that the thermal interaction between the hydrogen flame and the burner is an important factor on the performance of the hydrogen micro-burner (Hossain and Nakamura, 2015; Gao et al., 2016; Zhang et al., 2016; Gao et al., 2017). However, the effect of wall thickness, which is a primary parameter of the burner, on the combustion characteristics of the hydrogen flame was not clarified.

The primary target of the present work is to investigate the effect of the tube wall thickness on the hydrogen micro-jet flame. The combustion characteristics of a hydrogen burner with the same inner diameter and three different wall thicknesses were investigated by including the heat exchange between solid tube and gases. The temperature and species distributions and combustion efficiency were compared in detail. The effect of wall heat transfer characteristics was also investigated.

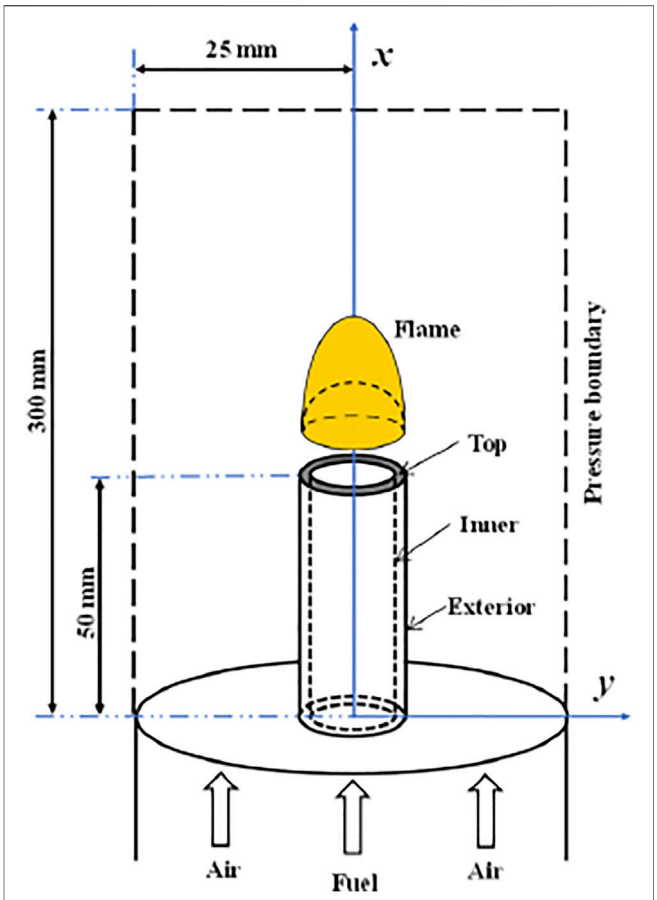

FIGURE 1 | Physical model.

COMPUTATIONAL METHODS

The schematic diagram of the physical model of the micro-jet flame in the present study is drawn in **Figure 1**. The hydrogen gas is issued into air through a stainless steel micro fuel tube, and a diffusion flame is formed near the nozzle exit. A two-dimensional axisymmetric geometric model was employed for the micro-jet flame. The inner diameter (d) and length of the micro-tube were fixed at 0.42 and 50 mm, respectively. Three different tube wall thicknesses (δ), 0.14, 0.36, and 0.84 mm were selected for the numerical study and comparison.

The continuum hypothesis and the Navier–Stokes equations are still suited to the present case for the Knudsen number, which is much smaller than the critical value of 10^{-3} (Beskok and Kamiadakis, 1999). The governing equations for the gaseous mixture includes mass, momentum, energy, and species conservation equations:

$$\nabla \cdot (\rho u_i) = 0 \tag{1}$$

$$\nabla \cdot (\rho u_i u_i) = -\nabla p + \nabla \cdot (\mu \nabla u_i) + \rho g \quad (2)$$

$$\nabla \cdot (\rho u_i T) = \frac{1}{C_p}\nabla \cdot (\lambda \nabla T) - \frac{1}{C_p}\sum_n h_n\{\omega_n + \nabla \cdot [\rho D_n \nabla Y_n + \rho D_n^T \nabla (\ln T)]\} \quad (3)$$

$$\nabla \cdot (\rho u_i Y_n) = \nabla \cdot [\rho D_n \nabla Y_n + \rho D_n^T \nabla (\ln T)] + \omega_n \quad (4)$$

and the state equation:

$$p = \rho R_0 T \sum_n \frac{Y_n}{M_n} \quad (5)$$

where u is the velocity vector; the subscript i represents the different direction components in the space; ρ, μ, p, g, T, λ, C_p, and R_0 are the density, viscosity, pressure, gravitational acceleration, temperature, thermal conductivity, heat capacity, and universal gas constant, respectively; and D_n, ω_n, Y_n, h_n, and M_n are the mass diffusion coefficient, species production rate, mass fraction, enthalpy, and molecular weight, respectively. The subscript n represents a certain species. D_n^T is the thermodiffusion coefficient. The solid tube wall was assumed as a nonslip boundary condition. The computation includes both fluid and solid domains. The heat transfer between the gases and surfaces of the micro-tube (inner, top, and exterior) was considered based on the coupling boundary condition.

The governing equations mentioned above were discretized by using the finite volume method and solved by using the open-source framework OpenFOAM (OpenFOAM, 2016). The SIMPLE algorithm was selected to deal with the pressure and velocity coupling in the equations. The laminar finite-rate reaction model was selected, since the experimental results showed that hydrogen micro-jet flame burn as laminar flame (Zhang et al., 2016). The C1 chemical mechanism (Bilger et al., 1999), which includes 17 species and 58 reactions, was employed in the study. Ever since, it was shown that the hydrogen micro-jet flames computed by using the C1 and GRI 3.0 (Smith et al., 1999) mechanisms are the same (Li et al., 2018). Thermodynamic and transport properties of the gaseous species were obtained from the database of CHEMKIN-PRO (CHEMKIN, 2013). The specific heat and density of mixture gas were calculated by mixing law and incompressible ideal gas law, respectively.

The velocity inlet boundaries were used for the fuel and air inlets, and the pressure boundary condition (1.0 atm) was specified at the outlet. The fuel stream was injected into the coflow air at a flow velocity of 5 cm/s. A uniform velocity profile of air coflow was achieved at the inlet by using a ceramic honeycomb. The initial temperatures of fuel and air were 300 K. The thermal conductivity of the stainless steel solid tube is set as 16.27 W/(m • K). The overall calculation domain is 300 mm × 25 mm, which is sufficiently larger than the jet flame. It was confirmed that a further increase in the computation domain has negligible effect on the computation results.

The quadrangular grids were adopted, and refined grids were utilized near the tube wall for high resolution in the numerical computation. The grid size is 17 μm at the tube exit and gradually stretched toward the far boundaries. The independence of the grid was confirmed under different flow conditions, and a set of grids with 169,000 cells was employed. The simulation convergence was confirmed when the residuals of all governing equations approached steady states. A steady state was declared until the fluctuation of the maximum flame temperature was less than 1 K. Convergence of the result was achieved based on the residuals to be less than 10^{-6}.

RESULTS AND DISCUSSION

Validation of the computational method

The experimental study of hydrogen micro-jet flames has been conducted in our previous work (Zhang et al., 2016). The present computation method was validated by comparison with the experimental results at different tube diameter and wall thickness conditions. The hydrogen micro-jet flames achieved by micro-tubes with inner diameters (4) of 0.28 and 0.71 mm and wall thickness (δ) of 0.1 and 0.17 mm were measured by using planar laser-induced fluorescence technique for OH radical (OH-PLIF). The OH-PLIF system, based on a LaVision LIF system, was employed. The OH fluorescence was captured by an ICCD camera, which was perpendicular to the laser sheet. The detailed OH-PLIF measurement method was given in the literature (Zhang et al., 2016; Li et al., 2017). To obtain the whole OH chemiluminescent image of the flame, the laser sheet covered the fuel tube tip. The missing OH fluorescence could be found on the bottom right corner of the flame due to the block of the opaque solid tube on the opposite side of the laser beam; therefore, the OH contours obtained from experiment are asymmetric. It was further demonstrated that the fuel tube tip is circled by the OH zone, and the flames attached to the exterior surface of the solid tube.

The measured and computed OH distributions are shown in **Figure 2**. The variations in measured and computed height to width aspect ratios of flames (defined by OH distributions of the micro-flames) at different fuel flow Reynolds numbers (Re) are plotted in **Figure 3**. The height-to-width ratio, which reflects the flame deformation rate, increases with Re, and the measurements agree well with the computed results with differences less than 4%. It can be found that the flame shapes obtained from both experiment and computation are in good agreement. Consequently, it is reasonable to believe that the characteristics of hydrogen micro-jet diffusion flame with different wall thicknesses can be captured by the present numerical method.

Temperature distributions and fuel conversion ratio

The hydrogen micro-jet flames with tube (d = 0.42 mm) wall thickness of 0.14, 0.36, and 0.84 mm at different fuel jet velocities were computed. **Figure 4** shows that the maximum flame temperature decreases smoothly with decreasing fuel flow velocity in the velocity range of 1–5 m/s. However, a rapid decrease can be seen in the velocity range of 0.4–1 m/s. It can be found that the maximum flame temperature decreases with the

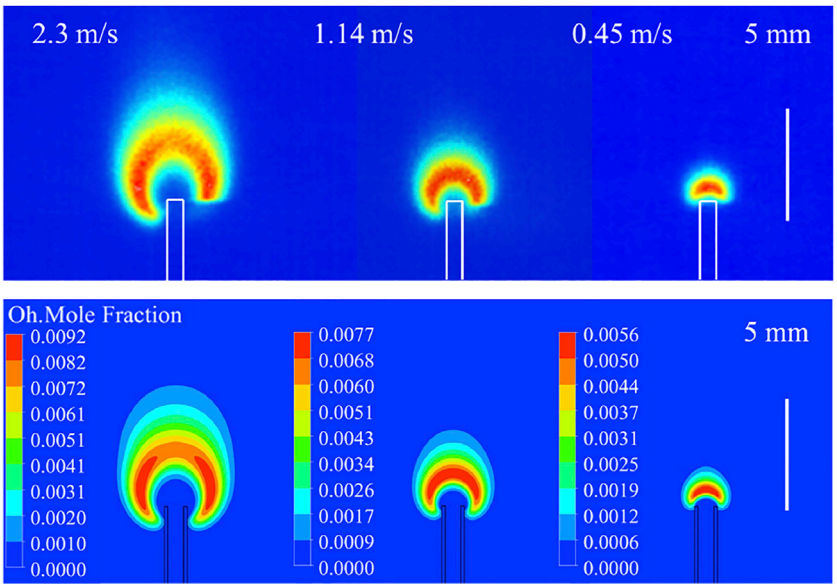

FIGURE 2 | Measured (above) and computed (below) OH contours of hydrogen micro-jet flames at different fuel flow velocities (d = 0.71 mm, δ = 0.17 mm).

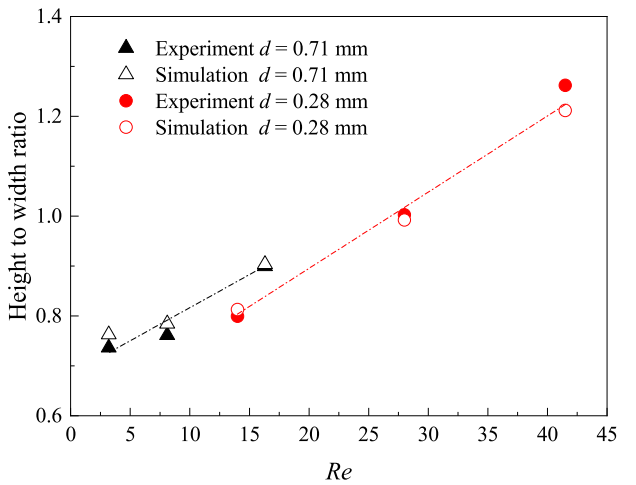

FIGURE 3 | Comparison of the measured and computed height-to-width ratios of the flame achieved by micro-tubes with different inner diameters and wall thicknesses (case 1: d = 0.71 mm, δ = 0.17 mm; case 2: d 0.28 mm, δ = 0.1 mm).

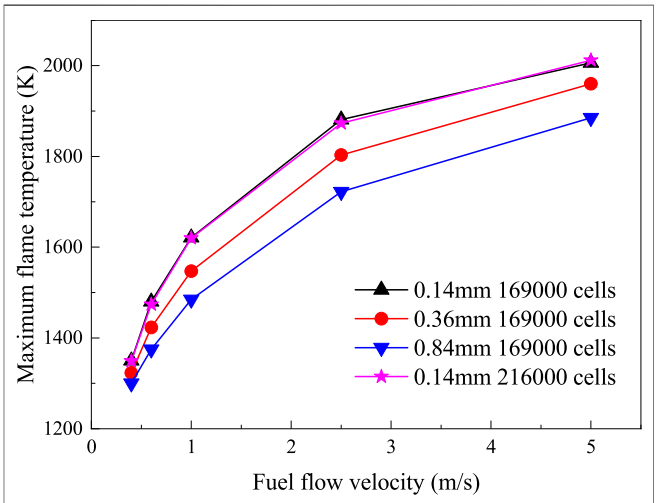

FIGURE 4 | The variation of computed maximum flame temperature versus fuel flow velocity with different wall thicknesses and mesh densities (δ = 0.14, 0.36, and 0.84 mm).

increasing wall thickness at the same fuel velocity. The temperature difference between the flames is significant in the high flow-velocity range, while the difference is modest in the low-velocity region.

Figure 5 shows the temperature contours of the nonpremixed hydrogen micro-jet flames with three different tube wall thicknesses. It can be seen that variations in temperature distributions versus fuel flow velocities are similar for the flames with thin- and thick-walled tubes. The high-temperature region shrinks gradually with the decreasing fuel velocity. The temperature distribution is influenced by the wall thickness. At high fuel velocity of 2.5 m/s, the top surface of the thick-walled tube is partly in the high-temperature region, while a greater area of the thin-walled tube is immersed in the region. Compared with the thin-walled tube case, the high-temperature region is smaller at a fuel velocity of 1 m/s for the thick-walled tube. Moreover, the high-temperature region moves to the tube exit at a low fuel velocity, 0.4 m/s, and the gaseous temperature around the exit of the thin-walled tube is significantly higher than that of the thick-walled tube.

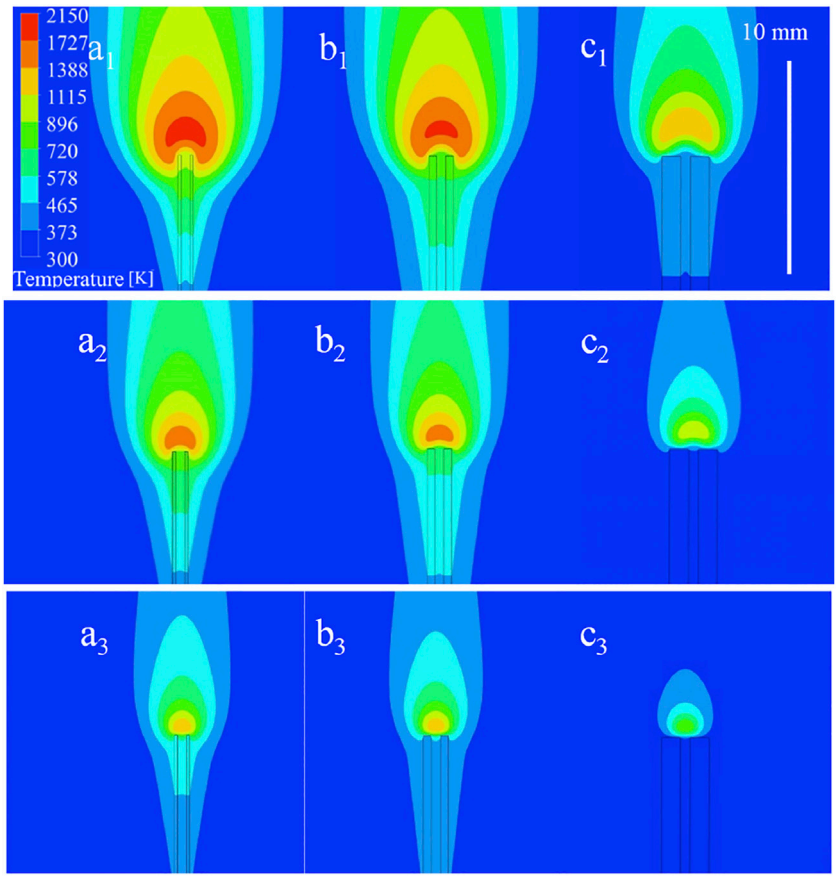

FIGURE 5 | Temperature distributions of flames at different flow conditions **(a1)** δ = 0.14 mm, 2.5 m/s; **(b1)** δ = 0.36 mm, 2.5 m/s; **(c1)** δ = 0.84 mm, 2.5 m/s; **(a2)** δ = 0.14 mm, 1 m/s; **(b2)** δ = 0.36 mm, 1 m/s; **(c2)** δ = 0.84 mm, 1 m/s; **(a3)** δ = 0.14 mm, 0.4 m/s; **(b3)** δ = 0.36 mm, 0.4 m/s; **(c3)** δ = 0.84 mm, 0.4 m/s.

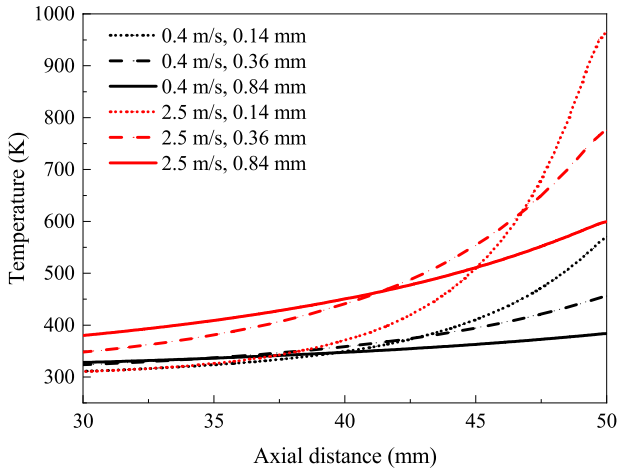

FIGURE 6 | Temperature profiles on the centerline of the tube walls for different wall thicknesses.

The computational temperature distributions in the solid tubes can also be seen in **Figure 5**. It can be seen that the solid micro-tube was heated by the micro-flame. The variation in the high-temperature region of flame affects the temperature of the solid micro-tube. The temperature profiles on the centerline of the solid tube wall (x direction) with different thicknesses were analyzed since it was reported that the preheating effect plays a key role in the temperature distributions and the flow fields around the tube exit (Fujiwara and Nakamura, 2013).

The temperature profiles on the centerline of the solid tube at different conditions are drawn in **Figure 6** (the tube exit is at x = 50 mm). The temperature in the solid tube increases along the distance from inlet to exit in all cases, and the peak temperature position is on the top surface of the tube exit. The maximum temperature (967 K) at δ = 0.14 mm, 2.5 m/s is higher than that of the other cases, and the maximum temperature (387 K) at δ = 0.84 mm, 0.4 m/s is the lowest. The comparison shows that the maximum temperature of the solid tube decreases with decreasing fuel jet velocity. Although the solid temperature of

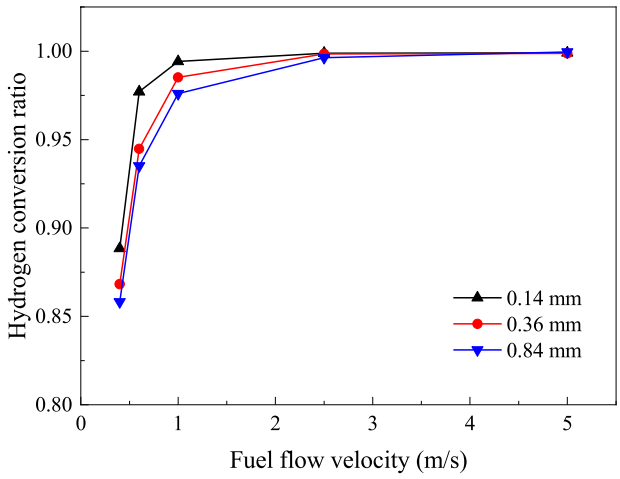

FIGURE 7 | The variation of hydrogen conversion ratio versus fuel flow velocity with different wall thicknesses (δ = 0.14, 0.36, and 0.84 mm).

the tube with a thick wall is relatively uniform, the maximum solid temperature of the thin-walled tube is much higher than the thick-walled tube at the same fuel flow velocity. It can be concluded that reduced wall thickness can increase the centerline temperature of the tube wall near the tube exit.

The fuel conversion ratios of flame with different wall thicknesses at the fuel jet velocity of 0.4–5 m/s were also compared. The hydrogen conversion ratio α is computed as follows:

$$\alpha = \frac{\dot{m}_\omega}{\dot{m}} \tag{6}$$

where $\dot{m}_\omega$, $\dot{m}$ are the hydrogen consumption rate and mass flow rate of input hydrogen, respectively. **Figure 7** shows that the hydrogen conversion ratio is rapidly increased in the low fuel velocity range (0.4–1.0 m/s), and the hydrogen conversion ratio is smoothly increased when the fuel flow velocity varies from 1.0 to 2.5 m/s. The conversion ratio for the thin-walled case (δ = 0.14 mm) is higher than those of the thick-walled cases at relatively low fuel flow velocity. It illustrates that the wall thickness has significant effects on the conversion ratio at low fuel flow velocities, and the combustion efficiency needs to be improved.

The maximum conversion ratio (approaching 100%) can be achieved at high fuel flow velocity (≥2.5 m/s) for the tubes with different wall thicknesses, and there exists a strong preheating effect. It is observed that the maximum conversion ratio values for these cases have little distinctions. However, the flame issued from the thin-walled tube (δ = 0.14 mm) reaches the peak value at a smaller fuel velocity. The results reveals that the thin-walled tube is more appropriate in achieving a relatively complete combustion.

Flame structures

In order to further clarify the effects of wall thickness on the flame structures and thermal interactions, the computational OH distributions of the micro diffusion flames were analyzed, as shown in **Figure 8**. It can be seen that the OH distributions are affected by the wall thickness.

The top section of the solid tube is tightly circled by the OH zone for the thin-walled tube at a fuel flow velocity of 2.5 m/s (**Figure 8a1**), and a spherical flame attaches the lip of the tube, whereas the contact area between the flame and the thick-walled tube is significantly smaller for the thick tube (**Figure 8c1**). The attachment region is transferred from the exterior surface to the top surface, and the shape of the flames changed from sphere to hemisphere. When the fuel velocity decreases to 1 m/s, the OH zone shifts to the exit of the tube, the OH zone locates on the top surface of the thick wall in **Figures 8b2, c2**, and the flames turn from hemisphere shape to umbrella shape. However, the flame achieved by the thin-walled tube still adheres to the exterior surface (**Figure 8a2**). At the near-extinction limit, where the fuel velocity is 0.4 m/s, the umbrella-shaped OH regions are floated on the tube exit, the bottom of the small OH zones are flat, and it can be seen that the effect of wall thickness on the OH distribution is not significant.

The maximum OH mole concentrations of flames achieved by the different tube wall thicknesses also show distinction, except the main difference in flame shape and attachment behavior. It can be found that the maximum OH mole concentration decreases with increase in the wall thickness.

Effect of wall thickness on heat recirculation

To further compare the heat recirculation through the tube walls to the fuel, which can enhance the combustion, the thermal interactions at three different wall thicknesses (δ = 0.14, 0.36, and 0.84 mm) were also analyzed. The heat transfers through the wall surfaces at different fuel flow velocities were analyzed, and the case at a fuel flow velocity of 2.5 m/s are shown in **Figure 9** for a demonstration. The heats absorbed from the flame through the top and exterior surfaces are finally transferred to the fuel steam via the inner surface for the thin-walled case (δ = 0.14 mm). However, the absorbed heats from the top surfaces are dissipated to the fuel and air streams through the inner and exterior surfaces for the thick-walled tube cases. The heat dissipated to coflow ambient through the exterior surfaces is increased with increasing wall thickness, and the corresponding maximum temperature of the solid tube is decreased. The results also show that the heat transfers through the inner surface deceases with increasing thickness.

The net heat transfer to the fuel steam, which can benefit the flame, was calculated and normalized by the total heat absorbed by the wall surfaces. The normalized heat exchanges for preheating fuel Q_N was defined as follows:

$$Q_N = \frac{\int q \mathrm{d}A}{Q_t} \tag{7}$$

where q, A are the local heat flux density and the corresponding surface (inner surface) area, respectively. Q_t is the total heat absorption through other wall surfaces. The results at different fuel flow velocities are plotted in **Figure 10**, and the positive and

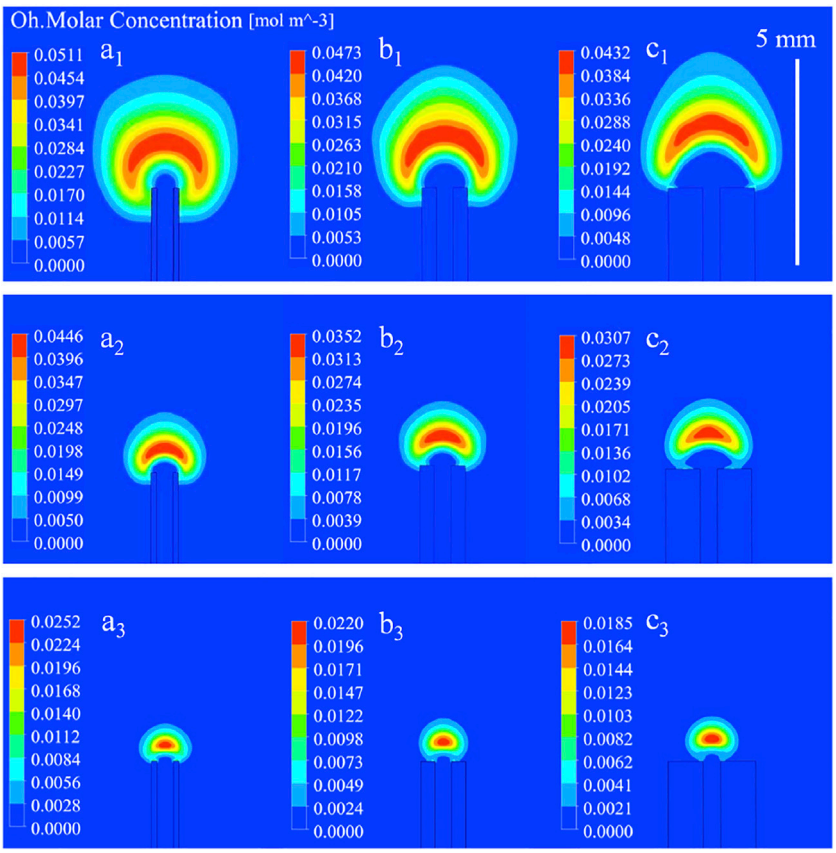

FIGURE 8 | Computed OH mole concentrations of flames at different flow conditions **(a1)** δ = 0.14 mm, 2.5 m/s; **(b1)** δ = 0.36 mm, 2.5 m/s; **(c1)** δ = 0.84 mm, 2.5 m/s; **(a2)** δ = 0.14 mm, 1 m/s; **(b2)** δ = 0.36 mm, 1 m/s; **(c2)** δ = 0.84 mm, 1 m/s; **(a3)** δ = 0.14 mm, 0.4 m/s; **(b3)** δ = 0.36 mm, 0.4 m/s; **(c3)** δ = 0.84 mm, 0.4 m/s.

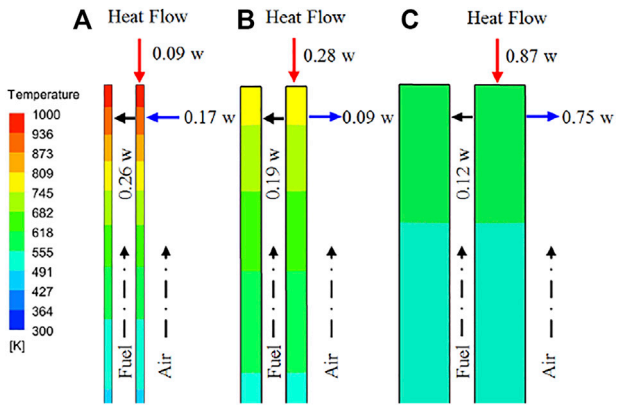

FIGURE 9 | Schematic of heat exchanges through surfaces at fuel flow velocity of 2.5 m/s: **(A)** δ = 0.14 mm; **(B)** δ = 0.36 mm; **(C)** δ = 0.84 mm.

negative values on the vertical axis mean heat absorption and heat dissipation, respectively. The results reveal that reducing the thermal conductive wall thickness can improve the heat recirculation at fuel velocities of 1 and 2.5 m/s, while all the micro-tubes play a negative role on the hydrogen flame at the fuel velocity of 0.4 m/s because the heat is transferred from the gas to the inner surfaces. It can be seen that the heat loss through the inner surface of thin-walled cases is lower than those of thick-walled cases, due to the difference in flame structure and temperature distribution (**Figures 5** and **8**). However, the heat exchanges through inner surfaces only account for a small percentage of the total heat absorption at low fuel velocity. The heat loss through the exterior surfaces is mainly from the absorbed heat from the top surface of the solid tube.

Numerical experiment

As known, a properly maintained high wall temperature and utilized heat recirculation can facilitate the gas reaction and enhance the flame. To provide guidance for the thermal management of the jet flame burner, especially for the thick-walled tube, an innovative numerical experiment was conducted to compensate for the negative effect of heat loss. An artificial wall boundary condition was used, where the exterior surface of the tube wall was treated as an adiabatic wall boundary, while the top and inner surfaces were thermal coupling boundaries.

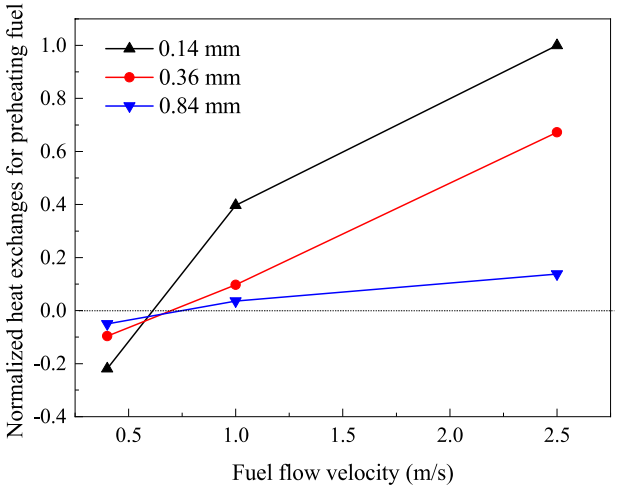

FIGURE 10 | Normalized heat exchanges responsible for preheating fuel at different fuel flow velocities (δ = 0.14, 0.36, and 0.84 mm).

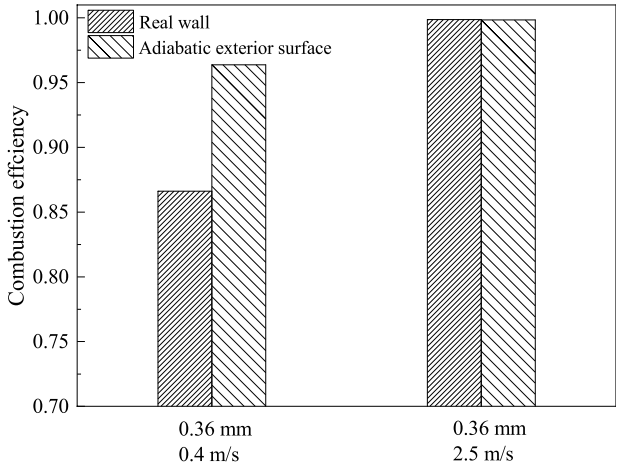

FIGURE 12 | The variation in combustion efficiency under real and artificial wall boundary conditions (0.4 and 2.5 m/s, δ = 0.36 mm).

The computational flame temperature with real and artificial wall conditions at the fuel velocities of 0.4 and 2.5 m/s were compared, and the wall thickness was fixed at $\delta = 0.36$ mm. The gas temperature profiles along the centerline (x direction, $y = 0$) with both the conjugate wall and adiabatic wall boundary conditions are shown in **Figure 11** (the tube exit is at the position $x = 50$ mm). At the fuel velocity of 0.4 m/s, the maximum temperature of the flame and the fuel temperature in the tube with the adiabatic exterior surface are significantly higher than those of the real wall tubes. A similar behavior can be found in the case of the high fuel velocity (2.5 m/s), although the temperature difference is reduced. The numerical results indicate that the preheating effect on the fuel is enhanced, and the maximum flame temperature on the centerline is increased when the heat loss through the exterior surface of the relatively thick wall tube is suppressed.

The results of combustion efficiency (η) with different wall boundaries are calculated and shown in **Figure 12**, and the combustion efficiency is defined as follows:

$$\eta = \frac{Q}{H \cdot \dot{m}_f} \tag{8}$$

where Q, H, and $\dot{m}_f$ are the overall heat generation of flame, low heat value of fuel, and mass flow rate of input fuel, respectively. It can be seen that the combustion efficiency with the adiabatic exterior surface is obviously increased compared with that of the real wall tube at a low fuel velocity of 0.4 m/s. However, the combustion efficiencies for the high fuel velocity of 2.5 m/s are the same. The results of the numerical experiments above suggest that wall thickness and surface material should be considered when developing and optimizing micro-jet combustors. The thick-walled burner with the insulating exterior surface can also stabilize a jet flame and realize an enhanced combustion.

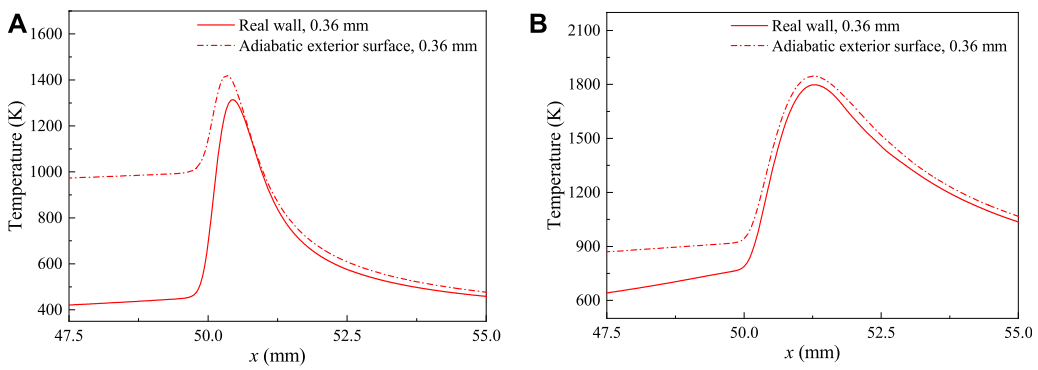

FIGURE 11 | Temperature profiles along the centerline under real and artificial wall boundary conditions: **(A)** 0.4 m/s, δ = 0.36 mm; **(B)** 2.5 m/s, δ = 0.36 mm.

CONCLUSION

The combustion characteristics of hydrogen diffusion flames achieved by micro-tubes with different wall thicknesses and the same inner diameter were investigated numerically to clarify the effect of wall thickness on the flame behaviors and combustion efficiency.

The computed temperature and OH distributions show a remarkable difference when wall thickness is changed. The hydrogen conversion ratios, which reflect the combustion efficiency for tubes with different all thicknesses are almost the same at high fuel jet velocity. However, the hydrogen conversion ratio is decreased with the increase in wall thickness at low fuel flow velocity. The thin-walled tube is more appropriate in maintaining a high fuel conversion ratio.

The computational maximum flame, solid temperatures, and maximum OH mole concentration decrease with increasing wall thickness at a fixed fuel flow velocity. The heat exchange between the flame and solid tube through the top surface is increased with the wall thickness. However, the heat recirculation to the fuel stream is decreased, since the heat loss from the exterior surface is increased. The effect of wall thickness on the micro-jet flame is mainly through its influence on the flame shapes and heat exchange areas of the exterior and top surfaces.

A numerical experiment on the heat conduction characteristics of the exterior surface has been conducted. The results show that the hydrogen micro-jet flame achieved by a tube with a thick wall can be prompted by restraining the heat loss from the exterior surface.

DATA AVAILABILITY STATEMENT

The original contributions presented in the study are included in the article/Supplementary Material, further inquiries can be directed to the corresponding authors.

AUTHOR CONTRIBUTIONS

XL: conceptualization, supervision, methodology, investigation, reviewing and editing, and funding acquisition. SX: data curation, reviewing, and editing. JZ: methodology and investigation. DZ: supervision, reviewing, and editing. XW: reviewing and editing.

FUNDING

This work was supported by the DNL Cooperation Fund, CAS (DNL202006), and National Natural Science Foundation of China (No. 52176139).

REFERENCES

Alazemi, J., and Andrews, J. (2015). Automotive Hydrogen Fuelling Stations: An International Review. *Renew. Sust. Energ. Rev.* 48, 483–499. doi:10.1016/j.rser.2015.03.085

Beskok, A., and Kamiadakis, G. E. (1999). A Model for Flows in Channels Pipes, and Ducts at Micro and Nano Scales. *Microscale Therm. Eng.* 3, 43–77. doi:10.1080/108939599199864

Bilger, R. W., Starner, S. H., and Kee, R. J. (1999). On Reduced Mechanisms for Methane-Air Combustion in Nonpremixed Flames. *Combust. Flame* 80, 135–149. doi:10.1016/0010-2180(90)90122-8

Cappelletti, A., and Martelli, F. (2017). Investigation of a Pure Hydrogen Fueled Gas Turbine Burner. *Int. J. Hydrogen Energ.* 42, 10513–10523. doi:10.1016/j.ijhydene.2017.02.104

CHEMKIN (2013). *CHEMKIN-PRO 15131*. San Diego: Reaction Design.

Cheng, T. S., Chao, Y. C., Chen, C. P., and Wu, C. Y. (2008). Further Analysis of Chemical Kinetic Structure of a Standoff Microjet Methane Diffusion Flame Near Extinction. *Combust. Flame* 152, 461–467. doi:10.1016/j.combustflame.2007.10.007

Cheng, T. S., Chao, Y. C., Wu, C. Y., Li, Y. H., Nakamura, Y., Lee, K. Y., et al. (2005). Experimental and Numerical Investigation of Microscale Hydrogen Diffusion Flames. *Proc. Combust. Inst.* 30, 2489–2497. doi:10.1016/j.proci.2004.07.025

Choi, J., Lee, W., Rajasegar, R., Lee, T., and Yoo, J. (2021). Effects of Hydrogen Enhancement on Mesoscale Burner Array Flame Stability under Acoustic Perturbations. *Int. J. Hydrogen Energ.* 46, 37098–37107. doi:10.1016/j.ijhydene.2021.08.192

Dimitriou, P., and Tsujimura, T. (2017). A Review of Hydrogen as a Compression Ignition Engine Fuel. *Int. J. Hydrogen Energ.* 42, 24470–24486. doi:10.1016/j.ijhydene.2017.07.232

Fujiwara, K., and Nakamura, Y. (2013). Experimental Study on the Unique Stability Mechanism via Miniaturization of Jet Diffusion Flames (Micro-flame) by Utilizing Preheated Air System. *Combust. Flame* 160, 1373–1380. doi:10.1016/j.combustflame.2013.03.002

Gao, J., Hossain, A., Matsuoka, T., and Nakamura, Y. (2017). A Numerical Study on Heat-Recirculation Assisted Combustion for Small Scale Jet Diffusion Flames at Near-Extinction Condition. *Combust. Flame* 178, 182–194. doi:10.1016/j.combustflame.2016.12.028

Gao, J., Hossain, A., and Nakamura, Y. (2016). Flame Base Structures of Micro-jet Hydrogen/methane Diffusion Flames. *Proc. Combust. Inst.* 36, 4209–4216. doi:10.1016/j.proci.2016.08.034

Hossain, A., and Nakamura, Y. (2015). Thermal and Chemical Structures Formed in the Micro Burner of Miniaturized Hydrogen-Air Jet Flames. *Proc. Combust. Inst.* 35, 3413–3420. doi:10.1016/j.proci.2014.08.008

Jia, Z., Ye, Q., Wang, H., Li, H., and Shi, S. (2018). Numerical Simulation of a New Porous Medium Burner with Two Sections and Double Decks. *Processes* 6, 1–18. doi:10.3390/pr6100185

Kahraman, N., Tangöz, S., and Akansu, S. O. (2018). Numerical Analysis of a Gas Turbine Combustor Fueled by Hydrogen in Comparison with Jet-A Fuel. *Fuel* 217, 66–77. doi:10.1016/j.fuel.2017.12.071

Kuwana, K., Kato, S., Kosugi, A., Hirasawa, T., and Nakamura, Y. (2016). Experimental and Theoretical Study on the Interaction between Two Identical Micro-slot Diffusion Flames: Burner Pitch Effects. *Combustion and Flame* 165, 346–353. doi:10.1016/j.combustflame.2015.12.017

Li, J., Huang, H., Bai, Y., Li, S., and Kobayashi, N. (2018). Combustion and Heat Release Characteristics of Hydrogen/air Diffusion Flame on a Micro-jet Array Burner. *Int. J. Hydrogen Energ.* 43, 13563–13574. doi:10.1016/j.ijhydene.2018.04.195

Li, X., Zhang, J., Yang, H., Jiang, L., Wang, X., and Zhao, D. (2017). Combustion Characteristics of Non-premixed Methane Micro-jet Flame in Coflow Air and thermal Interaction between Flame and Micro Tube. *Appl. Therm. Eng.* 112, 296–303. doi:10.1016/j.applthermaleng.2016.10.082

Nozari, H., Karaca, G., Tuncer, O., and Karabeyoglu, A. (2017). Porous Medium Based Burner for Efficient and Clean Combustion of Ammonia-Hydrogen-Air Systems. *Int. J. Hydrogen Energ.* 42, 14775–14785. doi:10.1016/j.ijhydene.2017.03.234

OpenFOAM (2016). The Open Source CFD Toolbox. Available at: http://www.openfoam.org.

Rajasegar, R., Choi, J., McGann, B., Oldani, A., Lee, T., Hammack, S. D., et al. (2019). Mesoscale Burner Array Performance Analysis. *Combust. Flame* 199, 324–337. doi:10.1016/j.combustflame.2018.10.020

Sharma, S., and Ghoshal, S. K. (2015). Hydrogen the Future Transportation Fuel: From Production to Applications. *Renew. Sust. Energ. Rev.* 43, 1151–1158. doi:10.1016/j.rser.2014.11.093

Smith, G. P., Golden, D. M., Frenklach, M., Moriarty, N. W., Eiteneer, B., Goldenberg, M., et al. (1999). gri_mech. Available at: http://www.me.berkeley.edu/gri_mech/.

Yu, X., Du, Y., Sun, P., Liu, L., Wu, H., and Zuo, X. (2017). Effects of Hydrogen Direct Injection Strategy on Characteristics of Lean-Burn Hydrogen-Gasoline Engines. *Fuel* 208, 602–611. doi:10.1016/j.fuel.2017.07.059

Zareei, J., Rohani, A., and Wan Mahmood, W. M. F. (2018). Simulation of a Hydrogen/natural Gas Engine and Modelling of Engine Operating Parameters. *Int. J. Hydrogen Energ.* 43, 11639–11651. doi:10.1016/j.ijhydene.2018.02.047

Zhang, J., Li, X., Yang, H., Jiang, L., Wang, X., and Zhao, D. (2016). Study on the Combustion Characteristics of Non-premixed Hydrogen Micro-jet Flame and the thermal Interaction with Solid Micro Tube. *Int. J. Hydrogen Energ.* 42, 3853–3862. doi:10.1016/j.ijhydene.2016.07.255

Conflict of Interest: The authors declare that the research was conducted in the absence of any commercial or financial relationships that could be construed as a potential conflict of interest.

Advantages of publishing in Frontiers

OPEN ACCESS
Articles are free to read for greatest visibility and readership

FAST PUBLICATION
Around 90 days from submission to decision

HIGH QUALITY PEER-REVIEW
Rigorous, collaborative, and constructive peer-review

TRANSPARENT PEER-REVIEW
Editors and reviewers acknowledged by name on published articles

Frontiers
Avenue du Tribunal-Fédéral 34
1005 Lausanne | Switzerland

Visit us: www.frontiersin.org
Contact us: frontiersin.org/about/contact

REPRODUCIBILITY OF RESEARCH
Support open data and methods to enhance research reproducibility

DIGITAL PUBLISHING
Articles designed for optimal readership across devices

FOLLOW US
@frontiersin

IMPACT METRICS
Advanced article metrics track visibility across digital media

EXTENSIVE PROMOTION
Marketing and promotion of impactful research

LOOP RESEARCH NETWORK
Our network increases your article's readership